



AALBORG UNIVERSITY
STUDENT REPORT



Dynamic Modelling of Monopiles for Offshore Wind Turbines

MSc Structural and Civil Engineering

Aalborg University

7th June 2019



AALBORG UNIVERSITY
STUDENT REPORT

The School of Engineering and Science

Department of Civil Engineering

Thomas Manns Vej 23

9220 Aalborg East

Title:

Dynamic Modelling of Monopiles for
Offshore Wind Turbines

Project:

Master Thesis

Project period:

September 2018 - June 2019

Participants:

Casper Østergaard Nielsen

Kenneth Christiansen

Thomas Skov-Pedersen

Supervisors

Martin Underlin Østergaard

Johan Clausen

Pages:

Main report: 170

Appendix : 63

Hand in: 7th June 2019

Synopsis:

This thesis concerns the problematics of estimating the soil-structure interaction for a monopile using the current design guidelines in the offshore sector. These recommendations are implemented in a simple 1D Finite Element model used to estimate the first eigenfrequency of the OWT analysed.

The thesis is divided into four stages. The first stage serves as a base of knowledge, where the design tendencies within the field of OWT foundations are investigated and the theory for basic dynamics of soil is covered. Stage 2 considers the set up of a simple Finite Element model, representing the behaviour of an OWT by modelling a vertical stick with a mass on top and to analyse the importance of the input parameters. The purpose of Stage 3 is to incorporate the effect from the soil surrounding the foundation of the OWT, by modelling the soil-structure interaction using the original API p - y curves recommended in the current design guidelines. Investigations of improvements to the current design guidelines and the method proposed by the PISA project for estimating the soil-structure interaction are explored. Also, the Finite Element model is separated in order to model the OWT and the foundation separately and still being able to estimate the first eigenfrequency of the full system. Lastly, Stage 4 considers the utilisation of the commercial program Plaxis 3D to analyse the arising subjects from the previous stages. The stage will contain three analyses, concerning the estimation of the first eigenfrequency for an OWT, the extraction of p - y curves from a 3D model and the change in the displacement field of the soil around the monopile as the diameter of a monopile is increasing.

Resume

Det overordnede emne for dette speciale er modellering af jord-struktur interaktion, med henblik på at bestemme den første egenfrekvens for en havvindmølle. Hertil er der taget udgangspunkt i de nuværende anbefalinger, der er inden for modellering af jord-struktur interaktion for offshore sektoren.

Opstartsfasen i specialet inkluderer et litteraturstudie, hvor designmetoder inden for relevante emner som jord-struktur interaktion, modellering af dæmpning og udmattelse er præsenteret. Dernæst gennemgås relevante emner inden for dynamiske belastede konstruktioner og jorden, som konstruktionen er funderet i.

Som en indledende fase til bestemmelsen af egenfrekvenser opstilles en simpel 1D model, hvor jord-struktur interaktion er ekskluderet, med henblik på at undersøge hvordan den første egenfrekvens ændres i takt med at input til selve strukturen varieres. Dette leder videre til en udvidet 1D model, der inkluderer jord-struktur interaktion ved brug af p - y kurver på baggrund af de nuværende anbefalinger i offshore sektoren. Sensitiviteten af input parametre til metoden undersøges med henblik på ændringer i den første egenfrekvens. Efterfølgende er forbedringer til de anbefalede p - y kurver undersøgt og effekten af forbedringerne er præsenteret. Udover forbedringerne til p - y kurverne er en alternativ metode introduceret, der går under navnet PISA metoden (Pile Soil Analysis).

Udover den simple- og udvidede 1D model, er programmet Plaxis 3D anvendt til at opstille en mere avanceret model til f.eks. bestemmelse af den første egenfrekvens for en havvindmølle. Plaxis 3D er også anvendt til at sammenholde p - y kurver udtrukket fra programmet, med kurverne der er konstrueret til 1D modellerne ift. anbefalingerne fra offshore sektoren. Til sidst er der undersøgt hvordan et flytningsfelt ændres omkring en monopæl, når diameteren forøges i takt med at havvindmøllerne bliver større og større. Dette er udført med henblik på at kommentere på mangler ved de anbefalede metoder til modellering af jord-struktur interaktion.

Preface

This long Master Thesis is made by three 4th semester students, studying the Master's programme at Aalborg University in Structural and Civil Engineering. The subject of the Master has been chosen as a result of the three writers interests and curiosity within the field of offshore wind turbines. A long Master Thesis consists of 45 ECTS per person, i.e. 135 ECTS combined.

Reading Guide

The overall structure of the thesis is build up based on four stages, where each stage has its own specific purpose in the thesis.

Figures, tables and equations have a specific identification number, where the first number defines the chapter and the second number defines the number of figure, table or equation in the current chapter.

The references through the thesis can either be used as an active reference or a passive reference. Active references are defined as "Last-name, Year of publication" and should be read as a part of the sentence they are included in. Passive references are defined as "[Last-name, Year of publication]" and can be found at the end of the sentence. A passive reference before the dot means the reference is for the current sentence, while a passive reference after the dot means the reference applies for the full text section. In some cases it is more reasonable to refer to the reference by title. In such cases the title will be shown as italic to emphasise that the reference is to the title and not the author. In a few cases, multi-references are used, where the references will appear in the same bracket, separated by a ";". If a figure reference states "Modified" in the reference bracket, it implies that the figures origins from the reference, but it is modified by the authors to better illustrate its purpose in the Master Thesis. The list of references is located after the main report, but before the appendices.

Appendices are located after the main report where each appendix is named by a capital letter.

Throughout the thesis, the terms wind turbine and offshore wind turbine will be used extensively, and will therefore be referred to as WT and OWT respectively.

Two homemade 1D FE models are present in this report, the first appears in Stage 2 and the latter in Stage 3. These will be referred to as "Simple Model" and "Extended Model" respectively throughout the thesis.

CONTENTS

1	Introduction	1
I	Stage 1	
2	Literature Study	7
3	Dynamic Properties	17
II	Stage 2	
4	Simple Dynamic Model	29
III	Stage 3	
5	Soil Reaction Curves	49
6	Extended Model	61
7	Improvements	87
8	Separation of Extended Model	101
IV	Stage 4	
9	Application of Plaxis 3D	113
10	Convergence Analysis	123
11	Free Vibration Analysis	133
12	Extraction of <i>p-y</i> Curves	143

13	Displacement Field	153
----	--------------------------	-----

V	Closure
----------	----------------

14	Discussion	161
----	------------------	-----

15	Conclusion	165
----	------------------	-----

16	References	170
----	------------------	-----

VI	Appendix
-----------	-----------------

A	EOM SDOF OWT Model	173
---	--------------------------	-----

B	FEM - Stage 2	175
---	---------------------	-----

C	Elasticity	179
---	------------------	-----

D	SDOF Cantilever Beam	181
---	----------------------------	-----

E	Soil Reaction Curves	187
---	----------------------------	-----

F	FEM - Stage 3	189
---	---------------------	-----

G	Convergence of Extended Model	195
---	-------------------------------------	-----

H	Modal Decoupling	201
---	------------------------	-----

I	p - y Curve Distribution	203
---	------------------------------------	-----

J	Plaxis 3D Theory	211
---	------------------------	-----

K	Convergence Analysis	219
---	----------------------------	-----

L	Free Vibration Analysis Results	221
---	---------------------------------------	-----

M	Extraction of p - y Curves	231
---	--------------------------------------	-----

1. INTRODUCTION

Energy in form of electricity is a product which is used to drive all parts of the society. The world is relying on electricity more than ever before, and the demand is constantly rising. In fact, the demand for electricity more than doubled in the years from 1990 to 2016. Figure 1.1 illustrates the world wide electricity generation divided into different production categories, where it is observed that the majority of the generated electricity originates from fossil fuels. However, with the limited amount of available fossil fuels in the world, new energy sources like renewable energy is believed to be the future. Also with global warming being a problem which is considered more through the last decades, new sources of energy is needed to provide the necessary electricity to keep the society running, without ruining the environment. A renewable energy source which has the potential to replace fossil fuels is wind energy. The utilisation of wind energy as a source of electricity has increased through the last 25 years, see Figure 1.1, but the full potential of the wind sector is yet to be achieved. Electricity extracted from OWTs alone has the potential to make up for up to 25 % of EU's electricity demand according to a study performed by Hundleby and Freeman, 2017.

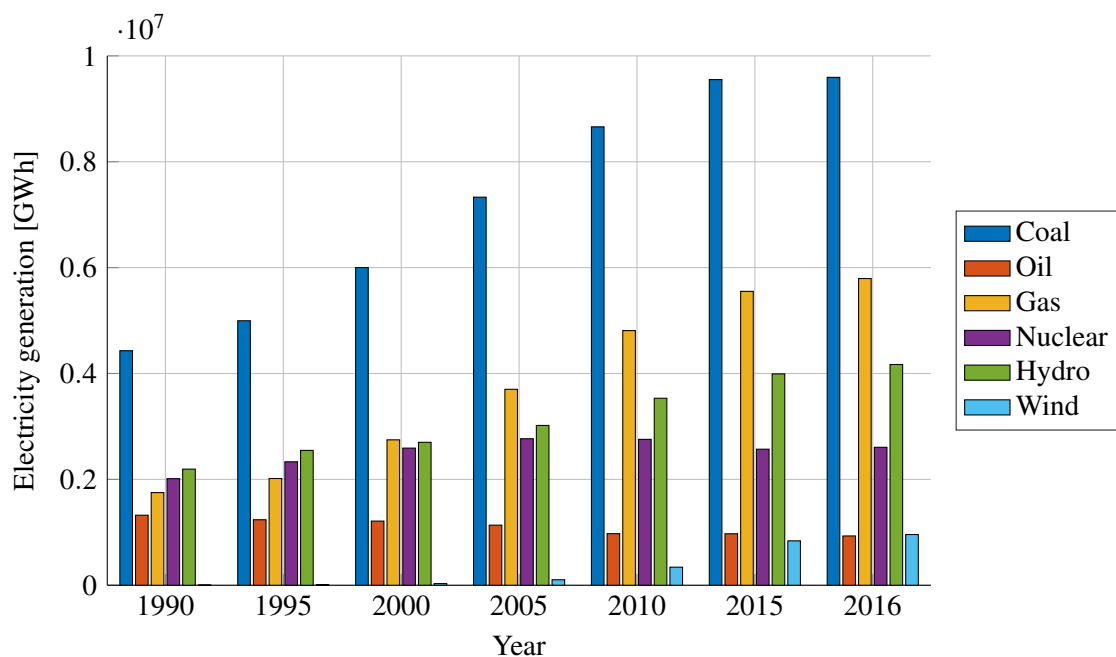


Figure 1.1: Illustration of the world electricity generation divided into production categories [Birol, 2018, Modified].

The idea of using wind energy has existed for more than a 1000 years. Through time wind power has been used to run machines for different purposes like grinding flour or pumping water. In 1887 the first known WT, which produced electricity was made in Scotland. For the next 100 years the concept of a WTs producing energy was further developed and in the 1980s WTs began to be placed offshore around in the Danish seas. In 1991 the first ever OWT farm was constructed, which was placed in the southern danish sea. [Shahan, 2014]

WT farms are more and more commonly placed offshore due to the space required for all the WTs and space onshore can thereby be saved for other use. Also, WTs are generating loud noises

and thereby if the structure is placed offshore, this noise will not affect any persons living near them. However, for OWTs more complicated foundation methods are necessary, as they are not placed directly on the ground, and they are subjected to wave loads as well as wind loads. Despite OWTs have been used for more than two decades, methods for improving the design of OWTs are still being developed. This is also true when looking into the OWT's foundations, as there are still aspects of the foundation design methods which are not fully covered and thereby there is no standard procedure for every part of the foundation design.

1.1 Offshore Foundation Types

When installing OWTs, different types of foundations are available. Some of the most commonly used foundation types are illustrated in Figure 1.2 and the distribution of the different OWT foundation installed at the end of 2018 is illustrated in Figure 1.3.

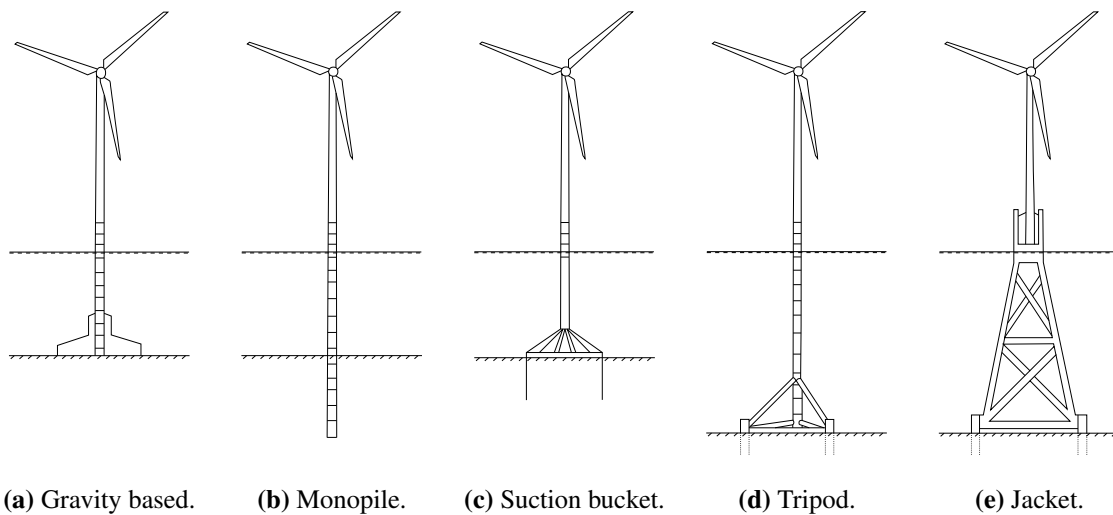


Figure 1.2: Illustration of different foundation types.

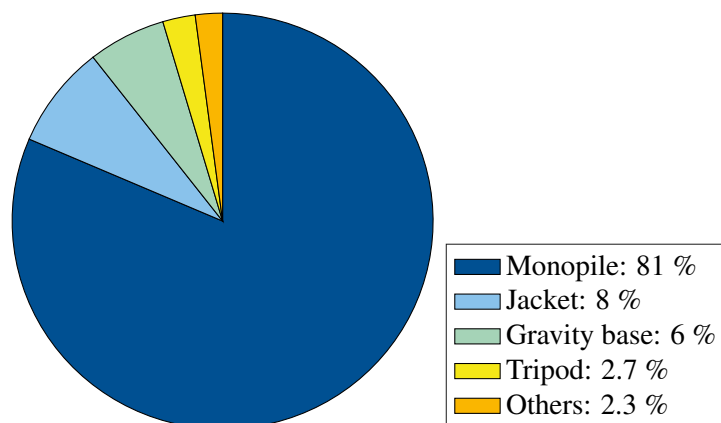


Figure 1.3: Distribution of different OWT foundations installed at the end of 2018 [Selot, Fraile, and Brindley, 2019, Modified].

According to Figure 1.3, the monopile is used for the vast majority of offshore projects. This is partly due to that the offshore field is a field where the construction, the operation and the test of new foundation types are very expensive, which makes it harder to come up with new and trusted methods. Also, when the costs of offshore projects are so high, insurance companies and other investors would rather use a more tested and commonly used foundation method like the monopile where more knowledge has been obtained through many years of usage. It should be mentioned that new foundation types are being developed like e.g. the suction bucket, the twisted jacket and floating foundations. These are still at a stage where further testing and development is necessary, but they could be a possibility for future offshore foundation designs. [Seidel, 2014]

Of the mentioned foundation types, the monopile will be the main focus of this thesis. When designing a monopile foundation, the length of the monopile is often determined by the overturning capacity during extreme condition. Alternatively the length of the monopile can be determined the maximum acceptable tilt of the structure over the lifetime caused by accumulated rotations from cyclic loading. The diameter of the monopile is often determined by requirements for the eigenfrequency of the structure. The wall thickness of the monopile is typically governed by either fatigue loads or shell buckling during extreme events or installation. [Kallehave, Byrne, et al., 2015]

1.2 Problem Statement

This thesis considers the dynamic aspect of the foundation for an OWT where the main focus is the estimation of the first eigenfrequency. During the estimation of the first eigenfrequency of an OWT, the frequencies for the environmental effects like wind- and hydrodynamic loads have to be considered. These effects should be considered to make sure that they do not overlap with the first eigenfrequencies of the OWT to avoid resonance in the structure. The determination of the first eigenfrequency for the structures is an advanced problem where 3D finite element (FE) models can be used. However, as these models are very time consuming, faster estimates would be optimal for the work process.

The problem considered in this thesis is to examine the problematic of estimating the soil-structure interaction for a monopile and set up a simple model which is capable of estimating the first eigenfrequency of an OWT. In order to cover this problem, the thesis is divided into four stages. These are as follows:

- Stage 1: This stage consists of a literature study which aims to clarify the theories and methods used for the design of an OWT foundation nowadays. Furthermore this stage also supplies a brief introduction to the governing subjects regarding the dynamic properties of OWTs supported by monopiles.
 - Stage 2: This stage deals with the set up of a simple 1D finite element model (FE model) used to obtain the eigenfrequencies of structure. The Simple Model is also used to perform a sensitivity analysis of the input parameters in order to investigate the importance of these. In this stage, only the structural part of the simplified OWT above mudline is considered.
-

- Stage 3: This stage continues the development of the simple FE model from Stage 2, where also the part of the OWT below mudline is considered i.e. the monopile. The pile-soil interaction is added to the Simple Model by a consideration of the p - y curves. Furthermore, this stage also provides an investigation of improvements to the currently suggested p - y curves and an alternative method.
- Stage 4: This stage deals with the use of commercial software to obtain the response of an OWT. The stage deals with the determination of the dynamic response in regards to the first eigenfrequency of an OWT submerged into a reference layer of sand, a comparison of the API p - y curves and the corresponding p - y curves extracted from Plaxis 3D and an analysis of the difference in the behaviour of soil when the diameter of a monopile is increased.

During this thesis, not all aspects of the design phase will be covered due to the amount of work this will require. The main focus will be on the dynamic response of the structure and the interaction between the soil and the structure.



Stage 1

In the first stage of this thesis, a literature study is performed in order to obtain knowledge about previous work related to the dynamics of OWTs. The main focus of the literature study is to cover subjects concerning the current design guidelines, soil-structure interaction, modelling of soil damping and fatigue. Here the subject fatigue is only briefly introduced. Besides the literature study, an introduction to the dynamic properties regarding an OWT is presented. In this introduction, the effects regarding the location of the first eigenfrequency is presented together with an introduction to the dynamics regarding soil-structure interaction.

2	Literature Study	7
2.1	Current Design Guidelines	
2.2	Soil-Structure Interaction	
2.3	Damping	
2.4	Fatigue	
2.5	Conclusion	
3	Dynamic Properties	17
3.1	Dynamic Equation of Motion	
3.2	Offshore Wind Turbines	
3.3	Soil-Structure Interaction	
3.4	Dynamic Properties of Soil	
3.5	Conclusion	

2. LITERATURE STUDY

As the number of OWTs has increased rapidly in the recent years, the research within the field has been intensified. This has led to a discussion of the accuracy of the current design guidelines, especially in regards to the dynamic properties of an OWT. This discussion will be introduced in the following section, starting with a brief introduction to the current design guidelines followed by an investigation of alternatives and improvements.

2.1 Current Design Guidelines

Eurocode provides design requirements for OWTs in *Wind turbines - Part 3: Design requirements for offshore wind turbines*. The Eurocode covers what has to be investigated when designing OWTs, but it does not provide specific procedures and guidelines for designing OWTs. Instead these guidelines can be found in the current design guidelines provided by DNV-GL group, in order to help the offshore industry move forward. The organisation publishes guidelines in the form of standards in the offshore sector, where *DNVGL-ST-0126* provides guidelines for OWT's support structures. The standard *DNVGL-ST-0126* specifies how to design an OWT with the necessary safety margin.

The standard provides recommended methods to investigate the limit states with the following descriptions according to *DNVGL-ST-0126*:

- Ultimate limit state (ULS), corresponds to the maximum load-carrying resistance. Here it is important to ensure that every part of the structure can withstand the ultimate loads the structure is designed against.
- Serviceability limit state (SLS), corresponds to tolerance criteria applicable to normal use. For OWTs it is very important to control how much the foundation will rotate during its lifetime, to ensure that it is inside what is allowed for the specific OWT.
- Accidental limit state (ALS), corresponds to maximum load-carrying capacity for accidental loads or post-accidental integrity for damaged structures.
- Fatigue limit state (FLS), corresponds to failure due to the effect of dynamic loading. Here it is important to ensure that the structure can withstand etc. the dynamic loads from wind and waves during its lifetime.

The standard also contains guidelines on how to estimate the loads and load combinations for the limit state analyses. These guidelines include practices on how to handle metocean-, turbine- and geotechnical data to obtain a safe design for OWT foundations.

As mentioned before, the standard provides methods to calculate and combine the loads necessary for investigating the different limit states. Besides this the standard provides recommendations on how to handle subjects like scour, transportation and installation etc. which are also necessary to consider when designing the before mentioned limit states. This is because e.g. transportation and installation impacts the fatigue lifetime of the structure and that scour affects the bearing capacities and dynamic properties of the system.

The guidelines and recommendations in the standard are constantly changing as new methods are developed and documented, including the fact that the OWTs keep increasing in size. This leads to an evolution of methods for designing modern OWT foundations. As the evolution of design methods is ongoing, the guidelines are always a few steps behind in their recommendations. This leads to some guidelines are receiving criticism for being too inaccurate in for example estimating the dynamic properties of an OWT.

In the following literature study, alternative methods are presented. These alternative methods are developed as a result of the criticism the standard has received. The key points of the literature study will be introduced in the following sections based on the divisions and references presented in Figure 2.1.

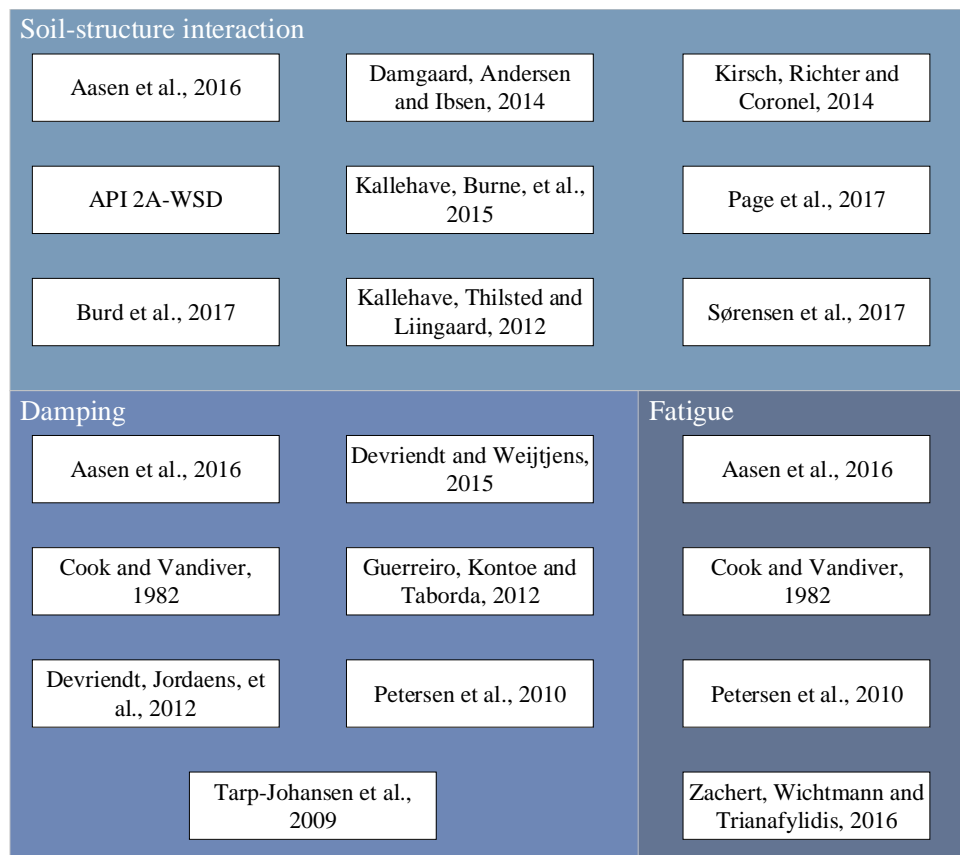


Figure 2.1: Divisions and references used in the literature study.

The literature study is divided in the three parts defined in Figure 2.1 due to the problematic this thesis is investigating. The main focus of this thesis is to describe the dynamic response of an OWT structure with a monopile as foundation. To be able to describe this system, the time varying effects from the reality have to be considered. This is e.g. the interaction between the structure and the soil and the damping which need to be defined. Also, an offshore structure is normally designed for a specific design lifetime where fatigue is a critical part influencing this estimation.

2.2 Soil-Structure Interaction

One of the most important subjects to deal with when designing an OWT is the soil-structure interaction. A review of different approaches for determining the effects of the soil-structure interaction will be performed in this section. This review is based on the following references:

- Aasen et al., 2016
- *API 2A-WSD*
- Burd et al., 2017
- Damgaard, Andersen, and Ibsen, 2014
- Kallehave, Byrne, et al., 2015
- Kallehave, Thilsted, and Liingaard, 2012
- Kirsch, Richter, and Coronel, 2014
- Page et al., 2017
- Sørensen et al., 2017

The suggestions in the previously mentioned current design guideline are based on the use of p - y curves. The p - y curves describes the relationship between the soil resistance per meter, p , and the horizontal displacement of the monopile at a certain point, u , at a certain depth, z . The lateral displacement is normally referred to as y , hence the name p - y curve. However, the lateral displacement is in this report referred to as u . When using the p - y curves, a monopile is modelled as a number of beam-column elements supported by a number of uncoupled non-linear springs, following the spring analogy, see Figure 2.2(a), where P is the lateral load. Each of these springs are characterised by a p - y curve, see Figure 2.2(b). The p - y curves are further described in Chapter 5. [API 2A-WSD]

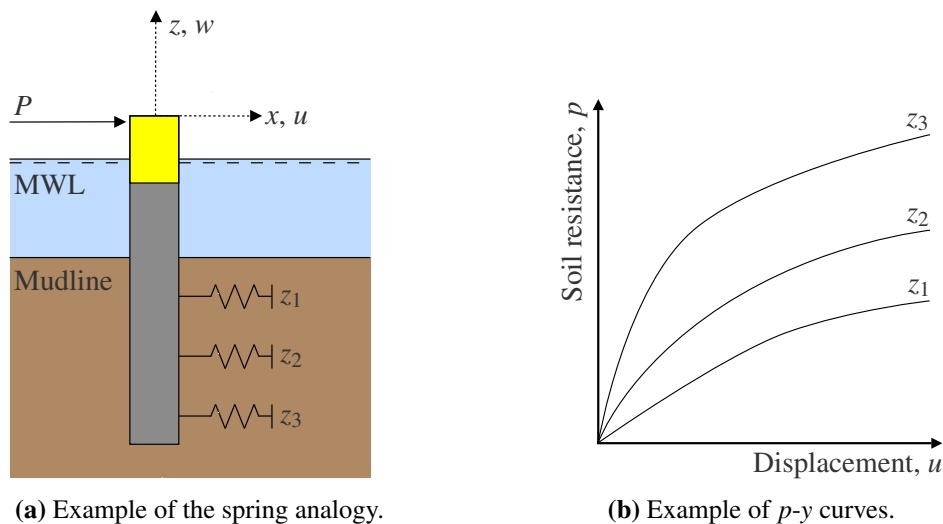


Figure 2.2: Illustration of the spring analogy and p - y curves.

The p - y curves recommended by *API 2A-WSD* were originally developed for the oil and gas industry in the 1970s and partly modified in the 1980s. The curves were developed based on a limited number of full scale tests of flexible and long slender piles. The fact that the currently

recommended p - y curves were developed for piles with diameters less than a tenth of the diameters of the modern monopiles makes the application questionable.

A paper by Kallehave, Byrne, et al., 2015 is questioning the accuracy of the current design guidelines. This paper claims that the current approach significantly underestimates the soil-structure stiffness of monopiles installed in sand especially. This underestimated soil-structure stiffness leads to an underestimation of the eigenfrequencies, and can be explained by the difference between the pile, for which the p - y curves are developed, and the monopiles used nowadays. This raises an issue, because it is on the unsafe side both to under- and overestimate the soil-structure stiffness in most cases. According to Kallehave, Byrne, et al., 2015, only an exact prediction of the soil-structure stiffness is on the safe side.

Kallehave, Thilsted, and Liingaard, 2012 has performed a further investigation of the original p - y formulation in order to increase the accuracy of the p - y curves and the estimation of the soil-structure stiffness of a monopile installed in sand. The paper performs an investigation of the governing parameters in the p - y formulation by *API 2A-WSD*, and concludes that the formulation can be improved by modifying the small strain stiffness variation with depth and the rate of stiffness degradation with increasing shear strain. A validation of the modified p - y formulation is performed based on measurements on operating OWTs. This validation concludes that the modified formulation yields results closer to the measurements compared to the original p - y formulation.

A paper by Kirsch, Richter, and Coronel, 2014 presents a study equally to Kallehave, Thilsted, and Liingaard, 2012 which investigate the potential for optimising the original p - y formulation in order to obtain a better estimate of the soil-structure stiffness. The paper compares the displacements of an embedded pile obtained from the p - y curves using the original formulation and a 3D numerical model. This comparison shows that the displacements obtained from the p - y curves are on the unsafe side. To compensate for this, the paper introduces a reduction of the angle of friction in regards to the diameter of the monopile. This reduction leads to a reduced ultimate soil resistance, and potentially bigger displacements.

A comparative study performed by Sørensen et al., 2017 compares the original p - y formulation presented by *API 2A-WSD* to the modifications presented by Kallehave, Thilsted, and Liingaard, 2012 and Kirsch, Richter, and Coronel, 2014 amongst others. This paper concludes that the two modifications in general yield the same response. Both modifications yield minor increase of the eigenfrequency compared to the original formulation by *API 2A-WSD*, but the paper concludes that the eigenfrequencies are on the low side compared to measurements from operating OWTs.

This concludes the literature study within the topic improvements of the current design approach. The study has revealed that there is a broad consensus about the fact that the original formulation of the p - y curves by API, 2014 yields too inaccurate solutions and that there is a need for a new and better approach. There is however no broad consensus about which approach to choose.

The studies performed by Kallehave, Thilsted, and Liingaard, 2012 and Kirsch, Richter, and Coronel, 2014 are both based on improving the estimation of the soil-structure stiffness by modifying the existing p - y curves. Both studies modify the existing p - y curves by adjusting the initial stiffness, and by taking the diameter of the monopile into consideration. A comparative study performed by Sørensen et al., 2017 compares the original formulation of the p - y curves by API, 2014 to

the modified formulations by Kallehave, Thilsted, and Liingaard, 2012 and Kirsch, Richter, and Coronel, 2014 amongst others. This comparison shows that modified formulations yield realistic values in terms of the eigenfrequency and displacements. The paper however concludes that the estimated eigenfrequencies still are too low compared to measured eigenfrequencies. The fact that the p - y curves underestimate the first eigenfrequency of OWTs when compared to in-situ measurements is supported by Østergaard et al., 2019.

When looking apart from modifications of the p - y curves, a few alternative approaches have been presented in the recent years. A paper by Aasen et al., 2016 compares three alternative approaches to the suggested approach in the current design guidelines. The comparison shows that the currently suggested p - y curve approach is too conservative when it does not include damping. The comparison introduces an alternative approach called the nonlinear rotational model. This approach is based on Iwan, 1967 and considers hysteretic damping. This alternative approach proves itself better at estimating the fatigue lifetime, and thereby less conservative than the current suggested approach.

Another alternative to the currently suggested approach is the so called consistent lumped-parameter model as described by Damgaard, Andersen, and Ibsen, 2014. A lumped-parameter model is describing an OWT, a monopile and the soil in which the monopile is embedded. Such a model consists of springs, dashpots and point masses, see Figure 2.3. The paper concludes that the lumped-parameter model yields a solution with a sufficient accuracy when the model is implemented correctly.

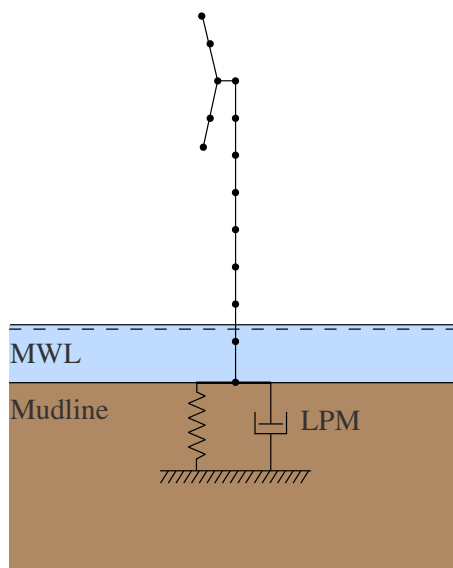


Figure 2.3: Example of the lumped-parameter model.

A newer paper presents a new formulation by Page et al., 2017. This formulation is based on the macro-element concept, where the response of the monopile and the surrounding soil is presented by a force-displacement relation. In this model, the embedded part of the monopile is simply modelled as a rigid element with an intersection at the top where it is connected to the OWT tower, and a stiffness matrix defining the boundary at the bottom. The thoughts behind this new model is inspired from finite element analysis of soil and foundations, where the response of the soil is

modelled as a constitutive model which imitates the behaviour of soil. This paper concludes that the advantage of this new formulation is within the simplicity that is reached by applying various assumptions which reduces the range where the formulation actually can be applied. More research and experience using this new formulation is needed before it really can be used.

Finally, a new approach, known as PISA (Pile Soil Analysis), has been introduced as an alternative to the currently suggested approach. The PISA formulation is an enhancement of the p - y formulation, that includes a distributed moment along the longitude axis of the monopile, see Figure 2.4. This distributed moment is induced by the vertical traction that is caused by rotation of the monopile. The influence of this distributed moment is increasing when the diameter of a monopile is increasing. A recent investigation of the PISA formulation compared to a 3D FE model concludes that this formulation actually yields quite accurate solutions in regards to displacements of an embedded monopile. [Burd et al., 2017]

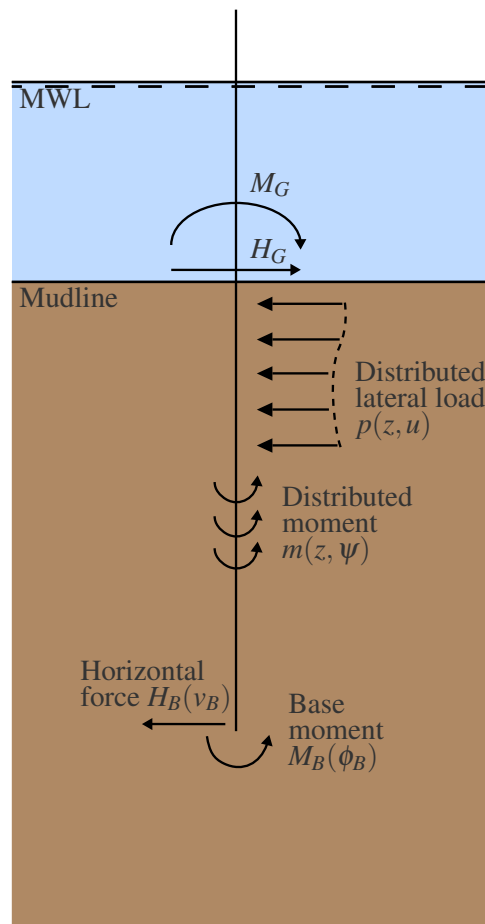


Figure 2.4: Example of the concept from the PISA formulation.

z	Depth
u	Lateral displacement
ψ	Local cross-section rotation
M_G	Moment applied to the pile at ground surface
H_G	Horizontal force applied to the pile at ground surface

This concludes the literature study of alternative approaches of modelling soil-structure interaction. In this study the lumped-parameter model, the macro-element concept and the PISA formulation have been investigated. Common for the three alternative approaches are that they are based or supported by finite-element analyses and numerical modelling. Benchmark testing has revealed that all three methods yield more accurate results compared to the original formulation of the p - y curves. However, more research is required for all of the methods before they can be incorporated as a design guideline. [Damgaard, Andersen, and Ibsen, 2014; Page et al., 2017; Burd et al., 2017]

2.3 Damping

Damping is another phenomena which is highly relevant when designing an OWT. Damping is defined as the ability to dissipate energy from a system, which is important as this can have a high effect on the fatigue lifetime of a structure. The vibrations of an OWT tower are caused by wind and waves affecting the structure and are usually dominated by the first mode shape in two directions e.i. fore-aft and side-side, see Figure 2.5.

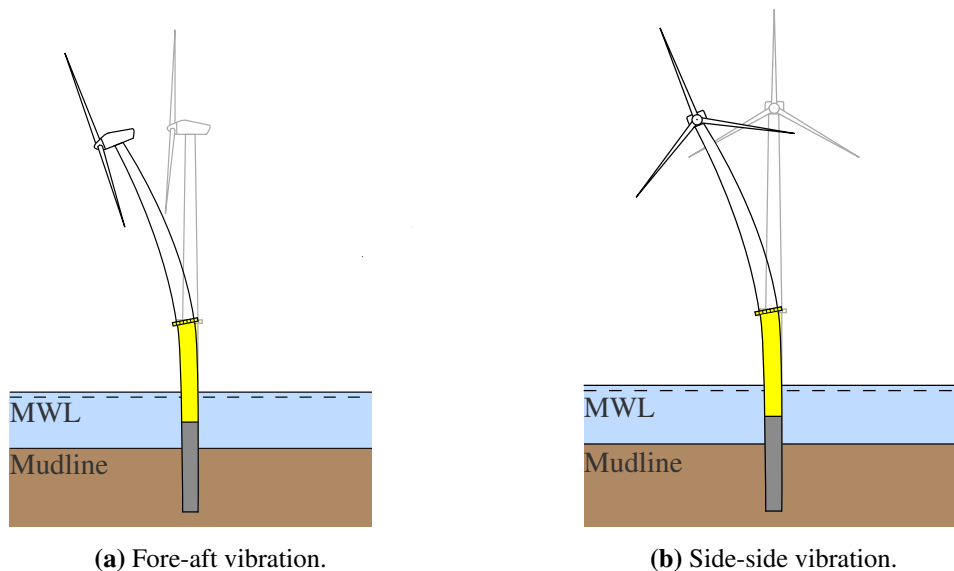


Figure 2.5: Illustration of the two dominating vibration directions for an OWT tower. Both directions are illustrated with the first eigenfrequency.

The amount of damping in a structure is defined by the damping ratio. The damping ratio is hard to estimate for an OWT, even when using FE modelling. The design values are thereby normally compared with measurements from the finished structure to verify the assumed values for damping. The problem of estimating the damping values has lead to a discussion of different methods of predicting the damping ratio. The key points of this discussion are introduced in this section, based on the following references:

- Aasen et al., 2016
- M. F. Cook and Vandiver, 1982
- Devriendt, Jordaens, et al., 2012
- Devriendt and Weijtjens, 2015

- Guerreiro, Kontoe, and Taborda, 2012
- Petersen et al., 2010
- Tarp-Johansen et al., 2009

Normally, damping can be divided in the four main categories hydrodynamic-, aerodynamic-, structural- and soil damping. Also, damping due to constructive devices can be used if needed in the form of e.g. a tuned mass damper. The damping in a system from all the contributions together is called the overall damping and is very dependent on the environmental and operational conditions, as these can change the individual damping ratios. [Devriendt and Weijtjens, 2015]

Hydrodynamic damping can be divided into viscous hydrodynamic damping and radiation damping. The viscous hydrodynamic damping is due to the separated flow drag force and the radiation damping is the loss of energy that appears when the structure is oscillating in the water. The oscillations create waves which radiate away from the structure and thereby dissipating energy away from the structure. [M. F. Cook and Vandiver, 1982]

Aerodynamic damping is the contribution to the damping from the wind affecting the structure, which is supposed to reduce vibrations in the blades and support structure and thereby increase the fatigue lifetime. A higher effect of damping is obtained with a soft- and light structure. Aerodynamic damping has found to be extremely important when working with the first eigenfrequencies. However, the aerodynamic damping is highly diminished when a WT is parked. [Petersen et al., 2010]

Structural damping covers steel hysteretic damping which is the loss of energy that appears from internal dissipation in a steel structure [M. F. Cook and Vandiver, 1982].

Soil damping can be divided in radiation damping and hysteretic damping. Radiation damping is where energy is dissipated through geometric spreading of the waves propagating through the soil. Hysteretic damping, which is also known as internal material damping, is where energy is dissipated through plastic deformations. Radiation damping can be neglected for frequencies below 1 Hz, and is thereby normally neglected when designing OWTs. [Aasen et al., 2016; M. F. Cook and Vandiver, 1982]

A study by Tarp-Johansen et al., 2009 examines the accuracy of estimating the damping ratios for the current design guidelines in regards to cross-wind motions. The study concludes that more damping is available compared to what is assumed in the current design guidelines which means there is a potential for optimising the design guidelines in regards of damping. It is however hard to estimate the magnitude of damping, even though some of the damping contributions can be neglected. Consequently, researchers have investigated the possibility to estimate the damping ratio with numerical tools. A research performed by Devriendt, Jordaens, et al., 2012 concludes that it is possible to estimate the damping ratio numerically, but it demands a lot of calibration.

Another approach is to use the shear modulus reduction curves (G/G_{\max}) and damping ratio curves (ζ). Shear modulus reduction and damping ratio curves are empirical curves based on laboratory tests. Different families of empirical shear modulus and damping ratio curves have been compared in Guerreiro, Kontoe, and Taborda, 2012 where it was found that the curves developed by Darendeli, 2001 are the most suitable curves for general application in engineering practise. This is due to these curves, unlike the others, seems to be able to capture all the major effects across the strain

range, because it is based on a wider range of tests. However, these curves are more suitable for non-plastic to medium plasticity soil and the use of these outside this field should be done with caution.

Finally, a very acknowledge approach to model damping in a material is proposed by Iwan, 1967. In this approach, damping in a material is modelled as Coulomb friction, which considers damping in terms of sliding friction. These Coulomb friction elements are governed by the yield stress of the material and remains locked until the stress level exceeds this yield stress. The principle of this approach is illustrated in Figure 2.6.

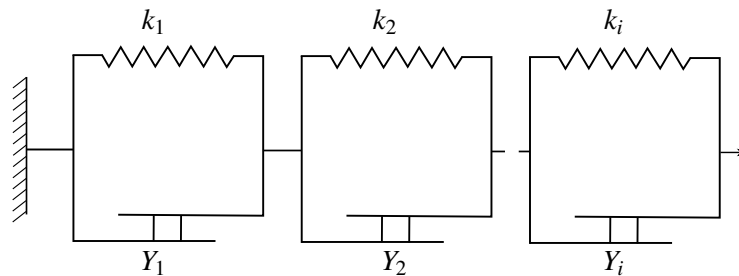


Figure 2.6: Illustration of the Iwan model [Gandomzadeh et al., 2010, Modified].

The approach proposed by Iwan, 1967 consists besides the Coulomb friction elements, of simple linear springs with the spring constant k_i . According to Gandomzadeh et al., 2010, this approach can be used to model the hysteresis loop of any material that obeys the Masing Rule which is a simple tool to predict the appearance of the backbone curve. The backbone curve is explained and illustrated in Chapter 3 page 23.

This concludes the literature study of the subject damping. The study has revealed that the damping of an OWT and the supporting structure consists of four damping contributions: hydrodynamic-, aerodynamic-, structural- and soil damping. Knowledge about all four contributions is necessary to determine the total damping where the four damping contributions are dependent on the eigenfrequency. This means that one of the contributions can be crucial around the first eigenfrequency where another can be crucial at higher eigenfrequencies. [Petersen et al., 2010; M. F. Cook and Vandiver, 1982]

The literature study of damping revealed that there is many different approaches for estimating the damping ratio, and no broad consensus about which approach is the best suited. However, the damping curves as presented in Devriendt, Jordaens, et al., 2012 are recommended by *DNVGL-RP-C212* and are relatively easy to apply. The damping phenomena is, despite a lot of research, still a field which is hard to describe and thereby further research is required. As stated in the beginning of this section, damping affects the fatigue lifetime of an OWT. This means that as research is being put into damping of OWTs, it will be possible to improve the lifetime of the structure.

The damping phenomena is neglected in Stage 2 and Stage 3 where FE models based on Bernoulli-Euler beam theory are developed. However, the damping phenomena is considered in Stage 4, where the commercial program Plaxis 3D is used to model the monopile. When dealing with the selected material models in Plaxis 3D both Rayleigh damping and hysteretic damping is considered. Hysteretic damping is a phenomena caused by the dynamic properties of soil and is elaborated in

Chapter 3. Rayleigh damping is not employed until Stage 4 and the theory and implementation of this in Plaxis 3D are explained in Appendix J.4.

2.4 Fatigue

As OWTs are exposed to dynamic loads, the estimation of the fatigue lifetime of an OWT is really critical and a crucial part of the design.

When designing an OWT in regards to fatigue, an approach using the so called S-N curve and the Palmgren-Miners rule is often used. The S-N curve is a plot showing the relation between different stress levels and number of cycles to failure for a given material. These curves are developed based on laboratory tests on different materials and different joints. Palmgren-Miners rule is a cumulative damage model which uses the S-N curves to estimate the lifetime of a structure. Today the usage of S-N curves and Palmgren-Miners rule is a basic concept. However, due to the complexity of an OWT, S-N curves and Palmgren-Miners rule are still used within this field. [DNVGL-ST-0126]

Despite fatigue is an important subject to consider when designing an OWT, it is disregarded in this thesis. It is disregarded since a study of fatigue would induce a large field of topics which would require much time to study. This time is assessed to be better spend on a study of the other subjects covered in the literature study. If however fatigue was going to be examined, a literature study could take point of departure in the following references:

- Aasen et al., 2016
- M. F. Cook and Vandiver, 1982
- Petersen et al., 2010
- Zachert, Wichtmann, and Triantafyllidis, 2016

2.5 Conclusion

The aim of the literature study performed is to clarify the more important subjects regarding dynamically loaded OWTs. These subject are soil-structure interaction, damping and fatigue as mentioned above. In the rest of this thesis it is chosen to continue with the subject soil-structure interaction and how it affects the eigenfrequencies of an OWT. As eigenfrequencies are of interest for dynamic loaded structures it is also investigated which factors affect them. The factors investigated are the geometric parameters of the structure and the soil which the structure is positioned in.

3. DYNAMIC PROPERTIES

An initial examination of the governing subjects regarding the dynamic properties of OWTs supported by monopiles will be introduced in this chapter. The dynamic properties of such a structure will be covered in the following order. Firstly, the governing dynamic equation of motion is introduced, followed by an introduction to the dynamic behaviour of the OWT itself, with focus on eigenfrequencies and load frequencies. Then dynamic soil-structure interaction will be introduced briefly, followed by an introduction to the dynamic properties of soil. Here the more important parameters, regarding the behaviour of cyclic loaded soil, will be introduced.

3.1 Dynamic Equation of Motion

An OWT is a complex system with multiple degrees of freedom (MDOF). The equation of motion for such a system can be written with the use of Newton's second law, as done in equation (3.1).

$$[\mathbf{M}]\{\ddot{\mathbf{u}}(t)\} = \{\mathbf{f}_{\text{ext}}(t)\} - \{\mathbf{f}_{\text{int}}(t)\} - \{\mathbf{f}_{\text{damp}}(t)\} \quad (3.1)$$

$[\mathbf{M}]$	Global mass matrix
$\{\ddot{\mathbf{u}}(t)\}$	Acceleration vector
$\{\mathbf{f}_{\text{ext}}(t)\}$	External forces
$\{\mathbf{f}_{\text{int}}(t)\}$	Internal forces
$\{\mathbf{f}_{\text{damp}}(t)\}$	Damping forces

Because of the assumptions used in the Simple Model, which are that the material is linear elastic, the damping is linear and the problem only considers small displacements, the equation of motion can be rewritten into equation (3.2).

$$[\mathbf{M}]\{\ddot{\mathbf{u}}(t)\} + [\mathbf{C}]\{\dot{\mathbf{u}}(t)\} + [\mathbf{K}]\{\mathbf{u}(t)\} = \{\mathbf{F}(t)\} \quad (3.2)$$

$[\mathbf{C}]$	Global damping matrix
$[\mathbf{K}]$	Global stiffness matrix
$\{\mathbf{F}(t)\}$	Load vector
$\{\mathbf{u}\}$	Displacement vector
$\{\dot{\mathbf{u}}\}$	Velocity vector

To describe what happens if an OWT e.g. is harmonically loaded, it is convenient to simplify the system into a single degree of freedom system (SDOF). The equation of motion for a SDOF system is expressed by equation (3.3) for the system illustrated in Figure 3.1.

$$m\ddot{u} + c\dot{u} + ku = F(t) \quad (3.3)$$

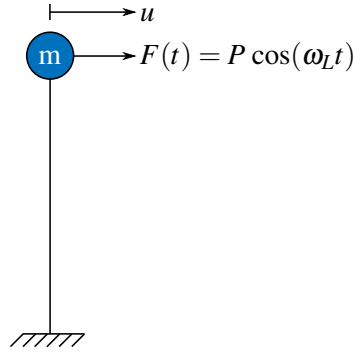


Figure 3.1: SDOF system for an OWT with a harmonic varying load.

The solution to the equation of motion given by equation (3.3) is provided in Appendix A. The solution in the appendix implies that the displacement, u , from the system illustrated in Figure 3.1 is equal to the static displacement times a dynamic amplification factor, f_{amp} . The dynamic amplification factor is an interesting factor, when looking at the response of a dynamic loaded system. The dynamic amplification factor is given by equation (3.4) [Damkilde, 2017]. This is also known as the frequency response function, as it states how much the response is amplified for a given load frequency.

$$f_{amp} = \sqrt{\frac{1}{\left(1 - \left(\frac{\omega_L}{\omega_1}\right)^2\right)^2 + \left(2\zeta\frac{\omega_L}{\omega_1}\right)^2}} \quad (3.4)$$

ω_L		Cyclic load frequency
ω_1		Cyclic eigenfrequency
ζ		Damping ratio

The dynamic amplification factor shows that when the cyclic loading frequency, ω_L , approaches the cyclic eigenfrequency of the system, ω_1 , then f_{amp} will increase, leading to a larger displacement of the system. This tendency is illustrated in Figure 3.2.

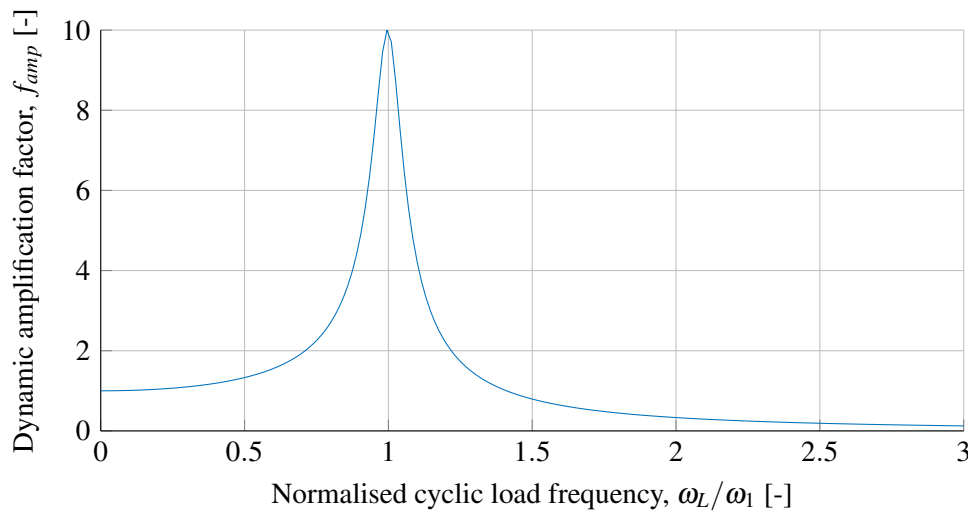


Figure 3.2: Example of the frequency response function where the cyclic load frequency is normalised to the first eigenfrequency and a damping ratio of 0.05 is used.

The first eigenfrequency of an OWT is thereby of great importance as this frequency has a corresponding mode shape that causes the turbine tower to vibrate in a fore-aft or side-side vibration mode as mentioned in Section 2.3, page 13. If this vibration mode is amplified a lot, the fatigue damage caused by this mode would be crucial for the lifetime of a WT. Thereby it is necessary to estimate the first eigenfrequency of the OWT, and model it so that it does not go into resonance with the loading frequency, meaning that ω_1 is equal to ω_L which causes resonance. The different mode shapes of an OWT are illustrated later in the report in Section 4.1.2 page 35.

3.2 Offshore Wind Turbines

The governing dynamic interactions for OWTs are generated by the dynamic loads caused by wind, waves and rotor excitations, see Figure 3.3.

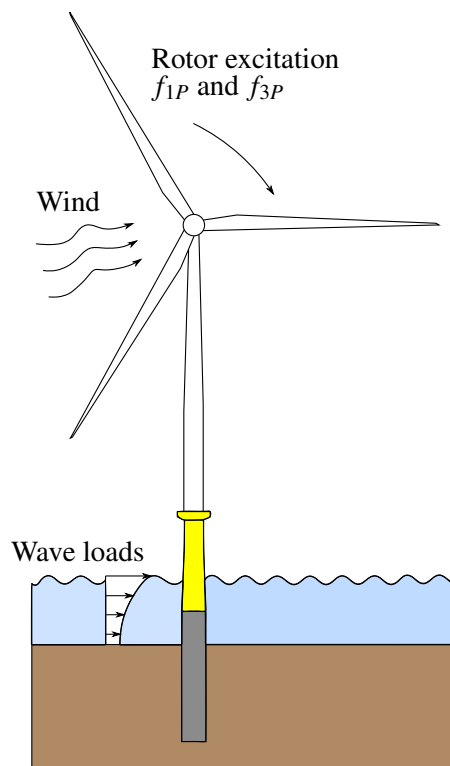


Figure 3.3: Illustration of OWT and dynamic loads [Kallehave, Byrne, et al., 2015, Modified].

Based on the governing dynamic equation and the amplification of the response, as the load and eigenfrequencies become close to each other, the load frequency ranges of these interactions have to be taken into account when designing OWTs. As mentioned earlier, the first mode shape is of great importance, as it should be outside the frequency range of the dynamic loads in order to avoid resonance. This means that OWTs typically are designed as soft-stiff structures. The characterisation of a soft-stiff OWT is that the first eigenfrequency, f_1 , is located between the two excitation frequencies, f_{1P} and f_{3P} , caused by the OWT's rotor. f_{1P} is the rotational frequency of the rotor, which is caused by motor imbalance and f_{3P} is the blade-passing frequency, that occurs due to the aerodynamic impulse loads happening as the blades pass the tower. The typical frequency ranges for rotor excitation, f_{1P} and f_{3P} , for an OWT are illustrated in Figure 3.4. [Kallehave, Byrne, et al., 2015]

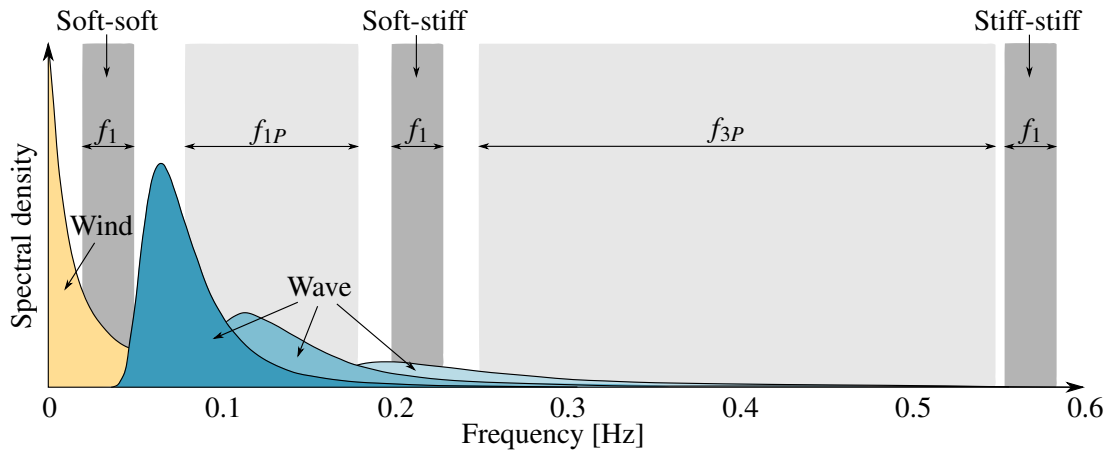


Figure 3.4: Typical excitation ranges for a modern OWT [Kallehave, Byrne, et al., 2015, Modified].

In Figure 3.4 the spectral density of the wind frequency is shown as a Kaimal spectrum together with three different JONSWAP wave spectra [DNV GL group, 2018]. The wave spectra differ from each other, by being generated from different wind speeds. Looking at spectra for wind and waves, it becomes clear why the structure is designed to have the first eigenfrequency in between the rotational frequency of the rotor and the blade-passing frequency. This places the frequency range for the first mode shape, f_1 , outside the critical wind and wave spectra, e.i. the first mode shape will resonate with the waves caused by lower wind speeds and not the waves with the highest spectral density. This is illustrated in Figure 3.4, where the typical range for the first eigenfrequency is the soft-stiff range, which is placed well outside of the waves with a high spectral density.

Alternatively, OWTs can also be designed as soft-soft or stiff-stiff structures. Soft-soft means that the first eigenfrequency of the structure is in between the wind and wave spectra, where stiff-stiff indicates that the frequency range for f_1 is located above the blade-passing frequency f_{3P} . Both the soft-soft and stiff-stiff frequency ranges for f_1 are illustrated in Figure 3.4. [Kallehave, Byrne, et al., 2015]

The excitation frequencies f_{1P} and f_{3P} are different for OWTs as they are determined by the rotation speed range for the individual turbines. There is however a tendency in the change in excitation frequency ranges as the turbines become larger and larger. Table 3.1 indicates how the excitation frequency ranges decrease as the turbines become larger.

Table 3.1: Development in excitation ranges as the OWTs increase in size [Desmond et al., 2016; Arany, Bhattachary, and Macdonald, 2010].

Turbine	f_{1P} [Hz]		f_{3P} [Hz]		Effect [MW]
Vestas V66	0.17	- 0.4	0.51	- 1.2	2
Vestas V90	0.14	- 0.3	0.42	- 0.9	3
Siemens SWT-3.6-107	0.082	- 0.22	0.246	- 0.66	3.6
Avera M5000	0.075	- 0.248	0.225	- 0.744	5
Siemens SWT-6.0-154	0.083	- 0.187	0.249	- 0.561	6
Vestas V164	0.08	- 0.2	0.24	- 0.6	8
DTU	0.1	- 0.158	0.3	- 0.474	10

The eigenfrequencies of an OWT supported by a monopile depends on the stiffness of the structure, the size and location of masses and the stiffness of the soil stabilising the structure. The importance of these parameters are investigated in Chapter 4, with a simple dynamic model.

3.3 Soil-Structure Interaction

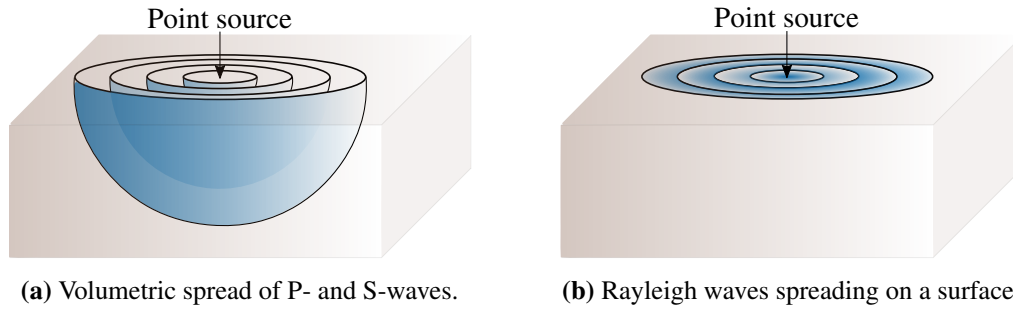
A big part of how the structure will behave and respond to loads is depending on the soil-structure interaction. If the characteristics of the soil surrounding the foundation vary as the structure is affected by loading over time, it will change how the structure responds to future loading. These changes could affect the eigenfrequencies of the system. Here it is important to determine how the characteristics of the soil surrounding the structure change as the number of load cycles increases. This is to make sure the critical eigenfrequencies do not change over time and end up interfering with the critical loading frequencies from wind, waves and rotor excitations.

The dynamic lateral loads affecting OWTs are transferred from the OWT through the monopile and into the soil by bending actions [Abhinav and Saha, 2015]. If these loads are in the elastic region of the soil, there will be no change over time in the system, meaning that the eigenfrequencies stays the same over time. However, if the loading is large enough to yield plastic straining in the soil, the shear stiffness of the soil will degrade over time, resulting in a change in the system's eigenfrequency. This degradation of shear stiffness will be introduced in Section 3.4. Modelling of this soil-structure interaction is very complex, and to understand what lies behind the different theories accounting for soil-structure interaction, e.g. the p - y curves as mentioned in the literature study Section 2.2, the p - y curves are further examined in Chapter 5. Some basic topics of soil dynamics are covered in the following section e.g. G/G_{max} and damping curves, as these topics are related to the change of dynamic properties for OWTs over their lifetime.

3.4 Dynamic Properties of Soil

The way soil responds to dynamic- and cyclic loading depends strongly on the mechanical properties of the soil. These properties are e.g. shear modulus, damping ratio, Poisson's ratio and the density.

The dynamic response of soil, as loads are transferred from the structure to the soil, is seen as different waves propagating through the soil domain surrounding the monopile. When measuring the response in the soil, three types of waves are usually encountered. These three wave types are P-waves, S-waves and Rayleigh waves. The primary- and secondary-waves (P- and S-waves) are propagating over a volume, whereas the Rayleigh waves travel on a half-space e.g. a surface. Figure 3.5(a) illustrates how the P- and S-waves spread over the volume, and Figure 3.5(b) illustrates that Rayleigh waves, which are bound to a surface, propagate like rings in water. [Andersen, 2016]



(a) Volumetric spread of P- and S-waves. (b) Rayleigh waves spreading on a surface.

Figure 3.5: Wave propagation for the different wave types [Andersen, 2016, Modified].

P-waves are often referred to as compression or dilation waves, and cause particle movement in the same direction as the waves are propagating. The S-waves move exactly in the same direction as the P-waves, but instead they cause particles to move in a direction perpendicular to the wave, which is why they are also referred to as shear waves. [Andersen, 2016]

The constitutive relationship for soil is normally categorised into two categories, which are perfectly elastic and plastic soil behaviour. When dealing with extremely small strain levels in soil it can be assumed to behave perfectly elastic, meaning that everything is fully recoverable. At larger strains the stiffness of soil decreases and the soil has to be treated plastic. [Jia, 2018]

When considering static loads, e.g. gravity loads, the material is often considered perfect-elastic for both sand and clay. However, for e.g. ocean storm wave-induced loads, the cyclic behaviour requires a more complex material model. The stress-strain relation is considered using an elasto-plastic where the strength of the soil is non-linear and depends on the strain, stress and possible the strain rate.

The most important parameters when considering dynamics of soil are the shear modulus, G , and the damping. The shear modulus is a stiffness parameter and describes the response to shear of a material. The determination of the shear modulus is normally well established, where modelling of soil damping is less clearly understood as it was found in the literature study. It is however well known that both parameters depends on e.g. the effective stress, the over-consolidation ratio, strain level, void ratio and plasticity index. The change in shear modulus and damping ratio, ζ , when soil is cyclic loaded will be described in the following sections.

3.4.1 Shear Modulus

The shear modulus for clean sand is mostly affected by the shear strain amplitude, effective stress level and void ratio. For clay it has been shown that when increasing the number of loading cycles, the shear modulus will decrease and the associated pore pressure will increase. The shear modulus for clay is also influenced by the over-consolidation ratio and the plasticity index. [Jia, 2018]

Figure 3.6 shows how the shear stresses, τ , and shear strains, γ , behave during one load cycle in a hysteresis loop. As seen in Figure 3.6 the tangential shear modulus, G_{tan} , changes during the entire hysteresis loop. The shear modulus is thereby often referred to as the secant shear modulus, G_{sec} , for a hysteresis loop. The secant shear modulus decreases when the strain increases as the soil is loaded over time.

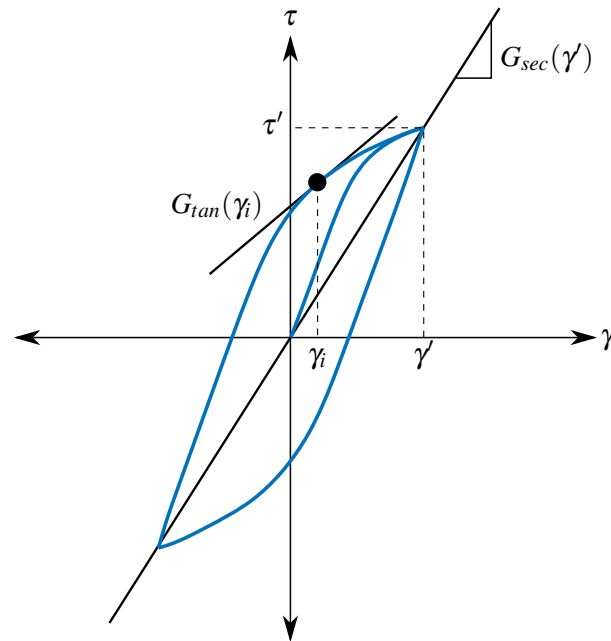


Figure 3.6: Secant shear modulus and tangent shear modulus in a hysteresis loop [Jia, 2018, Modified].

As the number of cycles and strain amplitudes increases, the secant shear modulus decreases as illustrated in Figure 3.7. It can be seen that fitting a curve to the tips of the cyclic hysteresis loops will result in a curve with the shape of a backbone (the blue curve in Figure 3.7) called the shear modulus reduction curve. Looking at the shear modulus reduction curve it can easily be seen that when the shear strain is equal to zero the secant shear modulus is at its largest, and that the secant shear modulus will decrease as the shear strain increases.

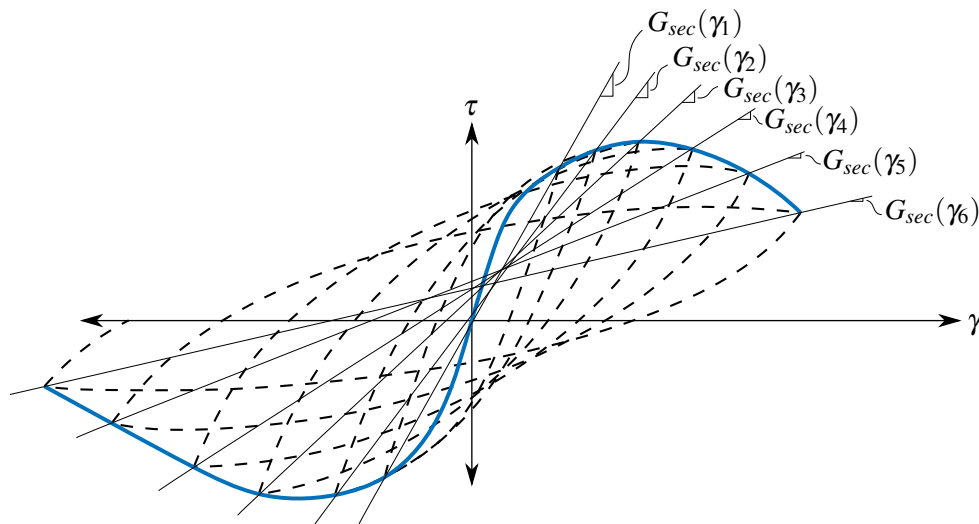


Figure 3.7: Principle sketch showing the variation of the secant shear modulus as the soil is cyclic loaded (γ_1 = first cycle and so on).

The shear modulus reduction curve which is also illustrated in Figure 3.8, is usually normalised according to the maximum shear modulus, G_{max} .

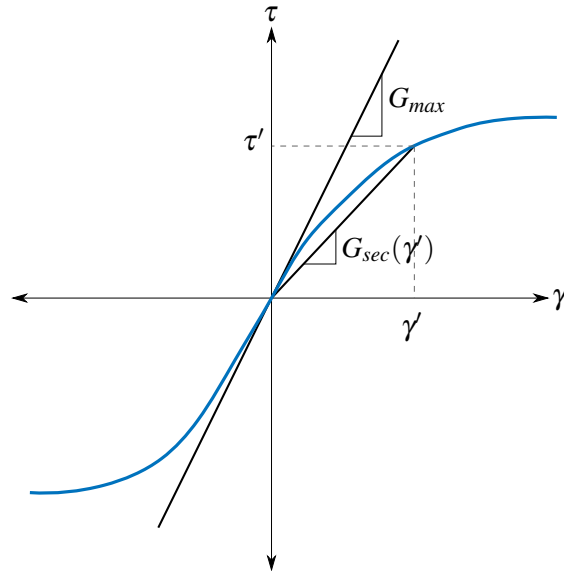


Figure 3.8: Shear modulus reduction curve, illustrating G_{max} and G_{sec} [Jia, 2018, Modified].

The normalised shear modulus reduction curve can be seen in Figure 3.9 and is often referred to as the G/G_{max} curve, which is also mentioned in the literature study for damping in Section 2.3.

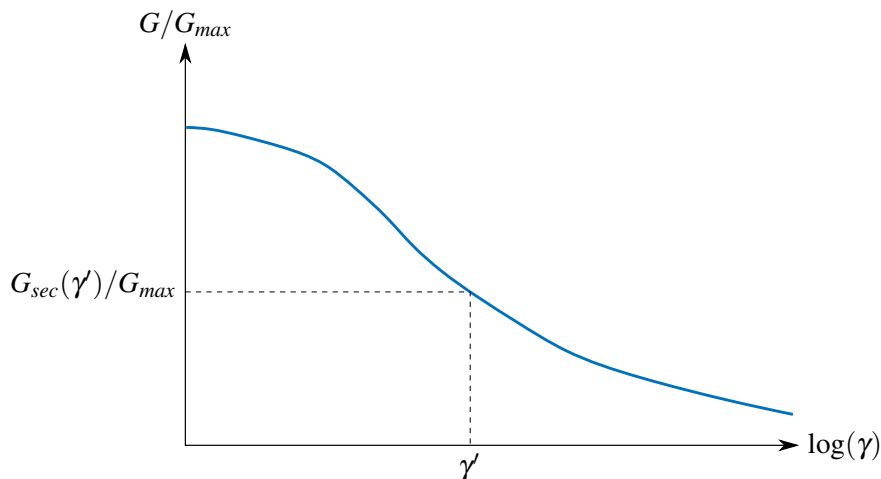


Figure 3.9: Normalised shear modulus reduction curve [Jia, 2018, Modified].

It has to be mentioned that the curves illustrated in Figure 3.8 and 3.9 are hypoelastic as unloading on these graphs will follow the loading curve. This shows that these models do not account for the hysteretic behaviour illustrated in Figure 3.6 and 3.7. Unloading does not follow the loading curve, as the secant shear modulus is degraded. This is because the degradation is caused by plastic deformations in the soil, which will leave a new unloading curve every time the stiffness of the soil is degraded. [Jia, 2018]

The theoretical way of calculating the maximum shear modulus, G_{max} , is done by subjecting soil to a strain smaller than $3 \cdot 10^{-6}$ and then measuring the shear wave velocity, v_s , and inserting the

values into equation (3.5). [Jia, 2018]

$$G_{max} = \rho v_s^2 \quad (3.5)$$

The shear wave velocity can be estimated from various test methods. These test methods will however not be covered here. Alternatively, it can be expressed in terms of the shear modulus, G , and the density of the soil, ρ , see equation (3.6) and (3.7).

$$v_s = \sqrt{\frac{G}{\rho}} \quad (3.6)$$

$$\rho = \frac{\gamma}{g} \quad (3.7)$$

γ | Unit weight of soil
 g | Gravitational acceleration

3.4.2 Damping

According to Jia, 2018 the work done by conservative forces, e.g. elastic-, inertia- and gravitational forces in a complete loading cycle will be equal to zero and thereby the energy dissipation happens due to damping alone. Figure 3.10 shows the energy that is dissipated in one hysteresis cycle, E_d , and the total strain energy stored in one cycle, E_{total} (maximum strain energy).

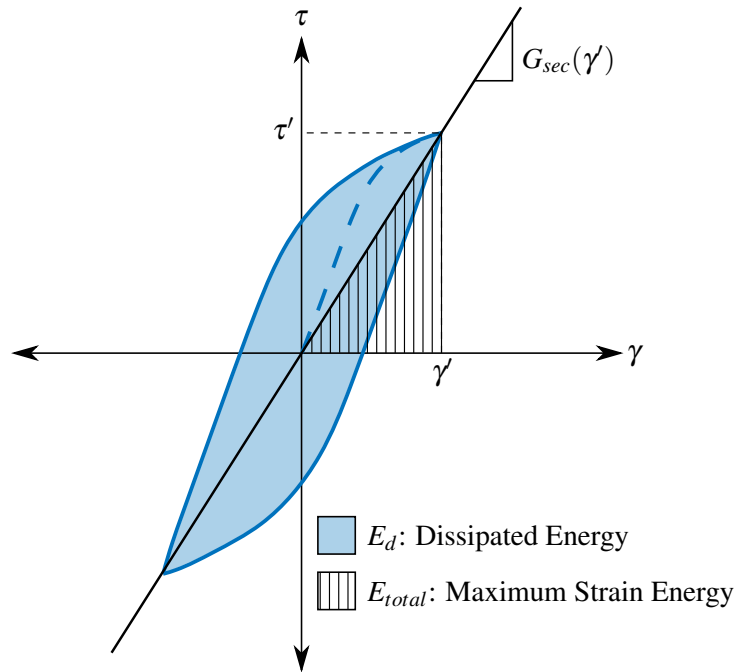


Figure 3.10: Dissipated energy, E_d , per cycle and the maximum strain energy, E_{total} , during one cycle in a hysteresis loop [Jia, 2018, Modified].

The equivalent damping ratio, ζ_{eq} , can then be determined as a ratio between the maximum strain energy, E_{total} , and the dissipated energy, E_d , by equation (3.8). Here A_{loop} is the area inside the

hysteresis loop shown in Figure 3.10. [Jia, 2018]

$$\zeta_{eq} = \frac{E_d}{4\pi E_{total}} = \frac{1}{2\pi} \frac{A_{loop}}{G_{sec}(\gamma') \gamma'^2} \quad (3.8)$$

This means that the behaviour of a hysteresis loop can describe both the damping ratio and the shear modulus of the soil. These properties are both related to the level of strain, γ' , caused by loading over time. The relation is illustrated in Figure 3.11, where the normalised shear reduction curve and the damping ratio curve are plotted. It is seen here that the shear modulus is reduced as the shear strain is increased, where the damping ratio is increasing with the shear strain. Figure 3.11 also illustrates the part of the curves that are in the elastic range, which is the range with very small strains and where the maximum shear modulus can be estimated with equation (3.5).

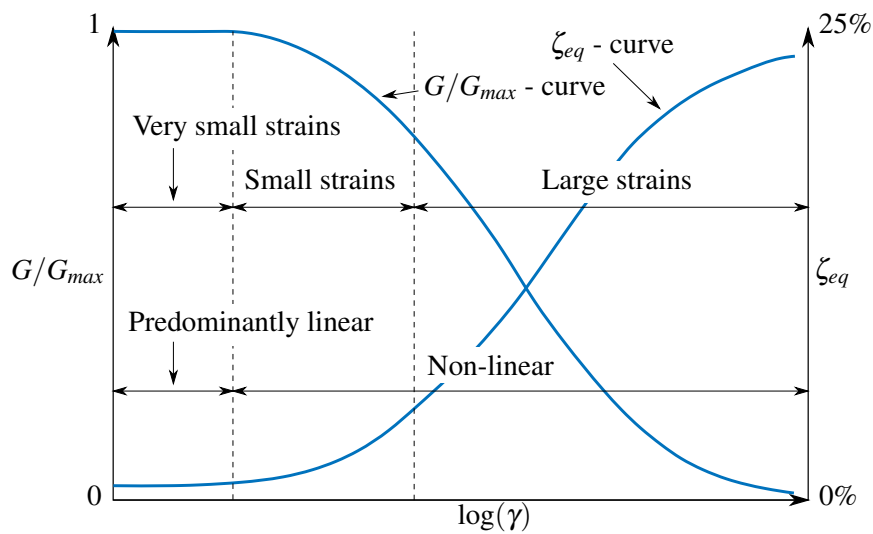
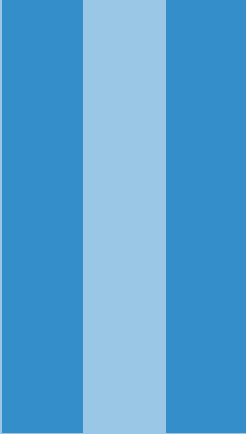


Figure 3.11: Relation between the normalised shear reduction curve and the damping ratio. The curves are illustrated to show the principle of the relation between them, and the values on the axes are from [Jia, 2018, Modified].

There is much more to this subject which is not covered here, as the point of this chapter is just to enlighten the reader about the main subjects that has to be taken into consideration when analysing the dynamic properties of an OWT.

3.5 Conclusion

This concludes a brief introduction to some of the important subjects regarding the dynamic properties of an OWT. The introduction is the basis for the following chapters, where the subjects will be reintroduced and elaborated. Initially, the knowledge acquired during this first part of the project, will be used to develop a simple dynamic model, which is capable of calculating eigenfrequencies of the system and to determine the importance of the parameters described in Section 3.2.



Stage 2

In this stage, a simple 1D FE model of an OWT is developed, to analyse the influence on the system's first eigenfrequency from the different input parameters and obtain knowledge for these. The set up of the model is described with the basic knowledge for this purpose. After, a parameter variation is performed, where the individual parameter's influence on the eigenfrequency is determined and the different parameter's influence is compared to each other, in order to determine which input parameters are the most sensitive.

4	Simple Dynamic Model	29
4.1	Set up of Model	
4.2	Parameter Variations	
4.3	Closure	

4. SIMPLE DYNAMIC MODEL

In this chapter a simple 1D finite element model (FE model) is used to investigate the dynamic properties of a very simplified OWT structure. It is simplified into being a fixed stick with a mass on the top. No damping is included, only stiffnesses and masses are considered. The model will be used to investigate the changes in the first eigenfrequency of the structure, as input parameters are changed, e.g. tower diameter, height or mass on top of the stick. The model in Stage 2 is the OWT structure from mudline and up, see Figure 4.1 where the part of the OWT considered in Stage 2 is illustrated. It should be noted that the effects from the water and soil are neglected in the Simple Model. All parametric variations are performed on a simplified system where the bottom is 100 % fixed. This means that the model is restricted against bending and horizontal movement at the mudline. This is however not a reflection of the real behaviour of an OWT. To capture the real behaviour of an OWT, a modified support at the bottom of the OWT tower is examined. This modified support will be introduced later.

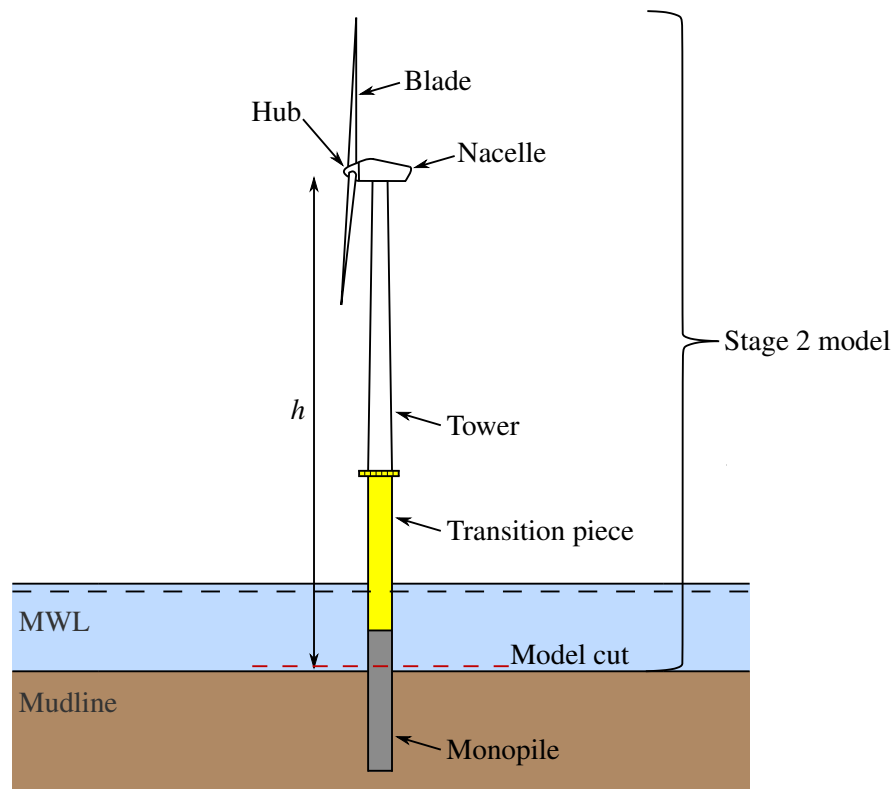


Figure 4.1: Illustration of an OWT, to specify what the Simple Model covers.

Eigenfrequencies are used as reference, for observing changes in dynamic properties of the system, as the input parameters to the model are varied. This is due to the fact that OWTs are dynamic loaded structures, and when a structure is dynamic loaded the eigenfrequencies of a system are of great importance, as explained in Section 3.2.

For an undamped system the equation of motion can be rewritten into equation (4.1) [R. D. Cook et al., 2002].

$$([\mathbf{K}] - \omega^2[\mathbf{M}]) \{\bar{\mathbf{D}}\} = \{\mathbf{D}_{st}\} \quad (4.1)$$

$[\mathbf{K}]$	Global stiffness matrix
ω	Cyclic eigenfrequency
$[\mathbf{M}]$	Global mass matrix
$\{\bar{\mathbf{D}}\}$	Nodal amplitude vector
$\{\mathbf{D}_{st}\}$	Static equilibrium displacement vector

The nodal amplitudes, $\{\bar{\mathbf{D}}\}$, varies sinusoidally with time relative to the static equilibrium displacements by time independent loads, $\{\mathbf{D}_{st}\}$. If time independent loads are zero, then $\{\mathbf{D}_{st}\}$ is equal to $\{\mathbf{0}\}$, which reduces the equation of motion to equation (4.2).

$$([\mathbf{K}] - \omega^2[\mathbf{M}]) \{\bar{\mathbf{D}}\} = \{\mathbf{0}\} \quad (4.2)$$

The nodal amplitude vector, $\{\bar{\mathbf{D}}\}$, represents the system's excursions from an unstressed configuration. The cyclic eigenfrequencies, ω , are independent of the static equilibrium displacements, $\{\mathbf{D}_{st}\}$, and a physical interpretation of the vibrations caused by the cyclic eigenfrequencies, ω , and their corresponding mode shapes is expressed by equation (4.3). [R. D. Cook et al., 2002]

$$[\mathbf{K}]\{\bar{\mathbf{D}}\} = \omega^2[\mathbf{M}]\{\bar{\mathbf{D}}\} \quad (4.3)$$

This results in a vibration mode which is a configuration where the elastic resistances are balanced by the inertia loads.

The above described equations are the governing equations for the Simple Model. The model is developed in order to be able to estimate eigenfrequencies for a simple system. The set up of the model is described in the following section.

4.1 Set up of Model

A 1D FE model is developed in MATLAB and the set up of the model is described in this section. The model is as mentioned earlier a structure, consisting of an OWT installed on a transition piece resting on a monopile, which is simplified into a mass on top of a fixed stick as illustrated in Figure 4.2.

In this chapter coordinate system references are referred to the x - and z -directions illustrated in Figure 4.2. The blue ball on top of the stick represents the mass of the OWT's hub, nacelle and blades shown in Figure 4.1. The mass is placed at a height equal to the distance from the mudline to the hub of the analysed OWT. A DTU 10 MW WT is used as reference for dimensions and weights of the OWT structure in the following analysis [Desmond et al., 2016]. The DTU 10 MW WT is an onshore WT, but as the purpose of the model is only to investigate how changing different

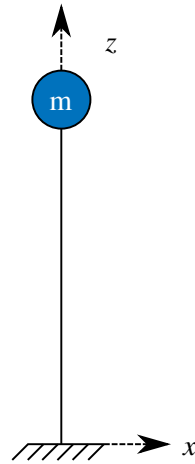


Figure 4.2: Illustration of the simple 1D model.

parameters influences the first eigenfrequency of the system, the data available for the turbine can still be used for this purpose even though it is not an OWT. The height of the structure is the sum of the WT, the height of the transition piece from mean water level and up, which is assumed to be 27 m and the water depth assumed to be 15 m. It is assumed the cross section of the transition piece and the monopile is identical to the cross section the WT. The structure is modelled with Bernoulli-Euler beam elements with two degrees of freedom per node, see Figure 4.3. This representation is chosen for the model, as it is sufficient to describe the system by two degrees of freedom per node. Also, this representation is suited for further analyses performed in Stage 3 where the soil-structure stiffness is implemented using the p - y curves. The cross section of the beam elements is illustrated in Figure 4.4, where d is the tower diameter and t is the tower wall thickness.

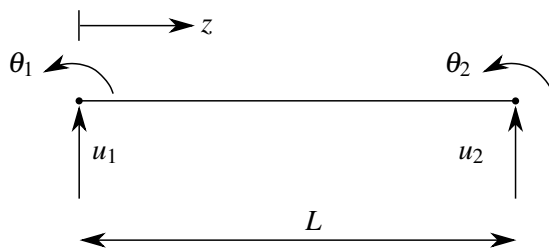


Figure 4.3: Illustration of a Bernoulli-Euler beam element with two degrees of freedom per node.

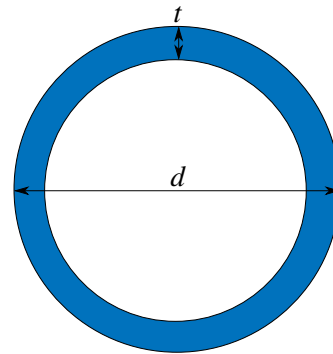


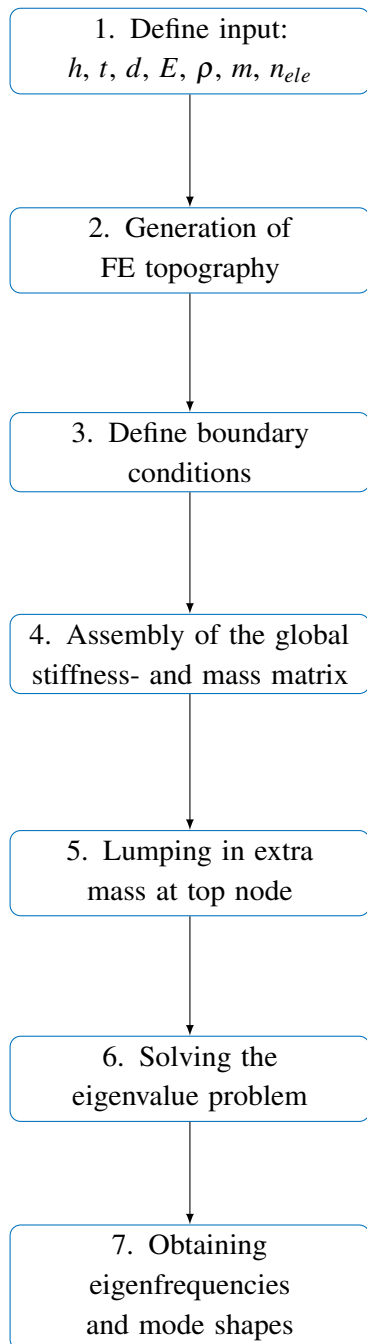
Figure 4.4: Cross section of the beam elements.

To present how the model is set up, the following subjects are covered in this section.

- A description of the FE calculation.
- A convergence analysis to determine the necessary number of elements needed to perform further analyses.
- A description of how the model simulates a certain percentage of fixation.
- A presentation of the final model used for the following parametric variations.

4.1.1 FE Calculation

To illustrate which steps the calculation goes through, a simple flowchart is presented. The chart covers the main subjects of the calculation step by step. Some of the steps will be elaborated further after the chart.



The first step is to define the input for the model, to be able to create a topology for the model and determine stiffness- and mass matrices.

The topography is generated using the height of the structure and the number of elements. This is done in order to set up node coordinates and define the elements in the FE model.

The degrees of freedom (DOFs) which are restricted from movement are defined. For a fixed support this is the two in the bottom node (x_1 and θ_1).

The local stiffness- and mass matrices are calculated for each element, transforming them to the global coordinate system and assemble them into the global stiffness- and mass matrix.

As the previous step of assembling the mass matrix only includes the tower weight, a mass is lumped in at the top node, which is equal to the weight of the nacelle, hub and the blades.

Solve $([\mathbf{K}] - \omega^2[\mathbf{M}]) \{\bar{\mathbf{D}}\} = \{\mathbf{0}\}$ for all ω^2 which are the squared cyclic eigenfrequencies with the unit $(\text{rad/s})^2$ and their corresponding mode shapes $\{\bar{\mathbf{D}}\}$.

The last step in the calculation collects all squared cyclic eigenfrequencies, ω^2 , and sort them from lowest to highest. The squared cyclic eigenfrequencies, ω^2 , are converted into eigenfrequencies, f , with the unit Hz.

1. As mentioned the DTU 10 MW WT is used as reference for dimensions and masses of the OWT. These dimensions are listed in Section 4.2. The DTU 10 MW WT tower has an inclination and also varying steel thickness. In this simplified FE model the average diameter, d , and thickness, t , are used.

The variable, n_{ele} , defines how many beam elements are used in the FE model to model the OWT structure.

The rest of the input parameters are the structure height, h , Young's modulus for the steel, E , density of the steel, ρ , and the mass on top of the turbine, m . This mass represents the weight of the nacelle, blades and hub.

4. To calculate the global stiffness matrix, $[\mathbf{K}]$, the local stiffness matrices, $[\mathbf{k}]$, has to be determined. These are calculated with equation (4.4) for each element where $[\mathbf{B}]$ is the strain interpolation matrix and $[\mathbf{D}]$ is the stress-strain relation, also known as the constitutive relation.

$$[\mathbf{k}] = \int_V [\mathbf{B}]^T [\mathbf{D}] [\mathbf{B}] dV \quad (4.4)$$

The same goes for the global mass matrix, $[\mathbf{M}]$, where the local mass matrices, $[\mathbf{m}]$, are calculated with equation (4.5) where $[\mathbf{N}]$ is the shape function matrix.

$$[\mathbf{m}] = \int_V \rho [\mathbf{N}]^T [\mathbf{N}] dV \quad (4.5)$$

A more detailed description of what goes into equation (4.4) and (4.5) can be found in Appendix B.

5. The combined mass of the nacelle, hub and the three blades is inserted into the global mass matrix, $[\mathbf{M}]$, at the position of the top node in the x -direction.
6. The eigenvalue problem is solved by equation (4.6), to obtain the non-trivial solution to equation (4.2).

$$\det([\mathbf{K}] - \omega^2 [\mathbf{M}]) = 0 \quad (4.6)$$

In this step the boundary conditions of the system have to be taken into consideration. This is done by removing the rows and columns in the global stiffness-, $[\mathbf{K}]$, and mass matrix, $[\mathbf{M}]$, connected to the degrees of freedom that are restricted to movement.

This results in a number of squared eigenfrequencies, ω^2 , also know as eigenvalues, equal to the number of degrees of freedom in the 1D FE model.

7. The eigenvalues, ω^2 , are put into equation (4.2) to obtain the mode shapes, $\{\bar{\mathbf{D}}\}$, corresponding to the eigenvalues. The eigenfrequencies, f_n , are calculated from the eigenvalues by equation (4.7).

$$f_n = \frac{\sqrt{\omega^2}}{2\pi} \quad (4.7)$$

The simple 1D FE model of an OWT structure described above has to be further calibrated in order to determine the important eigenfrequencies with a satisfactory precision. This calibration is done by performing a convergence analysis in regards to the number of elements necessary to obtain convergence in the eigenfrequencies.

4.1.2 Convergence Analysis

A convergence analysis is performed for the first four eigenfrequencies, f_1 through f_4 , as the higher the eigenfrequencies become, the less they interfere with the dominant dynamic loading frequencies. An illustration of these load frequencies was seen in Figure 3.4 page 20. The input parameters used in the model for the convergence analysis is based on the DTU 10 MW WT and are listed in Table 4.1.

Table 4.1: Data for the analysed structure based on the DTU 10 MW WT [Desmond et al., 2016].

Parameter	Symbol	Unit	DTU 10 MW WT value
Structure height	h	m	161
Structure diameter	d	m	6.9
Structure wall thickness	t	m	0.03
Mass at top (hub, nacelle, blades)	m	ton	593.27
Young's modulus	E	Pa	$2.1 \cdot 10^{11}$
Structure steel density	ρ	$\frac{kg}{m^3}$	7850

The convergence analysis is performed by executing the FE calculation described in Section 4.1.1. The variable in the calculation is the number of beam elements, n_{ele} , used to model the OWT structure. The number of elements is varied from 2 to 12 elements, and the result of the analysis is shown in Figure 4.5.

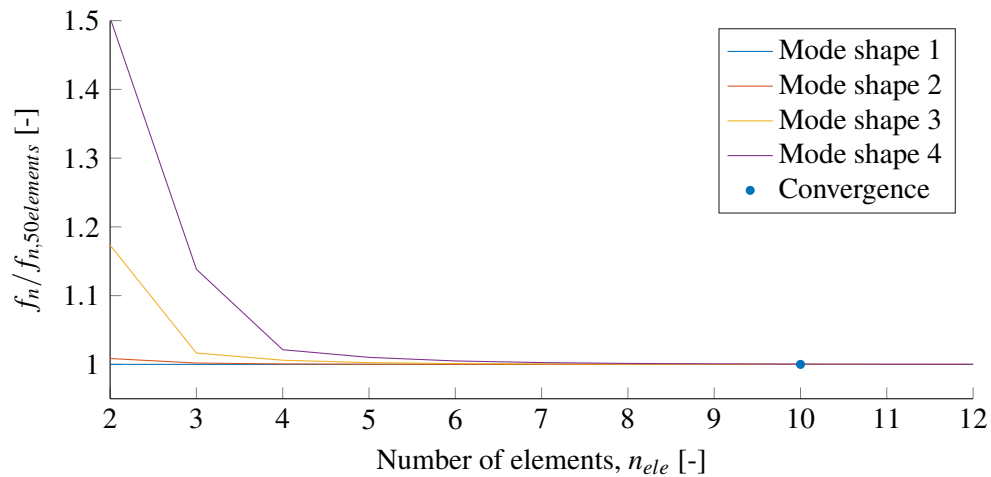


Figure 4.5: Convergence analysis of eigenfrequencies compared to number of elements. The blue dot represents the number of elements needed to obtain convergence for the first four eigenfrequencies. The eigenfrequencies, f_n , are normalised according to the eigenfrequencies calculated for the different modes with 50 elements.

From Figure 4.5 it can be seen that the first four mode shapes converge when 10 beam elements are used in the 1D FE model. An illustration of the first four mode shapes corresponding to the first four eigenfrequencies, f_n , can be seen in Figure 4.6.

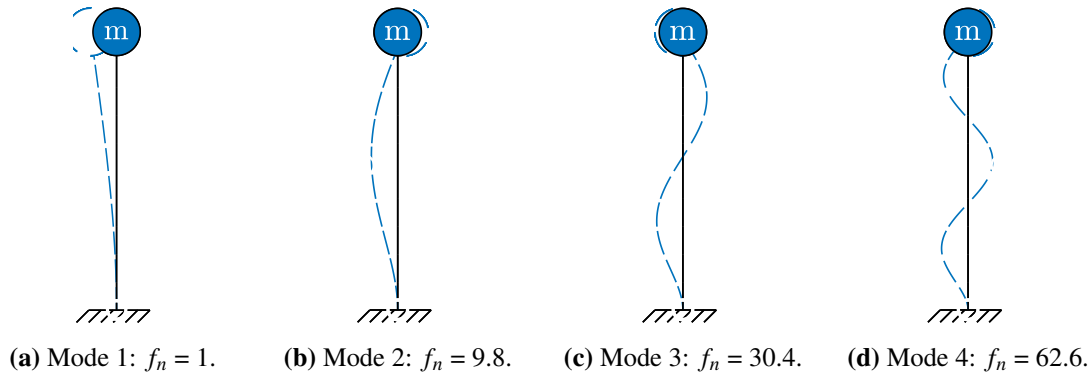


Figure 4.6: Stick with a mass, and the first four mode shapes for the model with their corresponding normalised eigenfrequencies. The normalised eigenfrequencies, f_n , are normalised according to the first eigenfrequency.

When observing the different mode shapes it becomes clear why mode 1, seen in Figure 4.6(a), converges right away. This shape can be described with one Bernoulli-Euler beam element. The opposite goes for mode 4, seen on Figure 4.6(d), where more elements are needed as the mode crosses the static equilibrium state three times. The convergence analysis concludes that it is necessary to use 10 elements in order to obtain a satisfactory accuracy. Therefore, 10 elements are used in the remaining analysis in this chapter.

4.1.3 Modelling of the Modified Support

The model of a stick with a mass at the top, as described in Section 4.1, is developed based on a fixed support at the bottom, see Figure 4.7(a). However, this model does not capture the real behaviour of an OWT, because it assumes that the OWT structure is fixed at the mudline and that the monopile below mudline is restrained against movement in the horizontal plane. A modified model is therefore developed, see Figure 4.7(b), where the support at the bottom consists of a horizontal stiffness k_x , allowing horizontal movement, and a rotational stiffness k_{rot} , replicating the behaviour at the mudline. The modified model is, equal to the Simple Model, restrained against movements in the axial direction, as these movements are assumed to be neglectable.

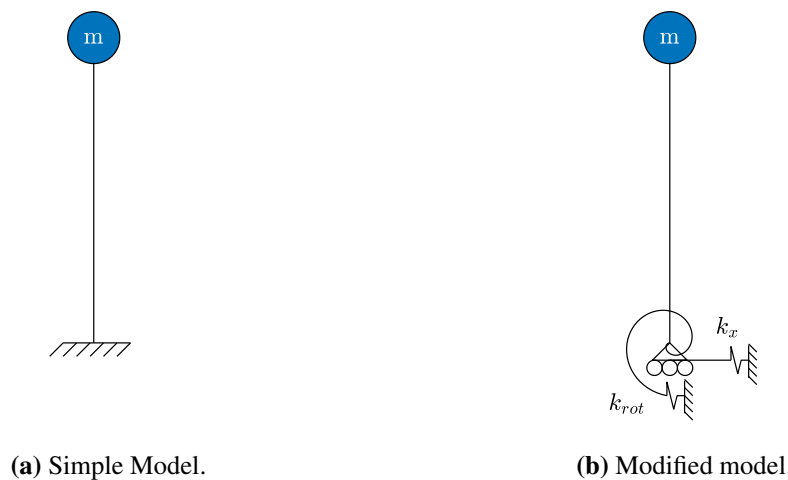


Figure 4.7: Illustration of the two models of a stick with a mass at the top.

If the values of the rotational and horizontal stiffness goes to infinity, model a and b from Figure 4.7 will behave equally. Instead of using infinity as the value for the two stiffnesses to make the model from Figure 4.7(b) behave as the model from Figure 4.7(a), they are assigned values that will give a precision of 0.01 Hz on the first eigenfrequency of both models. This value will be interpreted to be the stiffness necessary to make the modified model behave like the fixed model.

In the parametric variation section the horizontal and the rotational stiffness will both be varied in a range from zero to values of the chosen fixation with a precision of the mentioned 0.01 Hz, to see the effect of these combinations on the first eigenfrequency.

4.1.4 Final Simple 1D FE Model

The final model for performing parametric variations is a 1D FE model constructed of 10 Bernoulli-Euler beam elements. The bottom node is fixed in the restricted movement in any direction but the model has the option to change the rate of horizontal- and rotational fixation in the range from 0-100 %. Also, the model has a lumped mass in the top node to represent the mass of the nacelle, blades and the hub from an OWT. The final model, with a fixed support is illustrated in Figure 4.8.

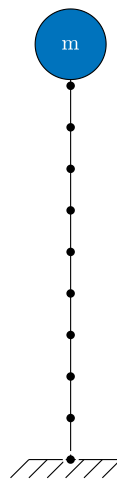


Figure 4.8: Final model used for the following parametric analyses.

4.2 Parameter Variations

A parameter analysis is performed for the model input. Here reference values are taken from the DTU 10 MW WT. The values for this WT and the ranges which will be used in the parameter analysis are listed in Table 4.2. The analyse will be performed with respect to the first eigenfrequency, i.e. how a change of the individual parameters will affect the first eigenfrequency. It has to be stated that some individual parameters will influence other parameters when varied, e.g. when the diameter is increased, the mass of the tower is also increased as the cross-sectional area of the steel is increased.

The mass and the geometric parameters (height, diameter and thickness) are investigated in a range of $\pm 10\%$. Larger variations of dimensions for OWTs are possible compared to the material parameters which are predefined for the materials. The material parameters are, contrarily to the

Table 4.2: Data for the analysed structure based on the DTU 10 MW WT from Desmond et al., 2016 and the ranges used in the parameter variations.

Parameter	Symbol	Unit	DTU 10 MW value	Minimum	Maximum
Structure height	h	m	161	90 %	110 %
Structure diameter	d	m	6.9	90 %	110 %
Structure wall thickness	t	m	0.03	90 %	110 %
Mass at top (hub, nacelle, blades)	m	ton	593.27	90 %	110 %
Young's modulus	E	Pa	$2.1 \cdot 10^{11}$	95 %	105 %
Structure steel density	ρ	$\frac{kg}{m^3}$	7850	95 %	105 %

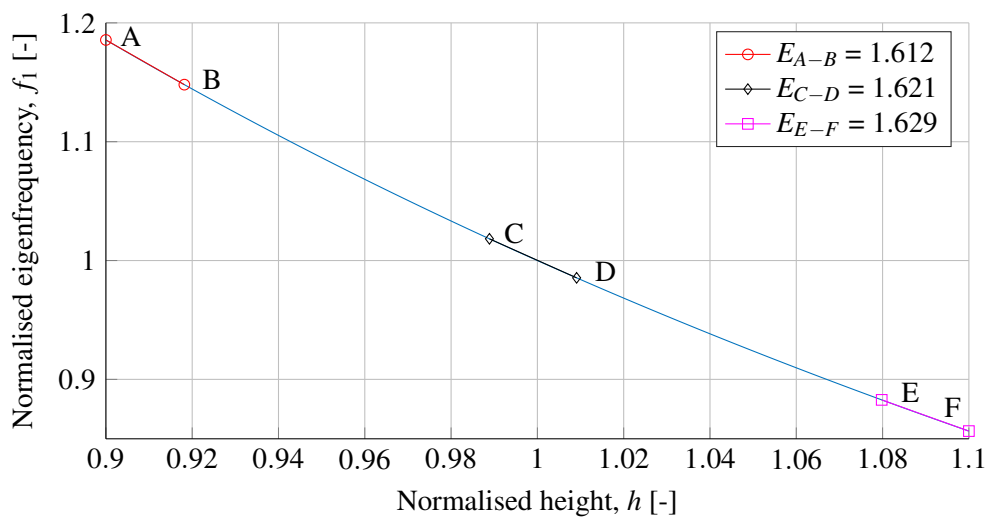
mass and geometric parameters, well known parameters. The ranges for these parameters are therefor reduced to a range of $\pm 5\%$ to account for uncertainties in the material and to analyse the influence of these.

Parametric variations are performed for all six variables listed in Table 4.2 including an extra variation of the horizontal- and rotational stiffness, k_x and k_{rot} respectively.

The parametric variations presented in the Section 4.2.1 to 4.2.7 show the effect a change in an individual parameter has on the first eigenfrequency of the system. The tendencies illustrated in those sections are commented on with words to explain why it behaves as it does. To finish up the parametric variations a more theoretical explanation of the tendencies can be found in Section 4.2.8, where the model is simplified into a SDOF system.

4.2.1 Structure Height

The first parametric variation is performed to estimate how a change in the structure height is affecting the first eigenfrequency. The result of this analysis can be seen in Figure 4.9.

**Figure 4.9:** Eigenfrequency depending on the height. Both axes are normalised with respect to the value from the DTU 10 MW WT.

It is seen that when the height of the OWT structure is increased the eigenfrequency decreases. This pattern is expected as the overall structure becomes less stiff, when the d/h -ratio is decreased. As the structure becomes less stiff, the oscillations of the structure will be larger and thereby one oscillation takes a longer period of time, resulting in a lower eigenfrequency. The legend in Figure 4.9 contains information about the elasticity of the varied parameter i.e. the height. The elasticity is calculated as the average elasticity for three different ranges illustrated in the figure by the red, black and purple line, see Appendix C for a deeper elaboration on how the elasticity is calculated. Varying the height has a great influence on the first eigenfrequency as the elasticity is above 1. This means that changing the height by 1 % will cause a change in the eigenfrequency which is larger than 1 %. The elasticities are determined for each parametric variation and they are commented on in Section 4.3.

4.2.2 Structure Diameter

The second parametric variation is performed to estimate how a change of the diameter affects the first eigenfrequency. The result of the analysis can be seen in Figure 4.10.

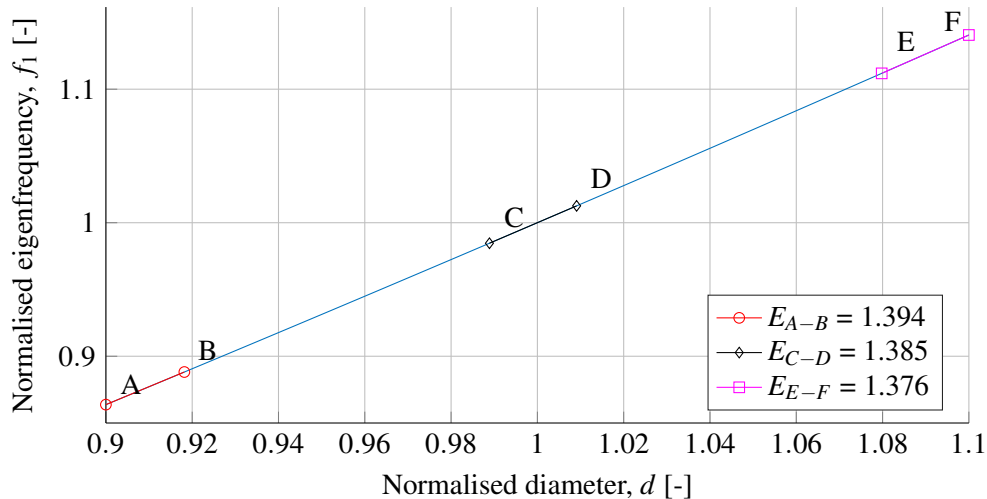


Figure 4.10: Eigenfrequency depending on the diameter of the structure. Both axes are normalised with respect to the value from the DTU 10 MW WT.

As the diameter is increasing, the moment of inertia is enlarged and the structure becomes stiffer. This causes the opposite reaction of what is described in Section 4.2.1 for the structure height, and the pattern illustrated in Figure 4.10 is thereby as expected.

4.2.3 Structure Thickness

The third parametric variation is performed on the thickness of the structure in regards to the first eigenfrequency. This analysis can be seen in Figure 4.11.

Increasing the tower steel thickness results in a larger moment of inertia, and like before the structure becomes stiffer. The increased stiffness causes smaller oscillations when the structure is vibrating in the first mode shape, which raises the number of oscillations over a period and thereby the eigenfrequency.

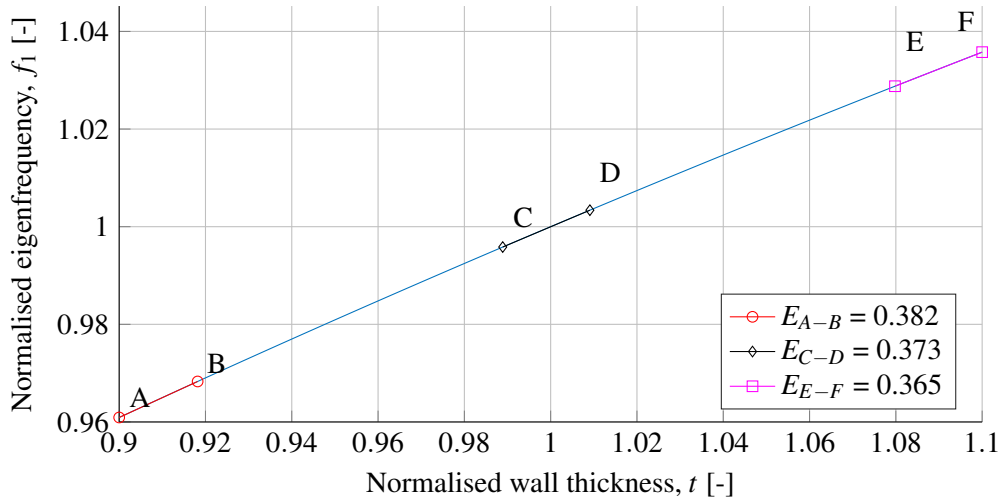


Figure 4.11: Eigenfrequency depending on the thickness of the structure. Both axes are normalised with respect to the value from the DTU 10 MW WT.

4.2.4 Lumped Mass

The fourth parametric variation is performed on the lumped mass in regards to the first eigenfrequency. The lumped mass involves both the mass of the nacelle, the hub and the blades. The result of this analysis can be seen in Figure 4.12.

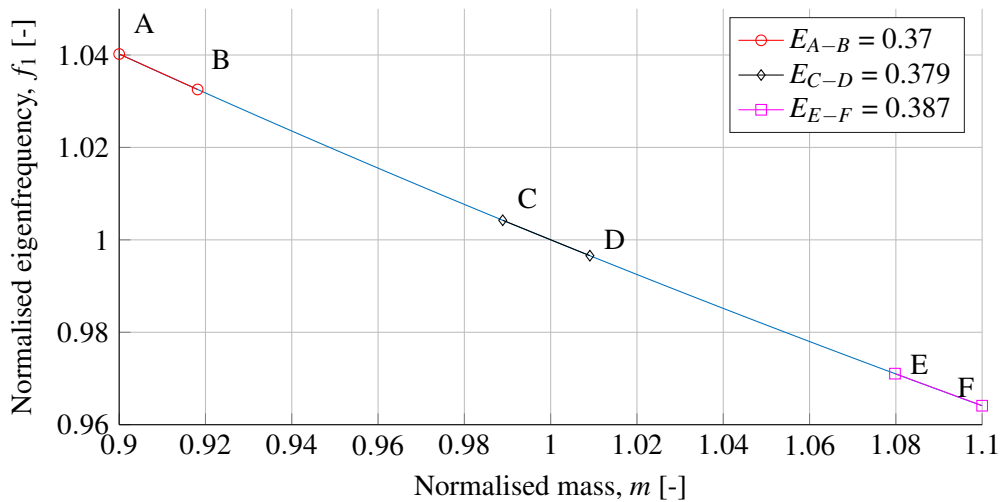


Figure 4.12: Eigenfrequency depending on the mass at the top. Both axes are normalised with respect to the value from the DTU 10 MW WT.

As the mass is increasing the first eigenfrequency is reduced, which can be seen in Figure 4.12. This is due to the fact that a larger mass has to be accelerated. This has to fulfil Newton's second law that states " $Force = Mass \cdot Acceleration$ ". Thereby a higher mass will cause a longer time for one oscillation and the first eigenfrequency will be lower.

4.2.5 Young's Modulus of Steel

The fifth parametric variation is performed on Young's modulus of steel in regards to the first eigenfrequency. The results of this analysis can be seen in Figure 4.13.

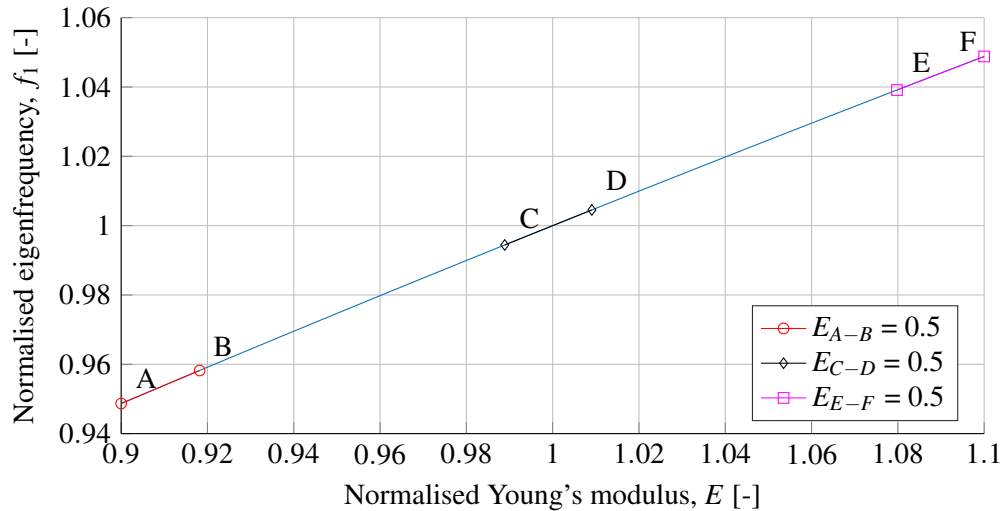


Figure 4.13: Eigenfrequency depending on Young's modulus. The x -axis is normalised for the standard value of Young's modulus and the y -axis for the calculated eigenfrequency with the standard value.

From Figure 4.13 it can be seen that the eigenfrequency is increased when Young's modulus is increased. This corresponds with that the stiffness of the structures material is defined by Young's modulus and an increase of this parameter results in a more stiff structure which increases the eigenfrequency.

4.2.6 Density of Steel

The sixth parametric variation is performed to estimate how a change in the density of the tower material affects the first eigenfrequency. The results of this analysis can be seen in Figure 4.14.

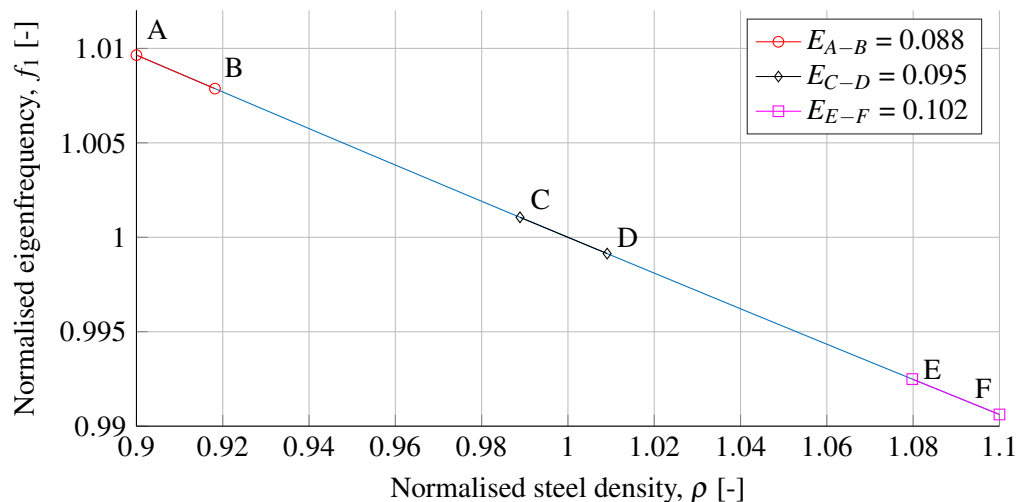
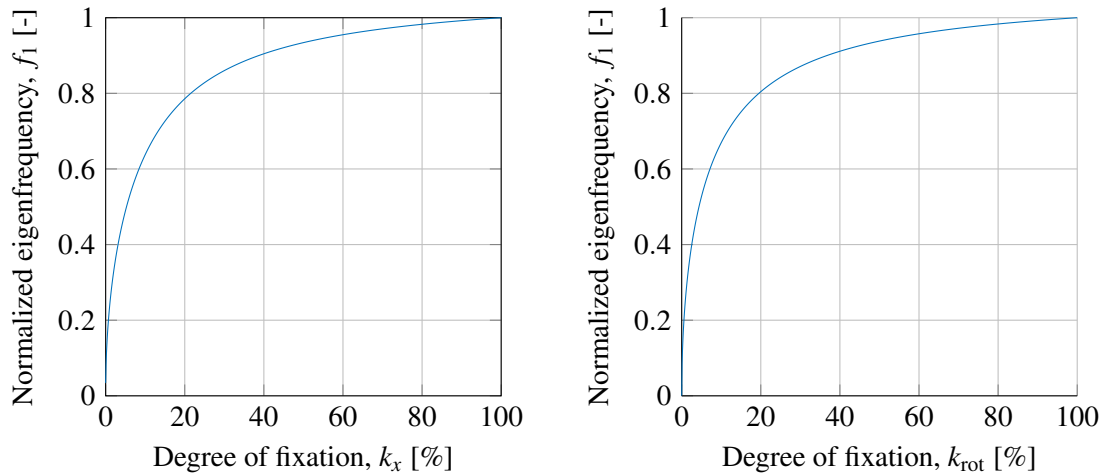


Figure 4.14: Eigenfrequency depending on the density. The x -axis is normalised for the standard value of steels density and the y -axis for the calculated eigenfrequency with the standard value.

From Figure 4.14 it can be seen that the density has a small influence on the first eigenfrequency. The eigenfrequency is affected at the third decimal and is thereby assumed to be so small the change is insignificant. The value of the eigenfrequency is expected to decrease as the density is increased. The tendency can be explained by a larger mass has to be accelerated which causes lower eigenfrequencies. This is the same tendency as for the parametric variation of the mass at the top of the OWT, which was seen in Figure 4.12.

4.2.7 Ratio of Fixation for the Modified Support

Finally, an analysis of the ratio of fixation is performed. This is done in order to estimate the influence of the fixation at the bottom of the OWT structure. The analysis can be seen in Figure 4.15. Here an analysis of both fixations are performed individually, where for the analysis in Figure 4.15(a) rotational movement is restricted and for the analysis in Figure 4.15(b) horizontal movement is restricted.



(a) The first eigenfrequency depending on the ratio of fixation in the horizontal direction.

(b) The first eigenfrequency depending on the ratio of fixation in the rotational direction.

Figure 4.15: Results from varying the two ratios of fixation individually.

The influence from the rate of fixation in horizontal and rotational direction can be seen in Figure 4.15. Here it is observed that at 50-60 % fixation for either the horizontal or rotational direction, the eigenfrequency is close to the final frequency of the system with a fixation of 100 %. Figure 4.15 illustrates the influence of each of the two fixations individually. However, in the real world both of these fixations are present. To illustrate the combined effects of the two fixations on the eigenfrequency, a surface plot is computed, see Figure 4.16.

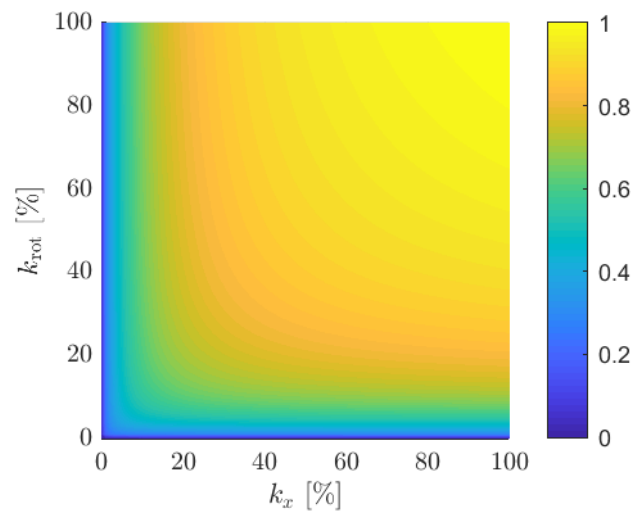


Figure 4.16: Surface plot of the eigenfrequency depending on both varied stiffnesses in the bottom node. The eigenfrequency is normalised with respect to the value when both stiffnesses are at 100 %.

Figure 4.16 shows how necessary it is to model the soil-structure interaction for monopiles, because it influences the rate of fixation at the bottom of the OWT e.g. if the soil-structure stiffness is very low, it will allow for a greater horizontal movement at the mudline, compared to if the soil-structure stiffness was very high. The rate of fixation is a crucial information that has to be known if the real eigenfrequencies are to be obtained through a FE model. The incorporation of the soil-structure interaction into the model is covered in Stage 3.

4.2.8 Simplified SDOF System

In this section, the tendencies derived from the parameter variation performed in Section 4.2 are verified. This verification is done by computing an equation for the first eigenfrequency of a SDOF system. In Appendix D.1 an equation to estimate the eigenfrequency of a SDOF system is derived. The system represents a fixed cantilever beam with a distributed mass and a point mass at the end, see Figure 4.17.

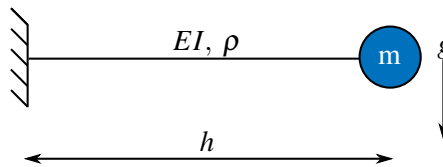


Figure 4.17: Cantilever beam with a point mass at the end.

This system is comparable to the earlier presented parametric variations. It should be mentioned the solution is an approximation and not an exact solution. The fundamental frequency for the simplified system can be estimated by equation (4.8).

$$f_1 \approx \frac{1}{2\pi} \sqrt{\frac{3EI}{(0.2235 h \rho \pi (d t - t^2) + m) h^3}} \quad (4.8)$$

f_1	The first eigenfrequency of the system
E	Young's modulus for the tower material
I	Area moment of inertia of the tower
m	Point mass (hub, nacelle and blades)
ρ	Density
h	The height of the turbine tower

The area moment of inertia for a tube is given by equation (4.9) where r_1 and r_2 are the inner and outer radius of the turbine tower. This can be rewritten to equation (4.10), which is explained in Appendix D.2.

$$I = \frac{\pi}{4} (r_2^4 - r_1^4) \quad (4.9)$$

$$= \frac{\pi}{64} (d^4 - (d - 2t)^4) \quad (4.10)$$

By substituting I from equation (4.10) into equation (4.8), an equation including all of the parameters from the parametric variations is obtained, see equation (4.11).

$$f_1 \approx \frac{1}{2\pi} \sqrt{\frac{3E \left(\frac{\pi}{64} (d^4 - (d - 2t)^4) \right)}{(0.2235 h \rho \pi (dt - t^2) + m)h^3}} \quad (4.11)$$

The equation is used to determine how the eigenfrequency is influenced by changes of different parameters. For doing this, each parameter is increased individually and the tendency of the response is obtained, see Table 4.3. From here it is seen the only parameters, which are negative correlated, is the height, the mass at top and the density of the tower material.

Table 4.3: Expected behaviour of parametric variations according to a simple SDOF system.

Variable increased	Symbol	Change in eigenfrequency
Structure height	h	↓
Structure diameter	d	↑
Structure wall thickness	t	↑
Mass (hub, nacelle, blades)	m	↓
Young's modulus	E	↑
Density	ρ	↓

By comparing Table 4.3 to the results from the parametric variations performed earlier it is seen that they show the same tendency.

4.3 Closure

In this section the parameter variations are further evaluated, where the effect from all parameters is shown together in one figure in order to determine the most sensitive parameters, when it comes to the dynamic properties of the system. Finally, a conclusion on the use of the Simple Model and the analysis is presented.

4.3.1 Combined Plot and Elasticity

To compare the importance of the different input parameters in the model, a combined plot including all parametric variations is shown in Figure 4.18. From this figure the determination of the most sensitive input parameters can be performed, as a variation in these parameters have a greater effect on the first eigenfrequency.

The comparison is made like the individual analyses by normalising the parameters with the value from the DTU 10 MW WT. In this way the effect of multiple parameters influence on the first eigenfrequency can be compared when they are changed with the same rate. The same ranges are used as in the individual analyses.

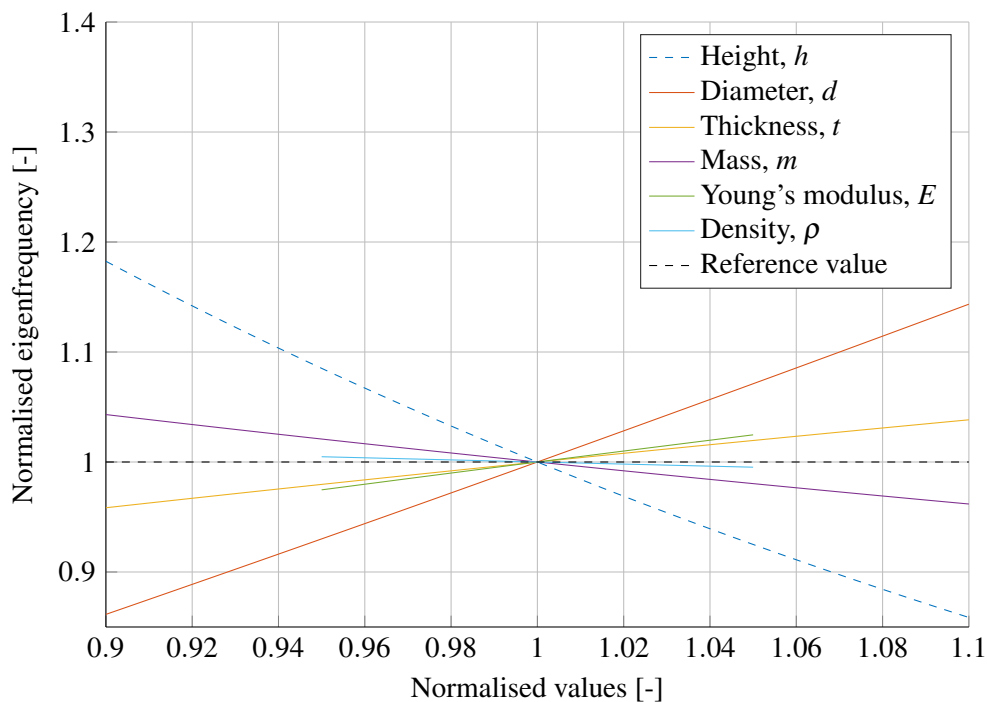


Figure 4.18: Different parameter's effect on the eigenfrequency when comparing to the DTU 10 MW WT.

From Figure 4.18 it can be seen that the most sensitive parameters for the system are the structure height and the diameter, as a change of these will have the largest effect on the eigenfrequency. The tendencies illustrated in Figure 4.18 shows exactly the same behaviour as the conducted elasticity analyses and the theoretical tendency of a SDOF system. The mean elasticity for each input parameter can be seen in Table 4.4 together with the theoretical tendencies found from equation (4.11) for the SDOF system. Here a positive value for the mean elasticity means there is

a positive correlation between the parameter and the eigenfrequency, and a negative value means there is a negative correlation between the parameter and the eigenfrequency.

Table 4.4: Mean elasticity for all parametric variations and the tendencies for the correlations between the input parameters and the eigenfrequency, found from the SDOF analysis.

Input parameter	Symbol	Mean elasticity	Theoretical correlation
Structure height	h	-1.62	Negative
Structure diameter	d	1.39	Positive
Structure wall thickness	t	0.37	Positive
Mass (hub, nacelle, blades)	m	-0.38	Negative
Young's modulus	E	0.50	Positive
Structure steel density	ρ	-0.10	Negative

As the offshore wind industry is developing, the OWTs become higher and higher, which according to this analysis could decrease the first eigenfrequency drastically. However, as the OWT towers becomes higher, the diameter is increased as well which according to this analysis will result in a higher first eigenfrequency, and thereby keep the first eigenfrequency of the system in a safe range, as the height and diameter are increased simultaneously. Despite the eigenfrequency is not changing drastic by varying parameters, it will still affect the structure as a small change in the eigenfrequency has a huge impact on the system's response to the dynamic loads. The safe range for the eigenfrequency mentioned here is referring back to Figure 3.4 page 20, where the load frequencies, that should be avoided, are illustrated. These load frequencies should be avoided to make sure that the system does not go into resonance by having the same fundamental eigenfrequencies as the load frequencies.

4.3.2 Conclusion of the Analysis

The analysis in this chapter has provided knowledge about the influence from the parameters which are input in the simple FE model. From the analysis it was found that the diameter and the height was the two input parameters which had the largest impact on the first eigenfrequency when changing all input parameters by the same rate. The material parameter Young's modulus does also have a relative large influence on the eigenfrequency compared to all the input parameters. However, this parameter does not have a wide range and the possible effect on the eigenfrequency is limited.

The model used in this chapter should not be used for providing results for the response of the full structure. This is due to no information about the soil is provided in the model nor any damping is considered. With these inputs excluded, an acceptable result can not be obtained, but the importance of the different parameters is observed by the simple dynamic model.

When the importance for the different input is analysed, further work with the model is made to include the soil in the model, where the knowledge from the literature study in Chapter 2 will be used to extend the model. The Extended Model is described and set up in Stage 3.

Stage 3

In this stage, the effects from the soil will be incorporated by extending the Simple Model introduced in Stage 2. Firstly, the p - y approach is examined, in order to obtain knowledge for what is necessary to include in the model. Secondly, the FE model from Stage 2 is further developed in order to incorporate the p - y curves, and parameter variations are performed for the new input. After, suggested improvements to the p - y curves are analysed and a new method, in the form of the PISA project, is introduced. Lastly, the Extended Model is separated at the mudline and a FE model for the upper- and lower part of the structure are developed, to be able to analyse different parts of the structure separately.

5	Soil Reaction Curves	49
5.1	Governing Equation	
5.2	p - y Curves by API	
6	Extended Model	61
6.1	Set up of the Model	
6.2	FE Calculation	
6.3	Convergence Analysis	
6.4	Parameter Variation	
6.5	Eigenfrequencies and Excitation Frequencies	
6.6	Discussion	
7	Improvements	87
7.1	Improvements to the API p - y curves	
7.2	PISA	
7.3	Comparison of p - y Curves	
7.4	Discussion	
8	Separation of Extended Model	101
8.1	Procedure	
8.2	Discussion of Application	
8.3	Results	

5. SOIL REACTION CURVES

In this chapter, one type of soil reaction curves, also known as the p - y curves, is introduced. The p - y curves represent the relationship between the soil resistance, p , and the lateral displacement, u , at a certain depth, z . The lateral displacement is normally referred to as y , hence the name p - y curve. However, the lateral displacement is in this report referred to as u . The p - y curves provides the input used to model soil-structure stiffness when calculating the lateral response of pile foundations, like an OWT monopile foundation, and is the currently suggested approach in the design guidelines DNV GL group, 2018 and API, 2014.

The p - y curves are in this project used as a tool to estimate the soil-structure stiffness between the monopile and the soil in which the monopile is embedded. This soil-structure stiffness is then used to include the effects of the soil surrounding the monopile in the Extended Model, which is developed in Chapter 6.

The following sections will introduce the p - y curves by the following steps. Firstly, the governing equation for a pile subjected to a lateral load is presented. After the presentation of the governing equation, the original p - y curves as suggested by API, 2014 will be introduced for soft clay, stiff clay and sand.

5.1 Governing Equation

When using the p - y curve approach, the pile is assumed to behave like a vertical Bernoulli-Euler beam. A pile subjected to lateral loads can be modelled from the equilibrium equation according to the Bernoulli-Euler beam theory, see equation (5.1). The equilibrium equation is derived by considering an infinitesimal small part of the monopile.

$$EI \frac{d^4 u}{dz^4} - N \frac{d^2 u}{dz^2} + p = 0 \quad (5.1)$$

EI	Bending stiffness
u	Displacement
z	Depth
N	Axis force
p	Soil resistance

The derivation of equation (5.1) is performed based on a few assumptions. The two main assumptions being that plane sections remain plane and that the equation only deals with small displacements and small rotations. This means that displacements caused by shear are neglected. Furthermore, it is assumed that the pile material is homogeneous, isotropic and linear elastic.

5.2 p - y Curves by API

The formulation of the p - y curves as presented by API, 2014 is the original formulation which is suggested in the current design guideline. The formulation is mainly based on field tests performed

on flexible and slender piles in the 1960s. Since then, the experimental derived p - y curves have been extrapolated to other pile dimensions.

The determination of the p - y curves are dependent on the type of soil. According to API, 2014, the p - y curves for different types of soil should be constructed according to the following recommendations.

- Soft clay according to Matlock, 1970
- Stiff clay according to Reese, Cox, and Koop, 1975
- Sand according to O'Neill and Murchison, 1983

5.2.1 Soft Clay

This section deals with the construction of the p - y curves for soft clay. The formulation of the p - y curves for soft clay is based on Matlock, 1970 which considers full scale tests performed on 12.75 inch diameter steel pipes (corresponding to approximately 0.32 m). These full scale tests were performed at two different test sites with soil characterised as soft clay.

Lateral Capacity

In order to be able to construct the p - y curves, the ultimate lateral soil resistance has to be calculated. The ultimate lateral soil resistance in clay is usually determined as the lowest of two possible failure mechanisms - a wedge failure mechanism which is dominating on shallower depths, see Figure 5.1(a), and a flow failure mechanism which is dominating at greater depths, see Figure 5.1(b).

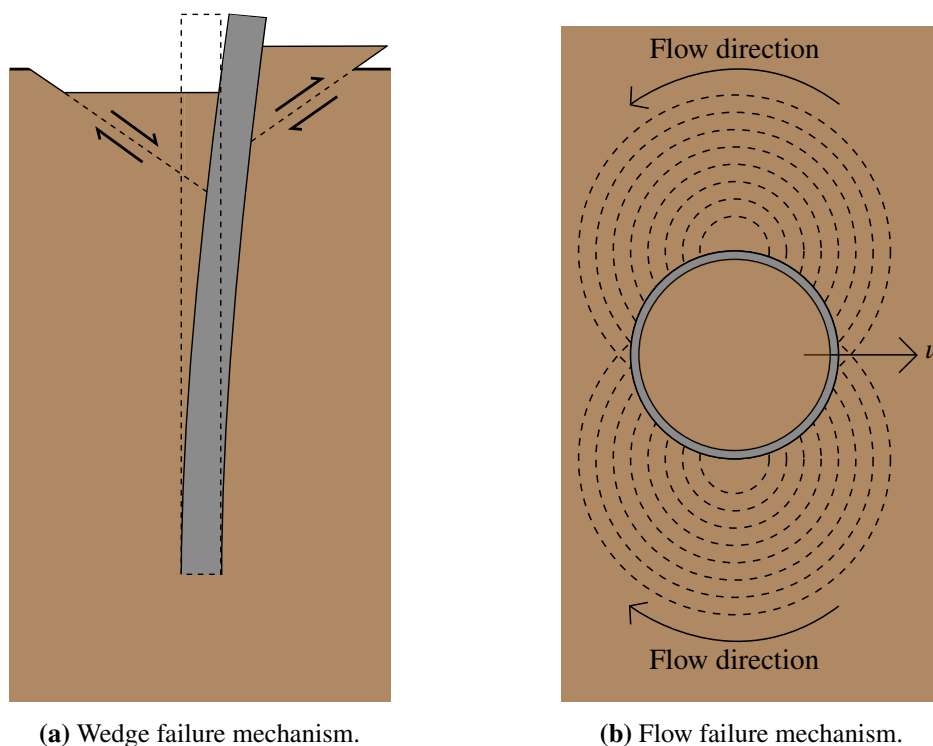


Figure 5.1: Illustration of the failure mechanisms for soft clay.

From the wedge failure at shallower depths illustrated in Figure 5.1(a), it can be seen that the pile is displaced adequately for a passive soil failure at the front of the pile and an active soil pressure behind the pile.

From the flow failure at greater depths illustrated in Figure 5.1(b), it can be seen that the soil is moving around the monopile. The soil is however staying in the same horizontal plane due to restraining of the overburden pressure.

The ultimate soil resistance for soft clay at shallow depth, where the wedge failure is dominating, can be expressed by equation (5.2) and at greater depths where the flow failure is dominating can be expressed by equation (5.3).

$$p_u = 3 s_u d + \gamma' z d + J s_u z \quad \text{for } z < z_R \quad (5.2)$$

$$p_u = 9 s_u d \quad \text{for } z \geq z_R \quad (5.3)$$

p_u	Ultimate soil resistance per unit length
s_u	Undrained shear strength
d	Pile diameter
γ'	Effective unit weight of submerged soil
J	Dimensionless empirical constant
z	Depth below original mudline
z_R	Depth below soil surface to bottom of reduced resistance zone (transition depth)

The dimensionless empirical constant, J , is dependent on the consistency of clay. It can vary between 0.25 and 0.5 and can be determined by field testing. According to Jia, 2018, J can be taken as 0.5 for soft clay and 0.25 for stiff clay.

The transition depth, z_R , indicates the depth for which equation (5.2) becomes greater or equal to equation (5.3). The transition depth is thereby also an indication of the depth where the most likely failure mechanism changes from the wedge mechanism, which was illustrated in Figure 5.1(a), to the flow mechanism, which was illustrated in Figure 5.1(b). For conditions with constant strength with depth the transition depth z_R can be expressed by equation (5.4).

$$z_R = \frac{6 d}{\frac{\gamma' d}{s_u} + J} \quad (5.4)$$

In cases where the strength varies with depth, the transition depth should be obtained by determining the depth where equation (5.2) yields a higher ultimate resistance compared to equation (5.3). According to *API 2A-WSD*, this depth should not be less than 2.5 times the average pile diameter.

Lateral Soil Resistance - Displacement

The construction of the p - y curves for soft clay is dependent on the ultimate soil resistance calculated in the previous section, the depth for which the curve is constructed, the type of loading and the reference displacement u_{50} , which is the displacement corresponding to the displacement occurring at 50 % of the ultimate soil resistance. The reference displacement can be expressed by

equation (5.5).

$$u_{50} = 2.5 \varepsilon_{50} d \quad (5.5)$$

The strain level ε_{50} is the strain level occurring at 50 % of the maximum principal stress in an undrained compression laboratory test. If no laboratory test is available, ε_{50} can be taken as 0.02 for soft clay and 0.005 for stiff clay according to A. W. Skempton, 1951.

As mentioned, the construction of the p - y curves is dependent on the depth which the curves represent and whether the soil is monotonic loaded or cyclic loaded. The p - y curves for monotonic loading are only considering a monotonic loading and a corresponding displacement and they do not account for unloading-reloading. The p - y curves for cyclically loading consider the effects of unloading-reloading and the soil response to such a loading. For monotonic loading, the p - y curves are established using equation (5.6) for a displacement lower than eight times the reference displacement, and using equation (5.7) if the displacement is greater than eight times the reference displacement.

$$p = \frac{p_u}{2} \left(\frac{u}{u_{50}} \right)^{\frac{1}{3}} \quad \text{for } u \leq 8 u_{50} \quad (5.6)$$

$$p = p_u \quad \text{for } u > 8 u_{50} \quad (5.7)$$

A p - y curve for monotonically loaded soft clay is illustrated in Figure 5.2. If the soft clay is loaded cyclic, another formulation for the p - y curves is available. This formulation is dependent on whether the depth is greater or smaller than the transition depth. If the depth is smaller than the transition depth, the p - y curve can be constructed using equation (5.8) for displacements lower than three times the reference displacement and equation (5.9) for displacements greater than three times the reference displacement.

$$p = \frac{p_u}{2} \left(\frac{u}{u_{50}} \right)^{\frac{1}{3}} \quad \text{for } u \leq 3 u_{50} \quad (5.8)$$

$$p = 0.72 p_u \quad \text{for } u > 3 u_{50} \quad (5.9)$$

A p - y curve for cyclically loaded soft clay in a depth lower than the transition depth is illustrated in Figure 5.2. When the depth becomes greater than the transition depth, a third and last formulation is used to construct the p - y curves. Once again, this formulation is dependent on the displacement. If the displacement are smaller than three times the reference displacement, the p - y curve can be constructed using equation (5.10). However, if the displacement are greater than 15 times the reference displacement, equation (5.11) is used for the construction. In case the displacement is in between the limits of the reference displacement, a linear interpolation is used between the values of three and 15 times the reference displacement.

$$p = \frac{p_u}{2} \left(\frac{u}{u_{50}} \right)^{\frac{1}{3}} \quad \text{for } u \leq 3 u_{50} \quad (5.10)$$

$$p = 0.72 p_u \frac{z}{z_R} \quad \text{for } u \geq 15 u_{50} \quad (5.11)$$

A p - y curve for cyclically loaded soft clay in a depth greater than the transition depth is illustrated in Figure 5.2.

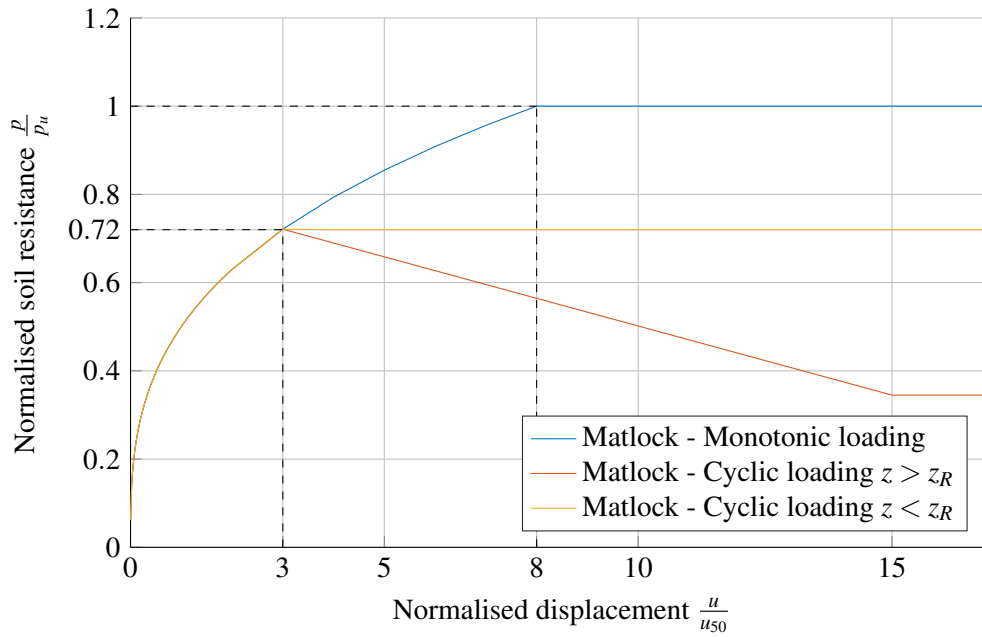


Figure 5.2: Example of p - y curves for soft clay according to Matlock, 1979.

From Figure 5.2 and equation (5.6), (5.8) and (5.10) it can be seen that the first part of the p - y curves for soft clay is constructed as a third order parabolic function. This means the p - y curves for soft clay according to API, 2014 have infinite initial slope, which means the curves predict an infinite initial stiffness. This is not physically possible and the p - y curves for soft clay are thereby corrected by a linear initial slope according to DNV GL group, 2017.

$$p = \frac{0.1p_u}{0.23u_{50}}u \quad \text{for } u \leq 0.23u_{50} \quad (5.12)$$

This concludes the presentation of the p - y curves for soft clay according to Matlock, 1970. From the presentation, it appears that the following parameters are input for the construction of the p - y curves:

s_u	Undrained shear strength
ϵ_{50}	Strain level occurring at 50 % of the maximum principal stress
J	Dimensionless empirical constant
σ'_v	Effective overburden pressure
d	Pile diameter
z	Depth below original mudline
u	Lateral displacement

From the description of the input parameters above, it can be seen that the behaviour of soft clay is described from a representation of the undrained shear strength, s_u , a strain level, ϵ_{50} , and a empirical constant, J . A parameter variation of these input parameters are performed with the Extended Model, see Section 6.4. Following this parameter variation, a discussion is addressing whether the behaviour of soft clay can be described from these input parameters alone, see Section 6.6.

5.2.2 Stiff Clay

This section deals with the construction of the p - y curves for stiff clay. The formulation of the p - y curves for stiff clay is based on Reese, Cox, and Koop, 1975. This formulation is based on lateral load tests of two 0.6 m diameter steel piles embedded in stiff clay beneath water table.

Lateral Capacity

In order to construct the p - y curves, the ultimate lateral soil resistance has to be calculated. As for soft clay, the ultimate lateral soil resistance is determined as the lowest of two possible failure mechanisms - a wedge failure mechanism and a flow failure mechanism.

The wedge failure mechanism is, as for soft clay, the dominating failure mechanism at shallower depths, when the depth is smaller than the transitional depth. The development of the wedge failure mechanism in stiff clay is dependent on the strength parameters of the clay. In stiff clay conditions with a high strength, the soil might have sufficient strength to stand vertically and thereby cause a gap behind the pile, while the passive wedge failure is happening in front of the pile, see Figure 5.3. However, in weaker stiff clay conditions, the wedge failure mechanism will happen like the one in soft clay, see Figure 5.1(a) page 50.

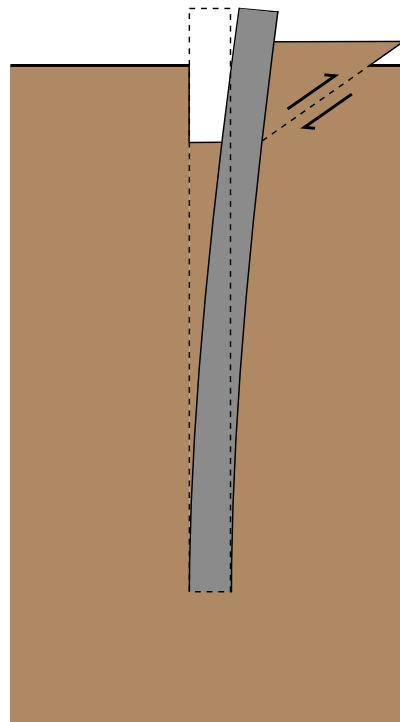


Figure 5.3: Wedge failure mechanism for strong stiff clay.

At greater depths, the flow failure mechanism is the dominating failure mechanism, as it was the case for soft clay. The flow failure mechanism is identical to the one introduced for soft clay, see Figure 5.1(b) page 50.

The ultimate lateral soil resistance per unit length in stiff clay, is estimated by using the lowest value from equation (5.13).

$$p_u = \min \begin{cases} p_{us} = 2s_a d + \gamma' d z + 2.83 s_a z \\ p_{ud} = 11 s_u d \end{cases} \quad (5.13)$$

The equation for p_{us} represents the ultimate lateral soil resistance for the wedge failure mechanism in stiff clay whereas the equation for p_{ud} represents the ultimate lateral soil resistance for the flow failure mechanism in stiff clay.

Lateral Soil Resistance - Displacement

In this section, the procedure for constructing the p - y curves in stiff clay is presented. The construction of the p - y curves for stiff clay is not as well described as the construction of the curves for soft clay. According to API, 2011, stiff clay has a non-linear stress-strain relationship, but the issue about the stiff clay is that it is more brittle than soft clay. However, according to API, 2011, the formulation developed by Reese, Cox, and Koop, 1975 can be used.

As mentioned, the construction of the p - y curves is in general dependent on the depth of where the curves are constructed and the type of loading. In cases where the loading can be defined as monotonic loading, the p - y curves for stiff clay can be composed of five parts. The initial part of the curve, defining the initial stiffness of the stiff clay, can be estimated from equation (5.14).

$$p = (k_s z) u \quad (5.14)$$

The slope of the initial part of the curve for monotonic loading, k_s , depends on the average undrained shear strength, s_a , see Table 5.1.

Table 5.1: Representative values for the initial slope of the p - y curves for stiff clay according to Reese, Cox, and Koop, 1975. k_s is the initial slope for monotonic loading and k_c is the initial slope for cyclic loading.

Parameter	Average undrained shear strength, s_a [kPa]		
	50 - 100	100 - 200	200 - 400
k_s [MN/m ³]	135	270	540
k_c [MN/m ³]	55	110	540

The next part of the curve is a parabolic part defined by equation (5.15). This part of the p - y curve starts at the intersection between equation (5.14) and (5.15).

$$p = 0.5 p_u \left(\frac{u}{u_{50}} \right)^{0.5} \quad (5.15)$$

The reference displacement, u_{50} , is in this formulation defined as equation (5.16).

$$u_{50} = \varepsilon_{50} d \quad (5.16)$$

Equation (5.17) defines the next part of the curve, from the point where it intersects with the part defined in equation (5.15) to the point where the displacement, u , is equal to $A_s u_{50}$. Here A_s is a

constant depending on the depth of where the p - y curve is constructed and the diameter of the pile. A_s can be determined in Appendix E.1.

$$p = 0.5p_u \left(\frac{u}{u_{50}} \right)^{0.5} - 0.055p_u \left(\frac{u - A_s u_{50}}{A_s u_{50}} \right)^{1.25} \quad (5.17)$$

The last two parts of the p - y curve is defined by two straight lines, equation (5.18) and (5.19) respectively.

$$p = 0.5p_u (6A_s)^{0.5} - 0.411p_u - \frac{0.0625}{u_{50}} p_u (u - 6A_s u_{50}) \quad \text{for } A_s u_{50} \leq u < 6A_s u_{50} \quad (5.18)$$

$$p = 0.5p_u (6A_s)^{0.5} - 0.411p_u - 0.75p_u A_s \quad \text{for } u \geq 18A_s u_{50} \quad (5.19)$$

The procedure of constructing the p - y curves during monotonic loading for stiff clay, which was presented above, assumes there is an intersection between the initial part of the curve, equation (5.14), and the parabolic function, equation (5.15). However, this might not always be the case. The p - y curve for stiff clay is defined by equation (5.14) until it intersects with another part of the p - y curve. If no intersection occurs, equation (5.14) defines the complete p - y curve [Reese, Cox, and Koop, 1975]. A p - y curve for monotonic loading of stiff clay is illustrated in Figure 5.4.

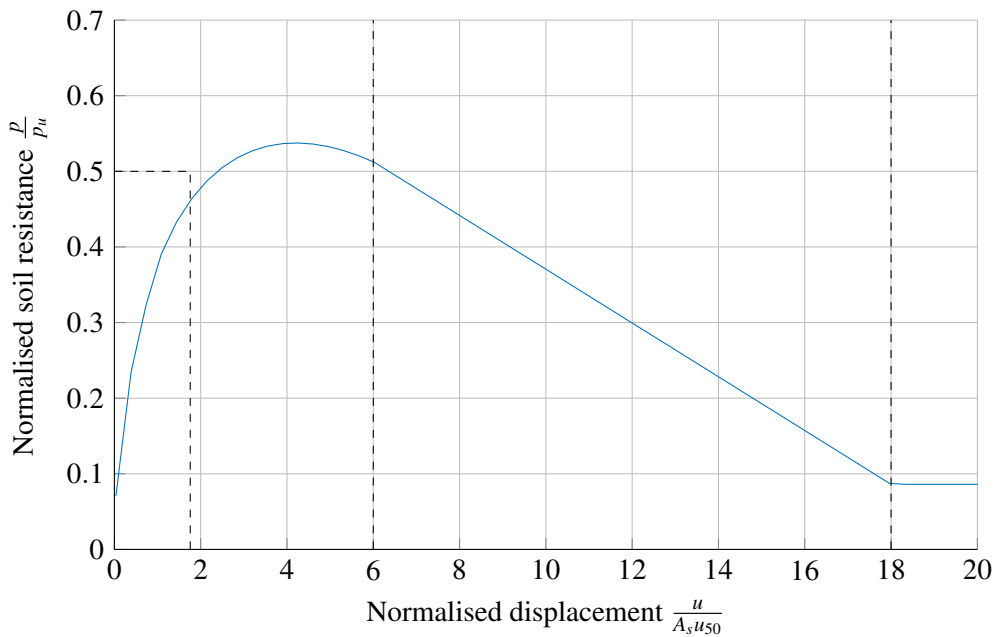


Figure 5.4: Example of p - y curve under monotonic loading for stiff clay according to Reese, Cox, and Koop, 1975.

If the stiff clay is loaded cyclic, another formulation is available where the p - y curves are constructed from four parts. The first part of the curve is almost identical to the first part of the p - y curve for monotonically loaded stiff clay, except from the slope for monotonic loading, k_s , being replaced by the slope for cyclic loading, k_c .

$$p = (k_c z) u \quad (5.20)$$

The next part of the p - y curve is defined by a parabolic function, see equation (5.21) and (5.22). This parabolic part starts at the intersection between equation (5.20) and (5.21).

$$p = A_c p_u \left(1 - \left(\frac{u - 0.45u_p}{0.45u_p} \right)^{2.5} \right) \quad (5.21)$$

$$u_p = 4.1 A_c u_{50} \quad (5.22)$$

The constant A_c can be determined in Appendix E.1. The last two parts of the curve are expressed as straight lines, see equation (5.23) and (5.24).

$$p = 0.936 A_c p_u - \frac{0.085}{u_{50}} p_u (u - 0.6u_p) \quad \text{for } 0.6 u_p \leq u < 1.8 u_p \quad (5.23)$$

$$p = 0.936 A_c p_u - \frac{0.102}{u_{50}} p_u u_p \quad \text{for } u \geq 1.8 u_p \quad (5.24)$$

The procedure of construction the p - y curves during cyclic loading for stiff clay is identical to the procedure of construction of the p - y curves during monotonic loading. This means that the procedure assumes that there is an intersection between the first linear part and the second parabolic part. If this is not the case, the equation that yields the smallest soil resistance, p , for any value of the displacement, u , should be employed. A p - y curve for cyclic loading of stiff clay is illustrated in Figure 5.5.

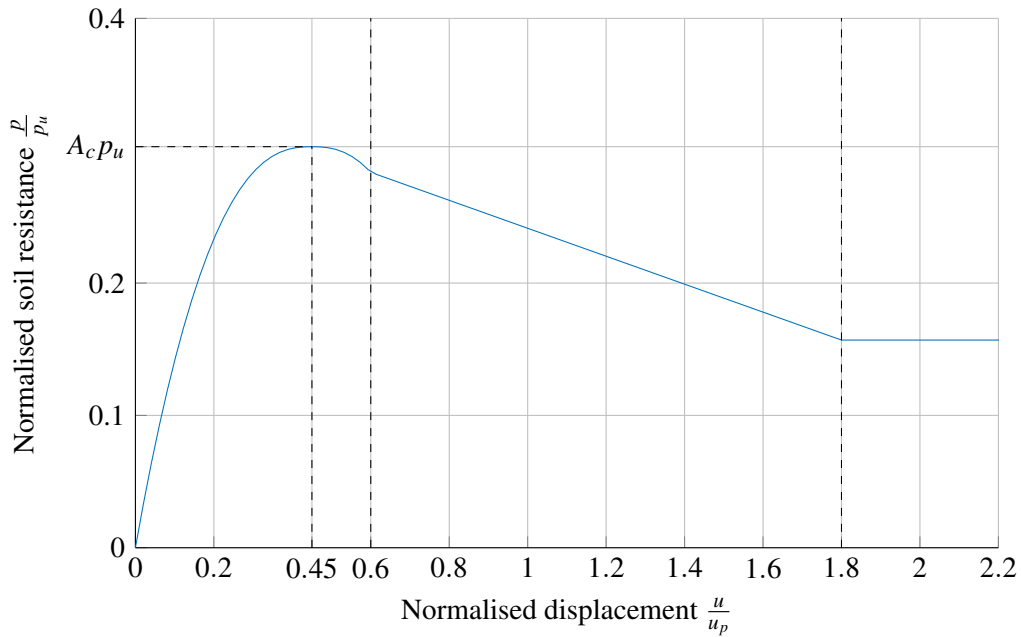


Figure 5.5: Example of p - y curve under cyclic loading for stiff clay according to Reese, Cox, and Koop, 1975.

When comparing the formulation for cyclic loading of stiff clay, see Figure 5.5, to the formulation used for soft clay, see Figure 5.2, it is noticed that the only difference is that the peak point is reduced drastically. This reduction of the peak point is a result of the more brittle properties of the stiff clay compared to soft clay.

This concludes the presentation of the p - y curves for stiff clay according to Reese, Cox, and Koop, 1975. From the presentation, it appears that the following parameters are input for the construction of the p - y curves.

s_u	Undrained shear strength
s_a	Average undrained shear strength
ϵ_{50}	Strain level occurring at 50 % of the maximum principal stress
J	Empirical constant
σ'_v	Effective overburden pressure
d	Diameter of the pile
z	Depth
u	Lateral displacement

From the description of the input parameters above, it can be seen that the behaviour of stiff clay is described from a representation of the undrained shear strength, s_u and s_a , a strain level, ϵ_{50} , and an empirical constant, J . Parameter variations of these input parameters are performed with the Extended Model, see Section 6.4. Following this parameter variation, a discussion is addressing whether the behaviour of stiff clay can be described from these input parameters alone, see Section 6.6.

5.2.3 Sand

This section deals with the construction of the p - y curves for sand. The formulation of the p - y curves for sand is based on O'Neill and Murchison, 1983 which considers full scale tests of two identical steel pipes with a diameter of 0.61 m, performed at Mustang Island. The tests were only performed on one type of sand.

Lateral Capacity

In order to be able to construct the p - y curves for sand, the ultimate lateral soil resistance first has to be determined. The ultimate lateral soil resistance for sand is expressed in terms of two possible failure mechanisms, which are identical to the ones introduced for soft clay - a wedge failure mechanism, see Figure 5.1(a), and a flow failure mechanism, see Figure 5.1(b) page 50.

The wedge failure mechanism occurs when the pile is displaced adequately for a passive failure to happen in front of the pile, which is dominant at shallower depths. The displacement of the pile does also cause an active failure to happen behind the pile as it was the case for soft clay. The flow failure is the dominating failure mechanism at greater depths where soil is moved around the pile as a result of the displacements. The ultimate lateral soil resistance for sand is expressed as the lowest value of the ultimate lateral resistance at shallow depth, p_{us} , and the ultimate lateral resistance at greater depths, p_{ud} , see equation (5.25).

$$p_u = \min \begin{cases} p_{us} = (C_1 z + C_2 d) \gamma' z \\ p_{ud} = C_3 d \gamma' z \end{cases} \quad (5.25)$$

C_1, C_2 & C_3 | Lateral resistance coefficients

The lateral resistance coefficients are dependent on the effective angle of internal friction of sand, ϕ' , and can be determined using the formulation presented in Appendix E.2.

Lateral Soil Resistance - Displacement

The p - y curves for sand can be constructed from equation (5.26) which is a hyperbolic tangent function.

$$p = A p_u \tanh\left(\frac{kz}{A p_u} u\right) \quad (5.26)$$

k | Initial modulus of subgrade reaction
 A | Factor to account for type of loading

The initial modulus of subgrade reaction is determined as a function of the effective internal friction angle. The determination of the initial modulus of subgrade reaction is described in Appendix E.2.

The A -factor is dependent on which type of loading the sand is subjected to, and can be estimated by equation (5.27) if the sand is subjected to cyclic loading or equation (5.28) if the sand is subjected to monotonic loading.

$$A = 0.9 \quad \text{for cyclic loading} \quad (5.27)$$

$$A = \left(3.0 - 0.8 \frac{z}{d}\right) \geq 0.9 \quad \text{for monotonic loading} \quad (5.28)$$

From equation (5.26) and (5.27) it can be seen that the factor A is a multiplier of the ultimate lateral soil resistance. It can be seen that the factor allows a soil resistance up to three times the ultimate soil resistance close to the surface, but the size of A decreases with increasing depth. From equation (5.26) it is further noticed that the p - y curves for sand are controlled by the initial stiffness of the soil kz , also known as E_{py} , and the ultimate soil resistance. Figure 5.6 illustrates an example of a p - y curve for sand.

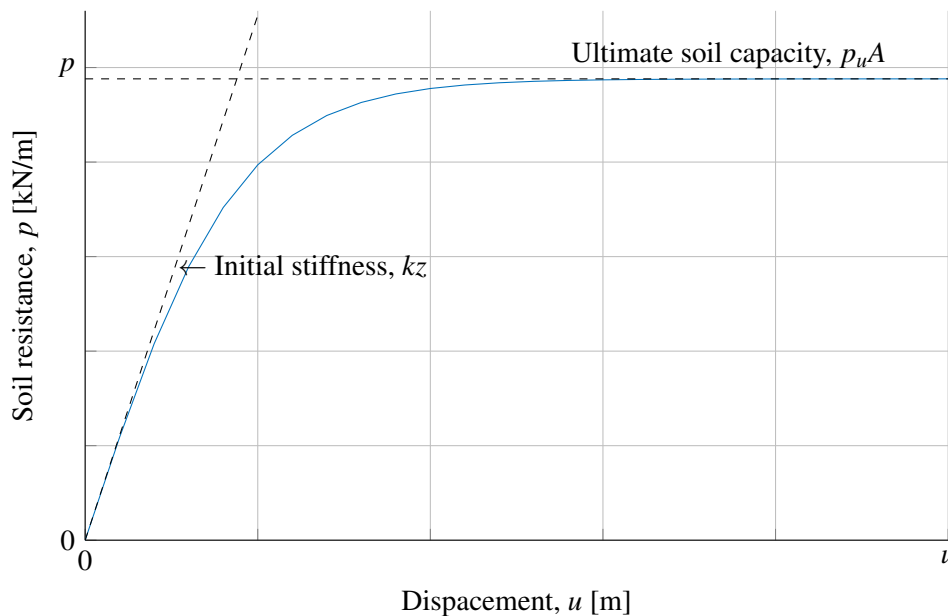


Figure 5.6: Example of p - y curve for sand according to API 2A-WSD.

This concludes the presentation of the p - y curves for sand according to *API Recommended Practise 2GEO*. From the presentation of the p - y curves for sand it appears that the following parameters are the input parameters.

ϕ'	Effective angle of internal friction
σ'_v	Effective overburden pressure
z	Depth below original mudline
d	Pile diameter
u	Lateral displacement

From the presentation of input parameters in the table above, it is concluded that the effective angle of internal friction, ϕ' , is the only parameter describing the behaviour of sand. A parameter variation of the effective angle of internal friction is performed with the Extended Model, see Section 6.4. Following this parameter variation, a discussion is addressing whether the behaviour of sand can be described from the effective angle of internal friction alone, see Section 6.6.

6. EXTENDED MODEL

This chapter considers an extension of the model from Stage 2, now considering the soil-structure interaction using the API p - y approach.

The geometric difference from this model compared to the Stage 2 model is, that instead of cutting the model at the transition piece the complete structure of the OWT supported by a monopile is included. Instead of the fixed support used in Stage 2, the support for the Stage 3 model consists of the soil surrounding the monopile. The system is illustrated in Figure 6.1.

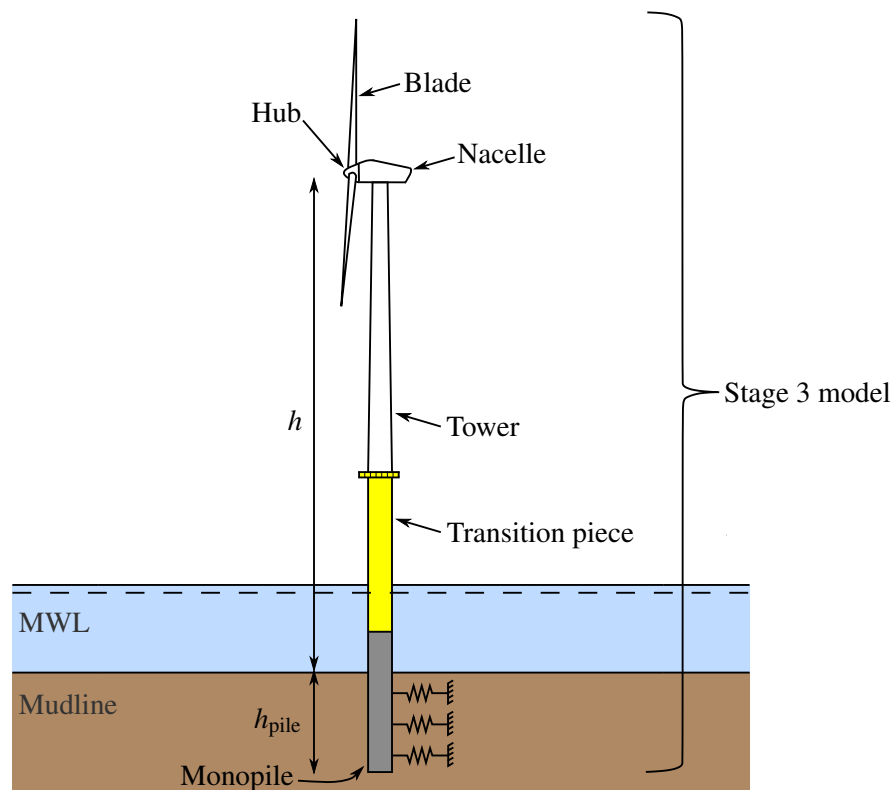


Figure 6.1: Illustration of an OWT and which parts that are considered in Stage 3.

As the full system is now modelled, more phenomena have been included in the model. These are the added mass from the water around the pile and the soil and water inside the pile. The implementation of these are explained in the set up of the model.

6.1 Set up of the Model

As for Stage 2, the Extended Model in Stage 3 model is programmed in MATLAB using Bernoulli-Euler beam elements, with the same tower and pile cross section from bottom to the top of the model. Beyond the addition of Bernoulli-Euler beam elements below the mudline, springs are added to the model perpendicular to the surface below the mudline to represent the soil-structure stiffness. The Stage 3 model is illustrated in Figure 6.2.

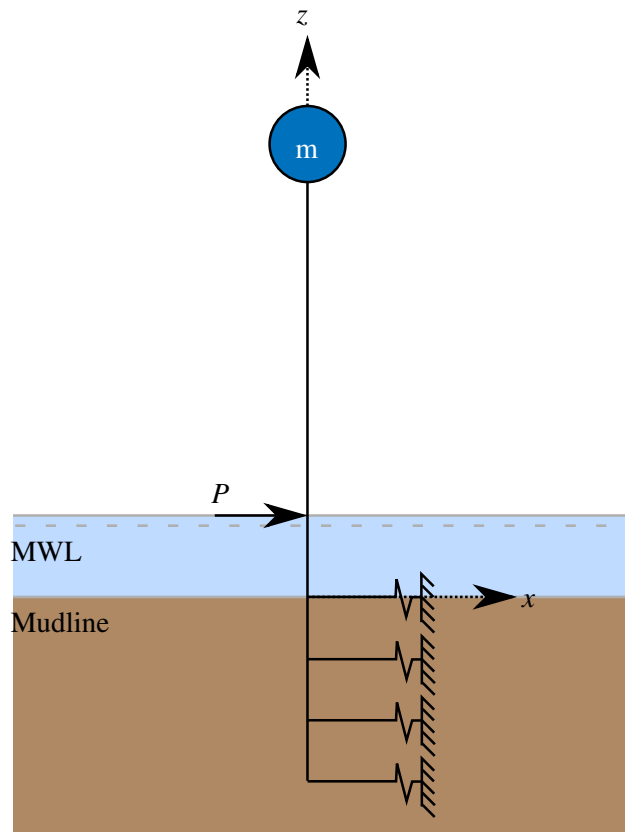


Figure 6.2: Illustration of the 1D model considered in Stage 3.

In the previous model the input were all linear-elastic, but as the p - y curves are implemented, a non-linearity is included in the model. To linearise this non-linearity from the p - y curves, a residual calculation is performed, using the tangential stiffness from the p - y curves to determine the soil-structure stiffness and the displacements of the system related to a load, P . The load is placed at the height of the mean water level, see Figure 6.2. The load, P , represents the load from current and small waves that are occurring at all times, even if no wind is present at the location. Instead of determining the load it is chosen to observe its effects on the eigenfrequency as the load is varied. The displacements of the structure caused by the load and the soil-structure stiffness caused by this displacement are considered as the stationary state for the model. It is for this state that the eigenfrequencies are determined.

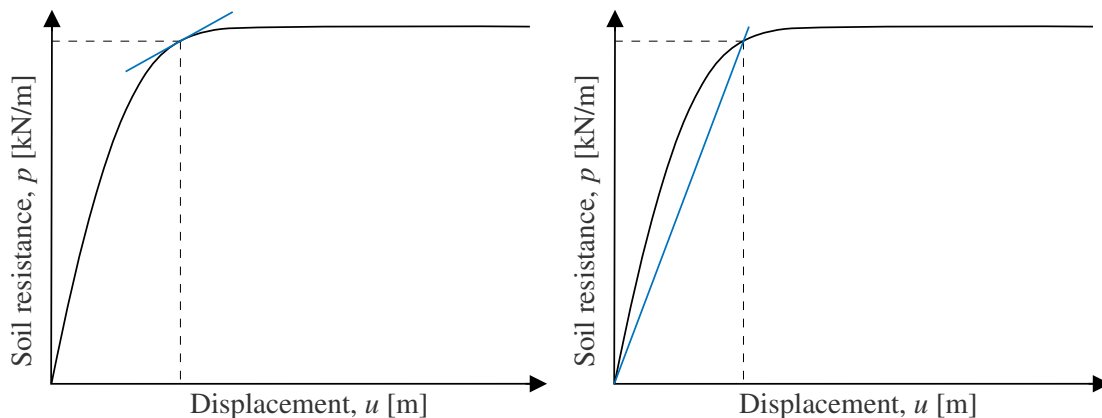
The implementation of the soil-structure stiffness is done with the previous described p - y curves for the soil. Here the standard API p - y curves, presented in Chapter 5, are used for the Extended Model in Stage 3.

To further describe how the Extended Model estimates the eigenfrequencies for an OWT, a description of the FE calculation is provided in the following section.

6.2 FE Calculation

For the Stage 3 FE calculation the goal is to determine the eigenfrequencies of an OWT, just as for the Stage 2 model. The p - y curves are, as stated earlier, non-linear, and therefore the calculation can not be performed in one step. The non-linearity from the p - y springs has to be linearised to perform the FE calculation. The linearisation can be performed in different ways e.g. using the tangential stiffness of the p - y curves as the soil-structure stiffness or using a secant stiffness on the curve. In this thesis both tangential and secant stiffness are used, where the tangential stiffness is the slope of the p - y curve at the displacement, u , see Figure 6.3(a) and the secant stiffness is used as the secant between the origin and the displacement, u , see Figure 6.3(b). Using the secant stiffness from the origin means that the system is assumed to oscillate around zero displacement. In this thesis two overall steps goes into the determination of the eigenfrequencies. These are:

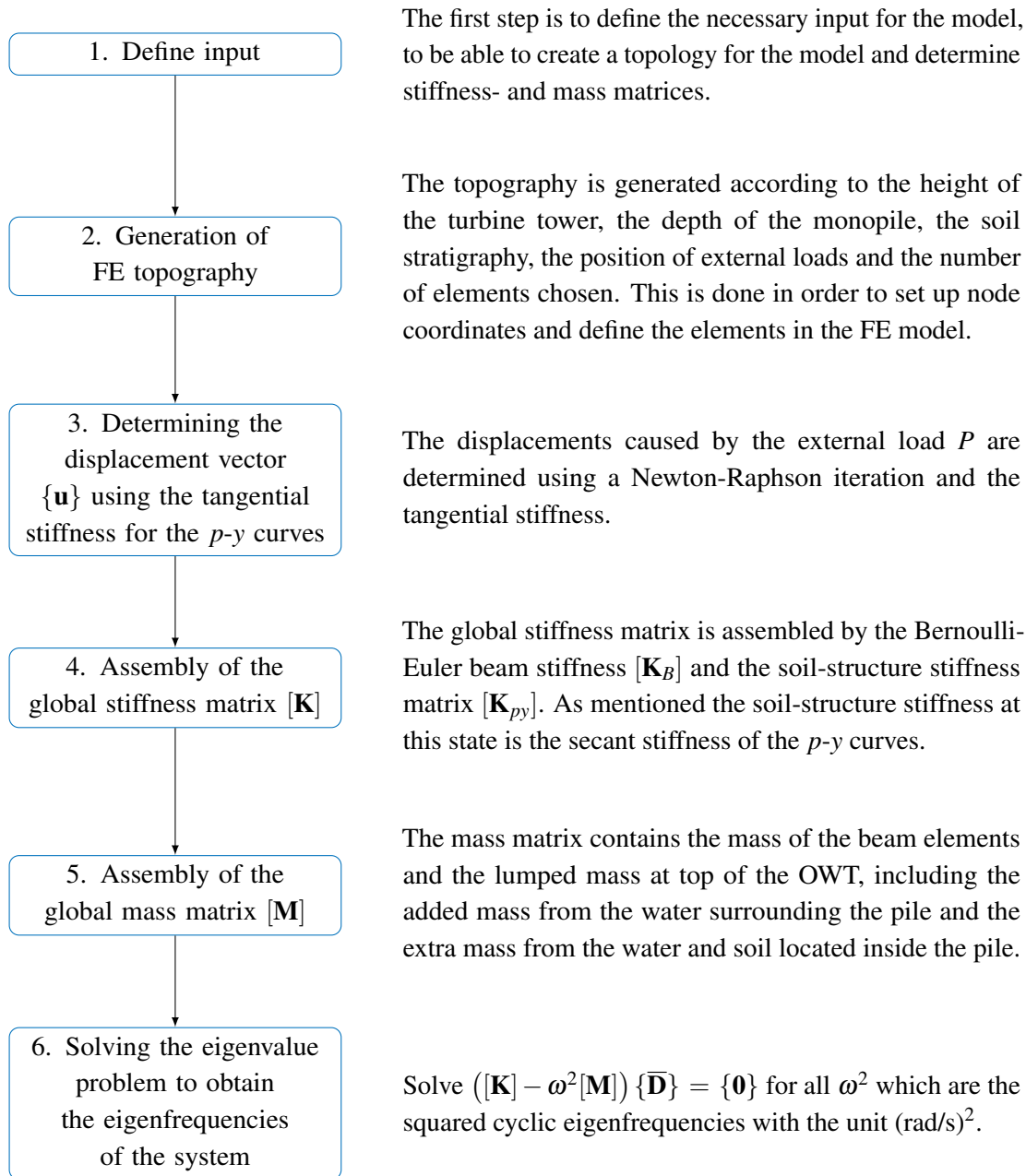
1. Determining the displacements of the system, as the system is subjected to the constant external load P , by the use of the tangential stiffness from the API p - y curves. The tangential stiffness is illustrated in Figure 6.3(a).
2. Determining the eigenfrequencies using the displacement of the system to determine the soil-structure stiffness and obtain the global stiffness matrix. This stiffness matrix is a combination of Bernoulli-Euler beam stiffness and the secant stiffness from the p - y curves instead of the tangential stiffness used in the first step. The secant stiffness is illustrated in Figure 6.3(b).



- (a) The tangential soil-structure stiffness from the API p - y curves, used to determine the displacements of the system according to the external loads.
- (b) The secant soil-structure stiffness from the API p - y curves, used for calculating the eigenfrequency of the system.

Figure 6.3: Illustration of tangential- and secant soil-structure stiffness from the API p - y curves.

These two steps are further illustrated in the following flowchart which describes the calculation process, and the different steps from the flowchart are further elaborated below the chart.



1. The input consists of a soil profile, geometric definitions e.g. the height, diameter and wall thickness of the OWT, material parameters e.g. Young's modulus and density, a lumped mass, external loads and meshing information e.g. number of beam elements below and above the mudline. The places the input parameters are used can be seen from Figure 6.4.
2. The FE model's topography is computed in two steps.
 - (a) First, nodes are positioned along the OWT model according to the number of elements chosen for the pile above and below the mudline.
 - (b) Afterwards, nodes are positioned at every soil layer boundary and at the height of the mean water level and the load P .

By this a node is placed wherever a change occurs in the input to the model. Figure 6.5 illustrates how the mesh is generated for the Extended Model.

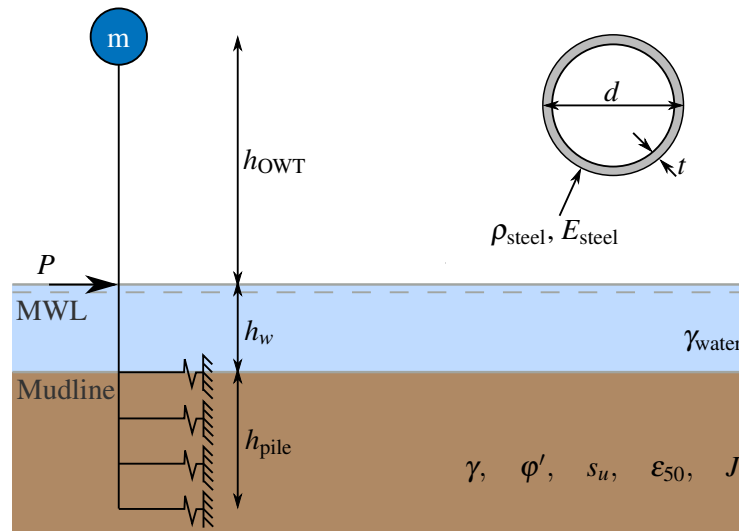


Figure 6.4: Illustration of the input parameters for the Extended Model.

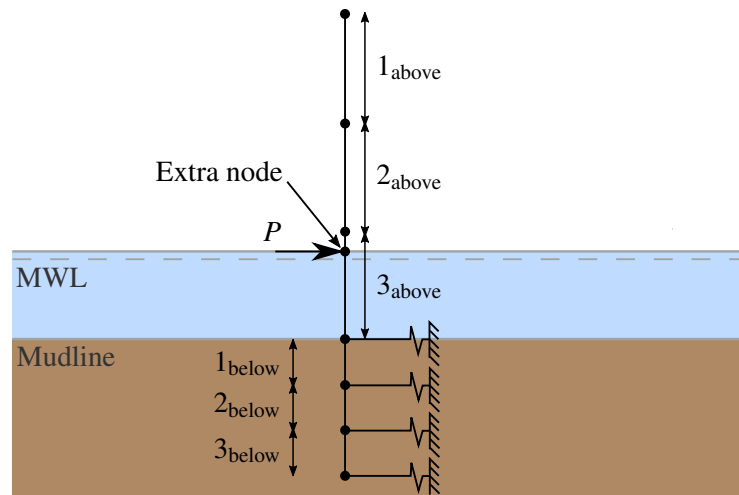


Figure 6.5: Illustration of the node positioning for the Extended Model.

3. The displacements caused by the external load, P , are as mentioned solved by a residual calculation to obtain the displacements that causes equilibrium between the internal- and external loads. As the load is modelled as stationary, the tangential soil-structure stiffness from the p - y curves is used. The residual calculation is illustrated in Figure 6.6 and the process is further elaborated in Appendix F.
4. The global stiffness matrix used to determine the eigenfrequencies of the system, is the sum of the global Bernoulli-Euler beam stiffness and the p - y stiffness matrix. The Bernoulli-Euler beam stiffness is calculated as for Stage 2. The soil-structure stiffness used to determine the eigenfrequencies is the secant stiffness of the p - y curves. Figure 6.7 illustrates how the secant stiffness for the p - y curve is determined.

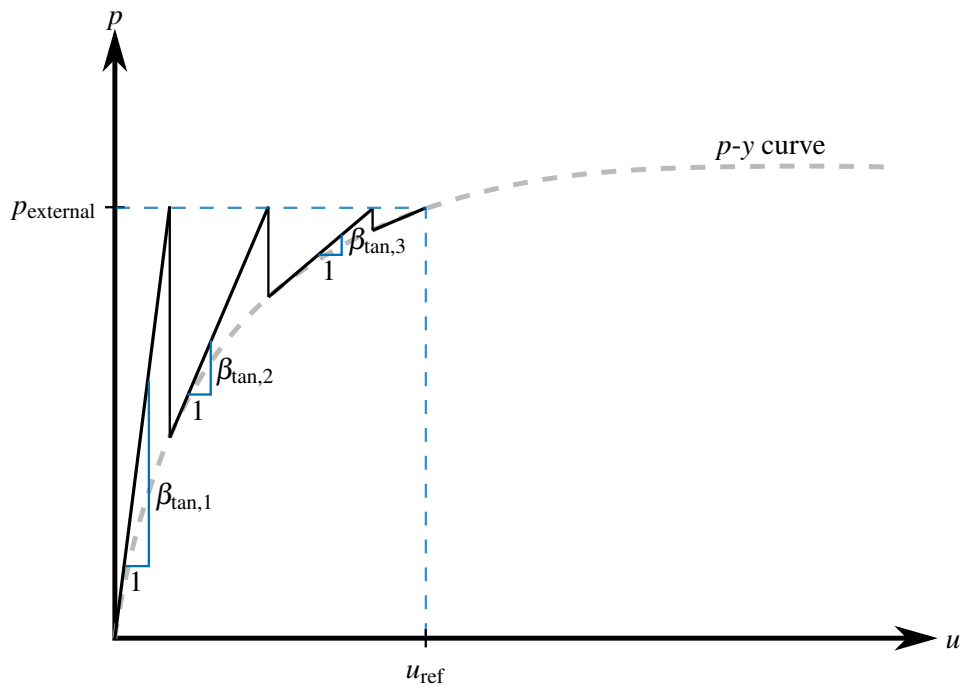


Figure 6.6: Illustration of Newton-Raphson iteration using the tangential stiffness to obtain equilibrium.

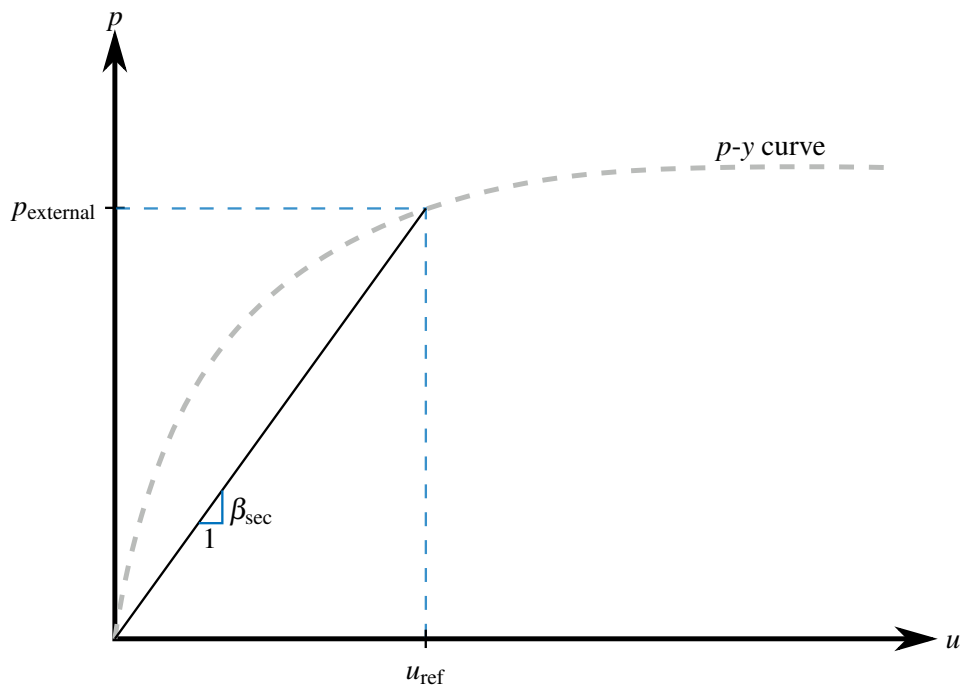


Figure 6.7: Illustration of the secant stiffness used according to the displacement determined by the previous step.

5. The mass of the beam elements and the mass on top of the OWT are calculated as stated in Stage 2. The masses from the soil and water inside the pile are calculated together with the added mass from the water surrounding the pile. These masses are then substituted into the

global mass matrix. The process for calculating the new contributions to the global mass matrix is described in Appendix F.4. The masses considered are illustrated in Figure 6.8.

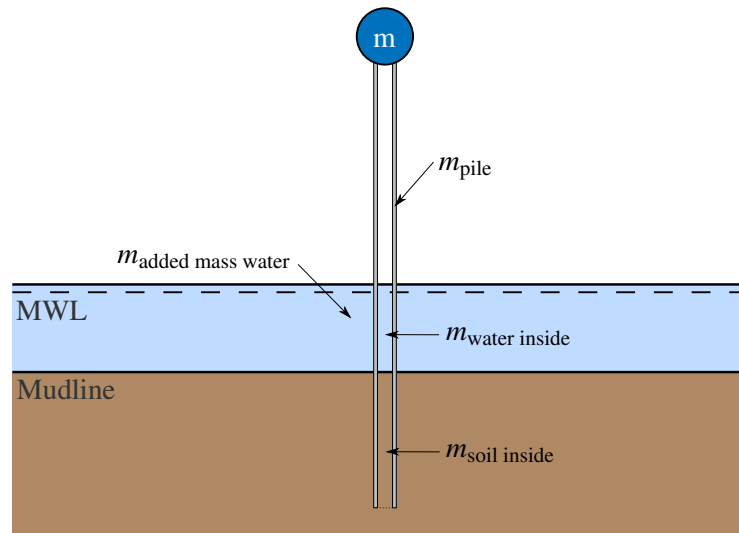


Figure 6.8: Illustration of the masses included in the Extended Model.

6. The solution of the eigenvalue problem is performed as described in the flowchart in Stage 2.

6.3 Convergence Analysis

Following the development of the Extended Model, an investigation of the convergence of the model is performed. This convergence analysis is performed in order to find a compromise between computational time and the accuracy of the results obtained from the model. The computational time is mainly governed by the number of calculations performed and thereby the number of elements the model consists of. There are three parameters that have an influence on the number of elements in the Extended Model developed in Stage 3, which are:

- Length of elements below the mudline
- Number of integration points per element below the mudline
- Length of elements above the mudline

The convergence analysis will be performed in two parts. The first part is regarding the number of elements and springs necessary to obtain a converged result below the mudline, and thereby the two first bullets on the list presented above. The second part is regarding the number of elements necessary to obtain a converged result above the mudline, and thereby the last bullet on the list presented above. Both parts of the convergence analysis will be performed on the three soil profiles, one consisting of sand, one of soft clay and one of stiff clay. The input parameters and their values are presented in Table 6.1. The diameter and the thickness is varied compared to the Simple Model in Stage 2, as the new values presented in the table are more realistic for an OWT compared to the reference turbine from DTU used in Stage 2 that is an onshore WT.

Table 6.1: Input parameters used to perform the convergence analysis of the Extended Model, if a certain input is not specified the value from Stage 2 is used for the Extended Model. *Reference strain level is the strain occurring at 50 % of the maximum principal stress in an undrained compression laboratory test.

Parameter	Symbol	Unit	Sand	Soft clay	Stiff clay
Effective angle of internal friction	ϕ'	°	37.5	-	-
Undrained shear strength	s_u	kPa	-	125	350
Effective unit weight of soil	γ'	kN/m ³	9.5	9	10
Reference strain level*	ϵ_{50}	-	-	0.015	0.008
Empirical constant	J	-	-	0.5	0.25
Diameter of the monopile	d	m	8	8	8
Length of the monopile below mudline	h_{pile}	m	30	30	30
Pile wall thickness	t	m	0.1	0.1	0.1

The values of the strength parameters e.g. the effective angle of internal friction, ϕ' , the undrained shear strength, s_u , and the effective unit weight, γ' , are based on the mean value of the suggested ranges according to Jensen et al., 2015. The reference strain level, ϵ_{50} , and the empirical constant, J , are based on suggestions by *API Recommended Practise 2GEO*.

The two parts of the convergence analysis are performed based on the ranges presented in Table 6.2.

Table 6.2: Ranges of the parameters used in the convergence analysis. An illustration of the integration points can be seen in Appendix F.1.1.1.

Parameter	Unit	Minimum	Maximum
Length of elements below the mudline	m	0.1	30
Number of integration points per element	-	2	10
Length of elements above the mudline	m	3	54

The ranges presented in Table 6.2 are based on the geometric parameters e.g. the length and diameter of the monopile, as described in Table 6.1.

6.3.1 Convergence Analysis Below the Mudline

In the convergence analysis the elements below the mudline are defined by two parameters in the Extended Model. They are defined by the element length and the number of integration points per element. The convergence analysis is performed for the ranges presented in Table 6.2 and for the first four eigenfrequencies to ensure that the higher eigenfrequencies are converged as well.

The convergence analysis below the mudline revealed, similarly to the convergence analysis performed on the Simple Model in Stage 2, that the fourth eigenfrequency converges slowest in general. The analysis also revealed the soil profile consisting of stiff clay yields the slowest converging eigenfrequency. The convergence analysis of the fourth eigenfrequency in stiff clay is

presented in Figure 6.9 as this eigenfrequency needs most elements for converging. The rest of the convergence analyses for the three other eigenfrequencies are presented in Appendix G.

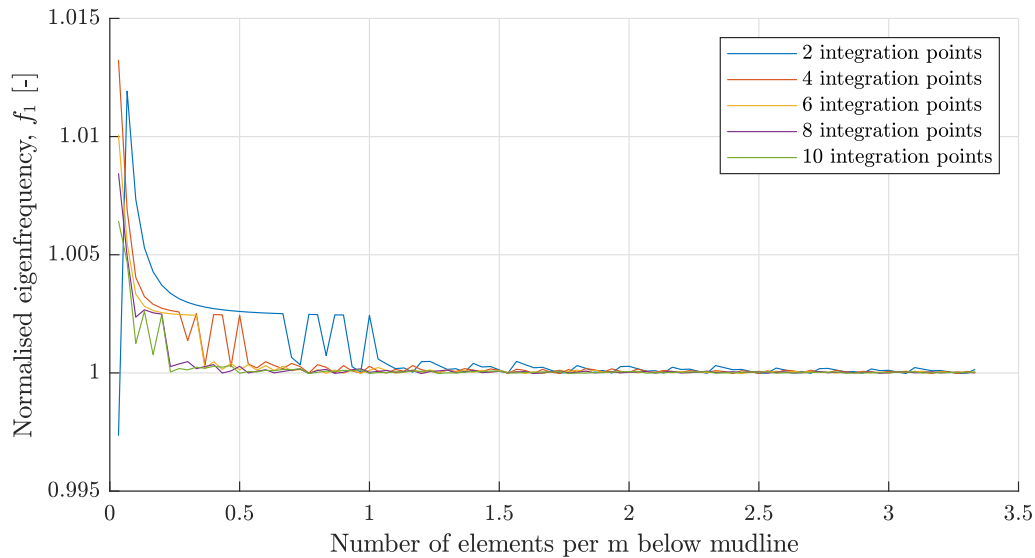


Figure 6.9: Convergence analysis of the fourth eigenfrequency in stiff clay performed with the Extended Model.

From Figure 6.9 it can be observed that when using more than four integration points, the fourth eigenfrequency is converged when using 40 elements, corresponding to 1.33 elements per meter below mudline, or more elements below the mudline. This means that the calculation performed with the Extended Model is performed with four integration points and an element length of 0.75 m prospectively in order to obtain reliable results, but also reduce the computational time.

6.3.2 Convergence Analysis Above the Mudline

In the convergence analysis the elements above the mudline is only defined by the element length. The convergence analysis above the mudline is, similar to the one below mudline, performed for the first four eigenfrequencies.

The convergence analysis above the mudline also revealed that the fourth eigenfrequency in general is the slowest of the four eigenfrequencies to converge, and that the eigenfrequency in soft clay converges slower compared to sand and stiff clay. The convergence analysis above the mudline for soft clay is presented in Figure 6.10. The rest of the convergence analyses are presented in Appendix G.

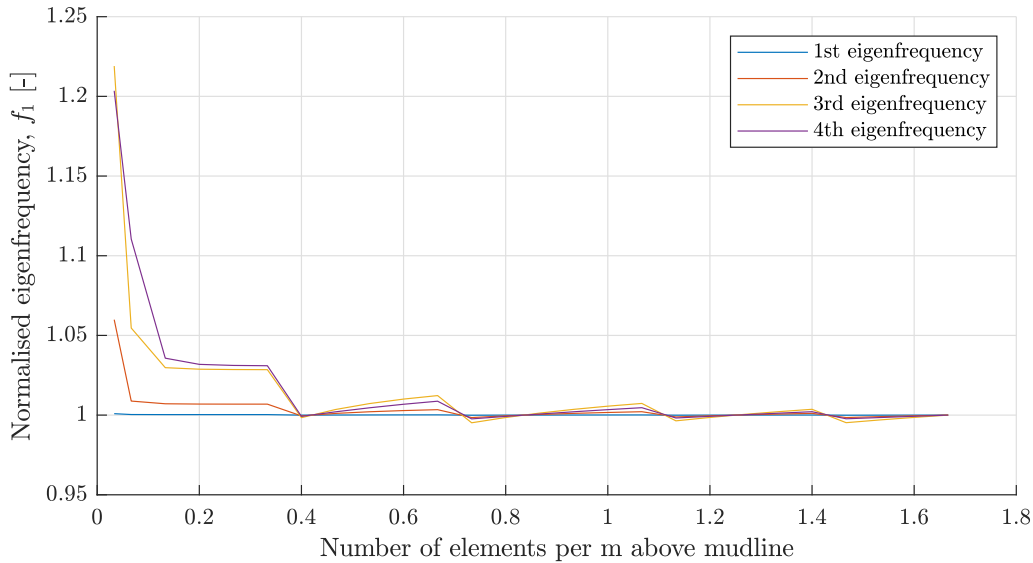


Figure 6.10: Convergence analysis above the mudline in soft clay performed by the Extended Model.

From Figure 6.10 it is observed that when using 0.4 elements per meter above mudline to describe the model, the first four eigenfrequencies are converged. This means that calculations performed with the Extended Model are performed using 65 elements above the mudline in order to obtain reliable results, but also to reduce the computational time

6.4 Parameter Variation

From the Extended Model developed in Stage 3, a parameter variation can be performed to analyse the influence on the first eigenfrequency of the different input parameters which have been added since the development of the Simple Model in Stage 2. The difference between the Extended Model developed in Stage 3 and the Simple Model from Stage 2, is, as already explained, the implementation of the effects from the soil, by using the p - y curves explained in Chapter 5. This means that the parameter analysis performed for the Extended Model will be concentrated around the input parameters for the p - y curves.

The parameter variation considers the three types of soil as introduced in Chapter 5, sand, soft clay and stiff clay. The input parameters for each of the three soil types were also introduced in the same chapter. These input parameters are however reduced in order to simplify the parameter variation. The parameters and the ranges for which they are varied in the parameter variation are presented in Table 6.3.

The ranges of the effective angle of internal friction, the undrained shear strength and the unit weight are based on suggestions by *Teknisk Ståbi* whereas the ranges for the reference strain level, ϵ_{50} , is based on suggestions by *API Recommended Practise 2GEO*. The geometric parameters of the monopile are identical to the ones used in the convergence analysis.

In order to simplify the parameter variation and isolate the effects from the varied parameter, some assumptions have been made. It is assumed that the monopile has the same diameter and length in the three types of soil, see Table 6.3. Additionally it is assumed when e.g. varying the effective

Table 6.3: Input parameters and ranges investigated in the parameter variation in Stage 3.

Parameter	Symbol	Unit	Sand	Soft clay	Stiff clay
Effective angle of internal friction	ϕ'	$^\circ$	35-40	-	-
Undrained shear strength	s_u	kPa	-	50-200	200-500
Reference strain level	ϵ_{50}	-	-	0.01-0.02	0.005-0.01
Effective unit weight of soil	γ'	kN/m ³	8-11	8-10	8-12
Diameter of the monopile	d	m	8	8	8
Length of the monopile below mudline	h_{pile}	m	30	30	30
Pile wall thickness	t	m	0.1	0.1	0.1

angle of internal friction for sand, that the soil surrounding the monopile only consists of one layer of sand with constant strength parameters throughout the entire depth of the layer. How the API p - y curves for the three soils vary with depth are illustrated in Appendix I.1. Prior to the variation of the input parameters to the p - y curves, an analysis of the relationship between the external load applied at the MWL and the lateral displacement at mudline is performed. It is assumed that the external load is the same in the three cases described in Table 6.3. Therefore, this analysis is performed in order to establish a suitable level for the external load. The relation between the externally applied load and the corresponding lateral displacement is illustrated in Figure 6.11. The magnitude of the externally applied load is selected, such that it is below the magnitude causing a failure in any of the three introduced soil profiles. Failure can be assumed to happen when the lateral displacement exceeds 10 % of the diameter of the pile, according to *DNVGL-RP-C212*. This criterion is also illustrated in Figure 6.11.

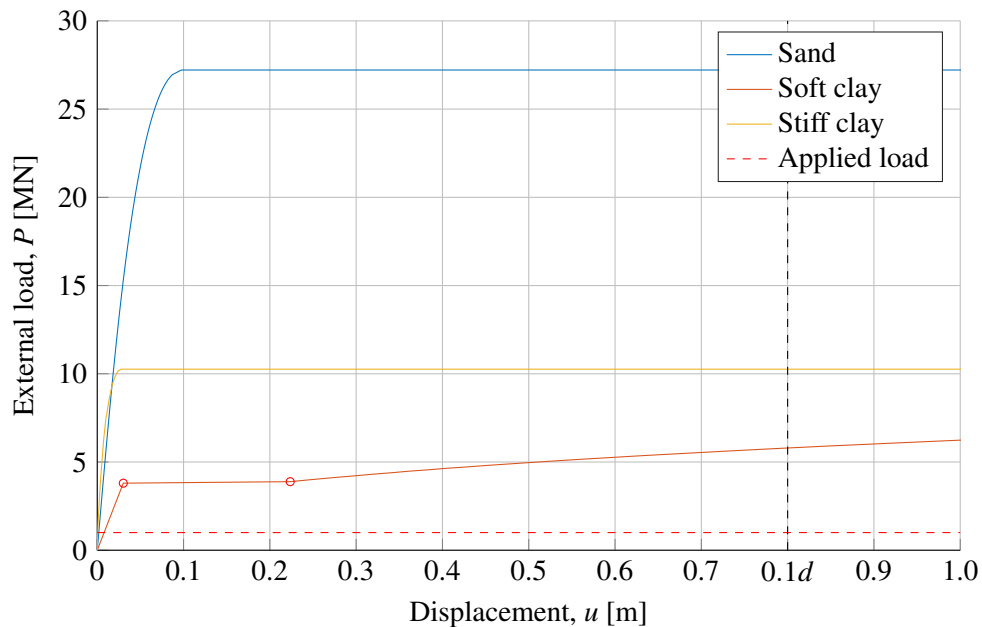


Figure 6.11: Load displacement curve for the three introduced cases, as well as the desired externally applied load. The two red dots illustrates the area of numerical error which will be elaborated later.

From Figure 6.11 it is observed that sand can resist a higher lateral load compared to both soft- and stiff clay. This tendency is expected and can be explained by the fact that sand has a higher ultimate lateral resistance compared to both soft- and stiff clay. From the figure it is observed that failure occurs in both the sand and stiff clay soil profile before a lateral displacement of 10 % of the pile diameter is reached. This is however not the case for the soft clay. From Figure 6.11 it is also observed that the load-displacement curve for soft clay jumps from one displacement to another for a load around 3.86 MN. This jump is caused by a numerical error, and is discussed later in Section 7.3.

The magnitude of the externally applied load is, based on Figure 6.11 and the observations presented above, fixed at a magnitude of 1 MN. This load is located at the initial part of the load-displacement curve for each of the three soil profiles, and is thereby lower than the failure load for the three cases. However, the estimation of this load level does not affect the tendencies presented in the parameter variation, but it does have an effect on the presented elasticity.

The parameter variations for sand, soft clay and stiff clay respectively are described in the following sections.

6.4.1 Sand

The parameter variation of the input parameters for the p - y curves for sand is performed in this section. When dealing with the original p - y curves as recommended by *API Recommended Practise 2GEO*, the input parameters are the effective angle of internal friction, φ' , the effective unit weight of soil, γ' , and geometric parameters such as the depth of the point where the p - y curve is constructed, the diameter of the monopile and the lateral displacement. In this parameter variation, the effective angle of internal friction and the effective unit weight of sand are varied according to the ranges presented in Table 6.3. The parameter variation in regards to the first eigenfrequency is presented in Figure 6.12.

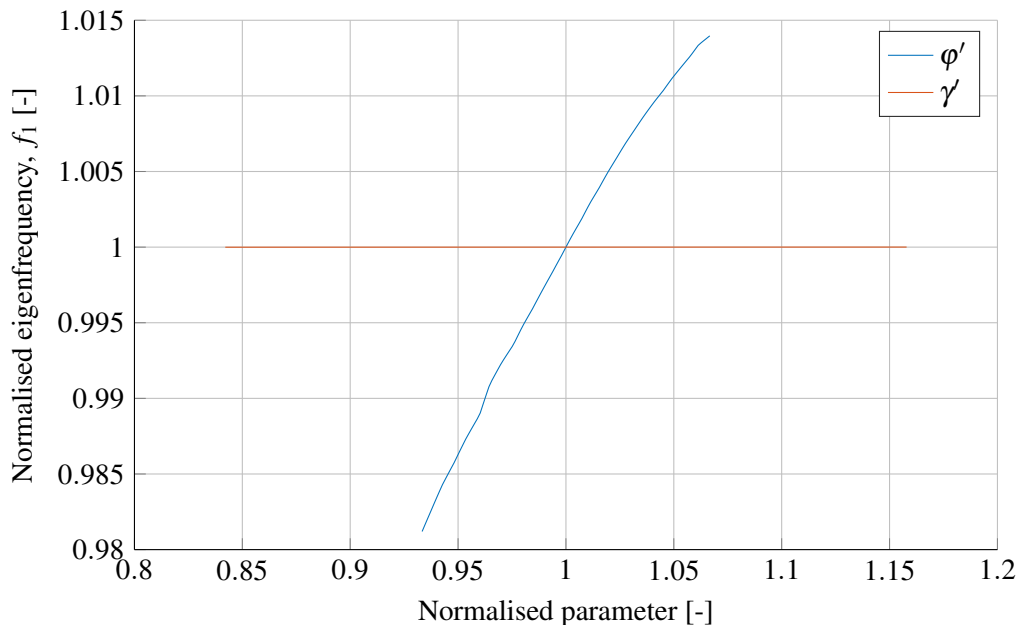


Figure 6.12: Parameter variation for input parameters for the p - y curves for sand. φ' : Effective angle of internal friction. γ' : Effective unit weight of soil.

The elasticities for the two varied parameters are listed in Table 6.4. In the table, three values of the elasticity for each parameter is presented. The elasticity is calculated with the same method as used in the parameter variations in Stage 2. However, the elasticity is referred to as left end, middle and right end in this stage for clarity. Left end is used for the elasticity for the first few points located at the very left of the current graph, whereas the middle is used for the elasticity of a few points around the middle of the graph for the current graph etc. In simple terms, the value of the elasticity correspond to the change (in percentage) of the eigenfrequency when the parameter is varied 1 %. For a deeper elaboration on how elasticity is calculated, see Appendix C.

Table 6.4: Elasticities of the input parameters for the p - y curves for sand.

Parameter	Symbol	Elasticity		
		Left end	Middle	Right end
Effective angle of internal friction	ϕ'	0.302	0.260	0.163
Effective unit weight of soil	γ'	0	0	0

From the parameter variation in Figure 6.12 and the elasticity values presented in Table 6.4, it is observed that a change in the effective unit weight of soil, γ' , has no noticeable influence on the eigenfrequency, and this parameter is thereby neglected. From Figure 6.12 and Table 6.4 it is also observed that a change in the effective angle of internal friction, ϕ' , has a bigger influence on the eigenfrequency. It can be seen that when the effective angle of internal friction is increased, so is the eigenfrequency of the system. This tendency is as expected because the initial modulus of subgrade reaction, k , is dependent on the effective angle of internal friction. The tendency can be explained by the fact that an increase of the effective angle of internal friction yields an increase of the initial modulus of subgrade reaction, which yields an increase of the soil-structure stiffness and thereby also an increase of the eigenfrequency. From Table 6.4 it can be seen that the rate of increase of the eigenfrequency, which is caused by an increase of the effective angle of internal friction, reduces slowly. This can be explained by the non-linear relation between the effective angle of internal friction and the initial modulus of subgrade reaction. This relation can be seen in Appendix E.2.

6.4.2 Soft Clay

The parameter variation of the input parameters for the p - y curves for soft clay is performed in this section. When dealing with the original p - y curves for soft clay as suggested by *API 2A-WSD*, the input parameters consist of the undrained shear strength, s_u , the reference strain level, ϵ_{50} and the effective unit weight, γ' , in addition to the geometric parameters, which are identical to the ones described for sand. In the parameter variation for soft clay, the input parameters are varied according to Table 6.3. The results for the parameter variation can be seen in Figure 6.13 and the elasticities for the three input parameters are presented in Table 6.5.

From the parameter variation seen in Figure 6.13 and the elasticities for the different parameters presented in Table 6.5, it can be concluded that the effective unit weight for soft clay also has a neglectable influence on the eigenfrequency.

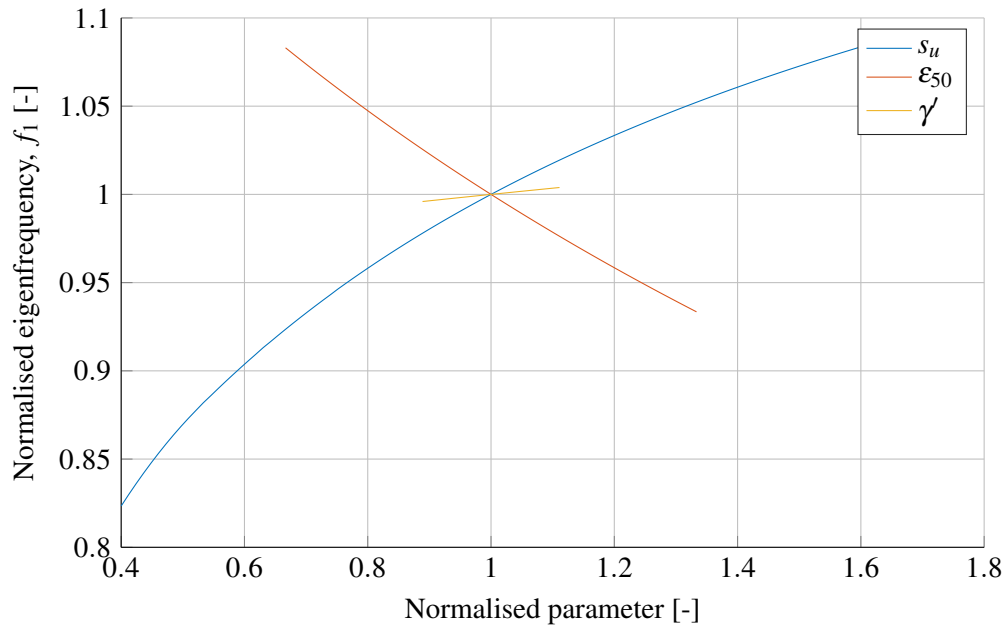


Figure 6.13: Parameter variation for input parameters for the p - y curves for soft clay. s_u : Undrained shear strength. ε_{50} : Reference strain level. γ' : Effective unit weight of soil.

Table 6.5: Elasticities of the input parameters for the p - y curves for soft clay.

Parameter	Symbol	Elasticity		
		Left end	Middle	Right end
Undrained shear strength	s_u	0.244	0.186	0.158
Reference strain level	ε_{50}	0.178	0.221	0.254
Effective unit weight of soil	γ'	0.033	0.036	0.038

When considering the influence of the undrained shear strength on the eigenfrequency of the system, Figure 6.13 and Table 6.5 reveals a positive correlation, meaning that when the undrained shear strength is increased, so is the eigenfrequency of the system. From the load-displacement curve in Figure 6.11 it can be seen that the external load at the system is within the range of the linear relation between the load and displacement. This means that the magnitude of the external load will provoke a soil-structure stiffness reflected by the initial slope of the p - y curve. Recalling the configurations of the p - y curves for soft clay, as described in Chapter 5, the initial slope of the curve is expressed by equation (6.1).

$$p = \frac{0.23p_u}{0.1u_c} \quad \text{for } u \leq 0.1 u_c \quad (6.1)$$

$$u_c = 2.5\varepsilon_{50}d \quad (6.2)$$

p_u | Ultimate lateral resistance of soft clay, see equation (5.2) and (5.3) page 51
 u_c | Reference displacement

From equation (6.1) it can be seen that the initial slope of a p - y curve for soft clay is dependent on the ultimate lateral resistance. The ultimate resistance is dependent on the undrained shear strength, meaning that when the ultimate shear strength is increasing, the initial slope of the p - y curve is increased. This is resulting in an increase in the soil-structure stiffness which yields an increase of the eigenfrequency. If the magnitude of the external load is increased above the linear relation between the load and displacement, the same tendency will be present, but with another ratio.

The last parameter considered in the variation for soft clay is the reference strain level. From Figure 6.13 and Table 6.5 it can be seen that there is a negative correlation between the reference strain level and the eigenfrequency, meaning that an increase in the reference strain level yields a decreased eigenfrequency. This tendency can be described by equation (6.1) and (6.2). From equation (6.2) it is observed that an increased reference strain level yields an increased reference displacement. When considering equation (6.1) it can be seen that an increased reference displacement yields a decreased initial slope of the p - y curve and thereby a decreased soil-structure stiffness which yield a decreased eigenfrequency.

6.4.3 Stiff Clay

The last parameter variation is performed for the input parameters of the p - y curves for stiff clay. When dealing with the formulation of the p - y curves for stiff clay as suggested by *API 2A-WSD*, the input parameters consists of the undrained shear strength, s_u , the reference strain level, ϵ_{50} , and the effective unit weight, γ' , in addition to the geometric parameters. In the parameter variation for stiff clay, the input parameters are varied according to Table 6.3. The results from the parameter analysis can be seen in Figure 6.14.

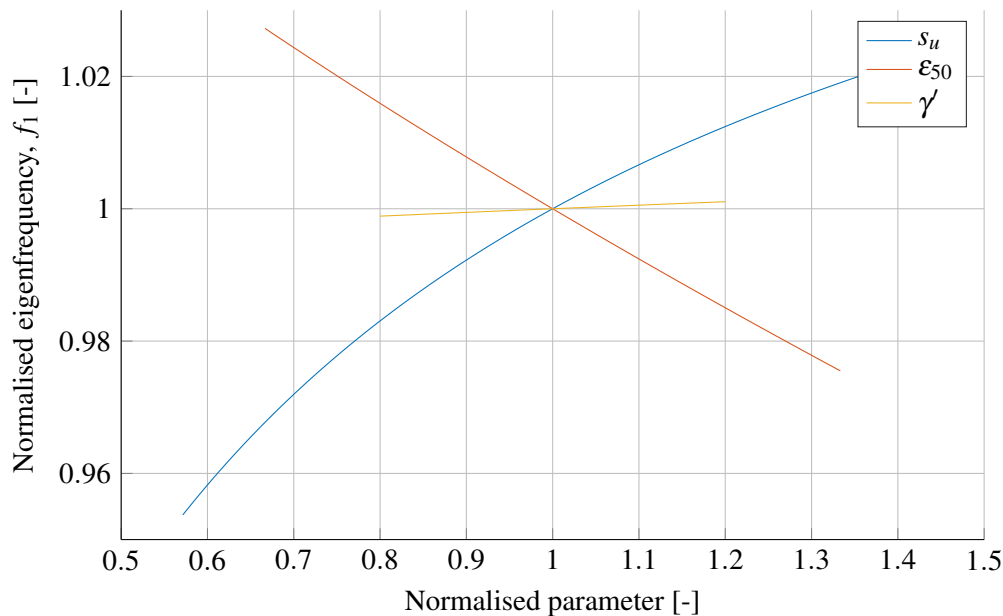


Figure 6.14: Parameter variation for input parameters for the p - y curves for stiff clay. s_u : Undrained shear strength. ϵ_{50} : Reference strain level. γ' : Effective unit weight of soil.

The elasticities for the three input parameters are presented in Table 6.6.

Table 6.6: Elasticities of the input parameters for the p - y curves for stiff clay.

Parameter	Symbol	Elasticity		
		Left end	Middle	Right end
Undrained shear strength	s_u	0.095	0.072	0.058
Reference strain level	ϵ_{50}	0.059	0.077	0.094
Effective unit weight of soil	γ'	0.005	0.005	0.006

From the parameter variation in Figure 6.14 and the elasticities of the three input parameters presented in Table 6.6, it can once again be concluded that the effective unit weight has little to no influence on the eigenfrequency of the system.

When considering the undrained shear strength, Figure 6.14 and Table 6.6 reveals a positive correlation with the eigenfrequency, meaning that an increase of the undrained shear strength yields an increased eigenfrequency of the system. This tendency is similar to the one described for soft clay but less pronounced. This can be explained by the fact that the ultimate lateral resistance is governed by the average undrained shear strength, s_a . This average undrained shear strength does not vary within the considered range for the undrained shear strength, see Table 5.1 page 55.

However, when considering the load-displacement relation for stiff clay, see Figure 6.11, it is hard to see whether the relation is linear, or the magnitude of the load is past the initial linear part of the p - y curve for stiff clay. Regardless if response of the stiff clay is on the linear part or not, the positive correlation can be explained by the fact that the ultimate lateral resistance, p_u , for stiff clay is dependent on the undrained shear strength. This means that an increase of the undrained shear strength causes an increased ultimate lateral resistance which yields an increased soil-structure stiffness and thereby an increased eigenfrequency of the system.

The last parameter considered in the variation for stiff clay is the reference strain level. From Figure 6.14 and Table 6.6, a negative correlation between the reference strain level and the eigenfrequency of the system is revealed. This tendency is as expected and is similar to the tendency for the same parameter for soft clay.

6.4.4 Conclusion of Parameter Variation

In Section 6.4.1 through 6.4.3 the parameter variations for three soil profiles consisting of sand, soft clay and stiff clay respectively were made. The parameter variations revealed the strength parameters, i.e. the effective angle of internal friction for sand and the undrained shear strength for clay, are positively correlated with the eigenfrequencies. This means that when the strength parameter for a soil increases, so does the eigenfrequency of the system. In the case of soft- and stiff clay, the parameter variation revealed that the reference strain level, ϵ_{50} , is negatively correlated with the eigenfrequency. Finally, the parameter variation revealed that the effective unit weight of soil has almost no influence on the eigenfrequency. The tendencies are summed up in Table 6.7.

Table 6.7: Tendencies revealed in the parameter variation of sand, soft clay and stiff clay.

Variable increased	Symbol	Change in eigenfrequency
Strength parameter	φ' or s_u	↑
Reference strain level	ε_{50}	↓
Effective unit weight of soil	γ'	—

6.5 Eigenfrequencies and Excitation Frequencies

As stated in Stage 1 page 20, it is important that the eigenfrequencies of the system are located outside the frequency ranges of the dynamic loads from wind, waves and excitations from rotor and blades to avoid resonance in the system. To observe how the response of the system is amplified as the system is exposed to external loads with different loading frequencies, the global system is modal decoupled. A modal decoupling can provide information about the response caused by individual eigenfrequencies and their corresponding mode shapes. A more thorough description of modal decoupling can be seen in Appendix H.

This section is based on a pile in sand using the API p - y curves, where the input values presented in Table 6.3 page 71 and an external load of 1 MN are used.

In this particular case the dynamic amplification factor for individual modes are of interest. The dynamic amplification factor was presented in equation (3.4) in Stage 1 page 18 and is repeated in equation (6.3).

$$f_{amp} = \sqrt{\frac{1}{\left(1 - \left(\frac{\omega_L}{\omega_1}\right)^2\right)^2 + \left(2\zeta \frac{\omega_L}{\omega_1}\right)^2}} \quad (6.3)$$

The dynamic amplification factor is used to observe where the peaks of the amplifications are located on the frequency band. To determine the dynamic amplification factor the damping ratio, ζ has to be determined. The damping ratio is given by equation (6.4).

$$\zeta = \frac{c}{2\sqrt{km}} \quad (6.4)$$

c	Modal damping for a specific mode
k	Modal stiffness for a specific mode
m	Modal mass for a specific mode

The global stiffness- and mass matrix are known from the Extended Model. To obtain modal parameters for damping, stiffness and mass the global damping matrix has to be determined. The global damping matrix is modelled as a Rayleigh damping matrix by equation (6.5) [R. D. Cook et al., 2002].

$$[\mathbf{C}] = \alpha [\mathbf{M}] + \beta [\mathbf{K}] \quad (6.5)$$

[C]	Global damping matrix (Rayleigh)
[M]	Global mass matrix
[K]	Global stiffness matrix
α & β	Damping fitting constants

The damping fitting constants α & β are set to 0.006 and 0.004 respectively. These are made up values, as no information is available about the structural damping ratios, and thereby they can not be fitted to specific modes. This Rayleigh damping is introduced in Appendix J.4

The dynamic amplification factor for mode 1 to 4 are illustrated in Figure 6.15, where it is observed that the chosen damping matrix provides the smallest damping on the first eigenfrequency.

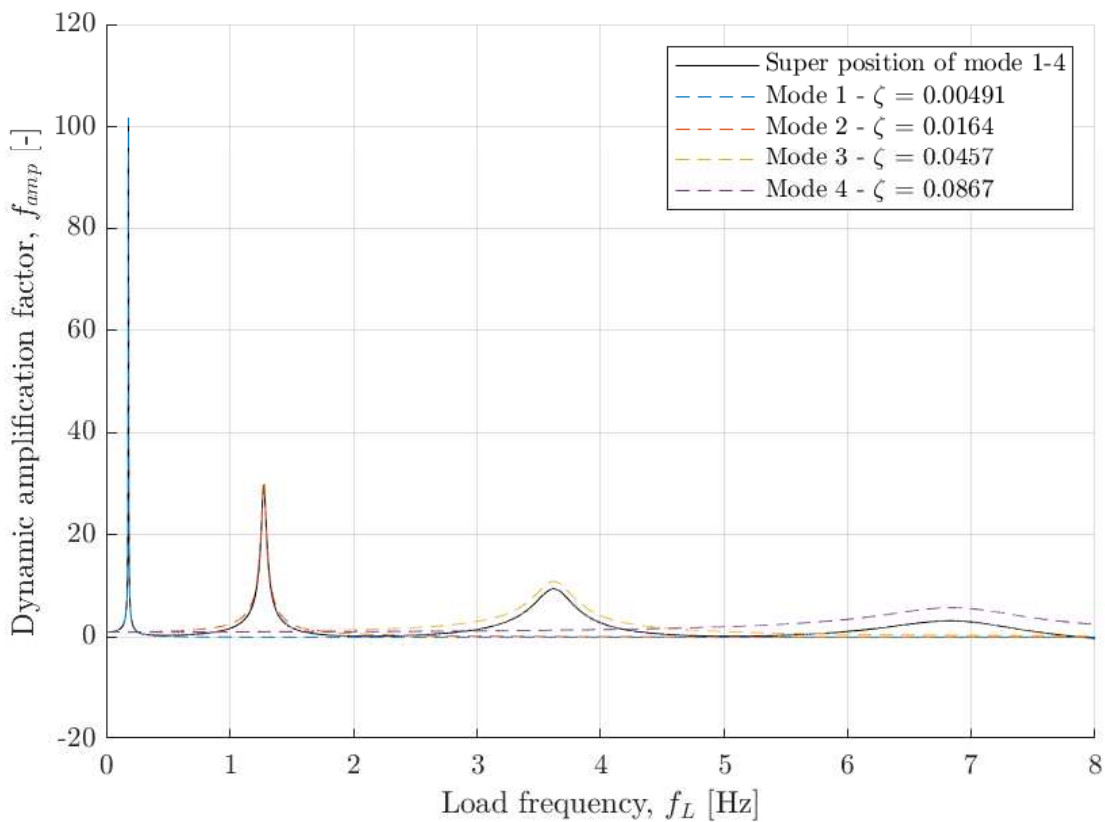


Figure 6.15: The dynamic amplification factor, for mode 1 to 4 according to varying load frequencies, including the combined amplification response from mode 1 to 4.

The low damping on the first eigenfrequency is optimal for an OWT as this allows the peak from the first eigenfrequency to be located in between the load excitation frequencies from rotor and blades.

In this thesis there is no information about the location of the investigated OWT and thereby no information about behaviour of the wind and sea state. Data is available for the DTU 10 MW WT and thereby the excitation ranges, f_{1p} and f_{3p} are known. The excitation ranges are illustrated in Figure 6.16, where also the combined dynamic amplification factor for mode 1 to 4 is plotted, to

illustrate that the amplification peak is located in between f_{1p} and f_{3p} . This means that the DTU 10 MW WT is designed as a soft-stiff structure, referring back to Figure 3.4 presented in Stage 1 page 20.

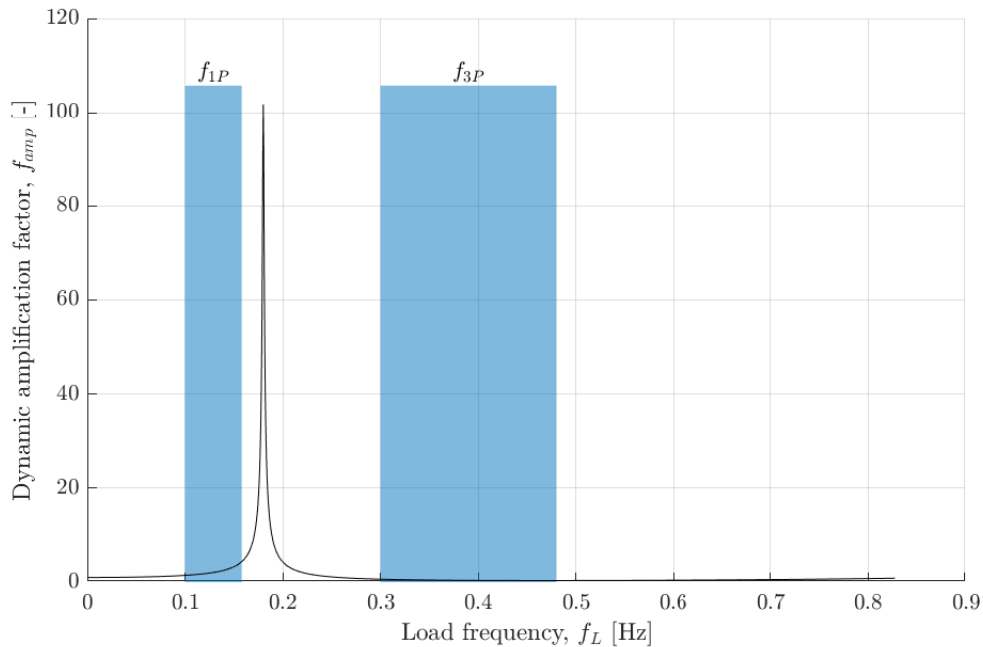


Figure 6.16: The superposition of the dynamic amplification factors from mode 1 to 4, and the excitation ranges f_{1p} and f_{3p} coming from rotor and blades respectively.

Figure 6.16 shows the superposition of mode 1 to 4. Here it is seen that the only crucial eigenfrequency is the first, when comparing to the excitation frequencies f_{1p} and f_{3p} . The peaks from mode 2 to 4 illustrated in Figure 3.4 are all located outside the loading frequencies and are thereby in this specific case not of interest. By this it can be concluded that the meshing of the Extended Model is sufficient to provide accurate results, as the model is converged for the first four eigenfrequencies, and only the first mode is of interest.

6.6 Discussion

In this section, the definition and the accuracy of the API p - y curves are discussed. These p - y curves were developed for the oil and gas industry in the 1970s, as already mentioned, and only partially modified in the 1980s. They were developed based on full scale tests using long and slender piles. The p - y curves for sand are based on full scale tests of a pile with a diameter of 0.61 m, whereas the p - y curves for clay are based on full scale tests of a pile with a diameter of 0.32 m. As the diameter of modern monopiles is more than a tenfold of the diameter for which the formulations was derived, the slenderness ratio of the monopiles has changed from being small slender flexible piles to larger and more rigid monopiles. This raises the question whether the API p - y curves still are applicable, or they are outdated. This question will be discussed in the following sections. However, to be able to discuss this, some topics regarding the shear strength of soil has to

be presented, to show the behaviour of different soil types as they are sheared to compare with the soil structure response modelled by the API p - y curves.

6.6.1 Shear Strength of Soils

In this section, the important parameters regarding the shear strength of soils is elaborated. The section is based on Budhu, 2010 and will be based on a division of soils into two groups. These are as follows:

1. **Type I soil:** Loose sands, normally consolidated and lightly overconsolidated clay ($OCR \leq 2$)
2. **Type II soil:** Dense sands and heavily overconsolidated clay ($OCR > 2$)

In the following sections, the behaviour of these two soil types will be investigated in regards to some of the important parameters and phenomena when the shear strength of soil is considered. These parameters and phenomena will also be the basis for the discussion of the API p - y curves later in this chapter.

6.6.1.1 Strain Hardening / Softening

In this section, the behaviour of the two types of soil is elaborated in regards to strain hardening and softening. Type I soils strain harden until they reach a critical state shear stress τ_{cs} , and a critical void ratio e_{cs} as the soil is compressed, see Figure 6.17 and 6.18(b). The Type II soils have a rapid increase of the shear stress at small shear strains until it reaches a peak value τ_p , where further increasing of the strains will soften the soil material and the shear stress will thereby decrease as seen in Figure 6.17.

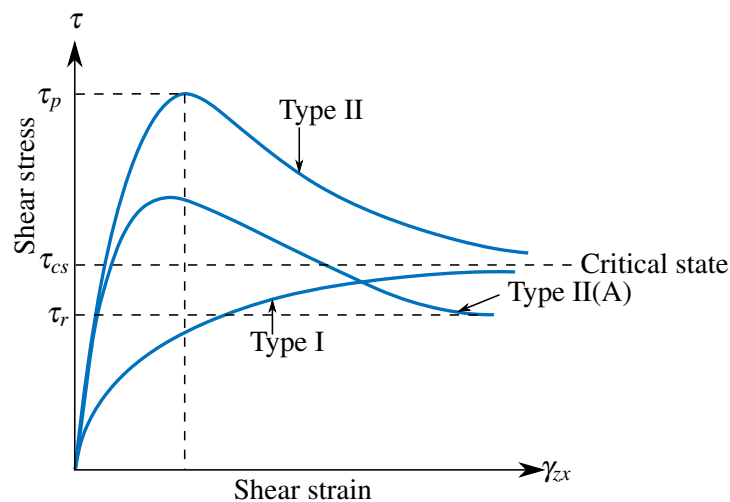
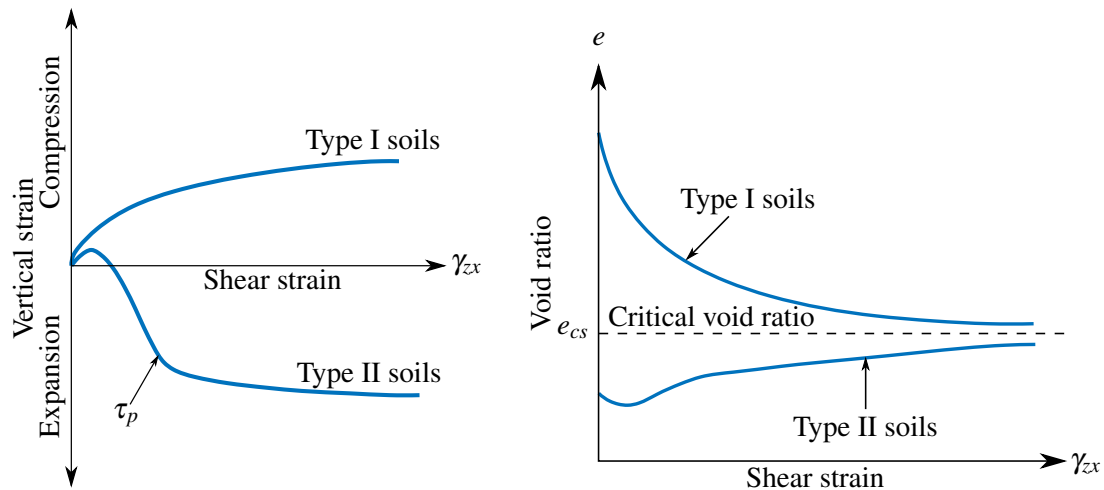


Figure 6.17: Responses of soils due to shearing [Budhu, 2010, Modified].

Figure 6.17 illustrates how Type I and II soils both go towards the critical shear stress, τ_{cs} , as the shear strain is increased. Some Type II soils e.g. overconsolidated clay referred to as Type II(A) reaches a shear stress below the critical shear stress named a residual shear stress τ_r . This happens as shear bands develop in overconsolidated clay when they are subjected to shear. This causes the clay particles to become oriented parallel to the direction of the shear bands, which results in a shear strength of the soil below the critical state shear stress.

6.6.1.2 Compression/Dilation of Sheared Soils

As the shear strain is increased for Type I soils, the soil is compressed until it reaches the critical void ratio. Contrary type II soils have an initial compression at small shear strains, where it afterwards dilates until reaching the critical void ratio. This behaviour is illustrated in Figure 6.18.



(a) Change in vertical strain as the soils are sheared [Budhu, 2010, Modified]. (b) Change in void ratio as the soils are sheared [Budhu, 2010, Modified].

Figure 6.18: Change in vertical strain and void ratios as the soils are sheared [Budhu, 2010, Modified].

6.6.1.3 Effective Stresses

A change in the effective vertical stress, σ'_v , affects the stress-path of Type I and II soils. Figure 6.19 illustrates how the stress-strain paths of the soil types changes as the effective vertical stress is increased. It is seen that for Type I soils the critical state shear stress is increased together with the effective vertical stress. For Type II soils an increase of the effective vertical stresses will eventually result in a stress-strain path with the same behaviour as for Type I soils. Type I soils can behave as Type II soils if the effective vertical stresses are low enough.

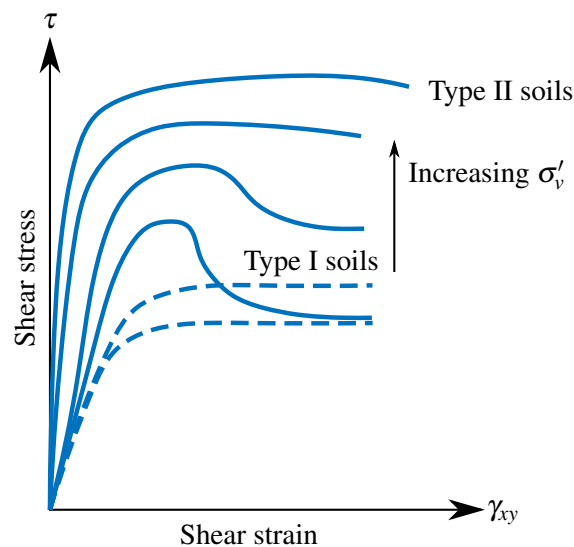


Figure 6.19: Effects on stress-strain path as the effective vertical stresses are increased. The solid lines are Type II soils and the dashed lines represent Type I soils [Budhu, 2010, Modified].

6.6.1.4 Overconsolidation Ratio

The overconsolidation ratio also affects the stress-strain path. Highly overconsolidated soils tend to have a higher peak shear stress and thereby a greater volume expansion, compared to a lower overconsolidated soil, see Figure 6.20.

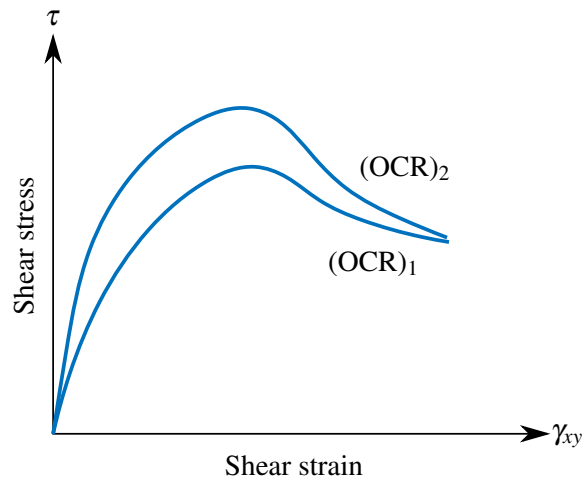


Figure 6.20: The effects of OCR on the peak shear stress ($OCR_1 < OCR_2$) [Budhu, 2010, Modified].

The behaviour of the two types of soil when shear strained, as explained above, is the behaviour which the p - y curves has to replicate. Whether the p - y curves are able to replicate the full behaviour or only part of the behaviour will be covered in the following discussion.

6.6.2 API p - y Curves Discussion

The discussion of the API p - y curves will be covering the curves for sand, soft clay and stiff clay. In general these three methods for modelling soil-structure interaction all face the same problematic, which is that they do not capture the correct stress-strain relation. This is because none of the curves have the ability of changing the stress-strain path and their hardening and softening patterns due to the input parameters for the formulations. The discussion is primarily general, but is divided into subsections in order to create a better overview of the main points.

6.6.2.1 Sand

As presented in the previous section the stress-strain path differs for Type I and II soils. This behaviour of the different stress-strain paths is however not fully covered by the API p - y curves. When observing the API formulation for sand the hardening and softening of the soils as they are sheared are worth to mention, together with the initial soil-structure stiffness and the effects of scaling the diameter of the monopiles.

Hardening / Softening

When observing the p - y curves presented by API for sands, it is observed that the sand hardens until it reaches the ultimate soil resistance. The input parameters used for the API p - y curves to

describe the state of sand are the effective angle of internal friction, ϕ' , and the effective vertical stresses, σ'_v . The correct stress-strain path for dense sandy soils has an initial part where the sand hardens as it is strained. This hardening occurs until it reaches its peak shear stress, whereas it softens afterwards until it reaches the critical state shear stress. This behaviour of dense sands is illustrated with the stress-strain path in Figure 6.17, where the dense sand acts as a Type II soil. This means that the API p - y curves do not account for the effects of the void ratio of the sandy soils, and the API formulation does thereby neglect the effects of expansion of soils as they are sheared.

The effects of varying the input parameters for the API sand formulation are illustrated in Figure 6.21(a). Here it is observed that as the effective angle of internal friction and the effective vertical stresses are changed, the p - y curves retain the same shape. Sand hardens until reaching the ultimate soil resistance, where very dense sands and loose sands with low effective vertical stresses both should harden at small displacements and afterwards soften as mentioned previously.

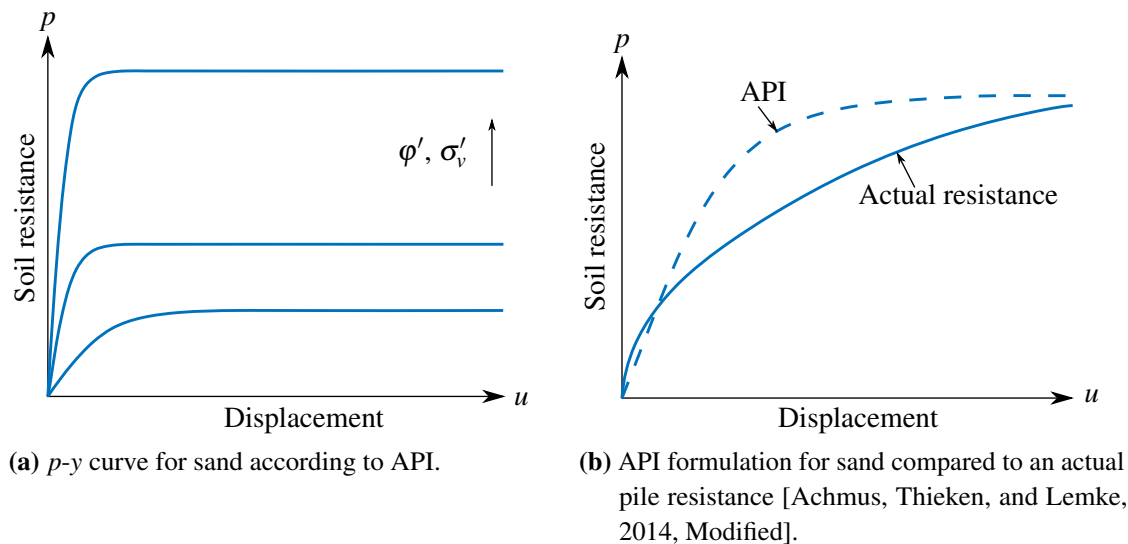


Figure 6.21: Illustration of p - y curves for sand.

Initial Stiffness

Another uncertainty of the p - y curves is the fact that the curves underestimate the initial soil-structure stiffness and overestimates the following soil-structure stiffness as the diameter of the pile is increased. This is presented in the paper Achmus, Thieken, and Lemke, 2014, where the actual resistance of a monopile in sand is compared to the API sand formulation, see Figure 6.21(b).

Diameter Effects

The p - y curves are developed on small diameter slender piles as already mentioned. When extrapolating the formulation to larger pile diameters, the diameter's effect on the initial stiffness from the API sand formulation is neglected. This is due to the fact that the initial stiffness is determined by multiplying the initial modulus of subgrade reaction, k , with the depth, z . This means that the diameter does not affect the initial stiffness [Kallehave, Thilsted, and Liingaard, 2012]. In general, the API p - y curves for sand, soft- and stiff clay do not take diameter effects caused by the rapid increase in pile diameters into account, as the diameters used nowadays are much larger

than the slender piles the formulations were developed for. As the diameter of the monopiles is increased the failure mechanism changes. Instead of being slender flexible piles they are now closer to rigid body motions as the larger structures result in a larger bending stiffness of the piles. When a large diameter pile rotates in the soil, shear forces develop on the surface of the pile. This is not accounted for in the API p - y formulation but it is included in the PISA approach which will be introduced in Section 7.2.

6.6.2.2 Soft Clay

Neither of the three p - y formulations presented in this thesis for sand, soft clay and stiff clay take the void ratio into account, when considering the input parameters of the API formulation. This means that it is unknown whether the regarded soil has a void ratio beyond or below the critical void ratio and the p - y curves can thereby not provide the actual stress-strain paths for the soils. The critical void ratio is illustrated in Figure 6.18(b). This means that none of the formulations can describe the correct stress-strain path, all though some effects are better described by the curves for clay than for sand. For example the p - y curves for soft clay presented in Figure 6.22 show that using the curves developed for cyclic loading, the soil hardens at small displacements followed by a softening as the displacement increases.

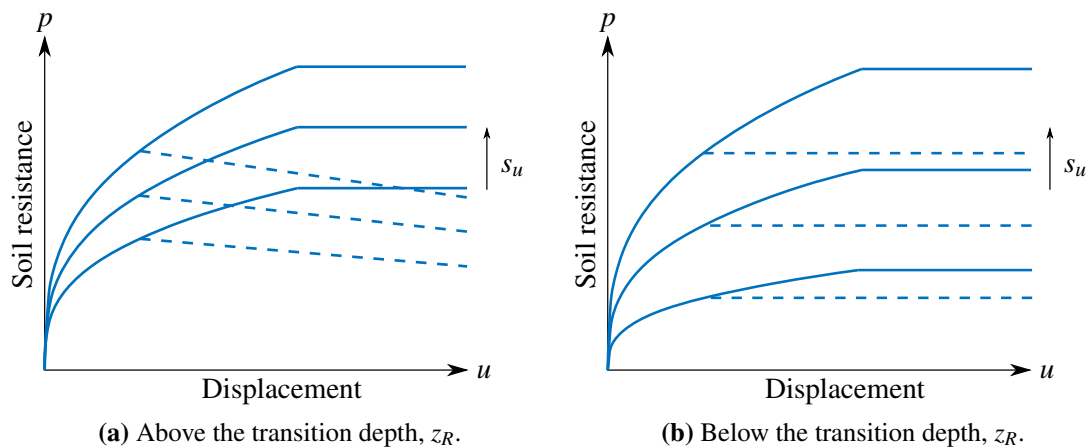


Figure 6.22: Illustration of p - y curves for soft clay. The dashed lines are for cyclic loading, where the solid lines illustrate the curves for monotonic loading.

Being below the transition depth i.e. $z > z_r$ (when z is positive downwards) means that the effective vertical stresses are higher than for the soil located above the transition depth. This higher vertical stress causes a flow failure in the soil instead of the wedge failure happening above the transition depth. Figure 6.22(a) illustrates the p - y curves for soft clay above the transition depth, where it is observed that the p - y curves consider the initial hardening followed by softening. Contrary, Figure 6.22(b) illustrates the p - y curves for soft clay below the transition depth, where it is observed that these p - y curves only consider hardening. This means that p - y curves for soft clay succeed in considering the hardening and softening behaviour of soft clay e.i. that the softening disappears when the effective vertical stresses are increased, see Figure 6.18(b).

Initial Stiffness

The p - y curves for soft clay are defined as a 3rd order polynomial, which means that the initial stiffness of the p - y curves is infinite. This is however not physically possible, and a modification of the initial stiffness is therefore performed. This modification is performed by replacing 3rd order polynomial by a linear relationship for small displacements, which yields a modified initial stiffness of the p - y curve.

Diameter Effects

The modified initial stiffness does, contrary to the p - y curves for sand, consider the effects of an increasing pile diameter. This diameter effect is scaled linearly according to the diameter of the pile and the reference strain level, ϵ_{50} .

6.6.2.3 Stiff Clay

If stiff clay was to be described by the previously introduced terms, it would be a Type II soil. This means that the soil initially hardens until reaching a peak shear stress, where it afterwards softens until reaching the critical void ratio.

Hardening / Softening

The hardening and softening behaviours are captured by both the curves for monotonic and cyclic loading for stiff clay presented in Figure 6.23. Although it is seen that when increasing the effective vertical stresses the softening is still present. This behaviour is against the argument presented earlier in Figure 6.18(b), stating that the softening should disappear as the effective vertical stresses are increased.

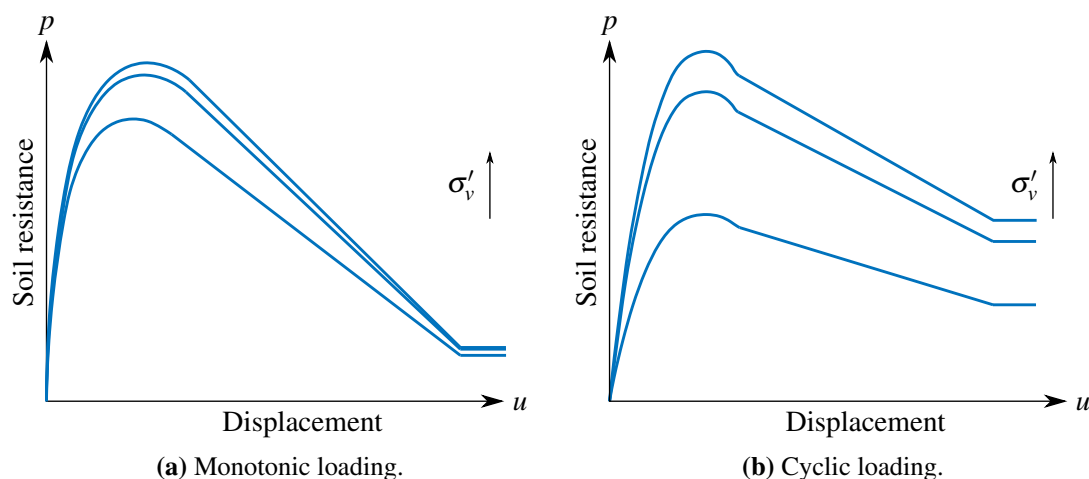


Figure 6.23: Illustration of p - y curves for stiff clay.

If the p - y curves are applied in cases where unloading and reloading occurs, then the unloading will follow the same path as for the loading, and not the correct path presented in Stage 1 in Figure 3.7 page 23. Here the hysteresis loops revealed an unloading path that is different from the loading path.

This concludes the discussion of the p - y curves presented by API. Through the discussion it was revealed that using the effective angle of internal friction and the undrained shear strength to describe the stress-strain path for sheared soils is not sufficient to describe the behaviour of soils. The state of the soil has to be described more thoroughly in order to determine how the stress-strain path turns out. This could be improved by creating curves based on the relative density i.e. by including the actual void ratio and the critical void ratio into the model which accounts for the stress-strain paths.

As stated earlier and illustrated in Figure 6.18(a), the API p - y formulation underestimated the initial stiffness of the soils. Some proposed improvements to this problem and an introduction to the PISA approach will be presented in the following chapter.

7. IMPROVEMENTS

In this chapter, improvements on the original API p - y curve formulation that is currently suggested design guideline are presented together with an alternative method of modelling soil-structure stiffness. As already mentioned, the current design guideline suggests to use the API p - y curves to analyse laterally loaded piles, which was the theory looked into in Chapter 5. However, as revealed in the literature study in Chapter 2, these curves have received some criticism for being too inaccurate when used for estimating the soil-structure stiffness on large diameter monopiles, and thereby also being inaccurate in the estimation of eigenfrequencies of OWTs. As a result of the criticism, several improvements and alternative formulations have been proposed in order to estimate the eigenfrequency of an OWT more precisely. The following chapter will be divided into three main parts. The first part consists of a presentation of two improvements to the API p - y curves. The second part consists of a presentation of a new alternative to the API p - y curves. The third and last part of this chapter consists of a comparison of the original API p - y curves and the presented improvements as well as a discussion of the different approaches.

7.1 Improvements to the API p - y curves

Due to the already addressed inaccuracy of the API p - y curves when used for monopiles with diameters larger than 2 m, several improvements have been proposed. In this thesis the improvements proposed by Kallehave, Thilsted, and Liingaard, 2012 for sand and by Kirsch, Richter, and Coronel, 2014 for clay are considered. These improvements have been selected because this thesis considers the estimation of eigenfrequencies of an OWT and both of these improvements are developed in order to optimise the initial stiffness of the p - y curves which can improve the estimation of eigenfrequencies.

7.1.1 Improvement Proposed by Kallehave

In this section the improvement to the original p - y curves presented by Kallehave, Thilsted, and Liingaard, 2012 will be introduced. This improved formulation is based on a study of estimation of eigenfrequencies for OWTs using the original p - y formulation for sand compared to nacelle measurements from OWTs installed in sand. This comparison shows that the eigenfrequency is underestimated in the range of 5-7 % when using the original formulation of the p - y curves.

The study performed by Kallehave, Thilsted, and Liingaard, 2012 revealed that while maintaining the overall format of the p - y curves by introducing a modified initial stiffness of the sand, a better estimate of the eigenfrequencies can be obtained. This modification of the initial stiffness is based on a modification of the stress and strain level respectively.

In the original formulation of the p - y curves it is assumed that the initial stiffness of sand increases linearly with depth. However, according to Kallehave, Thilsted, and Liingaard, 2012, the response of sand is governed by the isotropic stress level. One approach to account for the effects of isotropic

stress level is to express the soil modulus, E , as expressed in equation (7.1).

$$E = E_0 \left(\frac{\sigma'_v}{\sigma'_{v,0}} \right)^n \quad (7.1)$$

E_0	Reference soil modulus
σ'_v	Effective stress level
$\sigma'_{v,0}$	Reference effective stress level

The reference effective stress level, $\sigma'_{v,0}$, is defined such that at this level, the soil modulus, E , is equal to the reference soil modulus, E_0 . Based on the fundamental behaviour of sand, and an assumption regarding that the effective stress level in sand is proportional to the depth, z , equation (7.1) can be rewritten into equation (7.2), which is a modification of the stress level.

$$E_0^{py} \propto z_0 \left(\frac{z}{z_0} \right)^n \quad (7.2)$$

z_0	Reference depth
n	Depth exponent

The modification of the strain level is based on a consideration of the strain field around a pile, and how this strain field evolves as the diameter of the pile increases. The modification of the strain level performed by Kallehave, Thilsted, and Liingaard, 2012 is based on equation (7.3) as suggested by Stevens and Audibert, 1979.

$$E^{py} \propto E_0^{py} \left(\frac{d}{d_0} \right)^{m(u)} \quad (7.3)$$

d_0	Reference diameter (0.61 m)
m	Diameter exponent

The reference diameter, d_0 , is equal to the pile diameter used to derive the original p - y formulation. The diameter exponent, m , is dependent on the displacement of the pile, u . However, a constant value of 0.5 for the diameter exponent will yield representative results according to Kallehave, Thilsted, and Liingaard, 2012. This value yields an underestimation of the soil-structure stiffness of the top soil layers, while it yields an overestimation of the soil-structure stiffness of the lower layers.

When combining equation (7.2) and (7.3), an expression for the modification of the initial soil-structure stiffness is obtained, see equation (7.4).

$$E_{mod}^{py} = k z_0 \left(\frac{z}{z_0} \right)^n \left(\frac{d}{d_0} \right)^{0.5} \quad (7.4)$$

From equation (7.4), an expression for the initial modulus of subgrade reaction can be derived, see equation (7.5).

$$k_{\text{Kallehave}} = k \frac{z_0}{z} \left(\frac{z}{z_0} \right)^n \left(\frac{d}{d_0} \right)^{0.5} \quad (7.5)$$

From the expression of the initial modulus of subgrade reaction in equation (7.5), the p - y curve according to Kallehave, Thilsted, and Liingaard, 2012 can be compared to the original p - y curve according to *API 2A-WSD*. This comparison is illustrated in Figure 7.1.

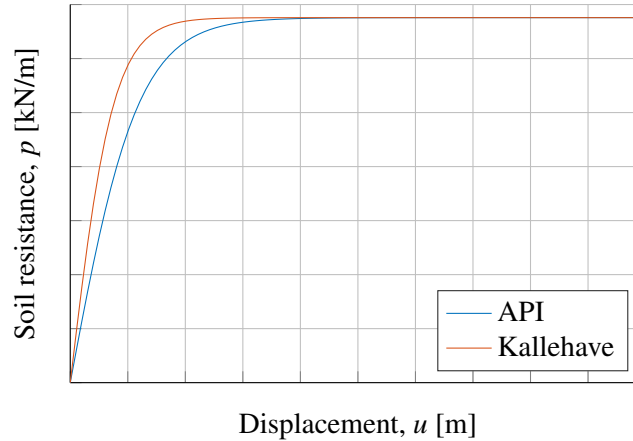


Figure 7.1: Comparison of p - y curves according to *API 2A-WSD* and Kallehave, Thilsted, and Liingaard, 2012.

From Figure 7.1 it is observed that the improvement proposed by Kallehave, Thilsted, and Liingaard, 2012 yields a higher initial stiffness of the p - y curve resulting in a higher initial soil-structure stiffness. This tendency is as expected, because Kallehave, Thilsted, and Liingaard, 2012 developed this formulation based on the revelation that the p - y curves according to *API 2A-WSD* underestimate the initial soil-structure stiffness and thereby the eigenfrequency of a monopile in sand.

7.1.2 Improvements Proposed by Kirsch

In this section the improvements to the original p - y formulation presented by Kirsch, Richter, and Coronel, 2014 will be introduced. This includes an improved formulation for the p - y curves for both soft- and stiff clay. These improvements are based on comparisons of the original p - y formulation and a numerical model.

The improvements to the p - y curves for clay as presented by Kirsch, Richter, and Coronel, 2014 are a modification of the approach presented by Matlock, 1970, where the ratio of the soil resistance, p , the ultimate resistance, p_u , and the ratio of the dynamic to static soil stiffness moduli, E_{sd} and E_s respectively, are considered. Kirsch, Richter, and Coronel, 2014 proposed a modification of the strain level, ϵ_c , which is the strain level occurring at 50 % of the maximum principal stress in an

undrained compression laboratory test. This modification is expressed by equation (7.6).

$$\varepsilon_{50, \text{Kirsch}} = \varepsilon_{50} \left(1 + \left(1 - \frac{p}{p_u} \right) \left(\frac{1}{\frac{E_{sd}}{E_s}} - 1 \right) \right) \quad (7.6)$$

E_s | Static soil stiffness modulus
 E_{sd} | Dynamic soil stiffness modulus

The dynamic soil stiffness modulus, E_{sd} , is according to Kirsch, Richter, and Coronel, 2014 expressed as a function of the static soil stiffness modulus, E_s . The expression for the dynamic soil stiffness modulus is presented in equation (7.7).

$$E_{sd} = 10^{-0.42 \cdot \log(0.0006 \cdot E_s)} E_s \quad (7.7)$$

The static soil stiffness modulus, E_s , is dependent on the consistency of the clay considered. The values used in this section is presented in Table 7.1.

Table 7.1: Stiffness moduli used in the comparison of the p - y curves obtained from API, 2014 and the modified p - y curves provided by Kirsch, Richter, and Coronel, 2014.

Soil type	E_s [MPa]	E_{sd} [MPa]
Soft clay	10	75
Stiff clay	100	400

From the modified expression of the reference strain level, ε_{50} , the improved p - y curves according to Kirsch, Richter, and Coronel, 2014 can be compared to the original formulation according to API 2A-WSD. This comparison is illustrated in Figure 7.2(a) and 7.2(b) for soft and stiff clay respectively.

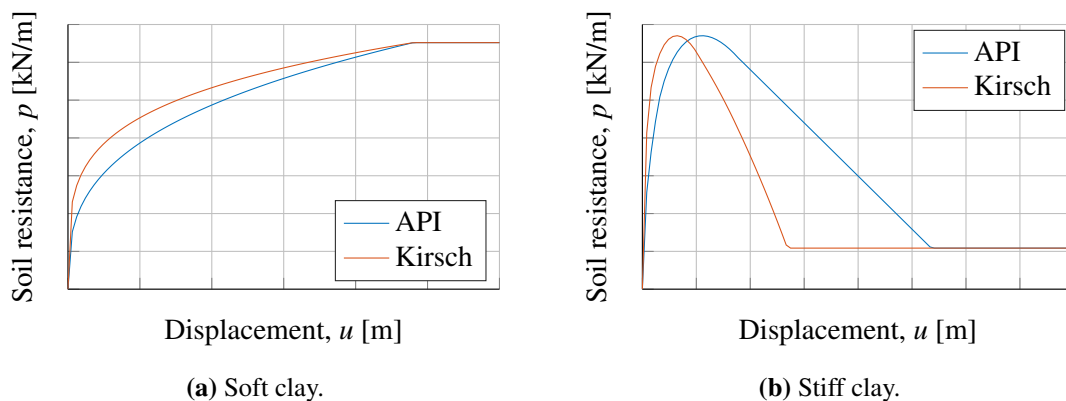


Figure 7.2: Comparison of the original p - y formulation for clay according to API 2A-WSD and the improvement presented by Kirsch, Richter, and Coronel, 2014 for soft- and stiff clay respectively.

From the comparison in Figure 7.2 it is observed that the improvements proposed by Kirsch, Richter, and Coronel, 2014 yields a higher slope of the initial part of the p - y curves. This increase in the slope of the p - y curves increases the soil-structure stiffness which increases the eigenfrequency of the system.

7.2 PISA

As mentioned earlier, the p - y curves was developed for the oil and gas industry, where the approach was used for platforms with slender piles. With the development in the OWT sector, the increase of the pile diameters results in inaccurate estimates. The p - y curves are becoming inaccurate as the slenderness ratio, L/d ratio is getting smaller for the pile, where L is the length of the monopile and d is the diameter.

The PISA (Pile Soil Analysis) project is a relative new project research, which was ongoing between 2013 and 2016. It considered the development of a new 1D design model for monopile foundations for OWTs. The 1D model was calibrated according to 3D models and experimental tests. The problem by only using 3D models is the computational time, and the goal of the research was thereby to make a simpler and faster 1D model, which can provide reliable results. This section about the PISA project is based on Burd et al., 2017.

7.2.1 PISA Theory

The theory behind the PISA approach is basically an extended version of the p - y curves where a horizontal force and moment acting on the bottom of the pile and a distributed moment along the pile are considered as well. Figure 7.3 illustrates the PISA concept.

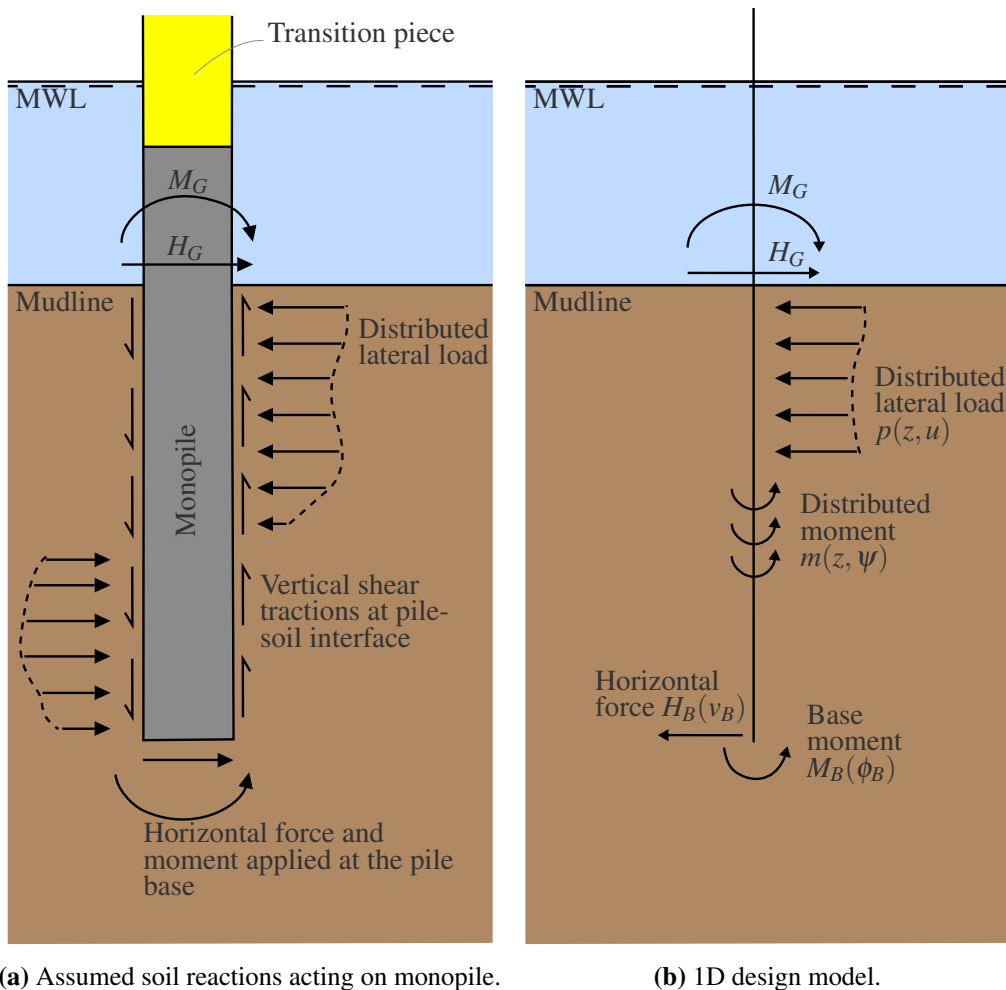


Figure 7.3: Illustration of the PISA concept [Burd et al., 2017, Modified].

The monopile is modelled as an embedded beam where the external loads are applied at the top as a moment, M_G , and a horizontal force, H_G . The soil effects on the embedded monopile can be regarded as four separated components.

- A distributed lateral load, p , acting on the pile as the p - y curves considers as well.
- A distributed moment, m , which is caused by the vertical traction occurring at the surface from the soil-structure interaction when local pile rotations occurring.
- A horizontal force, H_B , at the bottom of the pile.
- A moment, M_B , at the bottom of the pile.

The soil reactions are applied to the beam by the use of the Winkler assumption, which states that p and H_B components are defined as functions of the local pile displacement and m and M_B are defined as functions of the local pile cross-section rotation, ψ . The local rotation and the vertical shear traction can be seen at a small part dz of the pile in Figure 7.4. Despite the Winkler approach neglects the coupling, which occurs between adjacent soil layers, it gives a good basis for the design calculations.

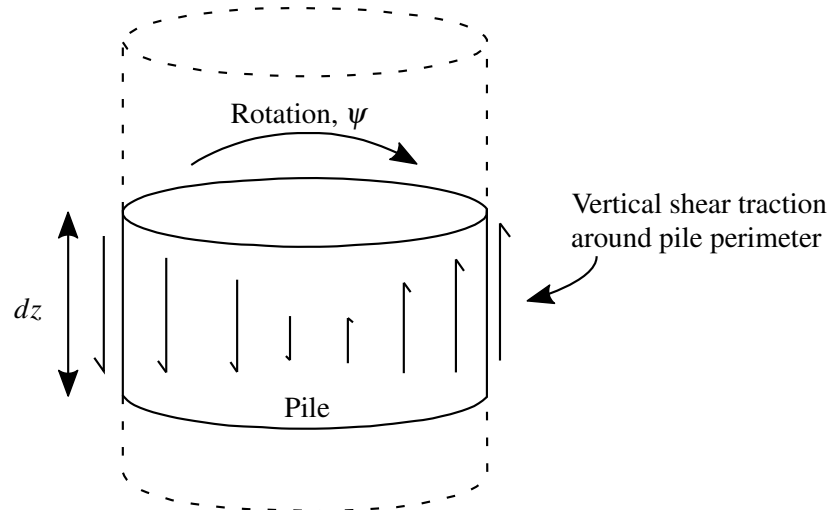


Figure 7.4: Illustration of small piece of the pile [Burd et al., 2017, Modified].

When the L/d ratio is large, the API p - y curves yields acceptable results and only the distributed lateral load has a large effect on the result. As the L/d ratio is decreasing the three other parameters are getting increasingly important. This is due to the distributed moment depends on the diameter and when the diameter increase, the moment does as well. Also, the force and moment at the bottom become increasingly important as the L/d ratio decreases. The effect from the three parameters depending on the L/d ratio is called the "diameter effect", which causes the original API p - y curves to become increasingly unreliable.

When the monopile is modelled as a beam, Timoshenko beam theory is used to be able to include the shear strains in the analysis. This is important to model, as an increase of the diameter of monopiles and thereby a reduction of the L/d ratio will give the shear strains a larger influence on the overall pile response. Using Timoshenko beam theory will thereby make the 1D model usable when the L/d ratio decrease as the development OWT sector causes an increase in diameter of monopiles.

7.2.2 PISA Research

The PISA research uses field tests which were conducted at the two sites Cowden and Dunkirk. Here multiple tests were performed with varying diameters (0.273 m, 0.762 m and 2.0 m) and L/d ratios of the monopiles between 2 and 10, where the range of the L/d ratio is based on the expected ratios for full-sized monopiles. The Cowden test site is a clay till site in the north-east England and the Dunkirk test site is a dense sand site in northern France. Both sites are located at land and have been used for testing before, which means that previous field tests and laboratory soil data are available for usage.

Cowden and Dunkirk were chosen as test sites because the soil conditions on these sites are similar to the conditions at the North Sea, where present and future OWT farms are located or planned to be. Due to the metocean conditions in the North Sea, the monopile is a feasible foundation solution.

3D modelling was performed for obtaining FE results, which the field test results could be compared to. This was done for confirming the validity of the procedure used for the 3D modelling. The constitutive modelling of the soil used in the 3D models were constructed with the knowledge obtained from site investigations for the locations and the preexisting data.

To be able to account for the difference from the field tests performed on land and the desired results for offshore, a calibration analysis is conducted. In this way the sand- and clay profiles, based on the field tests from the locations, are adjusted to be representative values for offshore conditions.

The numerical data from the calibration analysis is directly used for calibrating the soil reaction curves which are used in the PISA 1D model. This means the 1D model is dependent on the field data and the 3D FE procedure. The approach used for updating the curves used in the 1D model in the research is illustrated in Figure 7.5.

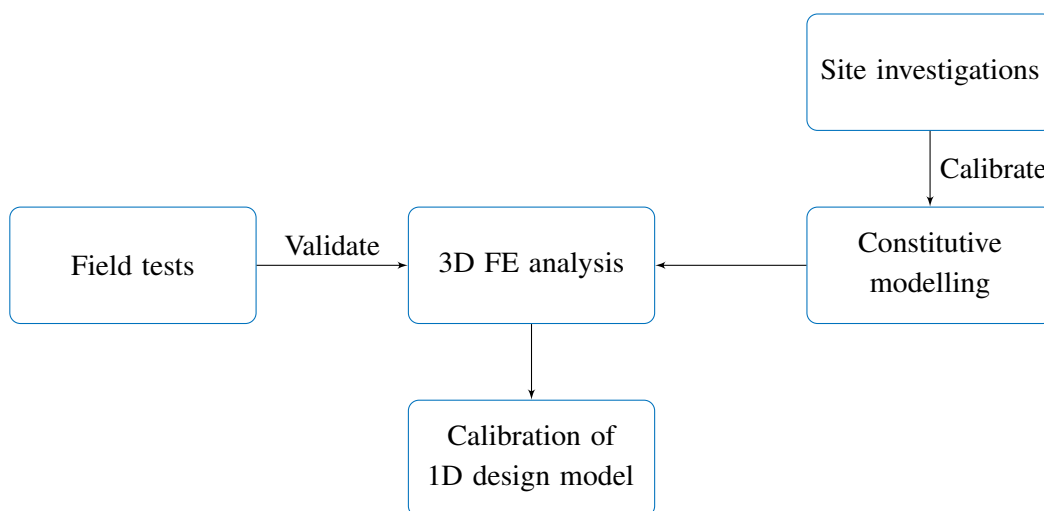


Figure 7.5: Flowchart of the PISA research approach [Burd et al., 2017, Modified].

7.2.3 Discussion

The PISA modelling approach can be used to obtain monopile design in two different ways, the "rule-based" method and the "numerical-based" method.

The rule-based method is similar to the current form of the p - y curves and is used for the initial design calculations. Here predefined functions and parameters can be used to represent the soil reaction curves. The predefined functions and parameters are determined from the soil profiles which are established for each individual site from relatively simple index or testing.

The numerical-based method is used to obtain more detailed and robust design calculations. This method was the one used in the PISA research in order to calibrate the soil reaction curves in the 1D model. In general the site conditions are investigated more intensively using advanced laboratory and field techniques to establish the behaviour in details for the soil present at a given location. The final design is then found from the 3D FE calculation using the likely ranges of soil profiles and parameter variations. At the end, the soil reaction curves can be found from the predictions for the soil-structure interface traction from the FE analysis.

The paper Burd et al., 2017 is using the numerical-based method for calibrating a 1D model for a specific case. Here a comparison indicates the various approximations and assumptions used in the 1D model do not make the results significantly less reliable.

Further work has to be made for obtaining more knowledge and extend the method for being able to handle other soil types and layered soils. The effect of cyclic loading should be considered in further work, as the current work is based on monotonic lateral loading of the piles. Also, more advanced geotechnical effects as multi-directional loading, damping, densification, age hardening, installation methods and creep can be included. In all, further work is needed for making the model able to consider more complex effects.

7.3 Comparison of p - y Curves

In this section, a comparison of the original API p - y curves and the modifications proposed by Kallehave, Thilsted, and Liingaard, 2012 and Kirsch, Richter, and Coronel, 2014 is performed. The comparison is performed based on the development of the first eigenfrequency as the external load is increased. This is done because the exact level for the external load is unknown as no specific case is considered. The input parameters for the p - y curves used in this comparison are identical to the input parameters used in the convergence analysis of the Extended Model, and is presented again in Table 7.2.

Table 7.2: Input parameters used to compare eigenfrequencies.

Parameter	Symbol	Unit	Sand	Soft clay	Stiff clay
Effective angle of internal friction	ϕ'	°	37.5	-	-
Undrained shear strength	s_u	kPa	-	125	350
Effective unit weight of soil	γ'	kN/m ³	9.5	9	10
Reference strain level	ϵ_{50}	-	-	0.015	0.008
Empirical constant	J	-	-	0.5	0.25
Diameter of the monopile	d	m	8	8	8
Length of the monopile below mudline	h_{pile}	m	30	30	30

The development of the first eigenfrequency in regards to the external load for the API p - y curves as well as the modifications proposed by Kallehave, Thilsted, and Liingaard, 2012 and Kirsch, Richter, and Coronel, 2014 is presented in Figure 7.6.

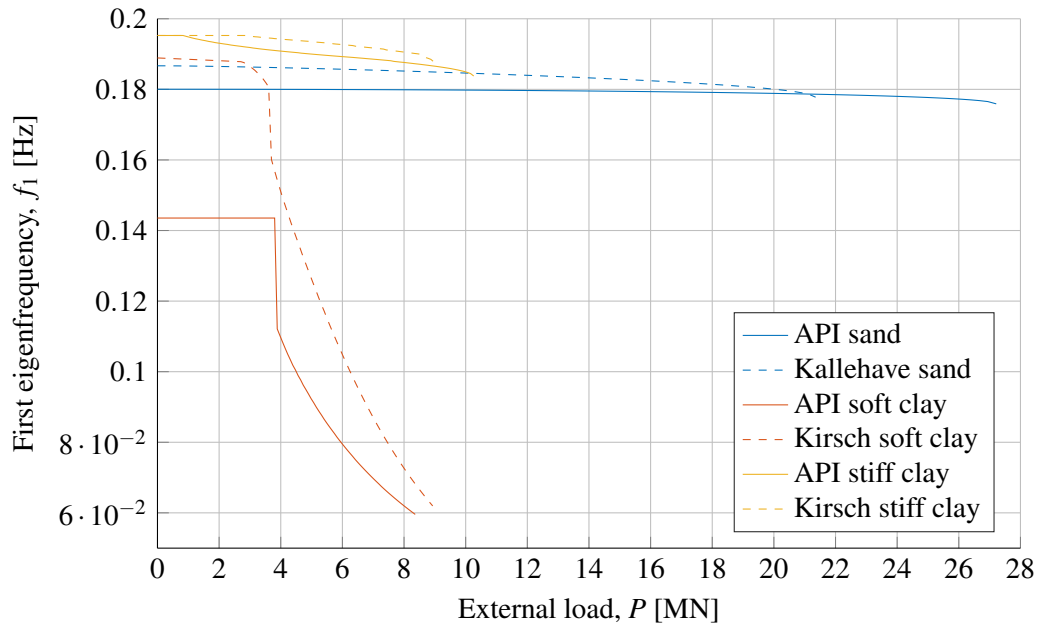


Figure 7.6: Comparison of eigenfrequencies obtained from the original formulation of the p - y curves according to API 2A-WSD and the modifications proposed by Kallehave, Thilsted, and Liingaard, 2012 and Kirsch, Richter, and Coronel, 2014.

For sand it is observed that the modification proposed by Kallehave at smaller loads yields higher eigenfrequencies as the slope on the initial part of the p - y curve provided by Kallehave is greater than the one by API. This results in a greater soil-structure stiffness i.e. a higher eigenfrequency. As the load is increasing, the eigenfrequencies from the modified approach by Kallehave are getting closer to the results using the API curves. At the end of the curves illustrated in Figure 7.6, the eigenfrequencies using the API p - y curves are getting larger than the ones obtained by using the modified Kallehave formulation. Here it should be noted the modification proposed by Kallehave is meant to be representative for the initial stiffness, and not with large displacements.

Thereby the eigenfrequencies from using the formulation by Kallehave are higher at smaller loads. This corresponds to the expectations as the modification from Kallehave, Thilsted, and Liingaard, 2012 was meant to increase the initial soil-structure stiffness where the API curves are claimed to yield too small eigenfrequencies. As the external loads and thereby the displacements are getting larger, the formulation by Kallehave should no longer be seen as valid, as the modification is not fitted for large displacements.

When considering soft clay, see Figure 7.6, it is observed that the eigenfrequency for both Kirsch and API has a significant drop at an external load just below 4 MN. This happens due to the fact that the displacements are calculated using the tangential stiffness of the p - y curves, and as both curves are a combination of a linear initial slope followed by a third order polynomial, there will be a significant change in the tangential stiffness going from the initial linearised curve to

the polynomial. This numerical error is illustrated and explained further in Appendix I.2. The significant change in the tangential stiffness yields an relative increment of the displacement and thereby a reduction of the eigenfrequency using the secant stiffness from the p - y curves. Beyond the drop of the eigenfrequencies, which is similar for both the API- and Kirsch formulation, the curves differ from each other as Kirsch provides higher stiffness in the beginning of the curves as illustrated in Figure 7.2(a) page 90. At a certain point the slope of the API p - y curve becomes steeper than the one provided by Kirsch, until they both reach the ultimate soil resistance. This behaviour is transferred to the eigenfrequencies illustrated in Figure 7.6 where Kirsch provides higher eigenfrequencies than API, but the gap between the curves decreases as the external load and thereby the displacements are increased.

When considering stiff clay, it is from Figure 7.6 observed that the eigenfrequency obtained when using the original API p - y curve is identical to the one obtained when using the modifications proposed by Kirsch, when the external load is low. This is due to the fact that the determination of the initial stiffness is independent of the modifications proposed by Kirsch. Following the initial part, the modified p - y curve yields a larger eigenfrequency compared to the API p - y curve. This tendency can be explained from a comparison of the API p - y curve and the modified p - y curve by Kirsch, see Figure 7.2(b), where it is observed that the parabolic part of the Kirsch p - y curve reaches a top point earlier than the API p - y curve, which makes the Kirsch p - y curve steeper and thereby increases the soil-structure stiffness. However, because of the larger stiffness, the graph is reaching a displacement, where no stiffness is left in the soil, earlier than the original API. This is also the explanation for why the Kirsch approach not is providing eigenfrequencies for the same maximum load as the API p - y curves, as the Kirsch method is loosing the stiffness from the soil before the API p - y curves.

7.4 Discussion

This discussion covers the improvements and the alternative formulation presented in this chapter, and will be divided into two main parts. The first part concerns the improvements to the original p - y curves whereas the second part concerns the alternative formulation.

7.4.1 Improvements to the API p - y curves

Two improved formulations for the original p - y curves are presented in this chapter. These are the improvement of the p - y curves for sand as suggested by Kallehave, Thilsted, and Liingaard, 2012 and the improvements of the p - y curves for soft- and stiff clay as suggested by Kirsch, Richter, and Coronel, 2014. Both the improvements proposed for sand and clay consider the fact that the p - y curves in general are derived based on tests performed on piles which are very different from monopiles. The original p - y curves were derived based on tests on long and slender piles compared to the dimensions of the monopiles used today. However, the formulation of the p - y curves has not changed accordingly, and the formulation might therefore be obsolete.

The improvement of the p - y curves for sand proposed by Kallehave, Thilsted, and Liingaard, 2012 is based on measurements from operating WTs and theoretical considerations. It considers a modification of the original p - y curves in regards to the depth and pile diameter for which the

p - y curve is constructed. This modification yields a higher initial stiffness and the formulation is thereby better at estimating the soil-structure stiffness at small loads. However, the modified p - y curve yields the same ultimate capacity as the original p - y curve and is thereby, equally to the original formulation, inaccurate in the determination of the soil-structure stiffness for extreme loads, see Figure 7.1 page 89.

A comparative study performed by Achmus, Thieken, and Lemke, 2014 compares soil resistances obtained from the original p - y curves and the improvement proposed by Kallehave, Thilsted, and Liingaard, 2012 to the soil resistance obtained from a 3D FE analysis, see Figure 7.7. The comparison supports the statement about that the original p - y curves underestimates the soil-structure stiffness for small loads whereas they overestimates the soil-structure stiffness for extreme loads. From the figure it is also observed that the improvement proposed by Kallehave, Thilsted, and Liingaard, 2012 yields a better estimation of the actual p - y curve for small loads, but converges towards the same ultimate capacity as the original p - y curves. The study concludes that none of the currently known p - y approaches are suited to the design of large diameter monopiles in sand and a new design formulation is needed in order to avoid the under- and overestimation of soil-structure stiffness dependent on the load level.

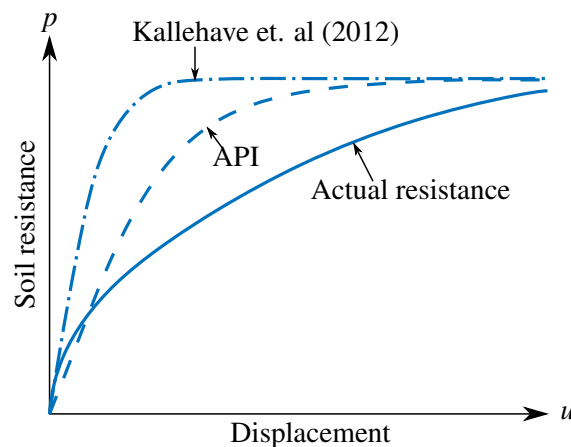


Figure 7.7: Illustrative comparison of p - y curves obtained from different approaches [Achmus, Thieken, and Lemke, 2014, Modified].

The improvements of the p - y curves for clay proposed by Kirsch, Richter, and Coronel, 2014 are based on theoretical considerations and a 3D numerical model which considers a modification of the reference strain level, ϵ_{50} . This strain reference level is modified in regards to the ratio of the present soil resistance to the ultimate soil resistance and the ratio of the dynamic soil stiffness modulus to the static soil stiffness modulus. This formulation is, contrary to the formulation proposed by Kallehave, Thilsted, and Liingaard, 2012, based on the cyclic p - y curves proposed by Matlock, 1970. The improvements proposed by Kirsch, Richter, and Coronel, 2014 yield a higher initial stiffness of Matlock p - y curves. However, these improvements do, similar to the improvement proposed by Kallehave, Thilsted, and Liingaard, 2012, converge towards the same level of soil resistance as the p - y curves, see Figure 7.2 page 90.

A comparative study performed by Achmus, Terceros, and Thieken, 2016 compares the improvements proposed by Kirsch, Richter, and Coronel, 2014 to the p - y curves proposed by

Matlock, 1970, the p - y curves proposed by both DNV GL group, 2018 and API, 2014, and results obtained from a 3D numerical model. The p - y curves proposed by Matlock, 1970 have an infinite initial stiffness yielding an overestimation of the soil-structure stiffness for small loads. This means that the improvements proposed by Kirsch, Richter, and Coronel, 2014 also yield an overestimation of the initial stiffness, since these improvements are increasing the initial stiffness of the cyclic Matlock p - y curves. The comparative study concludes that none of the currently know p - y approaches are well-suited to design large diameter monopiles in clay. The study however concludes that the approach proposed by DNV GL group, 2018 and API, 2014 is the best suited of the known approaches, since this approach bypasses the infinite initial stiffness and thereby an unrealistic overestimation of the soil-structure stiffness for small loads.

When designing an OWT, the first eigenfrequency is of particular interest, as earlier explained. The first eigenfrequency is often estimated based on a combination of loads, which are representable for the sea state, and the environment where the OWT is located. This means that these loads typically are relative small compared to the extreme load cases the OWT has to be designed against. Figure 7.8 illustrates the first eigenfrequency obtained from the different p - y approaches introduced so far in this thesis. The eigenfrequencies are estimated from the parameters presented in Table 7.2 page 94 and with an external load of 1 MN applied at the MWL, see Figure 6.2 page 62. This load level is assumed to be representative for a normal sea state on a location of an OWT.

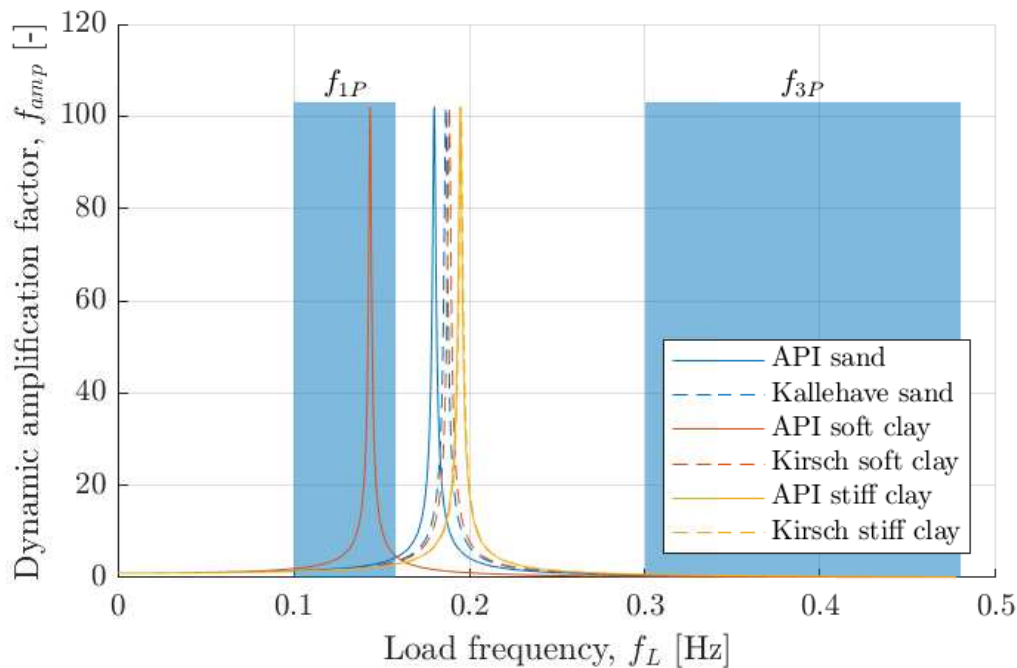


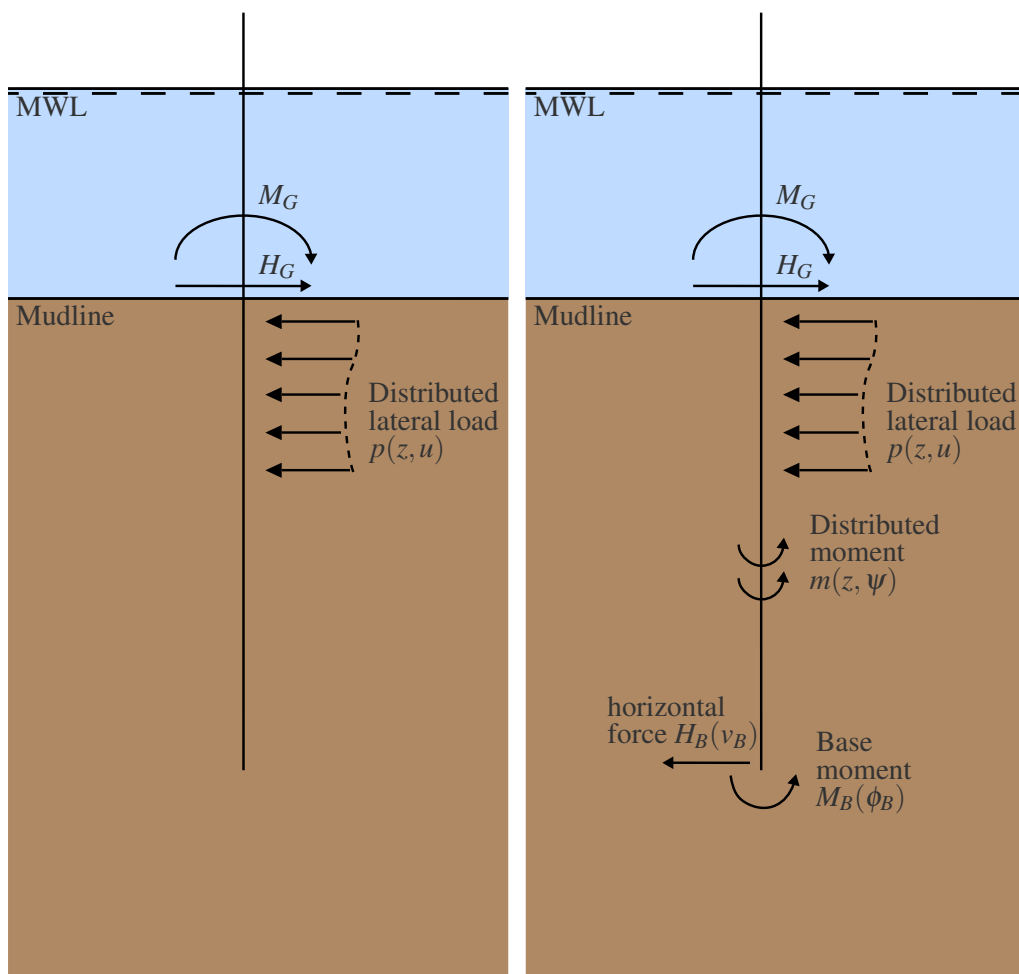
Figure 7.8: Comparison of the dynamic amplification factors obtained from the p - y curves and the excitation ranges f_{1P} and f_{3P} coming from rotor and blades respectively.

From Figure 7.8 it is observed that the first eigenfrequency obtained from the presented p - y approaches are located close to, or even within the area of the rotational frequency, f_{1P} . This tendency is as desired, as the p - y curves tend to underestimate the initial soil-structure stiffness and thereby also the eigenfrequency at small loads. This means that the first eigenfrequency in reality

might be closer to f_{3P} than illustrated in Figure 7.8. However, the first eigenfrequency estimated from the API p - y curves for soft clay is located within the area of f_{1P} , which is not allowable since this could cause the first eigenfrequency to resonate with f_{1P} . This concludes the discussion of the p - y curves and the improvements presented in this chapter.

7.4.2 PISA Approach

The PISA approach is a relatively new approach developed through a research project. The project concerned the development of a new alternative to accurately model laterally loaded piles. The PISA approach differs from the p - y approach in the way it succeeds in including the effects of a large diameter pile. A simple illustration of the differences in the two approaches are shown in Figure 7.9.



(a) 1D design model for the p - y approach. (b) 1D design model for the PISA approach.

Figure 7.9: Illustration of the difference between the p - y approach and the PISA approach.

From Figure 7.9(a) and 7.9(b) it is observed that where the p - y approach only considers the lateral load, p , the PISA approach also considers a distributed moment, m , a horizontal force at the base of the pile, H_B , and a moment at the base of the pile, M_B . The distributed moment is caused by vertical

traction that occurs when the pile rotates, see Figure 7.4 page 92. These additional parameters are included in the model because experiments reveal that the importance of these parameters increases when the diameter of the pile increases, or when the length-diameter-ratio (L/d ratio) decreases [Burd et al., 2017].

Equally to the p - y approach, the PISA approach provides curves which represent the load-displacement response for a particular case. These load-displacement curves can either be obtained from a series of normalised parameters, which are normalised in regards to the dimensions of the pile e.i. the pile length and the pile diameter, or through a 3D FE analysis which can then calibrate the load-displacement curves for the desired soil.

Despite the PISA approach is not yet included in the design guidelines, the approach seems to provide more accurate results compared to the API p - y approach. An illustration of a comparison of the API- and PISA p - y curves to a 3D FE model for sand can be seen in Figure 7.10, where it is clear the PISA approach provides a better fit to the 3D FE model curve. The 3D FE model curve represents the results obtained from a 3D FE analysis of sand during the PISA project, and should thereby reflect the behaviour of sand to a certain degree. [Byrne et al., 2015]

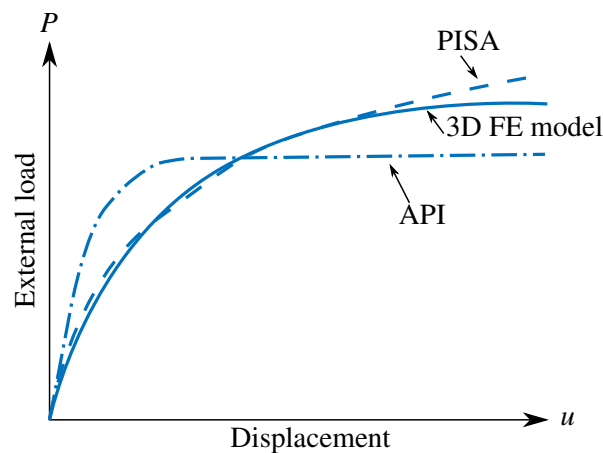


Figure 7.10: Illustration of comparison between API p - y curves, PISA approach and results obtained from a 3D FE model in sand [Byrne et al., 2015, Modified].

When the PISA approach is providing better results, as seen in Figure 7.10, it can be a possible replacement for the API approach used nowadays. However, the PISA approach is still relatively new and more experience with this approach is needed.

8. SEPARATION OF EXTENDED MODEL

A representative 1D FE model for the analysis of eigenfrequencies of an OWT has been set up and validated through Stage 3. The Extended Model from Stage 3 is a model for the full structure, where the user of it needs to have knowledge of the complete system to apply it i.e. the soil and the structure. However, the responsibilities for the design of an OWT are typically divided into different departments that cover e.g. the foundation or the structure, and thereby the set up of two separate models is therefore investigated. One model from the mudline and downwards covering the foundation and the use of the p - y curves, and a second model including the structure from the mudline and upwards. These substructures can be handled by different companies who do not want to share knowledge amongst each other. However, the companies still have to cooperate in order to obtain the correct response for the OWT.

In this chapter the Extended Model, which was described in Chapter 6, is separated into two parts called substructures, which yields a part for the model above mudline and a part below mudline, see Figure 8.1. The problem is to be able to work with each part separately, but still being able to analyse the response of the full structure.

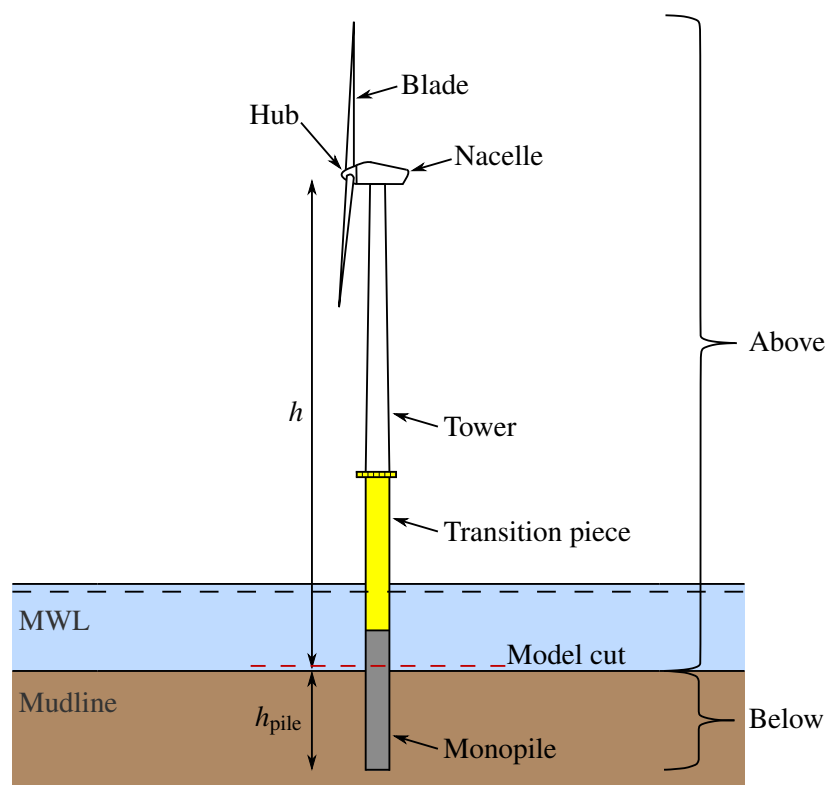


Figure 8.1: Illustration of where the OWT is to be separated, to indicate the two substructures.

The so called component mode synthesis is used to divide the model. The idea of the component mode synthesis is to divide the structure into substructures for different departments to be able to work with the different substructures at the same time.

Modifications of the design can be implemented in one substructure without including this modification in other substructures. This means a modification of one specific substructure does not affect other substructures individually and only the response of the considered substructure and the full structure will be affected. When the designs of the substructures are done, the response from the full structure can be obtained in the form of eigenfrequencies.

Many different approaches for component mode synthesis are available, but the most common used for dividing a structure into substructures is the Craig-Bampton method, which is the method considered in this chapter. The theory for the Craig-Bampton is based on R. D. Cook et al., 2002.

8.1 Procedure

The Craig-Bampton method uses a weighted matrix, $[\mathbf{W}]$, to reduce the mass- and stiffness matrix for each substructure. These reduced matrices are then used to obtain a global reduced mass- and stiffness matrix, $[\mathbf{M}]_{\text{CMS}}$ and $[\mathbf{K}]_{\text{CMS}}$ respectively, which can be used to estimate the eigenfrequency for the full structure by solving the eigenvalue problem. The global reduced mass- and stiffness matrix describe the full system despite the matrices have fewer entrances than the matrices for the original system. In order to obtain the weighted matrix, the mode shapes for each substructure are needed. The mode shapes for a substructure are obtained by fixing all substructure attachment DOFs and then solving the eigenvalue problem for this specific substructure, see equation (8.1). A substructure attachment DOF is characterised by a DOF which node is connected to other substructures, when considering the full structure. Conversely, nodes which are not attached to other substructures are called internal substructure nodes.

In order to be able to use the Craig-Bampton method, the Extended Model is separated at the mudline creating two substructures, see Figure 8.2. Here a FE model for each substructure is made, which is independent of other substructures. Thereby, it is possible to obtain the reduced matrices without sharing information of the substructures between different departments.

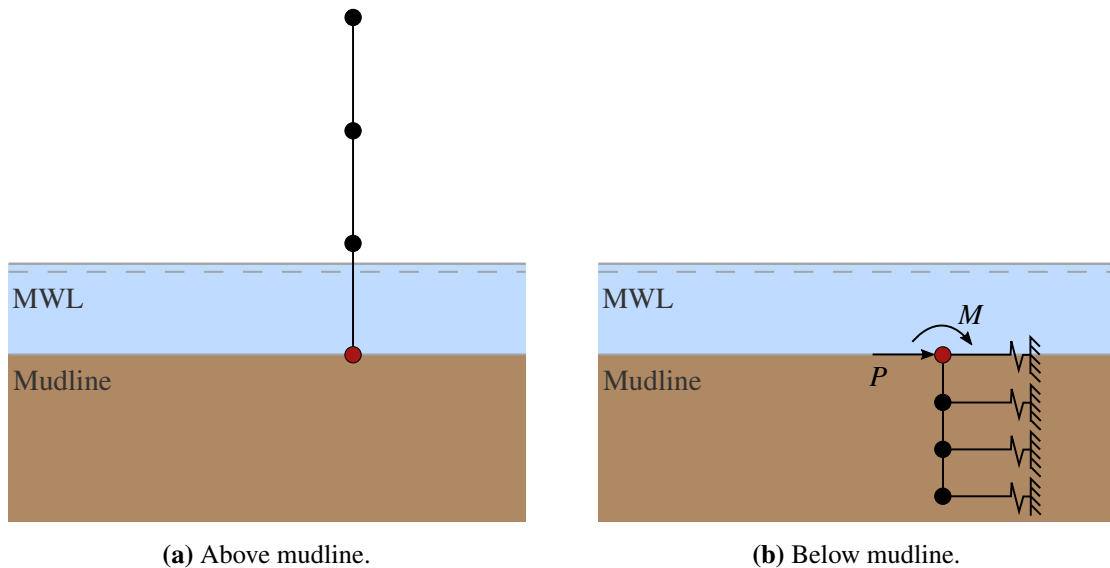


Figure 8.2: Illustration of the two separated models used for calculations. The red nodes represents the attachment DOFs and the black nodes represents the internal substructure DOFs.

The mass- and stiffness matrix for the two substructures are determined from the FE models created for each substructure. The load applied at the full structure does not affect the stiffness matrix for the substructure above mudline, as the stiffness only depends of the Bernoulli-Euler stiffness. Because of this, the load is not used in the FE model above mudline, see Figure 8.2(a). However, as the stiffness matrix for the substructure below mudline is influenced by both the Bernoulli-Euler stiffness and the soil stiffness, the load needs to be included in order to employ the p - y curves, which was investigated in Chapter 5. To be able to model the stiffness from the soil, the load affecting the structure above mudline is transferred to the separation point at the mudline by applying a moment corresponding to the relocated load. The moment is determined by assuming the load can be moved linearly. However, this assumption has to be verified in order to ensure the accuracy of the results obtained.

The mode shapes for the individual substructures can be determined by solving the eigenvalue problem as presented in equation (8.1). This is done because the mode shapes are necessary to determine the weighted matrix for the substructure later.

$$([\mathbf{K}_{nn}]_j - \omega_l^2 [\mathbf{M}_{nn}]_j) \{\mathbf{D}_l\}_j = \{\mathbf{0}\} \quad [\Phi]_j = [\{\mathbf{D}_1\} \{\mathbf{D}_2\} \dots \{\mathbf{D}_k\}]_j \quad (8.1)$$

n	Identification of substructure DOFs which is not attachment DOFs
j	Identification of substructure
l	Identification of specific substructure mode
k	Number of mode shapes retained in modal matrix

Here the mass- and stiffness matrix for each substructure is derived from the internal substructure DOFs. These are shown as the black nodes in Figure 8.2.

The connection between the internal loads of a substructure and the corresponding stiffness matrix is expressed in equation (8.2).

$$\begin{bmatrix} \mathbf{K}_{nn} & \mathbf{K}_{na} \\ \mathbf{K}_{na}^T & \mathbf{K}_{aa} \end{bmatrix}_j \begin{bmatrix} \Psi \\ \mathbf{I} \end{bmatrix}_j = \begin{bmatrix} \mathbf{0} \\ \mathbf{R} \end{bmatrix}_j \quad (8.2)$$

a	Identification of attachment DOFs
n	Identification of other substructure DOFs
j	Identification of substructure
$[\Psi]$	Matrix with resulting vectors of internal substructure DOFs
$[\mathbf{I}]$	Unit matrix
$[\mathbf{R}]$	Matrix for the resulting vectors of reactions at attachment DOFs

From equation (8.2) an expression for the matrix $[\Psi]$ can be derived, see equation 8.3. This matrix is necessary for the determination of the weighted matrix for each substructure.

$$[\Psi]_j = -[\mathbf{K}_{nn}]_j^{-1} [\mathbf{K}_{na}]_j \quad (8.3)$$

The idea of the Craig-Bampton method is to reduce the number of nodes, which represents the substructure. The transformation between the original DOFs representing the original substructure system and the substitute DOFs which represent the reduced substructure, is performed by the weighed matrix, see equation (8.4). The weighted matrix is used to reduce the number of nodes which are representing the substructure.

$$\{\mathbf{D}\}_j = \begin{Bmatrix} \mathbf{D}_n \\ \mathbf{D}_a \end{Bmatrix}_j = [\mathbf{W}] \begin{Bmatrix} \mathbf{a} \\ \mathbf{D}_a \end{Bmatrix}_j \quad \text{where} \quad [\mathbf{W}]_j = \begin{bmatrix} \Phi & \Psi \\ \mathbf{0} & \mathbf{I} \end{bmatrix} \quad (8.4)$$

$\{\mathbf{a}\}$		Vector containing modal coordinates
$\{\mathbf{D}_n\}$		Contains internal substructure DOFs
$\{\mathbf{D}_a\}$		Contains substructure attachment DOFs
$[\mathbf{W}]$		Weighted matrix
$[\Phi]$		Modal matrix containing mode shapes

A reduced stiffness- and mass matrix for each substructure can now be calculated as the weighted matrix is known for each substructure. These are calculated using equation (8.5) and (8.6) respectively. When the global reduced matrices are to be determined afterwards, only the reduced mass- and stiffness matrices for each substructure have to be shared amongst the different substructures, and the rest of the information used through the calculations can be kept secret if this is desired.

$$[\mathbf{K}_{\text{red}}]_j = [\mathbf{W}]_j^T [\mathbf{K}]_j [\mathbf{W}]_j \quad (8.5)$$

$$[\mathbf{M}_{\text{red}}]_j = [\mathbf{W}]_j^T [\mathbf{M}]_j [\mathbf{W}]_j \quad (8.6)$$

With the reduced mass- and stiffness matrices for the two substructures, the global reduced matrices, $[\mathbf{K}]_{\text{CMS}}$ and $[\mathbf{M}]_{\text{CMS}}$, are made by combining the obtained reduced matrices from the substructures. These global reduced matrices can describe the full structure. Finally, the eigenvalue problem can be solved in order to obtain the eigenfrequencies for the full structure with equation (8.7). This is the same equation as used previously in Stage 2 and 3 for estimating the eigenfrequency by solving the eigenvalue problem, which was first introduced in Chapter 4 page 30.

$$([\mathbf{K}]_{\text{CMS}} - \omega_i^2 [\mathbf{M}]_{\text{CMS}}) \{\mathbf{D}\}_i = \{\mathbf{0}\} \quad (8.7)$$

i | Mode shape and eigenfrequency number

The number of possible eigenfrequencies obtained from equation (8.7) depends on the number of mode shapes, which is included to obtain the weighted matrix in equation (8.4). In this thesis only the first eigenfrequency is considered, as this eigenfrequency is used as reference, and because of this only one mode shape is used in equation (8.4) to obtain the weighted matrix. If the obtained eigenfrequency deviates significantly to the eigenfrequencies obtained from the Extended Model or higher order eigenfrequencies are desired, more mode shapes can be applied to determine the weighted function. The method should thereby give a better estimate of the eigenfrequencies and be able to obtain the same number of eigenfrequencies as the number of mode shapes included in the weighted matrix.

8.2 Discussion of Application

As the theory described in the previously section should be used in the design phase, two FE models for the substructure above- and below mudline are set up respectively. The FE models, which are set up for both substructures, can be seen in Figure 8.3 where the applied external loads considered are illustrated.

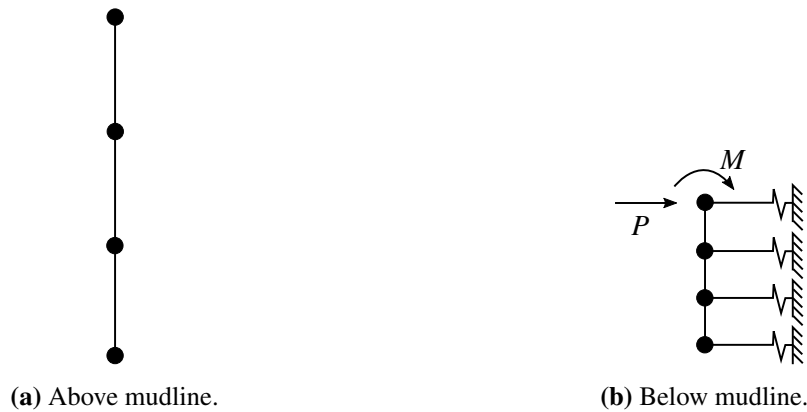


Figure 8.3: Illustration of the two FE models used, which are set up for the two substructures. Locations of applied external loads for each substructure are illustrated as well.

When the mass- and stiffness matrix are determined by the FE models illustrated in Figure 8.3, the Craig-Bampton method is applied. Here the boundary conditions illustrated in Figure 8.4 are used.

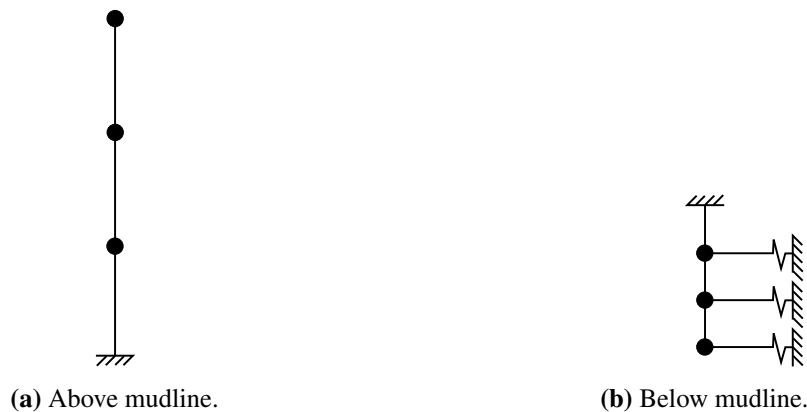
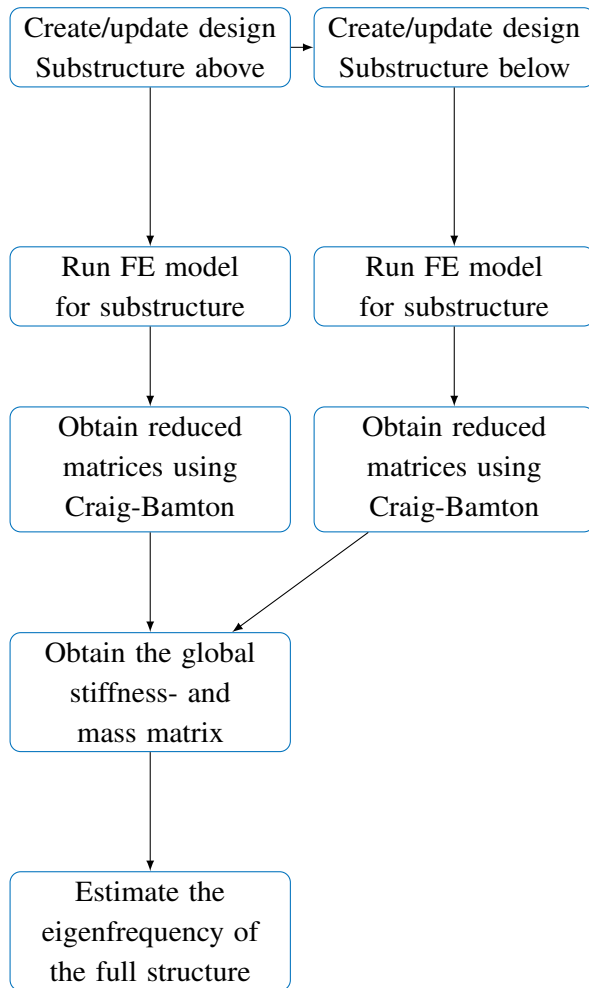


Figure 8.4: Illustration of the two FE models used with their considered boundary conditions when the Craig-Bampton method is used.

The procedure of estimating the eigenfrequency of the full structure is presented in the flowchart below. As already mention, this procedure is applicable both for the initial investigation of the eigenfrequency of a structure, but also applicable to update this eigenfrequency if a substructure is modified. Modifications of the substructures can be necessary if the eigenfrequency of the full structure is close to load frequencies or excitation frequencies, which causes resonance as introduced in Section 3.2. The following flowchart is valid both for the initial estimation of the eigenfrequency of a structure but also if a substructure has been modified.



The design for each substructure is either created or updated. In case any modifications are made for the substructure above mudline, which yields a changing load magnitude, this must be informed to the responsible of the substructure below mudline.

The FE model for each substructure run for obtaining their individual stiffness- and mass matrix.

The Craig-Bampton method is used to obtain the reduced stiffness- and mass matrix, $[\mathbf{K}_{\text{red}}]$ and $[\mathbf{M}_{\text{red}}]$, for each substructure.

With the reduced stiffness- and mass matrix from each substructure, the global reduced stiffness- and mass matrix $[\mathbf{K}]_{\text{CMS}}$ and $[\mathbf{M}]_{\text{CMS}}$, are determined as the combination of these.

By using the global reduced matrices, the eigenvalue problem is solved and the eigenfrequency for the structure is estimated.

From the flowchart it is observed that the load only affects the structure above mudline and that the reduced matrices from each substructure in the only information which have to be shared amongst the substructures. Thereby no specific information for the substructures are shared, which was the idea of this separation of the Extended Model. In order to employ the procedure presented in the flowchart, it should be noted the procedure has to start for the substructure above mudline, as the applied loads have to be passed on for the initial design of the substructure below mudline. However, no specific load cases are considered for the structure in this thesis, which is why a varying load is used. If other design aspects was considered, these could result in an update of the substructures design.

In order to obtain comparable results, the soil parameters used in the convergence analysis in Section 6.3 are also applied in this analysis. The parameters for the three different soil types are repeated in Table 8.1. It should be noted that these parameters are only used for the Extended Model and the Separated Model below mudline, as the Separated Model above mudline does not require any information about the soil.

Table 8.1: Input parameters used in the Extended Model and the Separated Model below mudline for analysis. *Reference strain level is the strain occurring at 50 % of the maximum principal stress in an undrained compression laboratory test.

Parameter	Symbol	Unit	Sand	Soft clay	Stiff clay
Effective angle of internal friction	ϕ'	°	37.5	-	-
Undrained shear strength	s_u	kPa	-	125	350
Effective unit weight of soil	γ'	kN/m ³	9.5	9	10
Reference strain level*	ε_{50}	-	-	0.015	0.008
Empirical constant	J	-	-	0.5	0.25
Diameter of the monopile	d	m	8	8	8
Length of the monopile below mudline	h_{pile}	m	30	30	30

The information about the structure needed for the Separated Model above- and below mudline can be seen in Table 8.2.

Table 8.2: Structural data for the Separated Models above- and below mudline.

Parameter	Symbol	Unit	Value	
			Above	Below
Structure height	h / h_{pile}	m	161	30
Structure diameter	d	m	8	8
Structure wall thickness	t	m	0.1	0.1
Mass at top (hub, nacelle, blades)	m	ton	593.27	-
Young's modulus	E	GPa	210	210
Structure steel density	ρ	$\frac{\text{kg}}{\text{m}^3}$	7850	7850
Applied load	P	MN	-	0-30

Most of the structure parameters for the Separated Model above- and below mudline are the same, but it is possible to use varying values, etc. the diameter, the wall thickness or the type of steel above- and below mudline could be different, and thereby resulting in different input for the two separated models.

8.3 Results

The results obtained by using the Separated Model are presented in this section. The results are presented in the form of displacements and eigenfrequencies and are compared to the results obtained by using the Extended Model.

The displacement at mudline for the Separated Model below mudline can be compared to the corresponding displacement at mudline for the Extended Model. This is done in order to verify the Separated Model and the assumption of the load at MWL can be represented of an equivalent load and moment at mudline, where the moment are estimated by a linear transformation. If there is a

difference between the displacements obtained from the two systems, the assumption of moving the load linearly is not applicable. Figure 8.5 shows the displacement at mudline for the Extended Model and the Separated Model below mudline for the different soil types and loads. From here it is seen the displacements at mudline, which are estimated by the Separated Model below mudline are identical to the displacements obtained from the Extended Model.

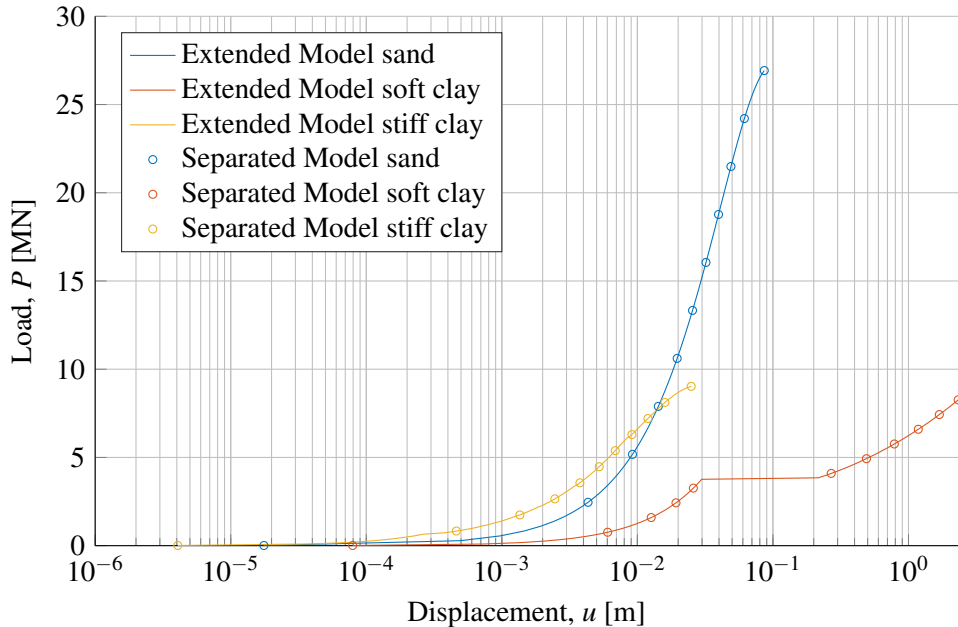


Figure 8.5: Comparison between the displacement at mudline using the Separated Model and the Extended Model to obtain results where the original API p - y curves are used. The displacement is shown by a logarithmic axis in order to see the comparison of the results better.

An example of the comparison of the displacements below mudline for the Extended Model and the Separated Model can be seen in Figure 8.6, where the comparison point used in Figure 8.5 is illustrated.

The assumption of moving the load linearly to the mudline is thereby verified for the Separated Model as it does not seem to have any influence at the obtained results in the form of displacements.

The eigenfrequencies estimated using the Craig-Bampton method are presented in Figure 8.7, where the solid lines are the original API curves for the full structure, which was obtained previously in Stage 3 using the Extended Model, see Figure 7.6 page 95. The results obtained with the Separated Model are illustrated with scatters.

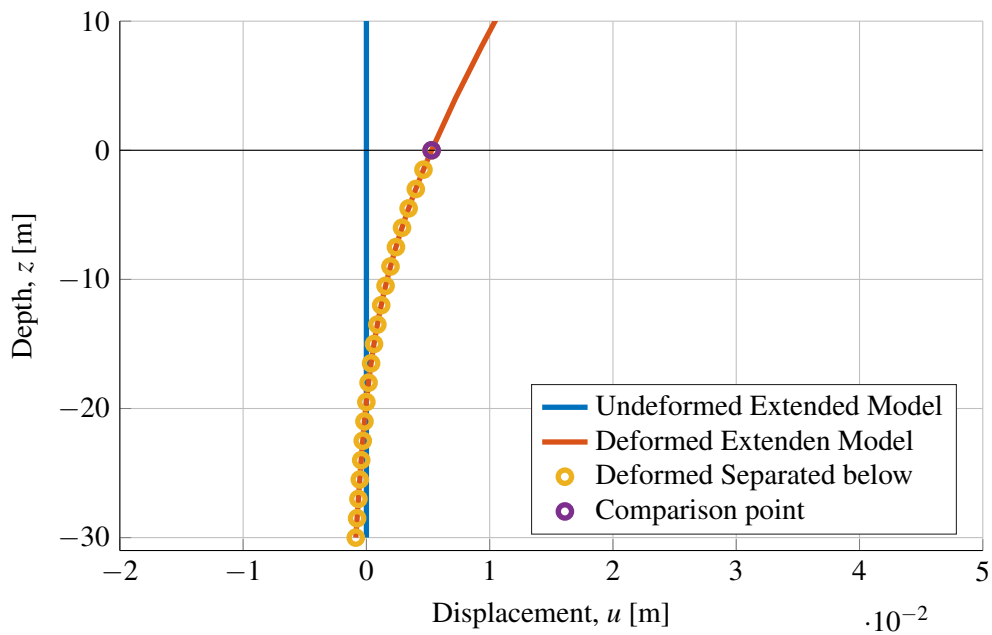


Figure 8.6: Example of the deformation below mudline obtained for the Extended Model and the Separated Model considering sand and an applied load, P , of 3 MN.

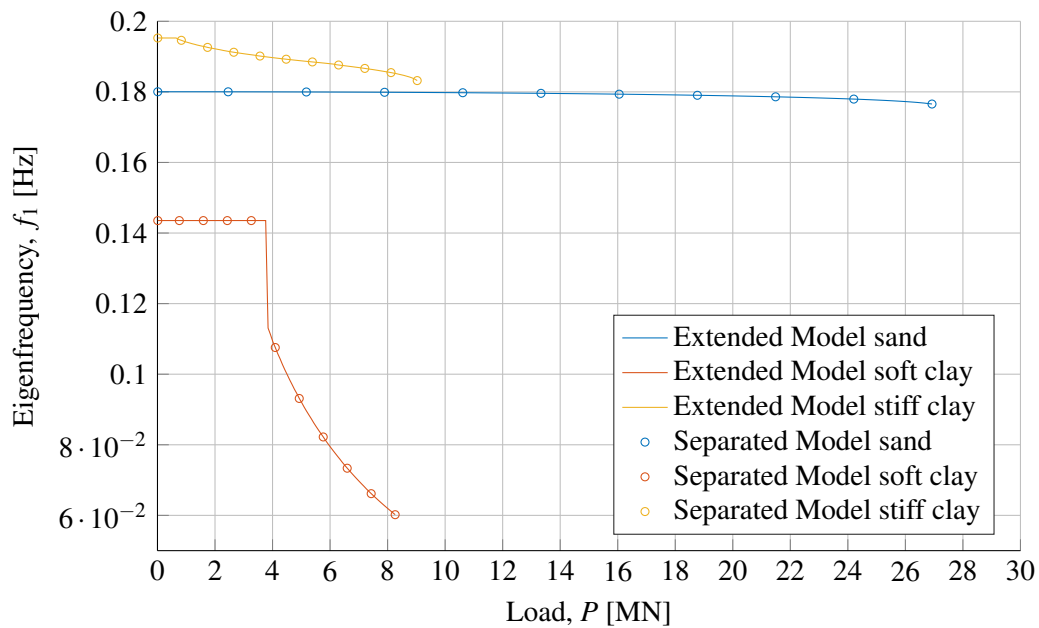


Figure 8.7: Estimated eigenfrequencies for the Separated Model compared to the Extended Model using the API p - y curves.

From Figure 8.7 it is observed that the results are very similar to the ones obtained using the Extended Model. The method yields acceptable results as the eigenfrequencies estimated are within 0.05% of the eigenfrequencies obtained by using the Extended Model for the three types of soil.

From the analysis it can be concluded that the Separated Model using the Craig-Bampton method yields close to identical eigenfrequencies and displacements, when comparing to the Extended

Model using the original API p - y curves. The Craig-Bampton method is thereby verified as being able to separate the Extended Model and keeping the information about each substructure secret without losing precision in estimating the eigenfrequency for the full structure.

IV

Stage 4

In this stage, the commercial FE program Plaxis 3D is used for analysing a monopile. The stage is consisting of a description of how a model is set up in Plaxis 3D, together with a convergence analysis for the dimensions of the soil domain and mesh size of the model. After, a free vibration analysis is performed to estimate the eigenfrequency of an OWT. This is followed by an analysis of p - y curves extracted from Plaxis 3D and an analysis of the displacement field around a monopile.

9	Application of Plaxis 3D	113
9.1	Purpose	
9.2	Reference Soil Profile	
9.3	Material Models	
9.4	Set up of Model in Plaxis 3D	
10	Convergence Analysis	123
10.1	Set up of Model	
10.2	Estimation of the Applied Horizontal Load	
10.3	Convergence Analysis of the Size of the Soil Domain	
10.4	Convergence Analysis of Mesh Size	
10.5	Conclusion on the Convergence Analysis	
11	Free Vibration Analysis	133
11.1	Set up of Model	
11.2	Analysis of Calculation Results	
11.3	Closure of the Free Vibration Analysis	
12	Extraction of p-y Curves	143
12.1	Set up of Model	
12.2	Principle of Extraction of the p - y Curves	
12.3	Comparison of p - y Curves	
12.4	Closure of the Analysis of p - y Curves	
13	Displacement Field	153
13.1	Set up of Model	
13.2	Analysis of the Diameter Effect	

9. APPLICATION OF PLAXIS 3D

9.1 Purpose

Stage 4 is the final stage of this thesis. The purpose of this stage is to further analyse some of the previously covered problematics using a commercial FE program. Here Plaxis 3D will be used as the available possibilities provided by the program within material models and analysis forms etc. covers the needs of this final stage. The analyses performed in Plaxis 3D in this stage are plastic and dynamic calculations. Analyses in a 3D FE program can be very time consuming, especially the dynamic calculations. Because of this, it is chosen that the analyses performed in Stage 4 will be performed with just a single soil profile e.i. the reference soil profile. This reference soil profile will be introduced in the following section.

Three different analyses are performed. The first analysis is a free vibration analysis of a simplified OWT. This analysis is performed to estimate the first eigenfrequency of the system and compare the result with the eigenfrequency obtained by using the Extended Model described in Chapter 6. The second analysis is an extraction of p - y curves from Plaxis 3D, to compare them to the API p - y curves described in Chapter 5. The third and final analysis is an observation of the different behaviour of piles, as they go from being very slender with a small diameter, to having larger diameters and becoming more like rigid structures.

Prior to the three analyses in Stage 4, the reference soil profile is described, the material models used are introduced together with a brief introduction to the set up of the model in Plaxis 3D. This is followed by a convergence analysis of the soil domain size and the meshing of the model.

9.2 Reference Soil Profile

As this thesis is not site specific nor conducted on any determined soil, a reference soil profile derived by the authors of this thesis during an earlier semester project is used to obtain input parameters for Plaxis 3D. The reference values provided in Table 9.1 covers the input parameters necessary to use the models in Plaxis 3D. It is chosen only to work with a single layer of soil, and the depth of the soil is thereby assumed infinite.

Table 9.1: Reference values for soil parameters used in Plaxis 3D models through Stage 4 [Nielsen et al., 2018].

Layer	Soil type	General			Stiffness						Strength		
		Bottom limit	γ_{sat}	γ_{dry}	E_{50}^{ref}	E_{oed}^{ref}	E_{ur}^{ref}	m	ν'_{ur}	ν	s_u	ϕ'	ψ
[No]	[-]	[m]	[kN/m ³]	[kN/m ³]	[MPa]	[MPa]	[MPa]	[-]	[-]	[-]	[kPa]	[°]	[°]
5	Sand	∞	19.0	14.0	34	34	204	0.54	0.2	0.3	-	36.6	10.8

γ_{dry}	Dry unit weight
γ_{sat}	Saturated unit weight
E_{50}^{ref}	Primary straining due to primary deviatoric loading
E_{oed}^{ref}	Primary straining due to primary compression
E_{ur}^{ref}	Elastic unloading/reloading
m	Stress dependency factor
ν	Poisson's ratio for primary loading
ν'_{ur}	Poisson's ratio for unloading/reloading
s_u	Undrained shear strength
ϕ'	Effective angle of internal friction
ψ	Angle of dilatancy

Determination of the stiffness parameters are elaborated in Appendix J.1.

9.3 Material Models

In the following sections the material models used in Plaxis 3D for this thesis will be introduced. The material models introduced from Section 9.3.1 to 9.3.4 are based on Plaxis, 2017a.

9.3.1 Linear-Elastic

The Linear-Elastic material model is the simplest material model. The material model is based on Hooke's law of isotropic elasticity. The input parameters for the Linear-Elastic material model are the elastic parameters Young's modulus and Poisson's ratio. In this thesis the Linear-Elastic material model is used to illustrate the importance of using more advanced soil models with more input parameters to mimic real soil behaviour. The input parameters are summed in Table 9.2. As Young's modulus is not given in the soil parameters for the sand stated in Table 9.1, it is instead derived based on Hooke's law, see Appendix J.2.

Table 9.2: Input parameters for the Linear-Elastic material model for Plaxis 3D.

Input	Symbol	Unit	Value
Saturated unit weight	γ_{sat}	kN/m ³	19
Dry unit weight	γ_{dry}	kN/m ³	14
Young's modulus	E	MPa	25.3
Poisson's ratio	ν	-	0.3

The stress-strain path for the Linear-Elastic material model is illustrated in Figure 9.1. Here it is seen that the Linear-Elastic material model has infinite strength, and the loading and unloading paths are the same.

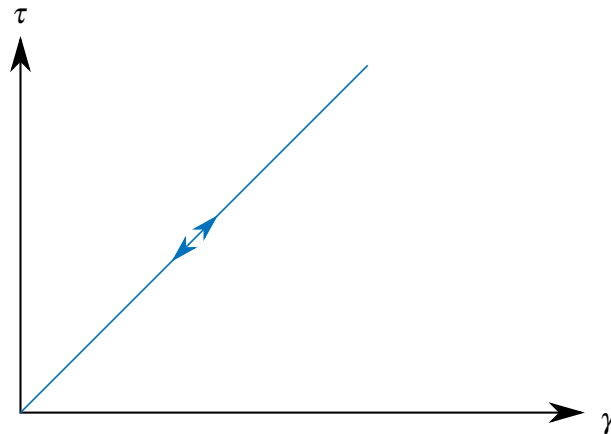


Figure 9.1: Stress-strain path for a Linear-Elastic material.

Application of the Linear-Elastic material model

The Linear-Elastic material model is not suited for modelling the behaviour of soil, as soil behave non-linear and the loading- and unloading paths are different from each other. The material model can be used if the user in Plaxis 3D wants to start with a soil model that is as simple as possible and add more advanced features over time to observe the behaviour of the 3D model, as more complex features are added. The only real application of the Linear-Elastic material model is when it is used to model massive structures in soil or bedrock layers.

Using a Linear-Elastic material model ensures infinite strength of the material and disregards plasticity. When such a model is used for dynamically loaded structures it disregards the effects of shear degradation over time due to rearrangements of soil grains when the soil is loaded. No matter the magnitude of the loading, linear-elastic soils will behave the same, and follow the same stress-strain path for primary loading and unloading/reloading. This makes the model unsuitable for dynamic models.

9.3.2 Mohr-Coulomb

The Mohr-Coulomb material model is a linear elastic perfectly-plastic material model. The material model uses Young's modulus and Poisson's ratio to model the elasticity of soil, equally as for the Linear-Elastic material model. However, the model considers the strength and plasticity of the soil. These effects are included by the following strength input parameters: Effective angle of internal friction, undrained shear strength and the angle of dilatancy. Using this material model allows for either estimating a constant average stiffness for a soil layer or a stiffness that increases linearly with depth. In this thesis the first option is utilised.

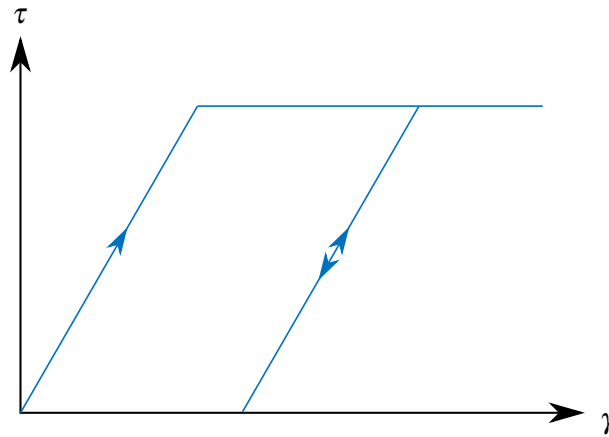
This simplicity of the stiffness modelling allows relative fast computational times, and the material model is therefor good for obtaining a first estimate of the soil-structure behaviour. The input parameters for the Mohr-Coulomb material model are given in Table 9.3.

The stress-strain path for the Mohr-Coulomb material model is illustrated in Figure 9.2. Different from the Linear-Elastic material model, the Mohr-Coulomb material model includes a yield criteria,

Table 9.3: Input parameters for the Mohr-Coulomb material model for Plaxis 3D.

Input	Symbol	Unit	Value
Saturated unit weight	γ_{sat}	kN/m ³	19
Dry unit weight	γ_{dry}	kN/m ³	14
Young's modulus	E	MPa	25.3
Poisson's ratio	ν	-	0.3
Effective angle of internal friction	ϕ'	°	36.6
Undrained shear strength	s_u	kPa	-
Angle of dilatancy	ψ	°	10.8

as strength parameters are included in the model. It is also observed that the material model includes plastic strains and that primary loading and unloading/reloading have the same slope.

**Figure 9.2:** Stress-strain path for a Mohr-Coulomb material.

Application of the Mohr-Coulomb material model

The Mohr-Coulomb material model introduces yielding and plasticity, but does not include strain- or stress dependency on the stiffness of the material. The Linear-Elastic perfectly-plastic material model can be used quite accurately to describe the effective stress states at failure. However, as the material model is still linear-elastic for loading and unloading, the material model is not suitable for dynamic models, as the hysteresis loops introduced in Stage 1 are non existing using the Mohr-Coulomb material model.

9.3.3 Hardening Soil

The Hardening Soil material model is a more advanced soil model compared to the Mohr-Coulomb material model. The strength of the material is as for the Mohr-Coulomb material model described by the effective angle of internal friction, the undrained shear strength and the dilatancy angle. The elasticity of the soil is though more well defined in this model than the Mohr-Coulomb material model, now including three different stiffness input parameters rather than just using Young's modulus. The three stiffnesses are the triaxial loading stiffness, the triaxial unloading/reloading stiffness and the loading stiffness from oedometer testing.

Plaxis suggests that the unloading/reloading stiffness often can be set to three times the triaxial loading stiffness. The triaxial stiffness and the oedometer stiffness can usually be set equal to each other if the soil is not very soft nor very stiff. In this thesis the unloading/reloading stiffness is set to a value greater than three times the loading stiffness, as this value has been fitted in Plaxis 3D to mimic the soil behaviour from test data.

Another difference from the Mohr-Coulomb material model is that the Hardening soil material model includes stress-dependency of the stiffness moduli. This differs from the Mohr-Coulomb material model, as this model only has the ability to increase the stiffness with depth for a soil layer. The input parameters for the Hardening soil material model are given in Table 9.4.

Table 9.4: Input parameters for the Hardening Soil material model for Plaxis 3D.

Input	Symbol	Unit	Value
Saturated unit weight	γ_{sat}	kN/m ³	19
Dry unit weight	γ_{dry}	kN/m ³	14
Primary straining due to primary deviatoric loading	E_{50}	MPa	34
Primary straining due to primary compression	E_{oed}	MPa	34
Elastic unloading/reloading	E_{ur}	MPa	204
Stress dependency factor	m	-	0.54
Poisson's ratio for primary loading	ν	-	0.3
Poisson's ratio for unloading/reloading	ν_{ur}	-	0.2
Effective angle of internal friction	φ'	°	36.6
Undrained shear strength	s_u	kPa	-
Angle of dilatancy	ψ	°	10.8

The stress-strain path for the Hardening Soil material model is illustrated in Figure 9.3, where it is observed that the stress-strain relation is now stress dependent and no longer linear. The Hardening Soil material model also introduces different stiffnesses for primary loading and reloading.

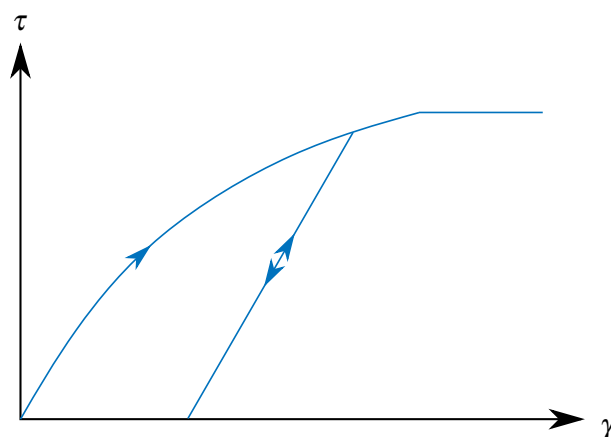


Figure 9.3: Stress-strain path for a Hardening Soil material.

Application of the Hardening Soil material model

The Hardening Soil material model is capturing more of the real soil behaviour as the model has different stiffnesses for primary loading, unloading and reloading, compared to the Mohr-Coulomb

material model, although the model still disregards a few effects according to real soil behaviour. The material model does not account for the softening of a material as the soil dilates. The model is not completely useful for dynamic problems, as it does not account for real hysteretic behaviour due to its isotropic hardening model. The isotropic hardening model causes the lack of shear degradation as the soil is cyclic loaded inside its yield surface, meaning that cyclic mobility is disregarded in the model. The large stiffness of soil at small strains is also excluded in this material model, but included in the Hardening Soil Small-strain material model. This means that in the free vibration analysis performed in Chapter 11, only the loading phase will affect the yield surface of the material model. This is due to the first oscillation is the biggest and the following oscillations are decreasing in size, meaning the stresses are kept inside the material yield surface. By this it can be concluded that the unloading/reloading stiffness is very important to determine correctly for these analyses, as this is the primary used soil stiffness in a free vibration analysis.

9.3.4 Hardening Soil Small-Strain

The Hardening Soil Small-strain material model is a modification of the previous mentioned Hardening Soil material model. This material model differs from the Hardening Soil material model by including an increased stiffness of soil when the strains are small. To include this behaviour where the small-strain stiffness is higher than for the Hardening Soil material model, two additional input parameters have to be included in the model. These parameters are the small-strain shear modulus and a value that indicates at which strain level the shear modulus has reduced to approximately 70 % of the small-strain shear modulus. When the material model is used in dynamic models, as for the free vibration analysis, it introduces hysteretic material damping.

The input parameters for the Hardening Soil Small-strain material model are given in Table 9.5. The small-strain shear modulus and the strain level for 70 % are determined in Appendix J.2, as these are unknown for the given soil profile.

Table 9.5: Input parameters for the Hardening Soil Small-strain material model for Plaxis 3D.

Input	Symbol	Unit	Value
Saturated unit weight	γ_{sat}	kN/m ³	19
Dry unit weight	γ_{dry}	kN/m ³	14
Primary straining due to primary deviatoric loading	E_{50}	MPa	34
Primary straining due to primary compression	E_{oed}	MPa	34
Elastic unloading/reloading	E_{ur}	MPa	204
Stress dependency factor	m	-	0.54
Poisson's ratio for primary loading	ν	-	0.3
Poisson's ratio for unloading/reloading	ν_{ur}	-	0.2
Effective angle of internal friction	ϕ'	°	36.6
Undrained shear strength	s_u	kPa	-
Angle of dilatancy	ψ	°	10.8
Small-strain shear modulus	G_0^{ref}	MPa	134.22
Strain level at 70 % of G_0	$\gamma_{0.7}$	-	10^{-4}

The stress-strain path for the Hardening Soil Small-strain material model is illustrated in Figure 9.4, where it compared to the Hardening-soil material model illustrated in Figure 9.3 now has a larger initial stiffness.

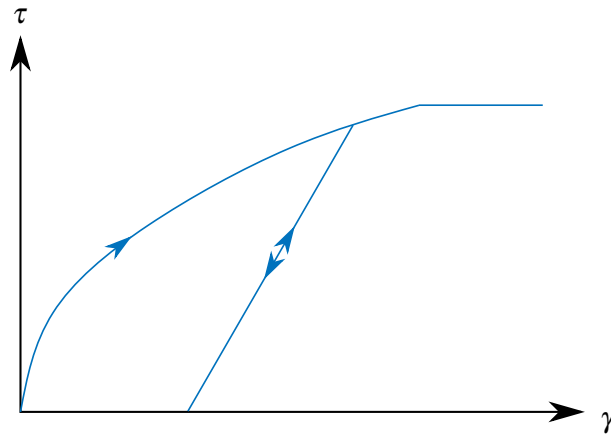


Figure 9.4: Stress-strain path for a Hardening Soil Small-strain material.

Application of the Hardening Soil Small-Strain material model

The Hardening Soil Small-strain material model has the same limitations as mentioned above for the Hardening Soil material model. This means that this material model does not capture the real hysteretic behaviour either, although this model introduces hysteretic damping for dynamic applications. The Hardening Soil Small-strain material model is superior to the Hardening Soil material model when it comes to calculating a model where the strain level is rather small. In the free vibration analysis of the OWT, the tower will be loaded until the deformation at hub height is somewhere above two meters. It will be commented at the end of the analysis if this small strain stiffness changed anything for this specific analysis.

9.3.5 Input for Plaxis 3D

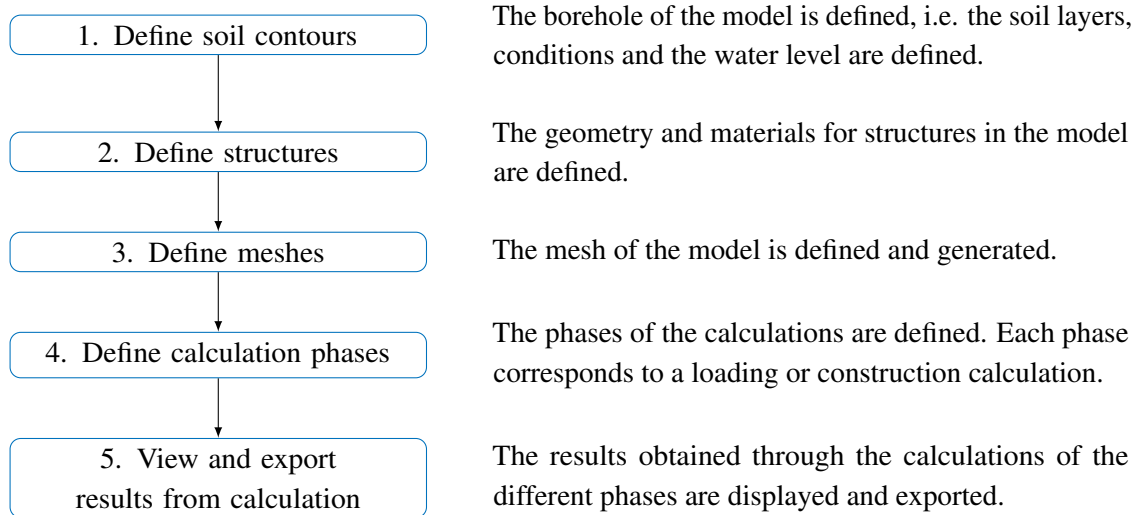
Table 9.6 sums the input parameters used in this thesis for the previously described material models.

Table 9.6: Input parameters for the used material models for Plaxis 3D.

Parameter	Symbol	Unit	Value	LE	MC	HS	HSS
Dry unit weight	γ_{sat}	kN/m ³	19	✓	✓	✓	✓
Saturated unit weight	γ_{dry}	kN/m ³	14	✓	✓	✓	✓
Young's modulus	E	MPa	25.3	✓	✓		
Primary straining due to primary deviatoric loading	E_{50}	MPa	34			✓	✓
Primary straining due to primary compression	E_{oed}	MPa	34			✓	✓
Elastic unloading/reloading	E_{ur}	MPa	204			✓	✓
Stress dependency factor	m	-	0.54			✓	✓
Poisson's ratio for primary loading	ν	-	0.3	✓	✓		
Poisson's ratio for unloading/reloading	ν_{ur}	-	0.2			✓	✓
Effective angle of internal friction	ϕ	°	36.6		✓	✓	✓
Undrained shear strength	s_u	kPa	0		✓	✓	✓
Angle of dilatancy	ψ	°	10.8		✓	✓	✓
Small-strain shear modulus	G_0^{ref}	MPa	134.22				✓
Strain level at 70 % of G_0	$\gamma_{0.7}$	-	10^{-4}				✓

9.4 Set up of Model in Plaxis 3D

In this section the set up of the Plaxis 3D model is explained briefly. Most of the models used in the analyses performed in Stage 4 are based on the same model composition. This section serves therefore as a general introduction to the way these models are composed. The following flowchart illustrates the five general steps of computing a Plaxis 3D model. Each of these five steps are elaborated below the flowchart.



1. Define Soil Contours

When creating a model in Plaxis 3D, the first option for the user is to define the size of the soil domain and to define soil stratification. The size of the soil domain is determined through a convergence analysis, see Chapter 10. The symbols and references used for the dimensions of the soil domain are illustrated in Figure 9.5, where the dark area around the pile will be described during the definition of meshes.

The Plaxis 3D model of the OWT is modelled as a symmetric model in order to reduce the computational time of the calculations. This can be done because the geometry of the monopile is symmetric, and because horizontal loads only are applied in one direction.

The soil stratification is characterised by defining a borehole where each soil layer is described by a material model and the corresponding material parameters. In Plaxis 3D, soil elements are composed of a 10-node tetrahedral 3D element. In this step, also the water head is requested in order to be able to calculate the overburden pressure at a later state.

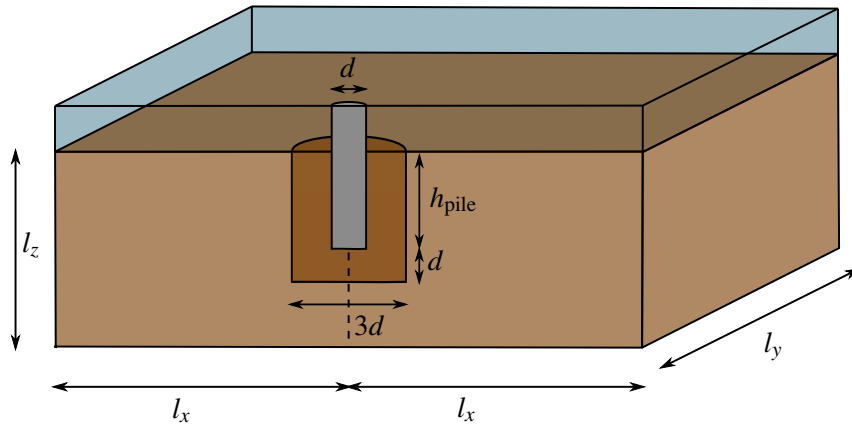


Figure 9.5: Illustration of dimensions and symbols used to refer to the dimensions of the numerical model.

2. Define Structures

The definition of the structures in the model depends on which kind of analysis is performed. The general idea behind defining structures in Plaxis 3D is described in this section. However, in the following chapters where models for the three specific analyses are performed, the set up of the desired model is elaborated.

When the size of the soil domain and the soil stratification are defined, the next step is to define the desired structure. In the case of this thesis, the desired structure is a monopile and possibly the OWT tower. These structures are modelled as plates which are composed of 6-noded triangular plate elements with six degrees of freedom per node, i.e. three translation degrees of freedom and three rotational degrees of freedom.

In order to model the soil-structure interaction between the submerged part of the monopile and the surrounding soil, interfaces are applied to the monopile. These interfaces are modelled as 12-noded interface elements, and are compatible with the 6-noded triangular side of either a soil element or plate element.

Finally, a plate is installed on the top of the desired structure. This plate is turned into a rigid-body where the external loads are applied. This is done to ensure that the external loads are applied evenly to the cross section of the monopile and that the application of the loads does not cause any numerical errors.

3. Define Meshes

Following the set up of the structures considered, the mesh of the model is defined and generated. Two different mesh sizes are applied in the 3D model i.e. the global mesh, which defines the mesh size far away from the monopile, and the local mesh, which defines the mesh size in the dark-brown area illustrated in Figure 9.5. The division of the soil domain in a global and local mesh is performed to reduce the computational time of the model, and because more critical changes are expected to occur closer to the monopile compared to far away. The sizes of the global- and local mesh are determined through a convergence analysis, see Chapter 10.

4. Define Calculation Phases

When the mesh has been generated, the configurations for the calculation of the numerical model are defined. Plaxis 3D divides a calculation into phases where each phase represent either a generation of the initial stress-state, an installation of a new structure or any kind of loading or unloading procedure.

The investigations performed with the numerical 3D model consists of a combination of the four phases presented in Table 9.7.

Table 9.7: Description of the phases used to perform calculations in Plaxis 3D.

Name	Description
Initial phase	The initial stress-state is generated
Installation phase	The monopile is added to the soil domain and the stress-state after the appearance of the monopile is generated
Loading phase	The external load is applied to the structure in steps
Dynamic phase	A free vibration analysis of the structures is performed

The investigations performed in following chapters can be divided into two model categories: static models and dynamic models. For the static models, the three first phases presented in Table 9.7 are considered, whereas for the dynamic models, all of the four presented phases are considered.

Another difference between the static- and the dynamic models is the boundary conditions. The static boundary conditions for the soil domain are normally considered fixed which means the nodes are fixed against motion in the direction normal to the boundary plane. This behaviour is implemented to retain the same size of the soil domain during the analysis.

The dynamic boundary conditions for the boundaries of the soil domain are, contrary to the static boundary conditions, viscous. Viscous boundaries absorb the outgoing wave energy produced by a structure inside the soil volume, and the energy is thereby not reflected back towards the structure as a result of the boundaries. This means that viscous boundaries induce the possibility to be able to model the far-field behaviour of the soil domain, and thereby make conditions which simulate an infinite soil domain despite the domain is finite. [Plaxis, 2017b]

5. View and Export Results from Calculations

When the phases of the calculation are defined and the calculation is executed, the results can be displayed or exported into a data file, if requested. A visual investigation of the calculations can be performed in Plaxis Output, which includes several opportunities for the presentation of the results. However, the results can also be exported to a text-file and processed using another software afterwards.

The execution of the numerical models in the following analyses and investigations are performed using the Python wrapper for Plaxis, because this software provides a convenient way to automate the process of assembling the models, performing the calculations and then exporting the desired results afterwards.

10. CONVERGENCE ANALYSIS

In this chapter the convergence analysis of the model developed in Plaxis 3D is presented. The convergence analysis is used to estimate the size of the soil domain and the mesh of the model, and is based on a consideration of a compromise between the computational time and the accuracy of the results obtained from the Plaxis 3D model. In this way, it is ensured that the model supplies results with a sufficient accuracy, while the computational time is within a reasonable time frame.

The following sections consider the procedure of performing the convergence analysis, starting with a brief introduction to the used material model and the considerations behind the execution of the convergence analysis. Following this introduction, the procedure of performing the convergence analysis and the results obtained from it, are explained.

10.1 Set up of Model

In order to obtain reliable results with the four chosen material models, which were introduced in Section 9.3, a convergence analysis should be performed for all of these material models. However, since the procedure of performing these convergence analyses is the same and the computation of these analyses are very time-consuming, only one material model will be considered initially. The Mohr-Coulomb material model has been chosen as the representative material model of the convergence analysis, because this material model provides a good first approximation and supplies a relatively fast computational time compared to the more complex material models. Finally, the convergence analysis will be performed on a soil profile consisting of a single layer of medium dense sand. The input parameters for this medium dense sand, when using the Mohr-Coulomb material model, were presented in Table 9.3 page 116.

The convergence analysis of the model in Plaxis 3D is divided into three main parts. In this section, each of the three parts are briefly introduced. Each part will be elaborated in their respective section. In the first part of the convergence analysis, the range of the applied horizontal load is estimated. This is done to ensure that the convergence analysis is valid for a large span of loads. When a representative load level has been established, the convergence analysis of the soil domain and the mesh size are performed. The convergence analysis of the size of the soil domain is performed by varying the dimensions of the soil domain, e.i. the length, l_x , the width, l_y , and the height, l_z , whereas the convergence analysis of the mesh is performed by varying the mesh size. The convergence analysis is performed on a monopile with a diameter, d , of 8 m and an embedded length, h_{pile} , of 30 m. The symbols and references used for the dimensions of the numerical model are illustrated in Figure 10.1.

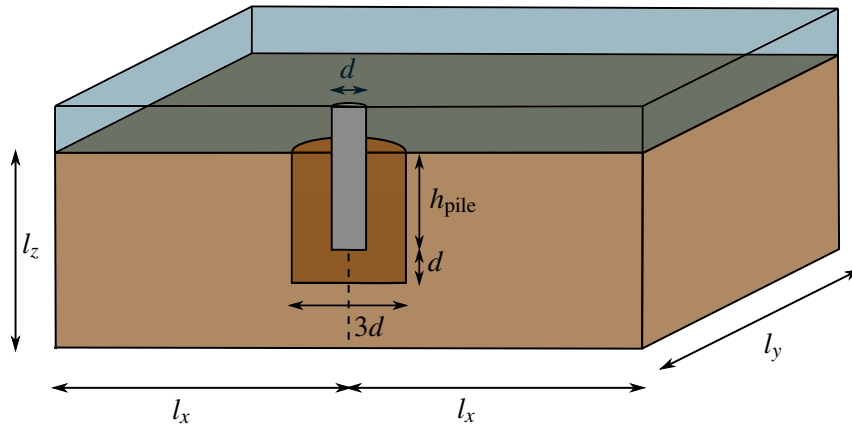


Figure 10.1: Illustration of dimensions and symbols used in the convergence analysis of the soil domain.

In order to obtain comparable results from the convergence analysis of the soil domain, a fixed mesh size is used in all of the analyses. In the convergence analysis, the mesh is defined by two parameters, the size of the global mesh and the coarseness factor. The size of the global mesh is the size of the mesh far away from the monopile, e.i. at the boundaries of the model and towards the monopile. This mesh is applied in the areas of the soil domain where changes in the soil are expected to happen at a slower rate, and it would therefore be advantageous to apply this mesh with a relatively large element size in order to reduce the total number of elements in the model, and thereby reduce the computational time.

Closer to the location of the monopile where changes in the soil domain are expected to be more critical, a refinement of the global mesh size is necessary. This refinement is performed by adjusting the coarseness factor of the soil domain and surfaces in this area. The coarseness factor is expressed in terms of the ratio of the element size in the refined area to the global element size. In this convergence analysis, the mesh is refined by the coarseness factor in the area of the model, which is illustrated in Figure 10.1 by a darker brown colour. Initially, the global mesh size is fixed with an element size of $0.7 d$, where the coarseness factor is set to 0.3. However, the size of the mesh is not of particular interest at this point, because a convergence analysis for the mesh size is performed later.

10.2 Estimation of the Applied Horizontal Load

The first analysis performed prior to the convergence analysis is an estimation of the range for the applied horizontal load. The range of this load is estimated with a wide variability from 1 N to the load provoking a displacement of 10 % of the pile diameter at mudline, because this displacement corresponds to failure of the soil surrounding the pile according to DNV GL group, 2017. At a later stage, a comparison of the API p - y curves and the corresponding p - y curves extracted from the numerical model in Plaxis 3D is performed. The aim is to perform this comparison for displacements varying from very small displacements to displacements close to the failure criteria. The convergence analysis is therefor performed with a load provoking failure, to ensure that the size of the domain and mesh are converged for this load. Figure 10.2 shows an analysis of the load level provoking the aforementioned displacement, where the load-displacement curve of three of the investigated soil domain sizes are illustrated.

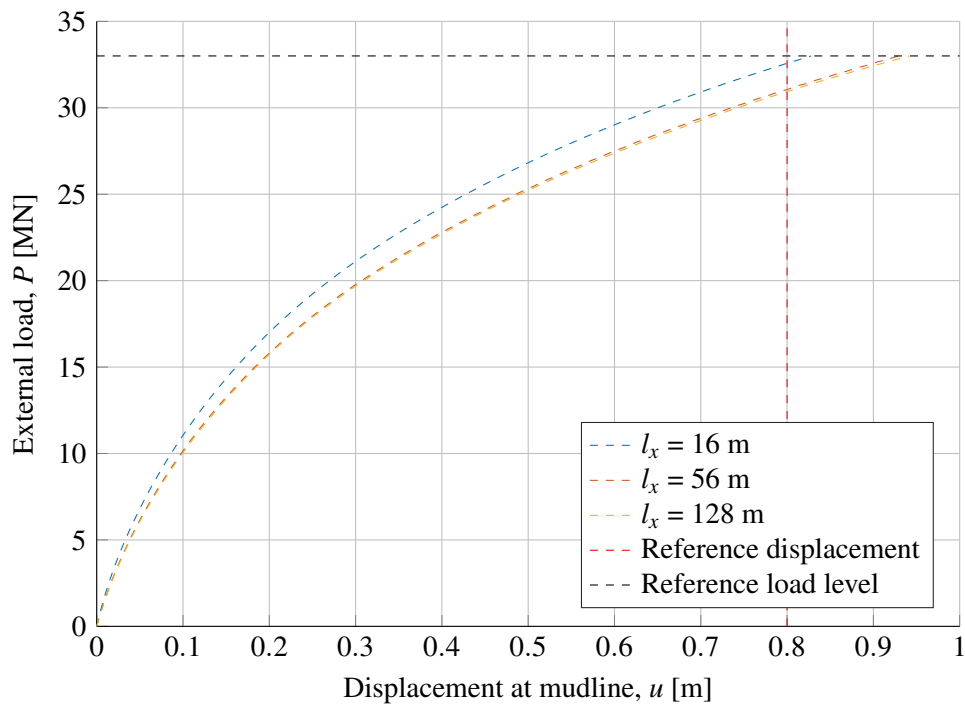


Figure 10.2: Load-displacement curve obtained from the convergence analysis.

From Figure 10.2 it is observed that a horizontal load of 33 MN corresponds to a displacement of at least 0.8 m for all of the presented soil domain sizes, and this load level is therefore used in future convergence analyses. From this it is observed that when the size of the domain is increased, the displacement is also increased. This tendency is as expected, because an increased domain size means that the infinity stiff domain boundaries are moved further away from the monopile, and thereby is affecting it less. The purpose of the convergence analysis of the domain size is mainly to estimate an adequately size of the domain, in order to avoid these effects.

10.3 Convergence Analysis of the Size of the Soil Domain

In order to determine the necessary size of the soil domain, a convergence analysis with different domain sizes is performed. This convergence analysis should be performed iterative for the three dimensions of the soil domain individually, i.e. l_x , l_y and l_z , see Figure 10.1. However, as this procedure would be very time consuming, the convergence analysis of the soil domain is instead performed in two parts. Firstly, a convergence analysis is performed where the length and width of the soil domain are estimated. In this analysis, the height of the soil domain is constant and the length and width are varied equally in order to reduce the number of analyses performed. Finally a convergence analysis of the height of the soil domain is performed. In this analysis the result from the previous analysis is used as the length and width of the soil domain. The analysis and the varied ranges are summarised in Table 10.1.

Table 10.1: Description of the ranges used in the two convergence analyses for the size of the soil domain.
* The length and width of the soil domain are estimated during the first convergence analysis.

Analysis	Varied parameter(s)	Range	Constant parameter(s)	Value
Length and width	l_x, l_y	$2d \leq l_x \leq 14d$ $2d \leq l_y \leq 14d$	l_z	$2h_{\text{pile}}$
Height	l_z	$1.2h_{\text{pile}} \leq l_z \leq 3h_{\text{pile}}$	l_x, l_y	-*

The ranges of the two convergence analyses presented in Table 10.1 are both established with a great variability. This is done in order to see the influence of the location of the domain boundaries according to the location of the monopile.

10.3.1 Convergence Analysis of Length and Width of the Soil Domain

In this section the convergence analysis of the length, l_x , and the width of the soil domain, l_y , is performed. This part of the convergence analysis should be performed by varying the width and the length of the soil domain individually. As mentioned earlier, this would be a very time consuming procedure and instead the analysis is performed by varying both the length and width at the same time, to reduce the number of analyses and thereby the computational time. The length and width of the soil domain are varied according to the ranges presented in Table 10.1.

The convergence of the size of the soil domain is evaluated based on a consideration of the difference between the effective stress-state in the initial phase, before the monopile is installed, and after the load has been applied. This stress difference is then evaluated in points near the vertical domain boundary in the direction of the applied load, i.e. the right-hand vertical domain boundary illustrated in Figure 10.3. If the stress difference approaches zero in these points, it means that the stress state near the boundary is identical to the stress state before the pile was loaded, i.e. that the soil domain is sufficiently large and the boundaries do not have an influence on the results. This convergence analysis is thereby performed by comparing the maximum stress difference between the initial phase and the loading phase, in every single point close to the right-hand vertical domain boundary, see Figure 10.3. The convergence analysis for the length and width of the soil domain is illustrated in Figure 10.4, where the maximum stress difference is normalised against the maximum stress difference in the selected soil domain size.

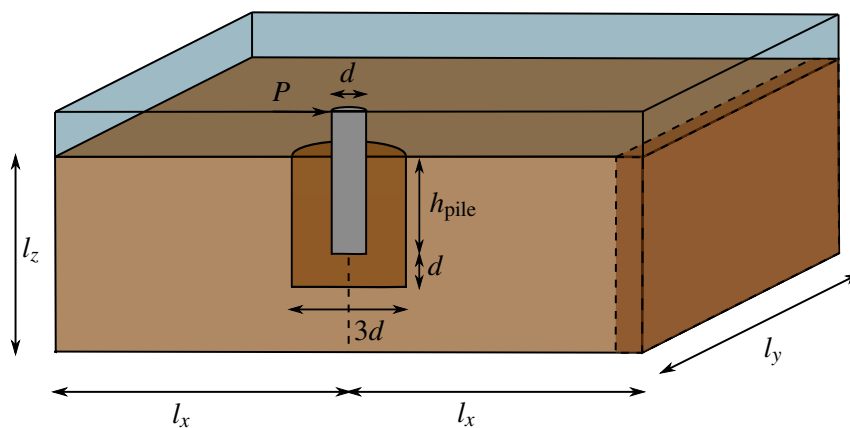


Figure 10.3: Illustration of the area of the domain boundary investigated for the stress difference in the convergence analysis of the length and width of the soil domain.

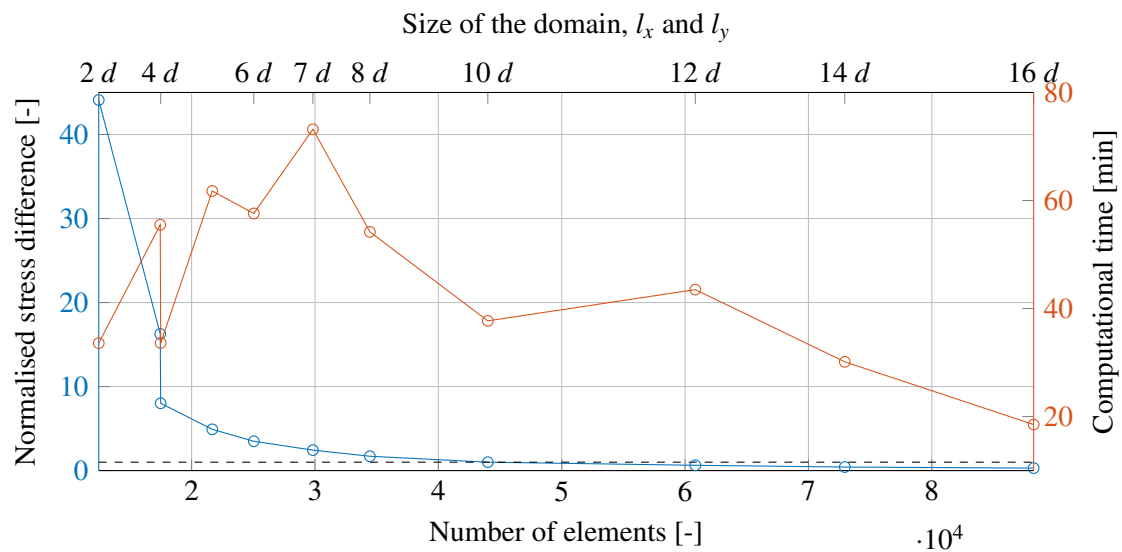


Figure 10.4: Convergence analysis of the length and width of the soil domain. The length, l_x , and the width, l_y , are varied equally i.e. $l_x = l_y$. The stress difference is normalised against the maximum stress difference in the selected soil domain size.

From Figure 10.4 it is observed that the maximum stress difference converges rapidly when increasing the domain length and width in the start. This effect does however decrease as the domain size is increasing. It is also observed that the computational time peaks for a domain length and width around $7 d$, whereas the computational time decreases with an increasing domain size subsequently.

A domain length and width of $10 d$ are selected because this domain size provides a good convergence of the maximum stress difference as well as a relatively low computational time. From the tendency of the maximum stress difference illustrated in Figure 10.4, it is observed that the stress difference is almost fully converged with this domain size, and only a small improvement is gained by increasing the domain size further. From the figure it is also observed that the computational time reaches a local minimum at this domain size. This computational time should however only be regarded as a tendency because the height of the soil domain, l_z , and the size of the meshes are yet to be determined.

10.3.2 Convergence Analysis of the Height of the Soil Domain

In this section the convergence analysis of the height of the soil domain, l_z , is performed. This is done by varying the height according to the range presented in Table 10.1. Equally to the analysis performed for the length and width of the soil domain, the convergence analysis of the height of the soil domain is evaluated based on the maximum stress difference between the initial phase and the loading phase. However, in this analysis the stress difference is evaluated close to the domain boundary at the bottom, see Figure 10.6. The convergence analysis of the height of the soil domain is illustrated in Figure 10.6, where the maximum stress difference is normalised against the maximum stress difference in the selected soil domain boundary.

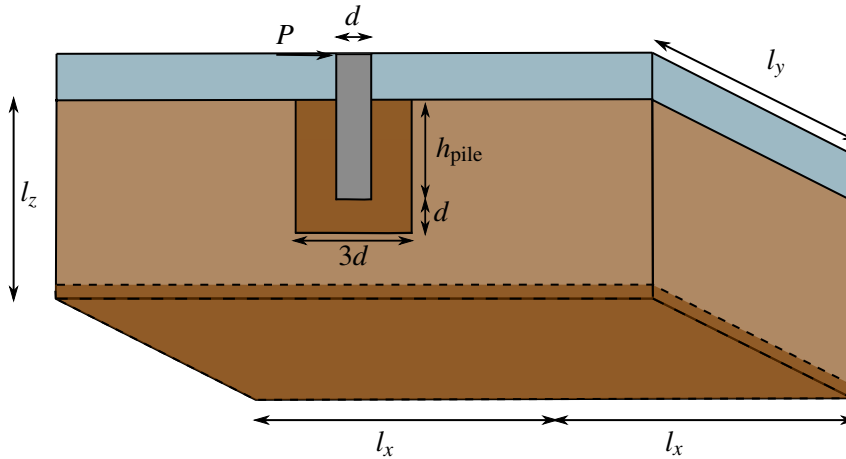


Figure 10.5: Illustration of the area of the domain boundary investigated for stress difference in the convergence analysis of the height of the soil domain.

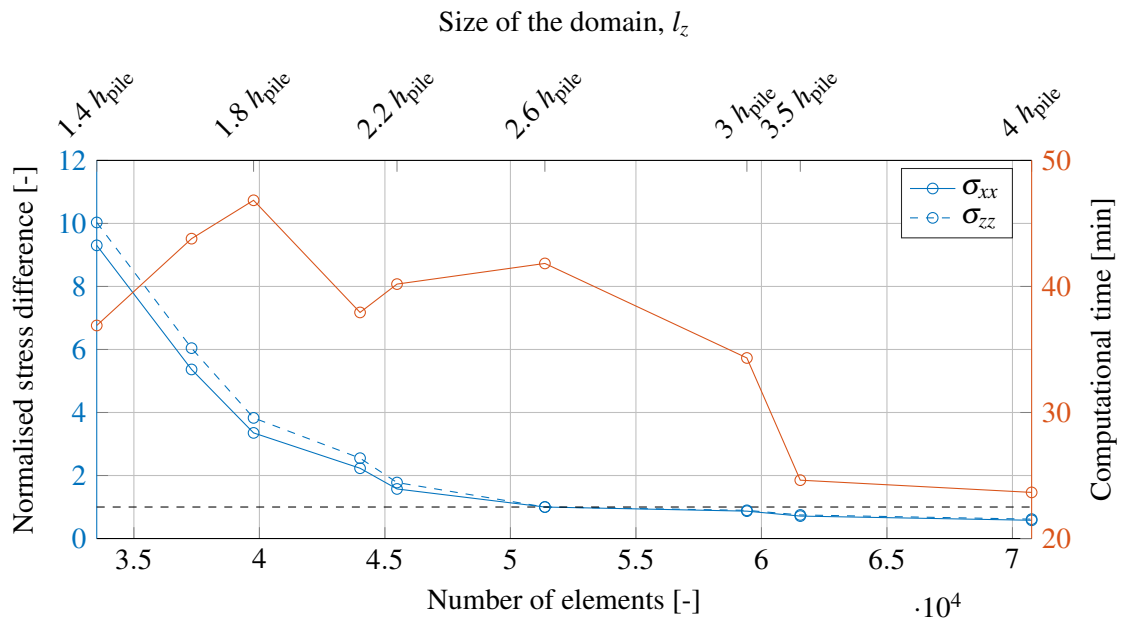


Figure 10.6: Convergence analysis of the height of the soil domain. The stress difference is normalised against the maximum stress difference in the selected soil domain boundary.

From Figure 10.6 it is observed, equally to the convergence analysis of the length and width, that the maximum stress difference converges rapidly with the smaller domain sizes, until a domain size of $2.6 h_{pile}$ is reached. From here the convergence rate decreases and the stress difference stabilise. From the figure it is also observed that the computational time increases until a domain height of $1.8 h_{pile}$ after which the computational time actually decreases.

The tendency of the maximum stress difference is as expected because a bigger domain yields a smaller maximum stress difference. However, the tendency of the computational time is not quite as expected because the computational time decreases as the domain size is increased and thereby the number of elements are increased as well.

A domain height of $2.6 h_{\text{pile}}$ is selected because this domain height provides a good convergence of the maximum stress difference, while limiting the number of elements in the model. By increasing the domain height, only a small improvement is gained, as illustrated in Figure 10.6. According to the figure, the computational time could be reduced by increasing the size of the domain height. However, the computational time illustrated in Figure 10.6 is only a tendency and the convergence analysis of the meshes could potentially have a big influence on this computational time. It is therefor assessed more advantageous to select the lowest converged domain size.

10.4 Convergence Analysis of Mesh Size

In this section the convergence analysis of the mesh is presented. When using Plaxis 3D, the user has the opportunity of generating a mesh according to a certain element size, or according to some relative mesh quality parameters suggested by Plaxis 3D. In this analysis, the opportunity of generating the mesh based on the element size is exploited to generate the global mesh, i.e. the mesh far away from the monopile, since this option yields better mesh control. Additionally to the global mesh, Plaxis 3D provides the opportunity to either coarsen or refine the mesh around the considered structure. This coarseness factor is applied to the surfaces of the monopile below mudline, and the soil surrounding the monopile within a distance of one diameter of the monopile. This soil was illustrated in Figure 10.1 page 124 as the dark soil near the monopile. The convergence analysis of the mesh is thereby dependent on the following two parameters:

- The global element size, which is the size of the elements far away from the structure
- The coarseness factor which is the ratio of the global element size to the refined element size

Ideally, the convergence analysis of the mesh should be performed as an iterative process between the analysis of the global element size and the coarseness factor. However, since this would be a very time-consuming process, an analysis for each of the above mentioned parameters is only performed once, assuming that this yields a sufficient impression of the effects from the global element size and the coarseness factor. The ranges used in the convergence analysis of the mesh are presented in Table 10.2.

Table 10.2: Description of the ranges used in the convergence analysis for the mesh. $l_{\text{ele,global}}$: size of global element. C_F : Coarseness factor. * The global element size is estimated during the convergence analysis.

Analysis	Varied parameter	Range	Constant parameter	Value
Global element size	$l_{\text{ele,global}}$	$0.25 d \leq l_{\text{ele,global}} \leq 2 d$	C_F	0.3
Coarseness factor	C_F	$0.2 \leq C_F \leq 1$	$l_{\text{ele,global}}$	-*

10.4.1 Convergence Analysis of the Global Mesh Size

The convergence analysis of the size of the global mesh is performed by varying the global mesh according to the range presented in Table 10.2, where the coarseness factor remains constant. The estimation of the size of the global mesh is performed based on the displacement at mudline in the direction of the applied load. The convergence analysis is illustrated in Figure 10.7 where

the displacement at mudline is normalised against the displacement at mudline obtained with the selected global mesh size.

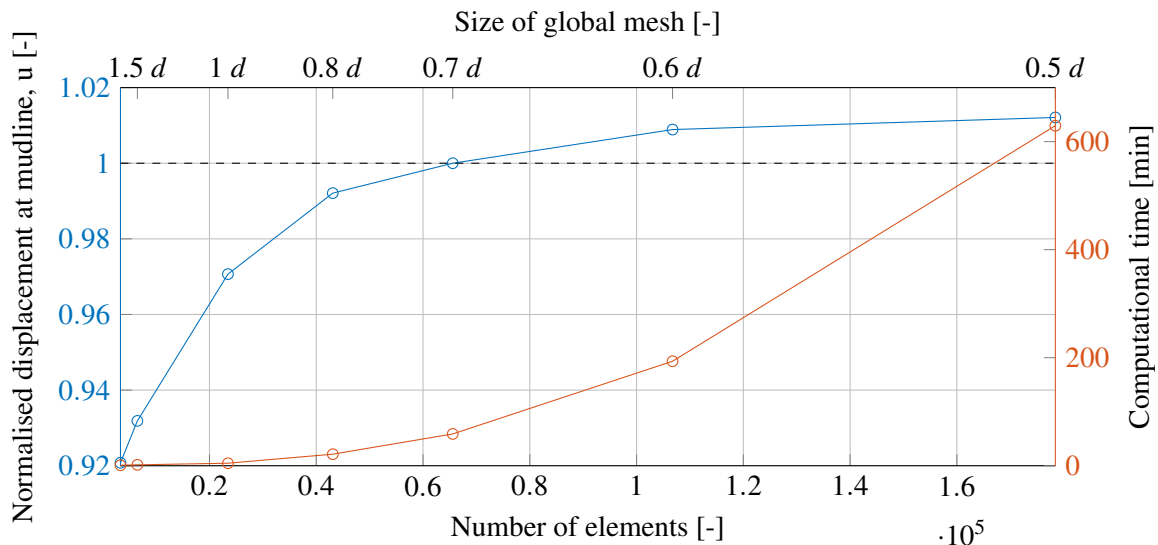


Figure 10.7: Convergence analysis of the size of the global mesh.

From Figure 10.7 a positive correlation between the computational time and the number of elements is observed. This tendency is as expected, because an increase of the number of element yields an increased number of calculations for each step in the model. This does however mean that the convergence analysis should be assessed by considering a compromise between the convergence of the displacement at mudline and the computational time, in order to avoid an unnecessary high computational time.

A global mesh size of $0.7 d$ is selected, which is identical to the mesh size used initially in the convergence analysis of the domain size. This mesh size is selected because this mesh size provides an acceptable compromise between the computational time and the convergence of the displacement at mudline. From the figure it can be seen that by decreasing the size of the global mesh, an increase in the displacement at mudline is obtained. However, this would also yield a threefold of the computational time, or even more. Therefore it is assessed to be more advantageous to retain a coarser global mesh, and then lower the coarseness factor applied to the soil surrounding the monopile. This assessment is based on the expectation that a refinement of the soil surrounding the monopile will have a greater effect on the convergence of the displacement, while the total number of elements are remained low due to the size of the global mesh.

10.4.2 Convergence Analysis of the Refined Mesh Size

The convergence analysis of the size of the refined mesh surrounding the monopile is performed by varying the coarseness factor according to the range presented in Table 10.2, while the global mesh size remains at a value of $0.7 d$. The convergence analysis is illustrated in Figure 10.8, where the displacement at mudline is normalised against the displacement at mudline obtained with the selected coarseness factor.

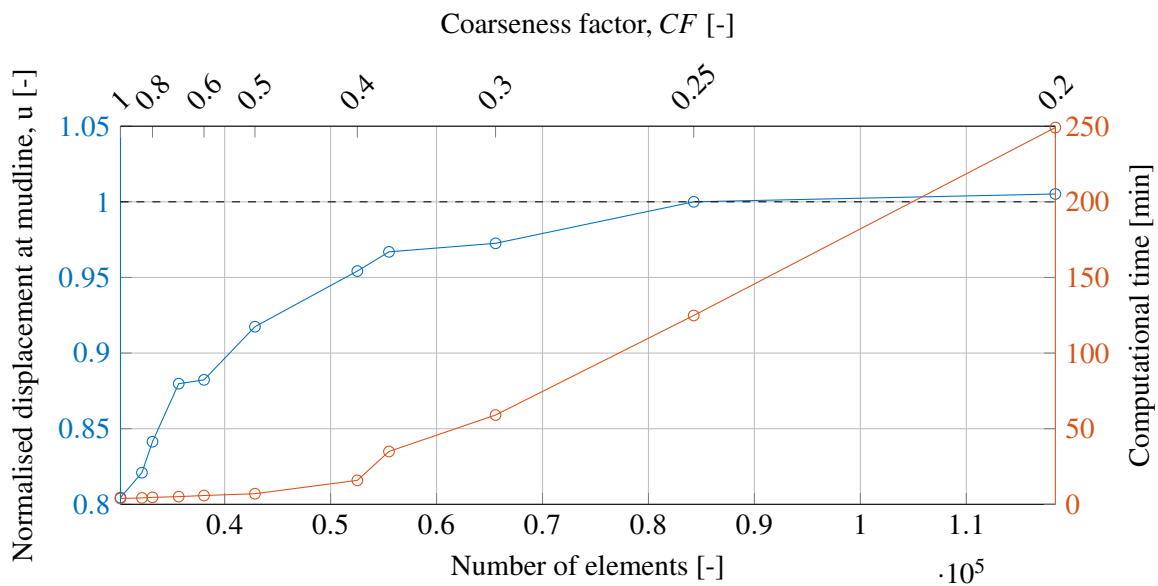


Figure 10.8: Convergence analysis of the refined mesh.

From Figure 10.8 a positive correlation between the computation time and the number of elements can be seen. Equally to the convergence analysis of the global mesh size, it is observed that when the number of elements is increased, the computational time is increased as well. This means that the convergence analysis of the refined mesh size should be based on both the convergence of the displacement at mudline as well as the computational time. However, since this refined mesh is expected to have a great influence on the displacement of the monopile, the convergence of the displacement should be considered with great importance.

A coarseness factor of 0.25 is selected because this coarseness factor provides a good correlation between the essential convergence of the displacement and the computational time. A minor increase in the displacement is gained if the coarseness factor is decreased to 0.2. This would however double the computational time and is therefore assessed not to be essential. From Figure 10.8 it is observed that the displacement does converge, and a refinement of the global mesh size is therefore not necessary even though the displacement did not convergence fully in the convergence analysis of the global mesh, see Figure 10.7.

10.5 Conclusion on the Convergence Analysis

This concludes the convergence analysis of the numerical model performed in Plaxis 3D. The convergence analysis was performed to estimate the dimensions of the soil domain and the mesh size in order to ensure that the numerical model supplies results with a sufficient accuracy, while the computational time is within a reasonable time frame. The dimensions determined through the convergence analysis are presented in Figure 10.9.

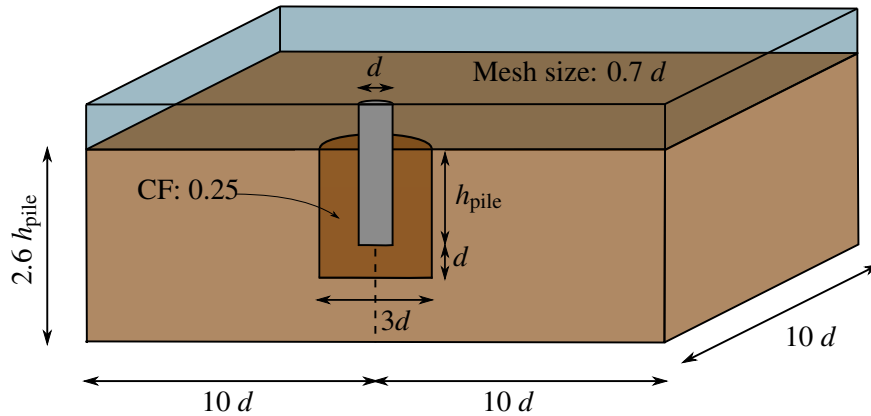


Figure 10.9: Illustration of dimensions obtained through the convergence analysis of the soil domain.

The convergence analysis was performed with the Mohr-Coulomb material model, but the results are assumed to be applicable for other material models as well. To be sure about this assumption, a convergence analysis for each of the other material models should also be performed. As mentioned earlier, this procedure would be very time consuming and will therefore not be performed.

However, during the implementation of the dynamic models in Plaxis 3D, which is presented in Chapter 11, the extend of a dynamic model computational-wise is discovered. The external load applied in the dynamic models is very small compared to the load applied during the above-described convergence analysis. An additional convergence analysis is therefore performed because this reduced load-level could be a source of decreasing the domain size and thereby also reduce the computational time of the models. This convergence analysis was performed using the Hardening Soil Small-strain material model, because this material model is expected to yield the most realistic response of the OWT. This analysis is performed by following the same procedure as the above-described convergence analysis and will not be described here, but is presented in Appendix K.

The convergence analysis is performed based on the dimensions of the monopile in consideration, e.i. the diameter, d , and the embedded pile length, h_{pile} . This is done in order to use the determined dimensions of the soil volume and the mesh for other diameters of the monopile and embedded pile lengths. In order to verify that these dimensions of domain and mesh are applicable for other combinations of diameter and embedded pile length, multiple test should be performed. The procedure for these tests would be similar to the convergence analysis presented in this chapter but would however be a very time consuming procedure. Therefore it is assumed that the dimensions of the soil domain and mesh obtained through the convergence analysis are applicable for other combinations of diameter and embedded pile length.

11. FREE VIBRATION ANALYSIS

The purpose of the free vibration analysis is to determine the first eigenfrequency of an OWT supported by a monopile. In order to determine eigenfrequencies in Plaxis 3D, a free vibration is provoked. The free vibration is caused by a horizontal point load, that is located at the top plate of the model. The load is applied in steps, and when a desired value is reached, the load is removed and the tower is allowed to oscillate freely. These oscillations are then used to estimate the first eigenfrequency of the system, by using a Fast Fourier Transformation (FFT). How this analysis is exactly performed is explained thoroughly in the following sections.

For the free vibration analysis the four material models introduced in Section 9.3 are employed in order to estimate their applicability in this specific problem. All four material models are employed in the free vibration problem using two different magnitudes of the point load, 2 MN and 3 MN respectively.

11.1 Set up of Model

The general composition of the model used in this analysis is similar to the model described in Section 9.4. The geometry of the model is presented in Table 11.1.

Table 11.1: Geometric input for the Plaxis 3D model. The mean water level is measured positive upwards from the mudline.

Height [m]	Diameter [m]	Wall thickness [cm]	Pile length [m]	Mean water level [m]
161	8	10	30	15

In the free vibration analysis the displacement of the structure is caused by a horizontal point load, P_x , and the weight of the nacelle, hub and blades is mimicked by adjusting the density of the top of the cylinder, so that it is equal to the mass of the nacelle, hub and blades, see Figure 11.1. For the first free vibration analyses performed, the mass from the nacelle, the hub and the blades was modelled differently. Initially this mass was modelled as a vertical point load, P_z , applied on the rigid plate on the top of the structure, see Figure 11.2. However, the eigenfrequencies obtained from these analyses turned out to be higher than expected, and the modelling of point loads in Plaxis 3D was therefore further investigated. From this point, the mass was modelled as illustrated in Figure 11.1, where the mass is introduced by adjusting the density of the top of the structure.

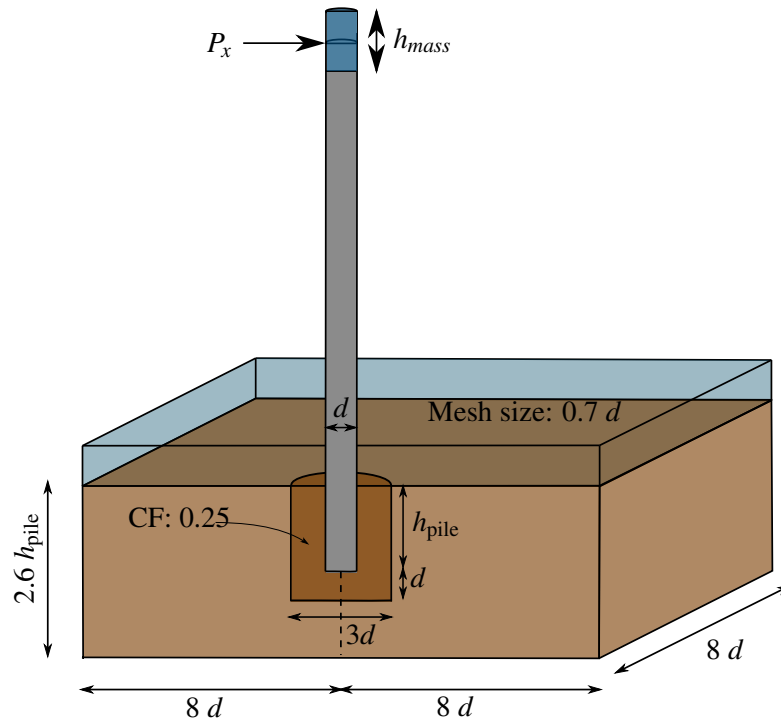


Figure 11.1: Illustration of the location of the horizontal load and the extra mass in the 3D model. The location of the increased density is the highlighted blue top part of the tower, which is centred around the point load and has a height, h_{mass} , of 5 m.

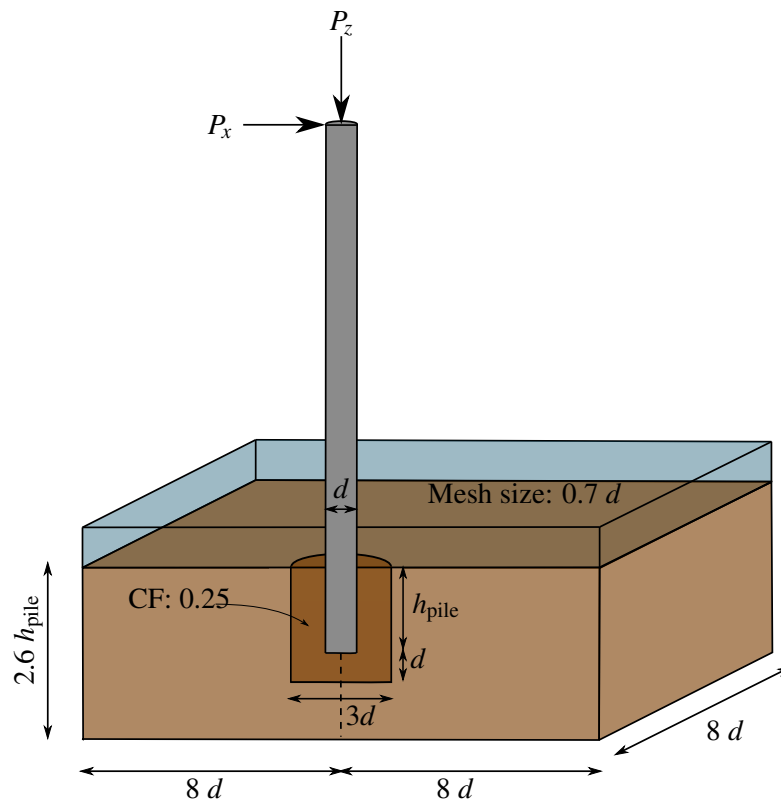


Figure 11.2: Illustration of the locations of the horizontal- and vertical load in the 3D model.

This change of procedure happened relatively late in this thesis, and the majority of the results obtained from the free vibration analysis are therefore obtained from the model configuration illustrated in Figure 11.2. As dynamic calculations are very time consuming, only two free vibration analyses were performed with the new updated configuration of the model, see Figure 11.1. These two analyses were performed using the Mohr-Coulomb and the Hardening Soil Small-strain material models, both subjected to a horizontal point load of 3 MN.

The results obtained from the model configuration presented in Figure 11.2 are however used to investigate the affects of the different material models, because these results are obtained from similar model configurations and are thereby comparable. The results obtained from the new and updated model configuration presented in Figure 11.1 are presented in the end of the chapter where they are compared to the rest of the results obtained. From this comparison the effects of adding the mass at the top of the structure can be evaluated in regards to the first eigenfrequency of the system.

Common to all of the calculation performed in the free vibration analysis is that the response of the structure is logged in 6 pre-selected nodes of the tower wall. The output from Plaxis 3D will be from the nodes located the closest to the locations illustrated in Figure 11.3. The scatter of these points are selected in order to observe the response in different points along the OWT tower. The output from Plaxis 3D is logged with a frequency of 250 Hz.

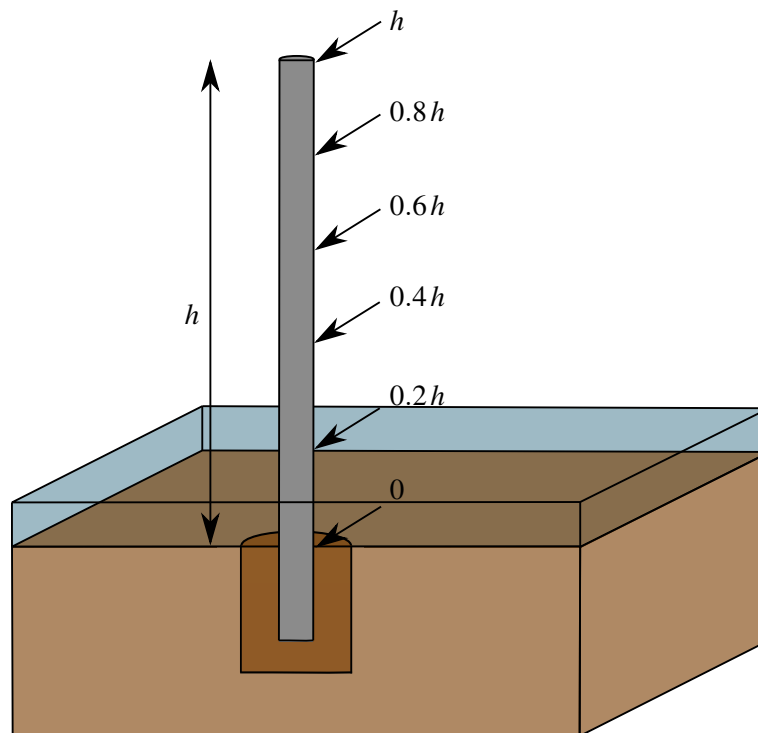
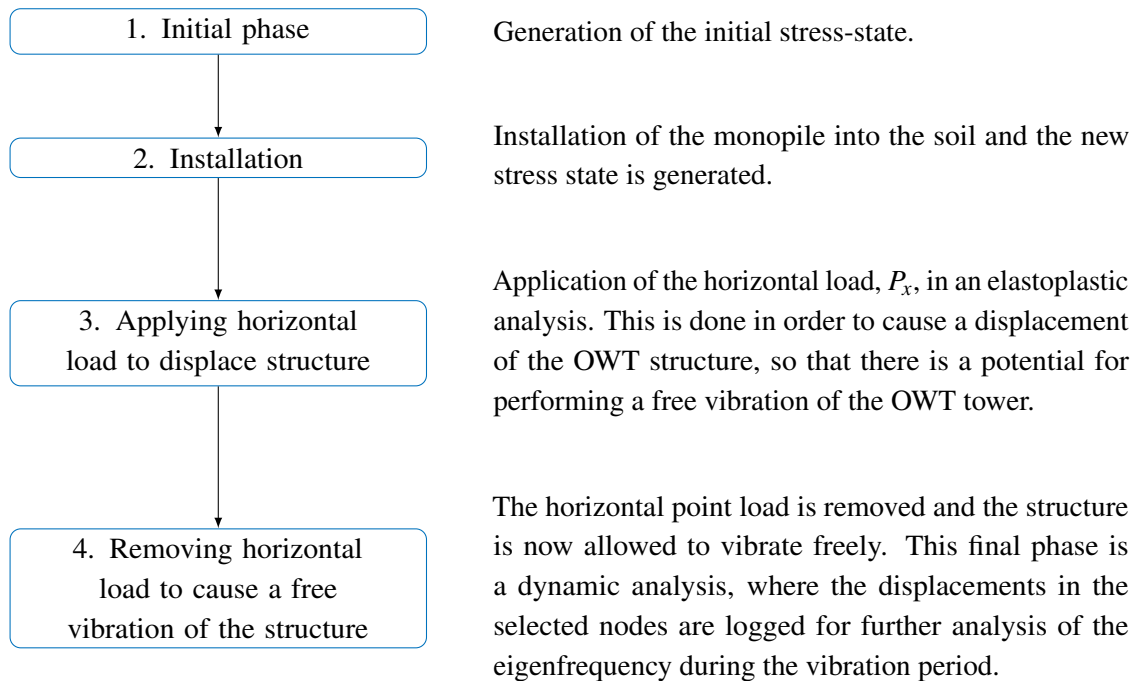


Figure 11.3: Illustration of the extraction points for curve results.

The phases used in Plaxis 3D for the free vibration analysis are described in the following flowchart. The final stage is a dynamic analysis performed using time integration during the vibration period, the time integration used in Plaxis 3D is introduced in Appendix J.3.



11.2 Analysis of Calculation Results

The results from the Plaxis 3D models are extracted in the form of multiple time series where the displacements of the selected points at the cylinder structure are considered. By the use of a FFT, the obtained results are transferred from the time domain to the frequency domain, in order to estimate the first eigenfrequency of the structure. The application of the FFT will not be covered in this chapter, but is further commented on in Appendix L.1.

As mentioned earlier, the free vibration analysis is very time consuming, where the majority of the calculation time is due to the tower is allowed to vibrate freely, while logging displacements and time. When the structure is allowed to vibrate longer, the obtained results off the FFT will become more precise. However, an increase of the signal length also increases the computational time of the model. To find an acceptable signal length, a convergence analysis is performed using a Mohr-Coulomb material model and a free vibration time of 60 seconds. The results from this analysis are presented in the following section.

11.2.1 Convergence Analysis on the Signal Length

Figure 11.4 illustrates the change of the first eigenfrequency according to the signal length of the time-displacement series. The eigenfrequency in the figure is normalised according to the eigenfrequency found using a 40 seconds signal, as this signal length is considered as acceptable from the figure. In the ideal world it would be preferred to have a longer signal length, but as the dynamic calculations are very time consuming, it is chosen to continue using signals with the length of 40 seconds through the rest of this chapter.

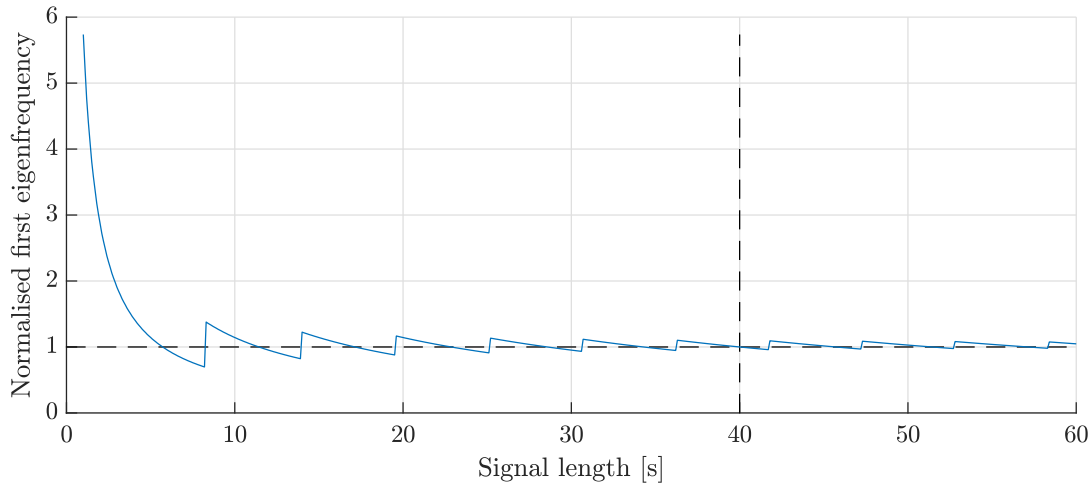


Figure 11.4: Convergence analysis investigating the necessary signal length for the FFT. The displacement signal is obtained using a Mohr-Coulomb material model and a horizontal point load, P_x , of 3 MN.

The convergence analysis indicates that the first eigenfrequency converges as the length of the signal is increased, but periodic changes with decreasing amplitudes are observed. The number of sudden changes in the convergence analysis corresponds with the number of periods, for which the cylinder oscillate. The change could be an affect by the signal cut, where a new period of the oscillation is entered. This explains the decreasing amplitude of the change, as one new entered period will correspond to a smaller part of the total signal, and thereby has a smaller influence at the obtained eigenfrequency.

The effects of using a longer signal and how the first eigenfrequency is becoming more well defined as the signal length is increased, are illustrated in Figure 11.5. Here the difference of using 10, 20, 30 and 40 seconds of data is illustrated in the frequency domain. In the figure, the magnitude of the signal is normalized for an easier comparison, as the signal magnitude is not of particular interest in the estimation of the first eigenfrequency, but the location of the first eigenfrequency is.

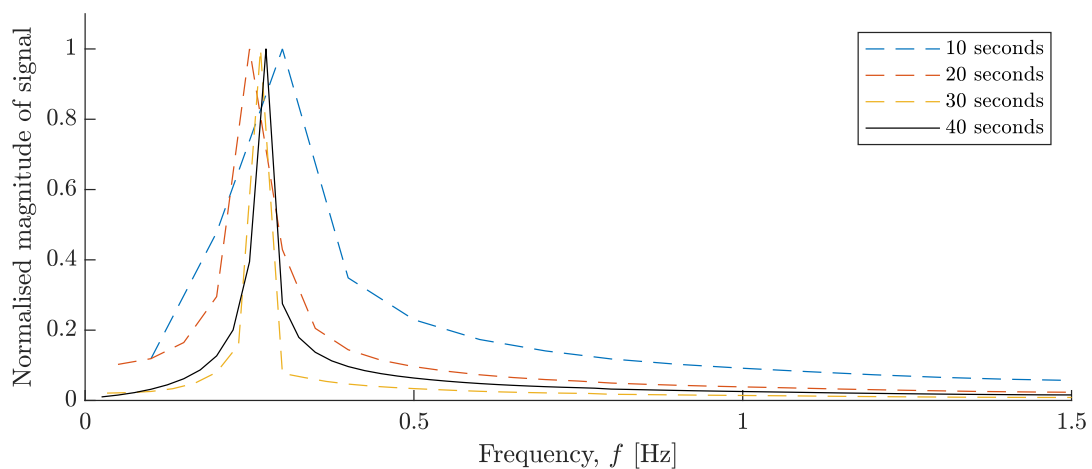


Figure 11.5: Results from observing the difference in the frequency domain, as the signal length is varied. This analysed signal is obtained using a Hardening Soil Small-strain material model and a horizontal point load, P_x , of 3 MN.

11.2.2 Data Extracted from Model

An example of the time-displacement curves extracted from Plaxis 3D in the pre-selected output nodes is presented in Figure 11.6. This figure illustrates how the structure is oscillating from side to side, as the horizontal point load is removed in the final phase of the Plaxis 3D analysis.

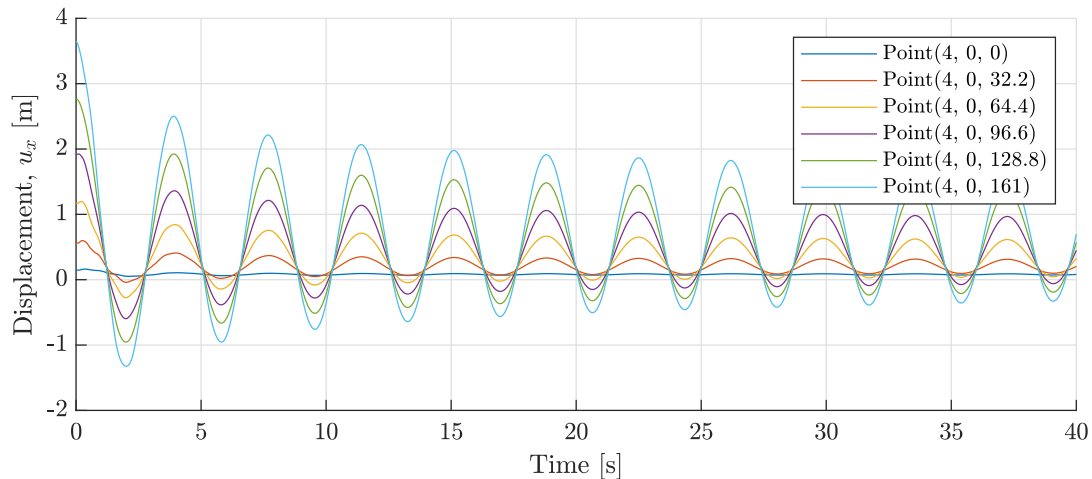


Figure 11.6: Changing displacement over time obtained by using the Hardening Soil Small-strain material model and a horizontal point load, P_x , of 3 MN.

These time-displacement signals are extracted for all presented material models i.e. Linear-Elastic, Mohr-Coulomb, Hardening Soil and Hardening Soil Small-strain. The time-displacement signals of these can be found in Appendix L.2. In this appendix load-displacement curves are found for free vibrations caused by a point load of 2 MN and 3 MN. The different loads are applied to observe if there is any significant change in the eigenfrequency, when increasing the horizontal load of 2 MN by 50 % to 3 MN. This is mainly to observe the behaviour of the Hardening Soil material models, as these models introduce the shear degradation behaviour of soil.

The time-displacement response at the top of the model for each material model are illustrated in Figure 11.7. Here it is observed that even though the same reference soil profile is used for all material models, the number of input parameters that goes into the different models affect the response significantly. Using the Linear-Elastic material model in this case causes the smallest displacement of the tower. This is due to the fact that the material will not yield at any point. The Mohr-Coulomb material model has the highest displacement as the material will yield at a certain stress causing larger deformations than the Hardening Soil material models, where the strain-stress path is stress dependent. The Hardening Soil Small-strain material model has a smaller deformation than the Hardening Soil material model, as the model includes small-strain stiffness as mentioned earlier.

From the time-displacement signals in Figure 11.7, it is also observed that the Linear-Elastic material model oscillated around zero. This behaviour is as expected when the model behaves linearly elastic. The results obtained by using the Mohr-Coulomb material model show that plastic strains occur when the pile is horizontally loaded, and the displacement signal obtained from this model is therefore offset in the direction of the horizontal point load. The time-displacement signals from the Hardening Soil material models have an even larger offset according to the zero line,

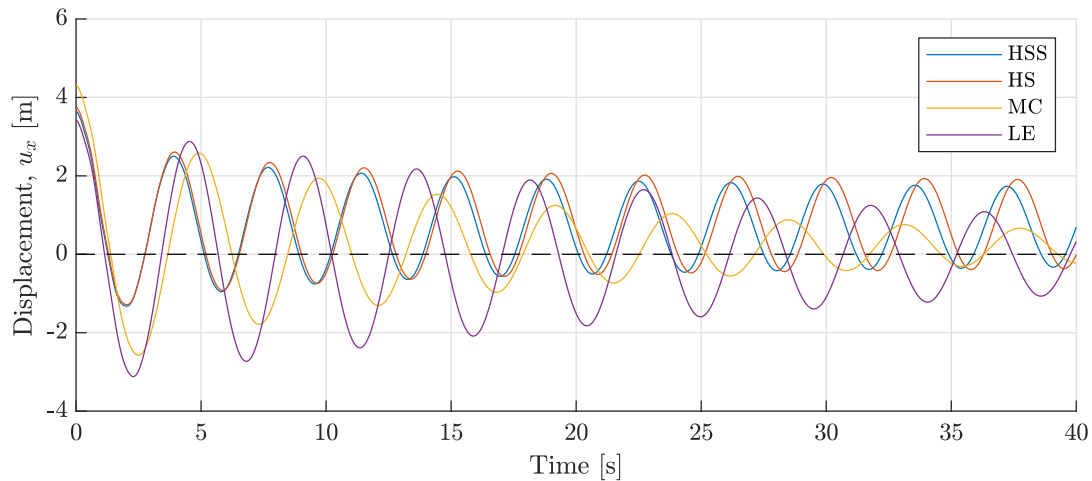


Figure 11.7: Comparison of the displacements over time in the height of the horizontal load, P_x . The location of P_x was seen in Figure 11.2.

compared to the Mohr-Coulomb material model. This is due to the fact that these models beyond plasticity includes a stress dependent stiffness, meaning that the shear modulus will degrade more where it has been exposed to a larger shear force.

11.2.3 Eigenfrequency Analysis

The eigenfrequency is estimated by transferring the time-displacement signals, extracted from the Plaxis 3D models, into the frequency domain using a FFT in MATLAB. The theory behind the FFT is elaborated in Appendix L.1.

FFTs have been performed on all of the extracted time-displacement signals presented above. An example of a time-displacement signal transformed to the frequency domain is presented in Figure 11.8. The rest of the FFTs can be found in Appendix L.3.

Figure 11.8 has a decent peak that illustrates the location of the first eigenfrequency for the model, using the Hardening Soil Small-strain material model. The eigenfrequency is taken as the peak of the spectrum in the frequency domain and has the value of 0.275 Hz which is also illustrated in the figure. Using the Extended Model developed in Stage 3 Chapter 6, to solve the eigenfrequency for the same system, the first eigenfrequency is estimated to 0.189 Hz, which is significantly lower than the eigenfrequency extracted from the Plaxis 3D model. The difference between these results is elaborated in Section 11.3. The eigenfrequencies obtained by using the four different material models, and the two different load-levels of 2 MN and 3 MN respectively are presented in Table 11.2. Here it is seen that varying the load from 2-3 MN does not affect the first eigenfrequency of the system. There is a small change in the eigenfrequency when observing the results from the Mohr-Coulomb material model. However this difference seems to have occurred because of a lack of data, as the Mohr-Coulomb spectrum illustrated in Appendix L.3 does not have a significant peak, and this peak could have been more significant if a longer time series had been generated.

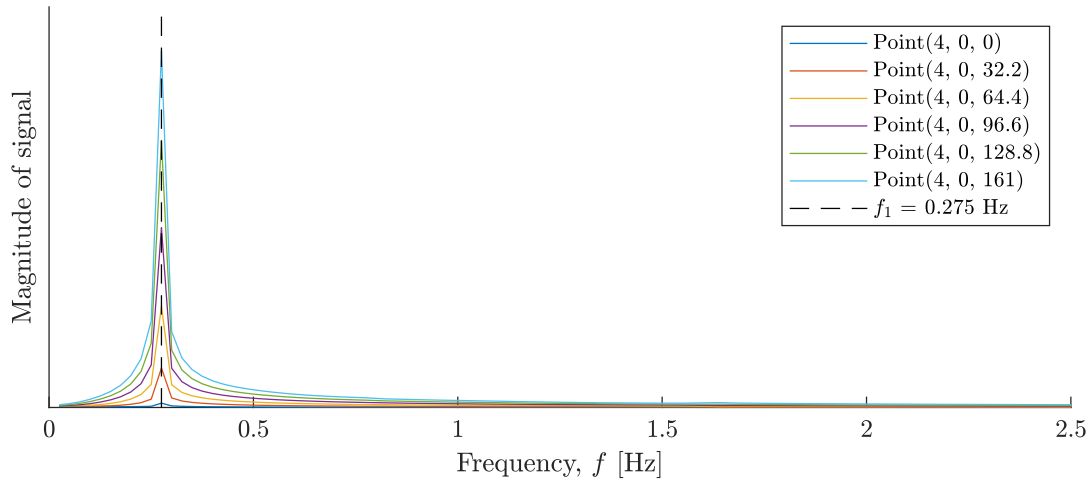


Figure 11.8: Results of the FFT performed on the displacement signal obtained by using the Hardening Soil Small-strain material model and a horizontal point load, P_x , of 3 MN.

Table 11.2: Results of the different free vibration analysis in form of the first eigenfrequency.

Load, P_x	[MN]	Linear-Elastic		Mohr-Coulomb		Hardening Soil		HS Small-strain	
		2	3	2	3	2	3	2	3
First eigenfrequency, f_1	[Hz]	0.225	0.225	0.225	0.2125	0.275	0.275	0.275	0.275

If the small divergence in the Mohr-Coulomb results is disregarded, it is observed that the Linear-Elastic material model and the Mohr-Coulomb material model provide the same eigenfrequency when performing a free vibration analysis. This is due to the fact that both models use the same input parameters to describe the stiffness of soil. The same goes for the Hardening Soil and Hardening Soil Small-strain material model. These models use the same stiffness parameters for loading and unloading/reloading. The only difference in the stiffness of the Hardening Soil Small-strain material model is, that the model includes the small strain stiffness, which does not seem to affect the results significantly when the eigenfrequency is found by a free vibration analysis.

11.3 Closure of the Free Vibration Analysis

When performing a free vibration analysis to obtain the first eigenfrequency of an OWT in Plaxis 3D, it is important to apply a material model that provides a sufficient level of functionality. From the analyses performed in this chapter, it is observed that the results obtained from both the Linear-Elastic and the Mohr-Coulomb material models with their relative simple input parameters do not converge with the results from the more advanced Hardening Soil material models. In this case the Hardening Soil material model is just as sufficient as the Hardening Soil Small-strain material model with respect to the estimation of the first eigenfrequency. During the analyses it was observed that the Hardening Soil Small-strain material model is more time consuming compared to the Hardening Soil material model, and the latter it thereby a better choice for the estimation of the first eigenfrequency. In Figure 11.9 time-displacement signals for Hardening Soil and Hardening Soil Small-strain material models under identical circumstances are presented. Here it is observed

that there is a tiny change in the length of the periods in the signal, as the Hardening Soil material model results in larger periods. This change is though not something which is visible in the results obtained from the FFT in MATLAB when using 250 Hz signals.

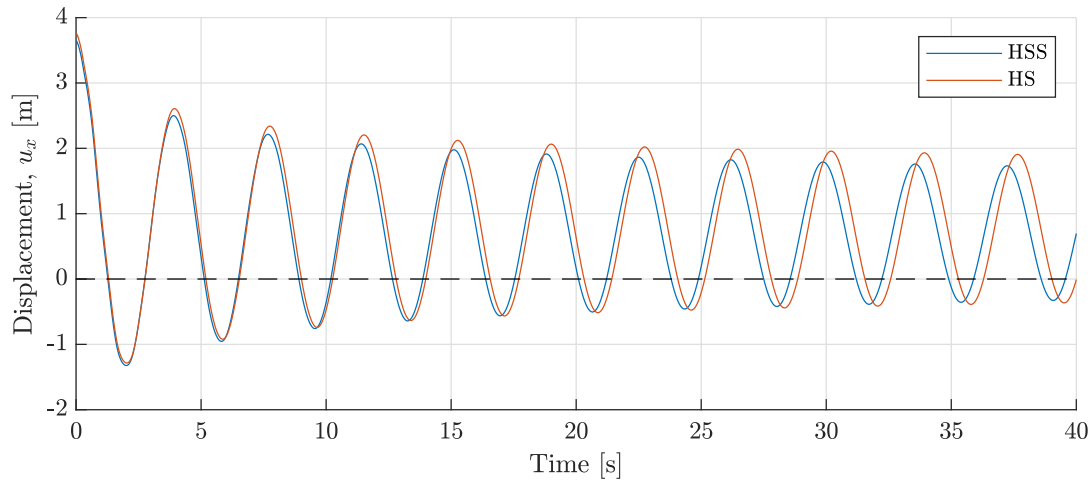


Figure 11.9: Comparison of the displacement over time signals for Hardening Soil and Hardening Soil Small-strain material models.

From the analysis of the first eigenfrequency, see Table 11.2, it was observed that the first eigenfrequency obtained by using the Hardening Soil and Hardening Soil Small-strain material models are identical. This means that when only an analysis of the first eigenfrequency is considered, the Hardening Soil material model yields the same level of accuracy as the Hardening Soil Small-strain material model, and that the advantage of the shorter computation time for the Hardening Soil material model can be exploited. However, when considering the response of the system in regards to the displacement signal, see Figure 11.9, it is observed that the Hardening Soil Small-strain material model is superior to the Hardening soil material model for fatigue calculations, as the hysteretic damping in the soil is included in the material model. In the figure, this behaviour is illustrated from the difference between the response obtained using the two material models, where it can be seen that the response obtained from the Hardening Soil Small-strain material model dampens earlier than the Hardening Soil material model, where only structural damping is present.

As mentioned there is a quite large divergence in the results obtained by the Plaxis 3D model and the Extended Model which is using the p - y curves provided by API, when using the same reference soil profile. This supports the subjects discussed in Stage 3 about the lack of input parameters in the API p - y curves. When using the API p - y curves, the soil-structure stiffness is only described by the effective angle of internal friction, ϕ' , where the more advanced material models in Plaxis 3D include different stiffness parameters in situations where the soil is being etc. loaded or unloaded/reloaded. The results of using the p - y curves with the same reference soil profile, the same horizontal load and the same dimensions of the structure as used here in Stage 4, can be seen in Appendix L.4. The Extended Model estimates the first eigenfrequency to become 0.189 Hz. As mentioned, this is a quite large underestimation compared to the eigenfrequencies calculated using Plaxis 3D, which are listed in Table 11.2. Modelling the mass using the up-scaled density instead of the point-load on a vertical plate on top of the pile, results in a decreased eigenfrequency. Only

two calculations with the more correct approach of modelling the mass are available and these are seen in Figure 11.10 and 11.11.

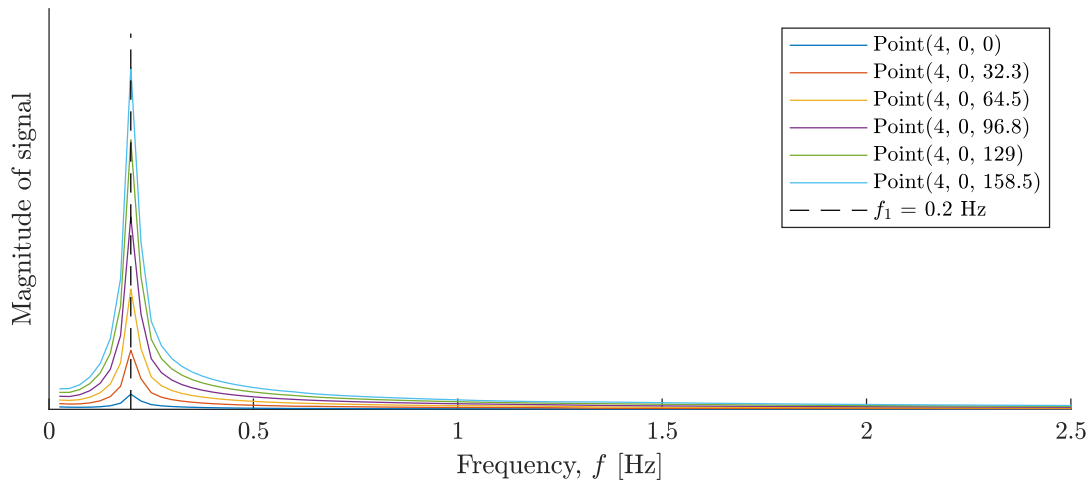


Figure 11.10: Results of the FFT performed on the displacement signal obtained by using the Mohr-Coulomb material model and a horizontal point load, P_x of 3 MN, including the extra mass at top of the modelled OWT.

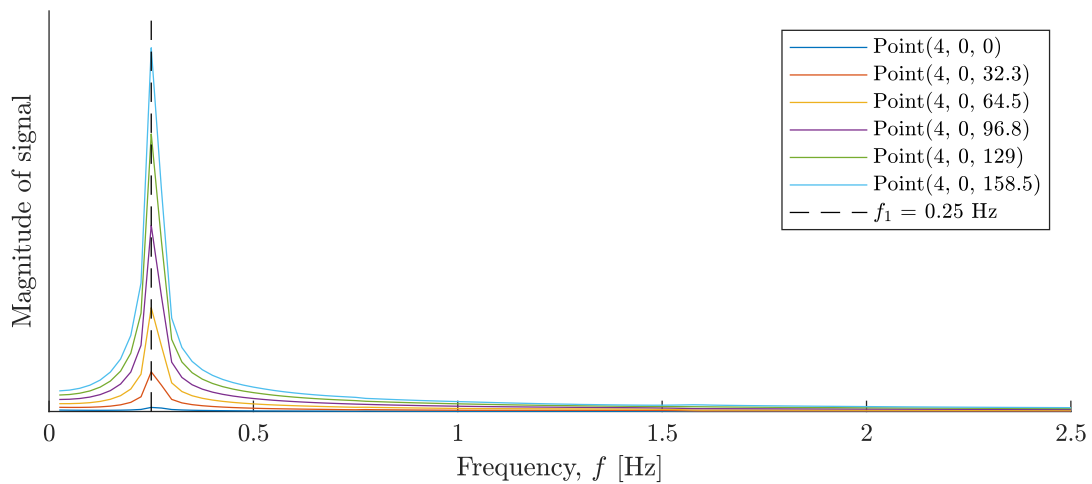


Figure 11.11: Results of the FFT performed on the displacement signal obtained by using the Hardening Soil material model and a horizontal point load, P_x , of 3 MN, including the extra mass at top of the modelled OWT.

From Figure 11.10 and 11.11 it is observed that the eigenfrequency is decreased by 0.025 Hz for both models, when compared to the results listed in Table 11.2. Even with the improved approach of modelling the mass on top of the OWT, there is still a large divergence between the eigenfrequency obtained using the Extended Model from Stage 3 and the free vibration analysis using the Hardening Soil material model in Stage 4. This supports the conclusion of the p - y curves in Stage 3, that the input parameters for the API p - y curves are not sufficient to replicate the behaviour of a more detailed material model, such as the Hardening Soil material model, when designing large diameter monopiles.

12. EXTRACTION OF p - y CURVES

In this chapter, a comparison of the API p - y curves and the corresponding curves extracted from Plaxis 3D is performed. In Stage 3, the application of the p - y curves was investigated. This investigation indicated that the current formulation of the p - y curves might be unsuited for the design of large diameter monopiles. In the discussion of the API p - y curves presented in Section 6.6, it was concluded that the API p - y curves are underestimating the initial soil-structure stiffness and overestimates the soil-structure stiffness for extreme loads, when employed for large diameter monopiles. The purpose of the comparison performed in this chapter is therefore to illustrate the difference between the API p - y curves and the corresponding p - y curves extracted from Plaxis 3D when analysing a large diameter monopile. The analysis in the following sections will be based on a monopile with a diameter of 8 m, which is the diameter of the monopile analysed in Stage 3 and 4 in this thesis.

The extraction of p - y curves from Plaxis 3D is however not straightforward. As mentioned in the convergence analysis of the domain- and mesh size, see Chapter 10, the mesh of a Plaxis 3D model is governed by the global mesh size, i.e. the mesh size far away from the analysed structure, and the coarseness factor, which defines the refinement of the mesh close to the analysed structure. This means that the mesh generation is rather random, and that the locations of nodes and Gauss-points are likewise. This makes the extraction of the p - y curves from the Plaxis 3D model complicated, and a few additional steps and calculations are therefore necessary.

In the following sections the procedure of extracting p - y curves from Plaxis 3D is explained, starting with a brief introduction to the composition of the model, and differences compared to the previous Plaxis 3D models. Following this introduction, the principles of extracting the p - y curves from Plaxis 3D are explained. Finally, the p - y curves extracted from Plaxis 3D using the Mohr-Coulomb and Hardening Soil Small-strain material models presented in Section 9.3 are compared to the API p - y curves. The Mohr Coulomb material model is selected because this material model is expected to behave most like the API p - y curves whereas the Hardening Soil Small-strain material model is selected because it is the most advanced material model employed in this thesis. The remaining two material models introduced in Section 9.3 will not be employed in this chapter.

12.1 Set up of Model

The general composition of the models used to extract the p - y curves from Plaxis is similar to the model presented in the convergence analysis, see Section 10.1. However, in order to increase the quality of the extracted p - y curves from the Plaxis 3D model, an additional measure is employed in these analyses. This extra measure is an additional refinement of the mesh close to the location of the pile which is applied in order to increase the quality and quantity of the stress components extracted to set up the p - y curves. The additional refinement of the mesh around the pile is implemented through a division of the monopile into sections, $h_{section}$, with a height of 1 m, see Figure 12.1. By doing this, Plaxis 3D is forced to generate the mesh according to each pile section, and some of the randomness of the generated mesh is therefore avoided. However, the principle

behind the improvement illustrated in Figure 12.1 has to be validated before it can be applied. This verification is performed in Appendix M.1.

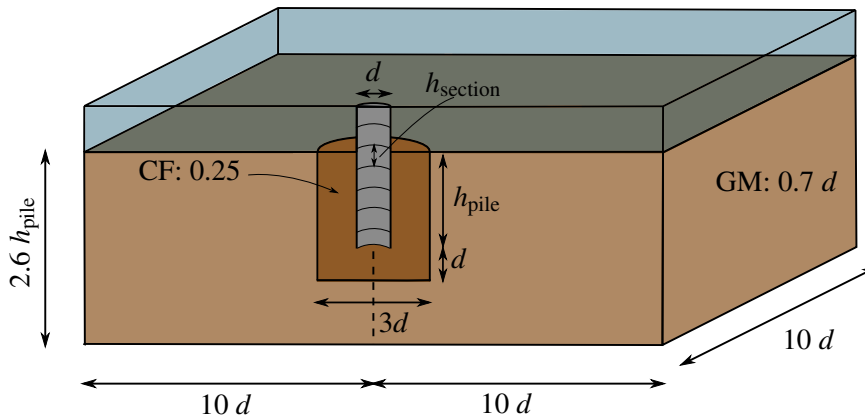


Figure 12.1: Illustration of the model used to extract the p - y curves from Plaxis 3D.

Similarly to the convergence analysis and the free vibration analysis presented previously in Stage 4, the properties of symmetry for the monopile is exploited in this analysis. This means that only half of the monopile is modelled in Plaxis 3D. From the results obtained from this model, the results on the other half of the monopile can thereby be obtained.

In this chapter, the p - y curves are extracted for a pile with the same cross section as used in the free vibration analysis, see Chapter 11. The pile- and domain dimensions applied in this analysis are repeated in Table 12.1.

Table 12.1: Dimensions of the model considered in the extraction of the p - y curves.

Diameter mudline, d [m]	Length above mudline [m]	Length below h_{pile} [m]	Wall thickness t [cm]	Mean water level MWL [m]
8	15	30	10	15

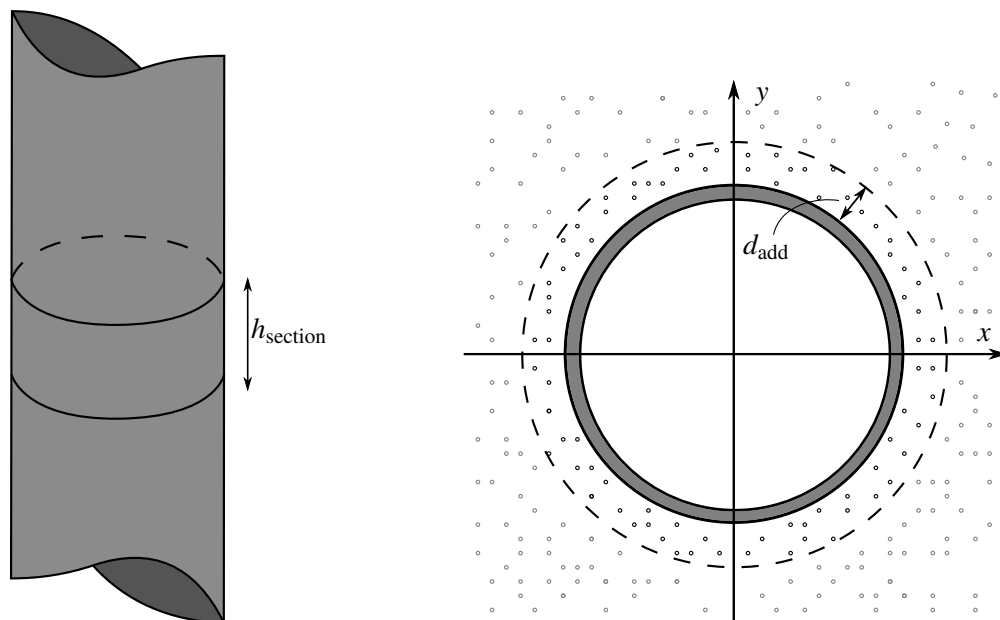
In the model used to extract the p - y curves, the loading phase is divided into several phases where each phase only represent a small step of the total loading. This is done in order to be able to extract the soil resistance, p , after every single loading phase, and thereby recreate the p - y curve from the Plaxis 3D model. This setup of the loading phases is different to the setup used in the free vibration analysis, and to the displacement analysis presented in Chapter 13.

12.2 Principle of Extraction of the p - y Curves

The p - y curves, which were introduced in Chapter 5, represent the relationship between the soil resistance, p , and the lateral displacement, u . The lateral displacement of the monopile in a certain depth is relatively easy to extract from a Plaxis 3D model. It is however more complicated to extract the soil resistance. The soil resistance is a measure of the resistance the soil produces on the pile. The theory described in this section is based on Fan and Long, 2005.

When using Plaxis 3D, the soil resistance can be extracted from two different procedures i.e. from the stresses appearing in the soil close to the monopile, or from the stresses in the interface between the monopile and the surrounding soil. When exploring the option of extracting the p - y curves from the interface between the monopile and the surrounding soil, the area of each element has to be taken into account in order to distribute the stress in a point across this area. This area is possible to extract from the model, but would however be a very time consuming procedure. This option is thereby neglected in this thesis.

Instead of extracting stresses from the interface, stresses are extracted from the soil surrounding the monopile. Because Plaxis 3D only supplies stress-states in Gauss-points, it is not possible to extract stress-states exactly next to the pile, when this procedure is employed. Instead, stresses are extracted from the Gauss-points located within a certain distance of the monopile, d_{add} . The principle of dividing the monopile into sections, where each section represents one p - y curve, and the principle of including the stress-states in the Gauss-points located within a certain distance from the monopile, are illustrated in Figure 12.2(a) and 12.2(b) respectively.



(a) Illustration of a part of the monopile, where the section referred to as h_{section} is the section considered, when establishing the p - y curves.

(b) Illustration of a cross section of the monopile and the surrounding Gauss-points.

Figure 12.2: Illustration of the principle of dividing the monopile into sections, where each section represents a p - y curve. The black points are included in the analysis, whereas the grey points are neglected. The full cross section for the monopile is illustrated for a better visualisation of the problem.

The number of Gauss-points, and thereby the number of stress-states considered in the extraction of the p - y curves from Plaxis 3D, are highly dependent on the distance to the circle surrounding the considered points, d_{add} . An analysis of the size of this distance should be performed, in order to be certain about the accuracy of the extracted p - y curves. Such an analysis is however not performed, due to limited time available. Instead, this distance is fixed to 0.25 m, which yields an average of 80 Gauss-points are available per section of the modelled half cross section of the monopile,

yielding a total of 160 Gauss-points per unit length for the full monopile sections. This number of Gauss-points included per section of the monopile is similar to the number of points included per unit length in a similar study performed by Wolf et al., 2013, and is thereby deemed acceptable.

The soil resistance for a laterally loaded pile can be calculated directly by integrating the stresses surrounding the monopile. In order to do so, firstly the soil resistance in each single Gauss-point is calculated. This is done by calculating the x -component of the stresses in each Gauss-point, which can be represented by a traction vector, T_x . The traction vector is expressed by equation (12.1) and the effective cartesian stresses considered are illustrated in Figure 12.3. The expression for the traction vector, T_x , is derived in Appendix M.2. [Fan and Long, 2005]

$$T_x = \sigma'_{xx} n_{xx} + \sigma'_{xy} n_{xy} + \sigma'_{xz} n_{xz} \quad (12.1)$$

$$n_{xx} = \cos \theta_x = \frac{x_g}{\sqrt{x_g^2 + y_g^2}} \quad (12.2)$$

$$n_{xy} = \cos \theta_y = \frac{y_g}{\sqrt{x_g^2 + y_g^2}} \quad (12.3)$$

$$n_{xz} = \cos \theta_x = 0 \quad (12.4)$$

$\sigma'_{xx}, \sigma'_{xy}, \sigma'_{xz}$	Effective cartesian stresses
n_{xx}, n_{xy}, n_{xz}	
x_g, y_g	
	Components of unit normal along the x -, y - and z -axis
	x - and y -coordinates of the Gauss-point

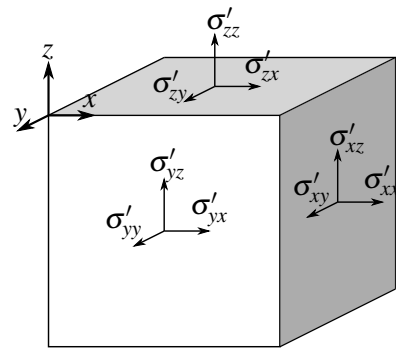


Figure 12.3: Illustration of the effective cartesian stresses.

The component of unit normal along the z -axis is zero, because a horizontal plane is considered. When the traction vector has been established for each of the Gauss-points, the next step is to integrate these traction vectors along the circumference of the monopile. This is done by dividing the cross section of the monopile into a number of sectors, see Figure 12.4. Each sector is represented by a number of Gauss-points and their corresponding traction vectors. Within each sector, the resulting traction vector is computed as the average traction vector. By utilising the average traction vector for each of the sectors, the consideration of the area of each element is avoided, and the procedure is thereby simplified significantly.

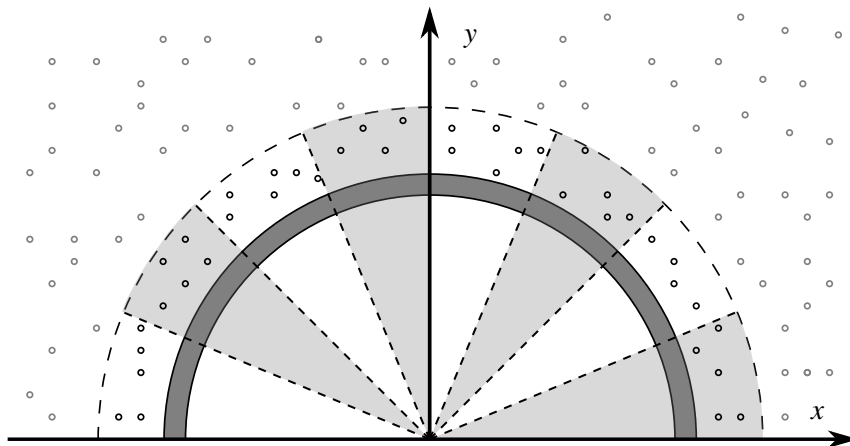


Figure 12.4: Illustration of the division of the cross section of the monopile into sectors. Only half of the monopile cross sections are illustrated because this is the part modelled in Plaxis 3D.

To ensure the quality of the extracted p - y curves is sufficient, an analysis of the number of sectors should be performed. This analysis will however not be performed. The cross section of the monopile is divided into 16 sectors, meaning that half of the monopile cross section consists of eight sectors, see Figure 12.4. This number of sectors is equal to the number of sectors applied in a similar analysis performed by Wolf et al., 2013 and is thereby deemed acceptable.

Following the estimation of the average traction vector for each of the sectors illustrated in Figure 12.4, the soil resistance for the considered depth can be established. This is done by integrating the average traction vector for each of the sectors, $T_{x,sector_i}$, along the circumference of the monopile. However, since each of the sectors are represented by the same arc length, see Figure 12.4, the estimation of the soil resistance at a certain depth can be simplified into equation (12.5).

$$p = \sum_{i=1}^n (T_{x,sector_i}) 2d\pi \quad (12.5)$$

When the soil resistance has been calculated, the p - y curves can be established by relating these soil reactions to the corresponding displacements of the pile. In the following sections, p - y curves obtained from Plaxis 3D using different material models are compared to the p - y curves suggested by API.

The procedure described above is regarding the extraction of the p - y curves from the Gauss-points in the soil surrounding the monopile. As already mentioned, an alternative approach would be to extract the stresses from the interface between the monopile and the soil. It is expected to obtain slightly lower stresses from the procedure described above when comparing to the stresses in the interface, because when the stresses are extracted from the soil surrounding the monopile, the forces are distributed to a larger area than when the stresses are extracted from the interface.

12.3 Comparison of p - y Curves

Using the procedure described in the previous section, the p - y curves can be extracted from Plaxis 3D. As mentioned earlier, the p - y curves are extracted from a Plaxis 3D model based on the Mohr-Coulomb material model and a model based on the Hardening Soil Small-strain material model. Each of the models will be subjected to a lateral load varying from zero to the load provoking a displacement of 10 % of the diameter at the mudline. The results obtained from these models are presented in to following sections.

12.3.1 The Mohr-Coulomb Material Model

The Mohr-Coulomb material model has been chosen for the extraction of the p - y curves from Plaxis 3D, because the input parameters for this material model are similar to the input parameters for the API p - y curves. The Mohr-Coulomb material model does however consider the stiffness parameter Young's modulus, which is not considered by the API p - y curves. Nonetheless, the Mohr-Coulomb material model is a very simple representation of the soil behaviour, similarly to the behaviour described by the API p - y curves. The comparison of the API p - y curves and the

p - y curves extracted from the Plaxis 3D model based on the Mohr-Coulomb material model is illustrated in Figure 12.5.

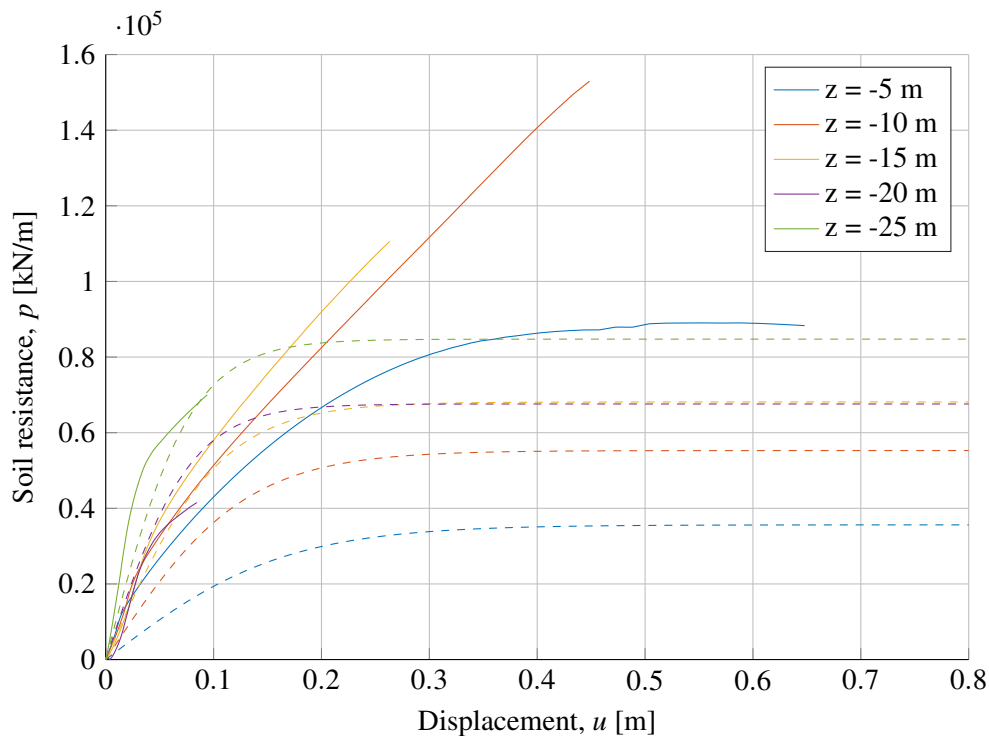


Figure 12.5: Comparison of API p - y curves and extracted p - y curves from Plaxis 3D using the Mohr-Coulomb material model in different depths, z . Solid line: p - y curve extracted from Plaxis 3D. Dashed line: API p - y curve. The displacements illustrated are absolute values.

From the comparison of the p - y curves for different depths in Figure 12.5, it is observed that the API p - y curves diverge from the p - y curves obtained from Plaxis 3D. This divergence is however expected and is consistent with the tendencies uncovered in Stage 3 and multiple studies performed by e.g. Kallehave, Thilsted, and Liingaard, 2012 and Kirsch, Richter, and Coronel, 2014.

When inspecting the left-hand side of Figure 12.5, i.e. the initial stiffness of the p - y curves, it is observed that the p - y curves extracted from Plaxis 3D yield a higher initial stiffness compared to the API p - y curves. This tendency is as expected, and is also consistent with the findings presented by Kallehave, Thilsted, and Liingaard, 2012. A close-up of the initial stiffness of the comparison presented in Figure 12.5 is illustrated in Figure 12.6.

From the close-up of the initial stiffness of the p - y curves illustrated in Figure 12.6, it is observed that the initial slope of the API p - y curves increases with an increasing depth. This is due to the linear increase of the initial modulus of subgrade reaction, as explained in Chapter 5. This tendency is however not present in the p - y curves extracted from Plaxis 3D where the initial-slopes are more identical to each other. This indicates that the assumption of a linear increase of the initial modulus of subgrade reaction is inaccurate, which also is consistent with the findings presented by Kallehave, Thilsted, and Liingaard, 2012. In the closeup it is also observed that the behaviour of the extracted curves is a bit messy, this could be due to a too rough mesh to capture the behaviour

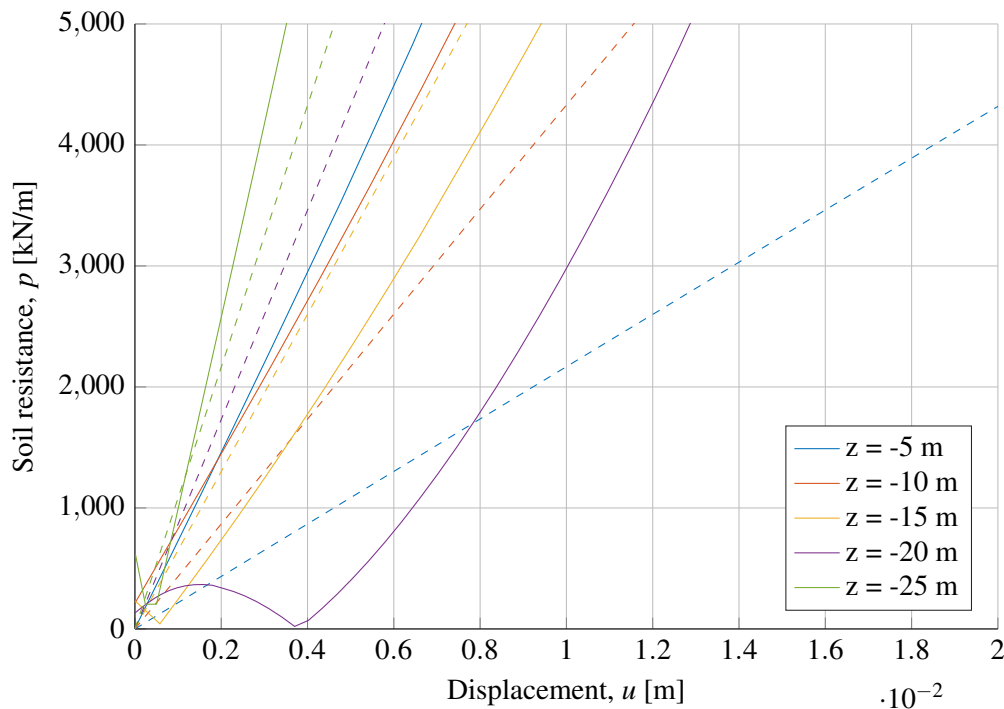


Figure 12.6: Close-up of the initial stiffness of the comparison of p - y curves and extracted p - y curves. Solid line: p - y curve extracted from Plaxis 3D. Dashed line: API p - y curve. The displacements illustrated are absolute values.

at small displacements. The load displacements curves of these extracted p - y curves can be found in Appendix M.3.

If the right-hand side of Figure 12.5 is inspected, it is observed that the p - y curves extracted from Plaxis 3D yield higher soil resistances and thereby a higher soil-structure stiffness compared to the API p - y curves. The right-hand side of Figure 12.5 is where the displacement are increasing and approaching the assumed failure displacement of 10 % of the pile diameter at mudline. This tendency is however not as expected because the broad consensus about the API p - y curves and their estimation of the soil-structure stiffness is that they underestimate the soil-structure stiffness for small loads whereas they overestimate the soil-structure stiffness for extreme loads [Achmus, Thieken, and Lemke, 2014]. Nonetheless, the fact that the API p - y curves according to Figure 12.5 also underestimates the soil-structure stiffness for larger loads and larger displacements indicates that the API p - y curves are unreliable for monopiles with large diameters.

From the free vibration analysis in Chapter 11 it was observed, that the model of the OWT in Plaxis 3D based on the Mohr-Coulomb material model overestimates the first eigenfrequency, when comparing to the first eigenfrequency obtained from the homemade 1D FE model presented in Chapter 6. This overestimation can be explained by the considerations presented above regarding the general overestimation of the soil-structure stiffness when considering the p - y curves extracted from the Mohr-Coulomb material model compared to the API p - y curves.

12.3.2 The Hardening Soil Small-Strain Material Model

The Hardening Soil Small-strain material model has been chosen for the extraction of the p - y curves from Plaxis 3D, because it is the most advanced material model considered in this thesis, and because it requires several input parameters which the API p - y curves do not consider. The aim of this comparison is thereby to investigate if the Hardening Soil Small-strain material model provides a better correlation with the API p - y curves or if it diverges even more than the Mohr-Coulomb material model. The comparison of the API p - y curves and the p - y curves extracted from the Plaxis 3D model, based on the Hardening Soil Small-strain material model, is illustrated in Figure 12.7.

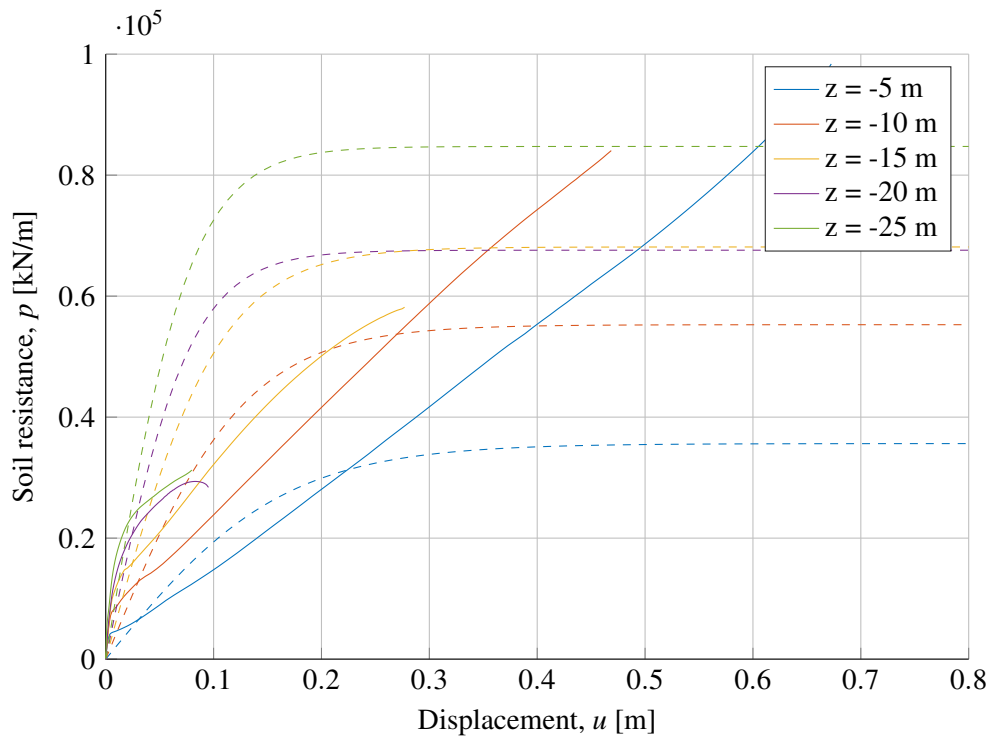


Figure 12.7: Comparison of API p - y curves and extracted p - y curves from Plaxis 3D using the Hardening Soil Small-strain material model in different depths, z . Solid line: p - y curve extracted from Plaxis 3D. Dashed line: API p - y curve. The displacements illustrated are absolute values.

From the comparison of the p - y curves for different depths in Figure 12.7 it is observed that the API p - y curves diverges from the p - y curves extracted from Plaxis 3D.

In order to compare the initial stiffness of the API p - y curves and the p - y curves extracted from the Hardening Soil Small-strain material model, a close-up of the initial part of Figure 12.7 is illustrated in Figure 12.8.

When observing the comparison of the initial stiffness in Figure 12.8, it is observed that the p - y curves extracted from Plaxis 3D yield a higher initial stiffness than the API p - y curves. This tendency is as expected and similar to the tendency observed in the previous section. As for the p - y curves extracted using the Mohr-Coulomb material model the abnormalities could be caused by

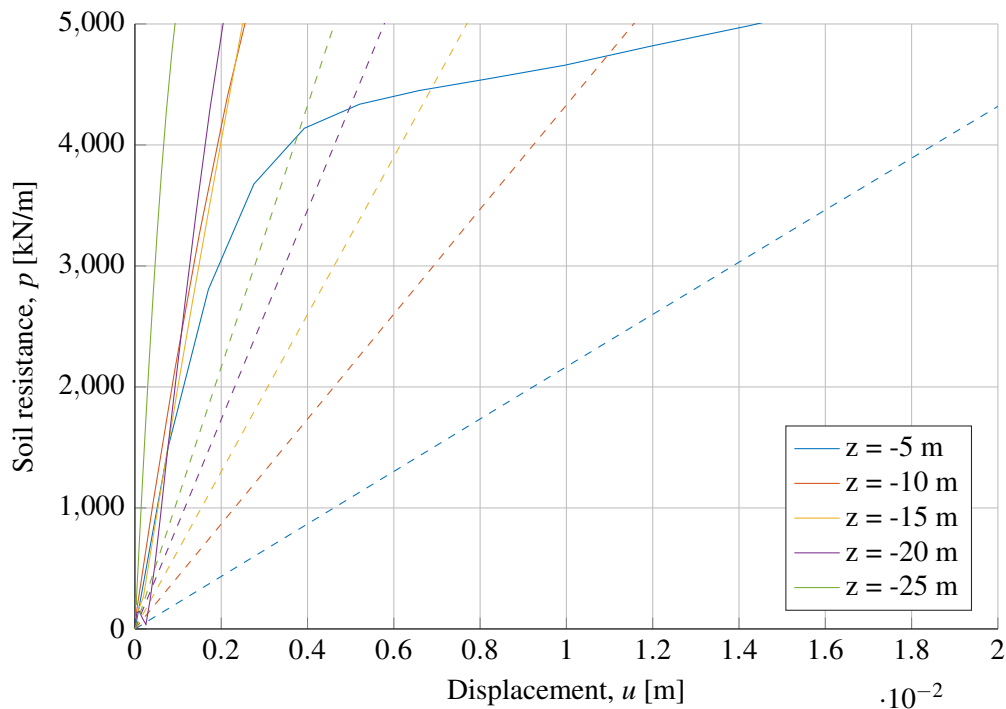


Figure 12.8: Close-up of the initial stiffness of the comparison of p - y curves and extracted p - y curves. Solid line: p - y curve extracted from Plaxis 3D. Dashed line: API p - y curve. The displacements illustrated are absolute values.

a too rough mesh to describe the behaviour at small displacements. The load displacements curves of these extracted p - y curves can be found in Appendix M.3.

If the right-hand side in Figure 12.7 is inspected, it is observed that the p - y curves extracted from the Hardening Soil Small-strain material model overestimates the soil-structure stiffness for the majority of the p - y curves. This tendency is similar to the one observed for the p - y curves extracted from the Mohr-Coulomb material model.

The first eigenfrequency of the OWT estimated in the free vibration analysis in Chapter 11, are, as already mentioned, higher compared to the first eigenfrequency estimated from the homemade 1D FE model in Chapter 6. This overestimation of the first eigenfrequency can also in the case of the Hardening Soil Small-strain material model be explained by the fact, that the p - y curves extracted from Plaxis 3D yield a higher soil-structure stiffness compared to the API p - y curves.

Finally, from Figure 12.7 it is also observed that the Plaxis 3D model based on the Hardening Soil Small-strain material model predicts a lower p - y response, compared to the Plaxis 3D model based on the Mohr-Coulomb material model. This tendency is as expected, because the Hardening Soil Small-strain material model provides a higher stiffness at smaller displacements compared to the Mohr-Coulomb material model. The Mohr-Coulomb material model has a constant stiffness until yielding is reached.

12.4 Closure of the Analysis of p - y Curves

This concludes the comparison of the API p - y curves and the p - y curves extracted from a Plaxis 3D model based on the Mohr-Coulomb material model and the Hardening Soil Small-strain material model. The main conclusions drawn through the comparison will be repeated and elaborated in this section.

For both of the comparisons performed in the previous sections, a significant divergence between the API p - y curves and the corresponding p - y curves extracted from the Mohr-Coulomb model and the Hardening Soil Small-strain model is observed. From the comparison of the API p - y curves and the Mohr-Coulomb p - y curves, see Figure 12.5, it is observed that the Mohr-Coulomb p - y curves has a similar shape to the API p - y curves, especially at shallower depths. This similarity is however not observed in the comparison of the API p - y curves and the Hardening Soil Small-strain p - y curves.

The comparisons presented in the previous sections both revealed that the API p - y curves underestimate the initial soil-structure stiffness of sand. This observation is consistent with studies performed by both Kallehave, Thilsted, and Liingaard, 2012 and Kirsch, Richter, and Coronel, 2014. Prior to the comparison, it was expected that the API p - y curves underestimate the soil-structure stiffness for small loads and small displacements whereas it overestimates the soil-structure stiffness for larger loads and displacements. This expectation is however not seen in the comparisons, which revealed that the API p - y curves underestimate the soil-structure stiffness in most cases for this specific combination of soil parameters and pile dimensions.

One of the assumptions behind the API p - y curves is, that the initial modulus of subgrade reaction is increasing linearly with the depth. The accuracy of this assumption is already addressed earlier in Stage 3 and is supported by multiple studies including Kallehave, Thilsted, and Liingaard, 2012. From the close-up of the two comparisons of the p - y curves, see Figure 12.6 and 12.8 respectively, this linear increase of initial stiffness is however not observed. This could indicate that the assumption of a linear increase of the initial modulus of subgrade is inaccurate.

Finally, through the free vibration analysis in Chapter 11 it was uncovered, that the first eigenfrequency of the OWT, obtained from the Plaxis 3D model using both the Mohr-Coulomb and the Hardening Soil Small-strain material models, is higher compared to the first eigenfrequency obtained from the homemade FE model using the API p - y curves. The difference in the first eigenfrequency can also be illustrated from the comparison of the p - y curves, where the soil-structure stiffness of the p - y curves extracted from Plaxis 3D using the two material models, are higher in almost all cases for this specific combination of soil parameters and pile dimensions.

These observations point towards that the API p - y curves are unsuited for the design of large diameter monopiles, and the need for a new updated design method is present. However, to be able to conclude this with certainty, more comparisons and analyses should be performed. One crucial limitation of the API p - y curves is that they fail to include shear stresses acting in the longitude axis of the monopile. The importance of these shear stresses is examined in the upcoming chapter.

13. DISPLACEMENT FIELD

In this chapter an analysis of the displacement field for two different pile diameters is performed. The purpose of this analysis is to compare the displacement field for a small slender pile and a pile with a larger diameter, and thereby investigate the problematics of applying theories developed on slender pile in the design of large diameter monopiles.

The comparison of the API p - y curves and the corresponding p - y curves extracted from Plaxis 3D models indicated a significant divergence. This divergence is as expected because the API p - y curves were developed based on tests performed on a pile with a diameter of 0.6 m, whereas the monopile considered in Stage 3 and 4 has a diameter of 8.0 m. Previously studies presented in e.g. Kallehave, Thilsted, and Liingaard, 2012 and Kirsch, Richter, and Coronel, 2014 have shown that the applicability of the API p - y curves decreases as the diameter of the monopile increases. The effect induced by the increased diameter is often referred to as the diameter effect. The analysis of the displacement field is thereby performed in order to observe the changes in the surrounding soil when the diameter of the monopile is increased from 0.6 m, corresponding to the pile diameter for which the API p - y curves are developed, to 8.0 m, corresponding to the monopile considered in Stage 3 and 4.

In the following sections the analysis of the displacement field is elaborated starting with a brief introduction to the composition of the models employed during the analysis of the displacement field. Following this introduction, the analysis of the diameter effect is presented where the variation in the soil surrounding the monopile is observed as the diameter of the monopile is increased from 0.6 m to 8.0 m.

13.1 Set up of Model

The procedure of setting up the models is identical to the one described in the convergence analysis, see Section 9.4. This means that the size of the domain and meshes obtained through the convergence analysis are employed in the analysis of the displacement field as well. The general dimensions of the models employed in this analysis are illustrated in Figure 13.1.

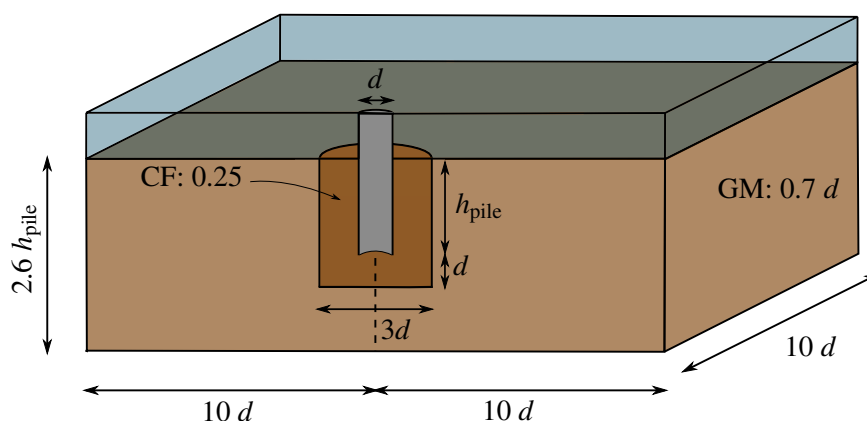


Figure 13.1: Illustration of the model dimensions used to analyse the displacement fields.

As already introduced, the analysis will be based on a comparison of the variation in the soil surrounding two monopiles with different diameters. The specific dimensions for the two models composed in this chapter are presented in Table 13.1.

Table 13.1: Dimensions of the models considered in the analysis of the displacement field.

Diameter mudline, d [m]	Length above mudline [m]	Length below h_{pile} [m]	Wall thickness t [cm]	Mean water level MWL [m]
0.6	15	30	10	15
8.0	15	30	10	15

The calculations of the models employed in this analysis are divided into three phases, the initial-, installation- and loading phase. These phases are considered because this analysis is a static analysis and thereby not time depending. The soil is modelled using the Hardening Soil Small-strain material model. This material model is selected because it is the most advanced material model considered in this thesis, and it is the material model which is expected to imitate the reality best.

The models composed for the comparison between the displacement fields are both subjected to a lateral load. This lateral load is estimated as the load is corresponding to a displacement at mudline of 10 % of the pile diameter, which is corresponding to the failure criterion. The results of the obtained loads needed to provoke a displacement corresponding to 10 % of the pile diameters are presented in Table 13.2.

Table 13.2: Loads used to provoke a displacement corresponding to 10 % of the pile diameter.

Pile diameter [m]	Displacement [m]	Load [kN]
0.6	0.06	172
8.0	0.80	55850

The displacements provokes by the piles in the two models, when the load from Table 13.2 is applied, are illustrated in Figure 13.2.

When observing the deformed structure for the pile with the small diameter, see Figure 13.2(a), the pile seems to be fixed in the soil, and the displacements happen mostly above mudline alone. The deformed structure for the monopile with the large diameter, see Figure 13.2(b), is very different to the deformed structure of the pile with the small diameter. From the figure of the deformed monopile with the large diameter, a rigid-body-like deformation is observed. These different patterns of deformations are as expected and consistence with studies performed by e.g. Kallehave, Thilsted, and Liingaard, 2012.

13.2 Analysis of the Diameter Effect

The results presented in this section are obtained from a 3D model, but presented in 2D plane illustrations in order to simplify the visualisation of the results. Firstly, the displacement fields of

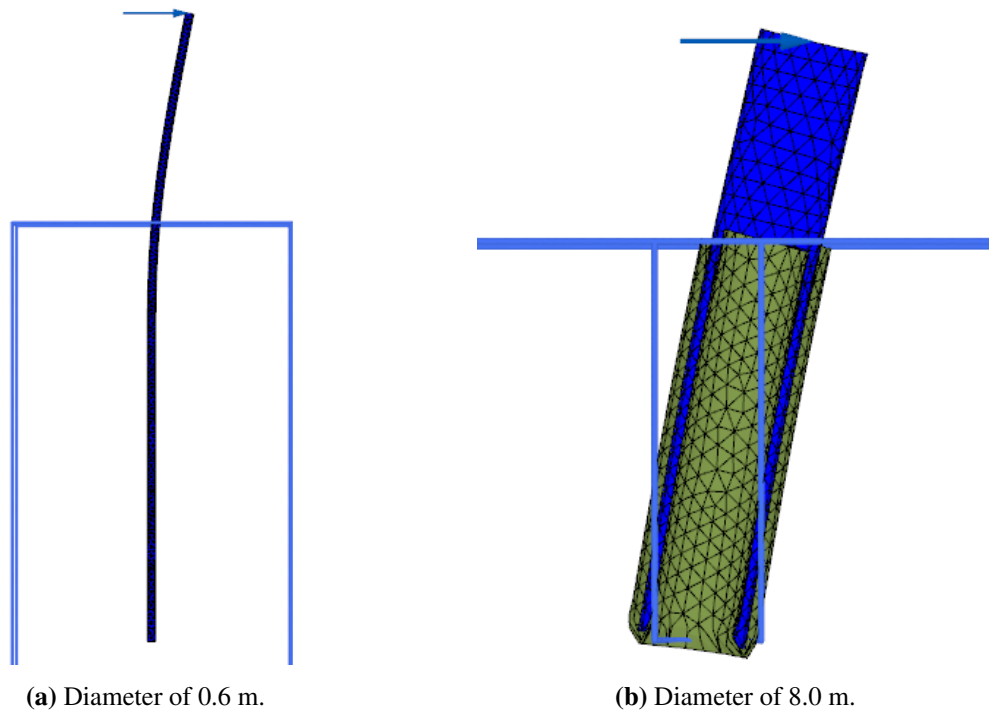


Figure 13.2: Displacements of the loaded structures for different diameters in the x - z plane in Plaxis 3D. The displacements are scaled with a factor of 5.0 for being able to see the deformation form more easily.

the two monopiles are compared. In this analysis, the monopiles are subjected to the load presented in Table 13.2, which provokes a horizontal displacement corresponding to 10 % of the pile diameter. Figure 13.3 shows the displacement fields for the two piles in the x - z plane, where the same length of the piles are used.

From Figure 13.3 is observed that the displacement fields for the two piles are very different from each other. It is observed that the displacement of the small diameter pile, see Figure 13.3(a), only activates the soil located at the very top of the soil domain. Conversely, for the large diameter monopile, see Figure 13.3(b), it is observed that the displacement activates soil almost along the full length of the pile, but especially the soil close to the top and bottom of the pile.

The original API p - y curves are, as already mentioned, developed for slender piles with small diameters, which is represented by the small diameter pile. For small and slender piles, the lateral load is dominating and the behaviour of the pile can be estimated based on this lateral load alone. However, when the diameter of the monopile increases, other effects must be taken into account. In the previous chapter, where the API p - y curves are compared to p - y curves extracted from a Plaxis 3D model, it was observed that the API p - y curves deviates significantly from the extracted p - y curves. One of the reasons for these deviations can be explained by the fact, that when the diameter of the monopile increases, the monopile starts to deform more like a rigid-body. The rotation induced by this approximated rigid-body-motion introduces shear stresses along the pile surface. These shear stresses are not considered by the API p - y curves, as already mentioned, and the API p - y curves can thereby be considered as unsuited for the design of large diameter monopiles.

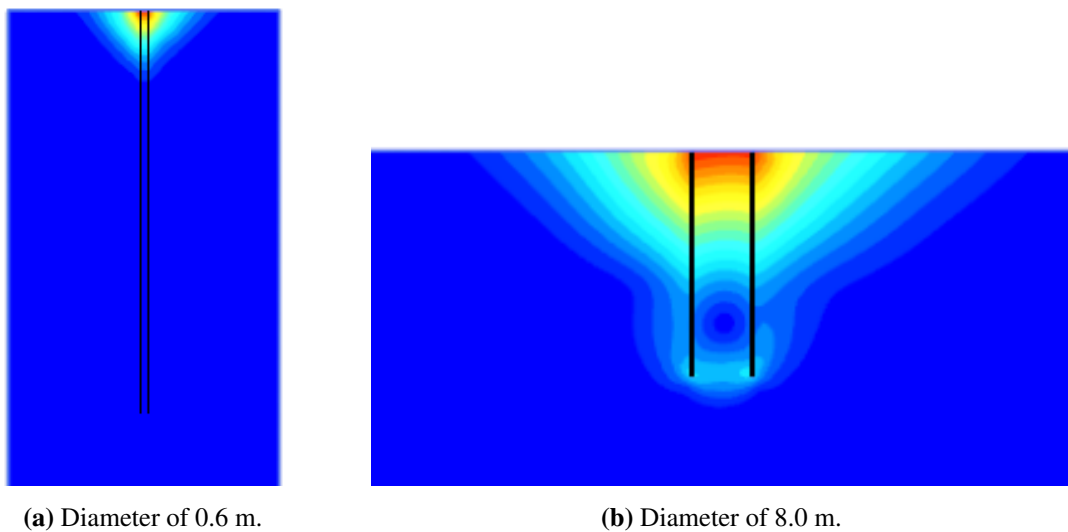


Figure 13.3: Displacement field from Plaxis 3D for different diameters in the x - z plane. The black lines defines the piles and the scales goes from blue, which represent no displacement, to red, which represent the largest displacement. It should be kept in mind both piles are 30 m long below mudline. The blue lines define the edges of the soil volume.

Contrary to the API p - y curves, the shear stresses are considered by the PISA approach which was introduced in Section 7.2. The PISA project recognised the importance of including the effect of the shear stresses along the longitude-axis of the monopile for large diameter monopiles. The shear stresses along the longitude-axis of the monopile are induced by the increasing eccentricity of the shear force according to the centre of the pile, which also increases the moment around the centre of the pile. The effect of the shear stresses along the longitude-axis of the pile can be investigated, by comparing the shear stresses occurring around the small diameter pile to the shear stresses occurring around the large diameter monopile. This comparison is illustrated in Figure 13.4.

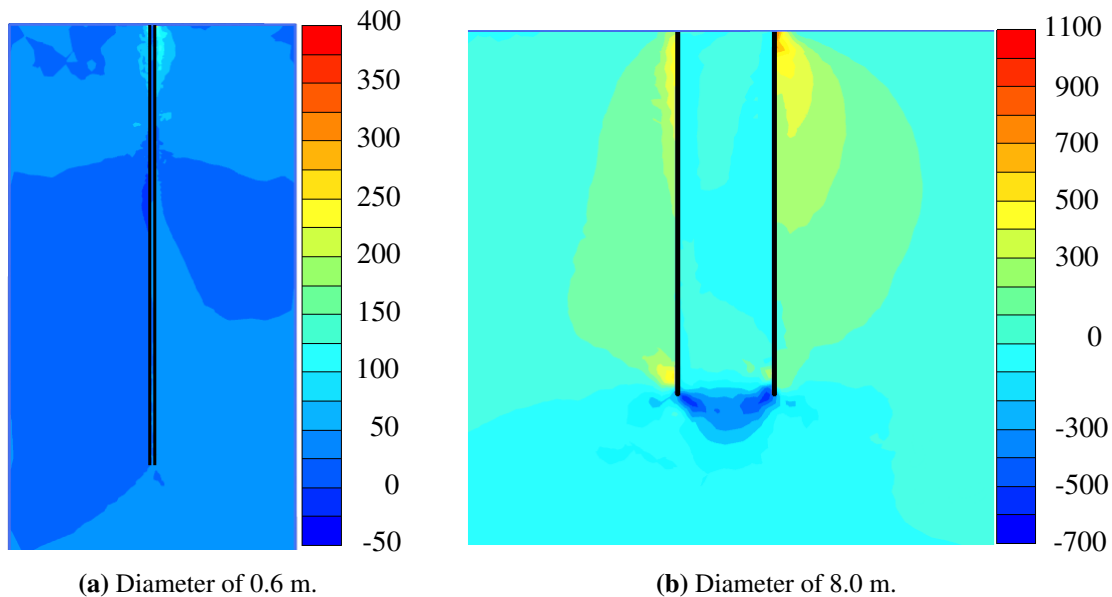


Figure 13.4: Shear stresses from Plaxis 3D for different diameters in the x - z plane. Values in kN/m^2 .

From Figure 13.4 it is observed that the shear stresses are much more apparent for the large diameter monopile in Figure 13.4(b). When considering the shear stresses along the small diameter pile, see Figure 13.4(a), it is observed that the shear stresses are small and mostly concentrated around the top of the pile. Contrary, when considering the shear stresses along the large diameter monopile, it is observed that the shear stresses are apparent along the full length of the monopile and that the variation in the shear stresses are larger compared to the small diameter pile. This means that the effect of including the shear stresses in a design method increases, when the diameter of the monopile increases.

From this it can be concluded that the accuracy of original API p - y curves decreases as the diameter of a monopile increases. This can be explained by the fact that the API p - y curves do not consider shear stresses which occurs from the rigid-body rotation of the monopile. These shear stresses have been proven to be crucial in the determination of the response of a large diameter monopile. These conclusions are identical to the ones drawn by the PISA project. [Byrne et al., 2015]



Closure

In the closure of the thesis, a discussion of the main subjects is presented. After, the final conclusion for the thesis is presented to round of the thesis. Finally, the references used through the thesis are listed.

14	Discussion	161
15	Conclusion	165
16	References	170

14. DISCUSSION

In this chapter the final discussion of the thesis is presented. Throughout the thesis, the estimation of the first eigenfrequency has been investigated, where the dynamic properties of an OWT and the estimation of the soil-structure interaction have been brought into focus. The important conclusions drawn through the thesis will be repeated and discussed in this chapter.

During Stage 2, a simple 1D FE model was developed. This Simple Model was developed to represent an OWT, which is simplified into a stick with a point mass attached at the top, corresponding to the combined mass of the hub, nacelle and blades. In this model, the contributions from soil are neglected and the stick is thereby assumed to be fixed at the mudline. The stick is additionally simplified into having the same diameter and wall thickness in the full length.

The purpose of the development of this simplified model was to analyse the influence of the different input parameters on the first eigenfrequency of the system. The analysis concluded that the diameter and the height, i.e. the slenderness ratio, of the model as well as the point mass, have the largest influence on the first eigenfrequency. Here the height of the structure and the first eigenfrequency are negative correlated, contrary to the diameter and the first eigenfrequency which are positive correlated.

In Stage 3, the Simple Model from Stage 2 was extended to include the effects from the soil, and thereby considers the soil-structure interaction. In this stage, the soil-structure interaction was considered via the p - y curves. In the literature study performed in Stage 1, the design methods currently suggested in the design guidelines were examined, and already here it was recognised that the currently suggested API p - y curves might be unsuited for the design of large diameter monopiles. However, because the API p - y curves are recommended in the current design guidelines, these curves were implemented in the Extended Model.

The input parameters for the API p - y curves consist primarily of the strength parameters, the effective angle of internal friction or the undrained shear strength, as well as the geometric input parameters such as the depth and the diameter of the pile. The strength parameters used as input for the API p - y curves, in order to describe soil-structure stiffness, are considered as state parameters, which means that they are unsuited to describe the general behaviour of soil. This is due to the fact that they fail to include the stress dependent stiffness of soil. Additionally, the formulation of the API p - y curves for sand fails to consider the diameter effect.

The considerations presented above about the p - y curves have caused multiple studies of improvements of the API p - y curves. In this thesis, the improvements proposed by Kallehave, Thilsted, and Liingaard, 2012 and Kirsch, Richter, and Coronel, 2014 for sand and clay respectively are considered. Both of these improvements provide modifications to the estimation of the initial soil-structure stiffness. Comparative studies of the API p - y curves and the improvements proposed by Kallehave, Thilsted, and Liingaard, 2012 and Kirsch, Richter, and Coronel, 2014 reveal that the improvements yield a better estimation of the initial soil-structure stiffness. However, because the improvements still are based on the formulation of the API p - y curves, and thereby based on the

aforementioned state parameters, the improvements are still unsuited for the general design of an OWT. [Achmus, Thieken, and Lemke, 2014; Achmus, Terceros, and Thieken, 2016]

In the last stage of this thesis, Stage 4, a comparison of the Extended Model from Stage 3 and results obtained from the commercial software Plaxis 3D was performed. During Stage 4, three different analyses were performed using Plaxis 3D:

- A free vibration analysis, where the first eigenfrequency is estimated in Plaxis 3D and compared to the first eigenfrequency obtained from the Extended Model.
- An extraction of the p - y curves from Plaxis 3D, where the extracted p - y curves are compared to the API p - y curves.
- A comparison of the displacement field for a slender pile and the reference pile used in Stage 3 and 4 in Plaxis 3D.

For the analyses presented above, a reference soil profile consisting of a single layer of sand was employed. This reference soil profile is derived by the authors of this thesis, during an earlier semester project. The sand layer is selected, because it provides the stiffness and strength parameters necessary for the Hardening Soil material model. The parameters of this reference sand layer are composed of CPTs, triaxial tests and oedometer tests from different locations and the sincerity of the sand is thereby questionable. However, the main focus of this Master Thesis is not to derive and justify the input parameters, and the composition of this sand was therefor chosen as the reference soil layer for Stage 4.

The dynamic 3D models calculated for the free vibration analysis are very time consuming and close to the end of the project period, it was discovered that the mass on top of the OWT was modelled incorrectly, as it did not provide eigenfrequencies in the expected range when comparing to Østergaard et al., 2019. To correct this, the mass was changed from being a point load located on a rigid plate, to an adjustment of the density of the top part of the OWT tower modelled in Plaxis 3D. This resulted in a reduction of the eigenfrequency of 0.025 Hz after the mass was added. The eigenfrequencies calculated during this thesis, based on the reference soil profile presented in Stage 4, are listed in Table 14.1.

Table 14.1: The first eigenfrequency according to different estimation methods. The deviation is according to the eigenfrequency calculated using the API p - y curves in the Extended Model.

	API	Kallehave	Mohr-Coulomb	Hardening Soil
First eigenfrequency, f_1 [Hz]	0.189	0.196	0.200	0.250
Deviation [%]	-	3.7	5.8	32.3

From Table 14.1 it is observed, that the first eigenfrequency using the Hardening Soil material model in Plaxis 3D is 32.5 % larger, compared to the first eigenfrequency obtained from the Extended Model. This deviation is quite significant and higher than expected.

If more time was available for this thesis, modelling of the mass on top of the OWT representing the hub, nacelle and blades should be looked further into. This should be done in order to verify if the mass is modelled correctly and brings the correct effects of decreasing the eigenfrequency in the free vibration analysis. Additionally, a further investigation of the deviation between the

first eigenfrequency obtained when using the Hardening Soil Small-strain material model and the Extended Model could be performed.

The second analysis of Stage 4 considers a comparison of the API p - y curves and the corresponding p - y curves extracted from the Mohr-Coulomb and Hardening Soil material models in Plaxis 3D. This comparison was performed on a monopile with a diameter of 8 m, which is more than ten times the diameter for which the API p - y curves were developed, and thereby regarded as a large diameter monopile. This comparison revealed a significant deviation and emphasises thereby the need for a new method for the design of large diameter monopiles.

The comparison of the API p - y curves and the p - y curves extracted from the Mohr-Coulomb material model, see Figure 12.5 page 148, reveals a significant difference between the two p - y curves. It was observed that the p - y curves extracted from Plaxis 3D yielded a higher soil resistance and thereby a higher soil-structure stiffness. However, the p - y curves extracted from Plaxis 3D did indicate a degradation of stiffness as the displacement is increased, like observed by the API p - y curves.

The comparison of the API p - y curves and the p - y curves extracted from the Hardening Soil Small-strain material model, see Figure 12.7 page 150, revealed a more significant difference than the Mohr-Coulomb material model. It was observed that the tendency of the p - y curves extracted from the Hardening Soil Small-strain material model is not as expected, which may be caused by the composition of the reference soil profile, as it was composed of parameters from different test locations. Due to the time limitation of the thesis, this behaviour will however not be investigated further.

One of the assumptions of the API p - y curves is a linear increase of the initial modulus of subgrade reaction with the depth. From the two comparisons presented above it is observed that none of these analyses indicates this relation.

The deviations of the first eigenfrequency of the OWT presented in Table 14.1 are consistent with the p - y curves extracted from Plaxis 3D. From the table it is observed that the Mohr-Coulomb material model yields a first eigenfrequency, which is slightly higher than the one obtained from the API and Kallehave formulations of the p - y curves. This can be explained by the fact, that the p - y curves extracted from the Mohr-Coulomb material model yield a higher soil-structure stiffness compared to the API p - y curves. The same explanation is applicable for the deviation of the Hardening Soil Small-strain material model, where the soil-structure stiffness is overestimated significantly in the extracted p - y curves.

Finally, one of the crucial assumptions of the API p - y curves is that the response of the pile is governed by the lateral load. However, when the diameter of the monopile is increased, other effects must be taken into account as well. These effects are investigated in the final analysis where the displacement field for a monopile with a diameter of 0.6 m is compared to the displacement field for a monopile with a diameter of 8 m. This comparison revealed that as the diameter of the monopile increases, the monopile starts to behave more like a rigid-body. The rotation induced by this approximated rigid-body-motion introduces shear stresses along the pile surface, and according to the analysis of the displacement field, the importance of these shear stresses increases as the diameter of the monopile increases.

This concludes that the accuracy of the original API p - y curves decreases, as the diameter of a monopile increases. The need for a new and well suited design method for the estimation of the soil-structure interaction is therefore present. The PISA approach is one of the new and acknowledged design methods, which considers the flaws of the API p - y curves. This PISA approach was briefly described in this thesis, but not included in the model because the API p - y curves are the design method suggested in the current design guidelines. However, a method like the PISA approach is expected to be the recommended design method in the future, as this is able to describe the behaviour of large diameter monopiles better.

15. CONCLUSION

In this thesis, the problematics of estimating the first eigenfrequency of OWTs have been considered. The majority of the thesis focuses on methods for modelling the soil-structure interaction between a monopile and the soil it is embedded in. A relative simple 1D FE model, which is capable of estimating the first eigenfrequency of OWTs, has been programmed in MATLAB based on the guidelines for OWT foundations and the validity of these methods are investigated and discussed.

The API p - y curves, for estimating the soil-structure interaction provided by the current design guidelines, was found not to be applicable when the diameter of monopiles is increased to a level beyond the diameters it was originally developed for. This is due to the fact that the API p - y curves were developed on rather slender piles and thereby not considering the rigid-body behaviour of modern, large diameter monopiles.

As the API p - y curves are not considering the effects of increasing the diameter of the monopiles, suggestions of modifications of the original API p - y curves are investigated in this thesis as well. These modifications are provided by Kallehave for sands and Kirsch for clay, and considers the up-scaling of the diameter. Both modifications are based on optimising the initial soil-structure stiffness of piles.

The API p - y curves are compared to p - y curves extracted from a 3D FE model. Here it is observed that the soil-structure stiffness obtained by using the API p - y curves differs from the soil-structure stiffness obtained by using a more advanced soil model, such as the Hardening Soil material model in Plaxis 3D.

By using a 3D FE model for a slender pile, corresponding to the piles for which the API p - y curves are developed, it has been shown that the effects of the shear stresses generated along the pile is at a minimum. However, the effects of the shear stresses generated along a large diameter pile are of a certain magnitude, which influences the soil-structure stiffness. By this it can be concluded, that the API p - y curves are not set up to include the shear stresses of modern large diameter monopiles.

This concludes that the p - y curves are outdated when it comes to the design of large diameter monopiles. As 1D models have a very low computational time, compared to 3D FE models, it is suggested to look further into studies like the PISA project, in order to be able to take the shear effects into account. In this way, a model with a low computational time can be used to obtain a more reliable result, when designing the foundation of an OWT in the early stages of a project.

REFERENCES

- A. W. Skempton, 1951, *The bearing capacity of clay*. Devision 1.
- Aasen, Steffen, Ana M. Page, Kristoffer Skjolden Skau, and Tor Andersen Nygaard, 2016, “Effect of the Foundation Modelling on the Fatigue Lifetime of a Monopile-based Offshore Wind Turbine”. In: *Wind Energ. Sci. Discuss.*, doi:10.5194/wes-2016-37, 2016.
- Abhinav, K.A. and Nilanjan Saha, 2015, “Dynamic Analysis of an Offshore Wind Turbine Including Soil Effects”. In: *8th International Conference on Asian and Pacific Coasts (APAC 2015)*.
- Achmus, M., M. Terceros, and K. Thieken, 2016, “Evaluation of p-y Approaches for Large Diameter Monopiles in Soft Clay”. In: *Proceedings of the Twenty-sixth (2016) International Ocean and Polar Engineering Conference Rhodes, Greece*.
- Achmus, M., K. Thieken, and K. Lemke, 2014, “Evaluation of p–y approaches for large diameter monopiles in sand”. In: *Proceedings of the 24th international ocean and polar engineering conference, Busan, Korea*.
- Andersen, Lars Vabbersgaard, 2016, *Linear Elastodynamic Analysis*. DCE Lecture Notes No. 3 ISSN: 1901-7286. Aalborg University.
- API, 2011, *API Recommended Practise 2GEO*. API.
- , 2014, *API 2A-WSD*. API.
- Arany, L., S. Bhattachary, and J. H. G. Macdonald, 2010, “Soil nonlinearities and dynamic soil-structure interaction”. In:
- Birol, Dr. Fatih, 2018, “Electricity information 2018”. In: *Key world energy statistics*.
- Budhu, Muni, 2010, *Soil Mechanics and Foundations*. John Wiley & Sons, INC.
- Burd, Harvey J., Byron W. Byrne, Ross A. McAdam, Guy T. Houlsby, Chris M. Martin, William J. A. P. Beuckelaers, Lidija Zsrankovic, David M. G. Taborda, David M. Potts, Richard J. Jardine, Ken Gavin, Paul Doherty, David Igoe, Jesper Skov Gretlund, Miguel Pacheco Andrade, and Alastair Muir Wood, 2017, “Design aspects for monopile foundations”. In: *Proceedings of TC 209 Workshop - 19th ICSMGE, Seoul 20 September 2017*.
- Byrne, Byron W., Harvey Burd, Ross Mcadam, and Guy Tinmouth Houlsby, 2015, “New design methods for large diameter piles under lateral loading for offshore wind applications”. In: *Third International Symposium on Frontiers in Offshore Geotechnics (ISFOG 2015), At Oslo Norway*.
- Cook, Michael F. and J. Kim Vandiver, 1982, “Measured and Predicted Dunamic Response of a Single Pile Platform to Random Wave Excitation”. In: *OTC 4285*.
- Cook, Robert D., David S. Malkus, Michael E. Plesha, and Robert J. Witt, 2002, *Concepts and applications of finite element analysis*. Fourth edition ISBN: 978-0-471-35605-9. John Wiley & Sons inc.
- Damgaard, M., Lars Vabbersgaard Andersen, and L. B. Ibsen, 2014, “The importance of including dynamic soil-structure interaction into wind turbine simulation codes”. In: *Numerical Methods in Geotechnical Engineering – Hicks, Brinkgreve & Rohe (Eds)*.
-

- Damkilde, Lars, 2017, *Introduction to Structural Dynamics*. Aalborg University.
- Dansk Standard, 1983, *Norm for pælefunderede offshore stålkonstruktioner*. Dansk Standard.
- , 2009, *Wind turbines - Part 3: Design requirements for offshore wind turbines*. Dansk Standard.
- Darendeli, Mehmet Baris, 2001, *Development of New Family of Normalized Modulus Reduction and Material Damping Curves*.
- Desmond, Cian James, Jimmy Murphy, Lindert Blonk, and Wouter Haans, 2016, “Description of an 8 MW reference wind turbine”. In: *Conference Series 753 (2016) 092013*.
- Devriendt, Christof, Pieter Jan Jordaens, Gert De Sitter, and Patrick Guillaume, 2012, *Damping Estimation of Offshore Wind Turbine on a Monopile Foundation*.
- Devriendt, Christof and Wout Weijtjens, 2015, *The overall damping of an offshore wind turbine during different operating conditions*. Visited 2018-10-19. URL: <http://www.owi-lab.be/sites/default/files/poster106.pdf>.
- DNV GL group, 2017, *DNVGL-RP-C212*. DNV GL group.
- , 2018, *DNVGL-ST-0126*. DNV GL group.
- Fan, Chia-Cheng and James H. Long, 2005, “Assessment of existing methods for predicting soil response of laterally loaded piles in sand”. In: *Computers and Geotechnics 32 (2005) 274–289*.
- Gandomzadeh, A., M. P. Santisi d’Avila, J. F. Semblat, L. Lenti, and F. Bonilla, 2010, “Soil nonlinearities and dynamic soil-structure interaction”. In: *ECEE 2010, 14*.
- Guerreiro, P., S. Kontoe, and D. Taborda, 2012, “Comparative Study Of Stiffness Reduction And Damping Curves”. In: *15 WCEE Lisboa 2012*.
- Hundleby, Giles and Kate Freeman, 2017, *Unleashing Europe’s offshore wind potential - A new resource assessment*. Wind Europe.
- Irvine, Tom, 2010, *Bending frequencies of beams, rods, and pipes*. Tech. rep.
- Iwan, W. D., 1967, “On a class of models for the yielding behavior of continuous and composite systems”. In: *Journal of Applied Mechanics, 34*.
- Jensen, Bjarne Chr., Gunner Mohr, Asta Nicolajsen, Bo Mortensen, Henrik Bygbjerg, Lars Pilegaard Hansen, Hans Jørgen Larsen, Svend Ole Hansen, Dirch H. Bager, Eilif Svensson, Ejnar Søndergaard, Carsten Munk Plum, Hilmer Riberholt, Lars Zenke Hansen, Kaare K. B. Dahl, Henning Larsen, Per Goltermann, Jørgen S. Steenfelt, Carsten S. Sørensen, and Werner Bai, 2015, *Teknisk Ståbi*. 23. udgave ISBN: 978-87-571-2844-4. Nyt Teknisk Forlag.
- Jia, Jumbo, 2018, *Soil Dynamics and Foundation Modeling, Offshore and Earthquake Engineering*. Springer International Publishing AG 2018.
- Kallehave, Dan, Byron W. Byrne, Christian Le Blanc Thilsted, and Kristian Kousgaard Mikkelsen, 2015, *Optimization of monopiles for offshore wind turbines*.
- Kallehave, Dan, Christian Le Blanc Thilsted, and Morten Liingaard, 2012, *Modification of the API P-Y formulation of initial stiffness of sand*.
-

- Kirsch, Fabil, Thomas Richter, and Maria Coronel, 2014, “[GER] Geotechnische Aspekte bei der Gründungsbemessung von Offshore-Windenergieanlagen auf Monopfählen mit sehr großen Durchmessern”. In: *Stahlbau Spezial 2014*.
- Matlock, Hudson, 1970, *Correlation for Design of Laterally Loaded Piles in Soft Clay*.
- , 1979, *Fugro Internal Memorandum*.
- McGinty, Bob, 2016, *Traction Vectors*. Visited 2019-06-05. URL: <http://www.finiteelements.org/tractionvector.html>.
- Nielsen, Casper Østergaard, Francisco Manuel Garcia Rodriguez, Hariesh Arulanantham, Kasper Glittrup, Kenneth Christiansen, Lasse Riis Christiansen, and Thomas Skov-Pedersen, 2018, *Offshore Wind Turbine Foundations at Anholt*. Tech. rep.
- O’Neill, M. W. and J. M. Murchison, 1983, *An evaluation of p–y relationships in sands*.
- Østergaard, M. U., A. H. Augustesen, S. P. H. Sørensen, C. Kramhøft, and M. T. Larsen, 2019, “Modelling of Soil-Pile Interaction for Monopiles for Offshore Wind Turbines: Back-Calculation of Eigenfrequencies”. In:
- Page, Ana M., Kristoffer Skjolden Skau, Hans Petter Jostad, and Gudmund Reidar Eiksund, 2017, “A New Foundation Model for Integrated Analyses of Monopile-based Offshore Wind Turbines”. In: *14th Deep Sea Offshore Wind R&D Conference*.
- Petersen, Brian, Marty Pollack, Benjamin Connel, David Greeley, Dwight Davis, Charles Slavik, and Benjamin Goldman, 2010, *Evaluate the effect of turbine period of vibration requirements on structural design parameters: technical report of findings*. Applied Physical Science.
- Plaxis, 2017a, *Material Models Manual*. Plaxis.
- , 2017b, *Material Reference Manual*. Plaxis.
- , 2017c, *Scientific Manual*. Plaxis.
- Reese, Lymon C., William R. Cox, and Francis D. Koop, 1975, “Field testing and analysis of laterally loaded piles in stiff clay”. In: *Proceedings of the VII Annual Offshore Technology Conference, Houston, Texas*.
- Seidel, Marc, 2014, “Substructures for offshore wind turbines, current trends and developments”. In: *Festschrift Peter Schaumann, Hannover 2014*.
- Selot, Florian, Daniel Fraile, and Guy Brindley, 2019, *Offshore Wind in Europe*. Wind Europe.
- Shahan, Zachary, 2014, *History of Wind Turbines*. Visited 2019-02-07. URL: <https://www.renewableenergyworld.com/ugc/articles/2014/11/history-of-wind-turbines.html>.
- Sørensen, S. P. H., A. H. Augustesen, C. T. Leth, M. U. Østergaard, and M. Møller, 2017, “Consequences of p-y curve selection for monopile design for offshore wind turbine”. In: *OSIG 2017*.
- Stevens, J.B. and J.M.E Audibert, 1979, “Reexamination of p-y curve formulations”. In: *11th Annual Offshore Technology Conference, Houston, USA*.
-

-
- Tarp-Johansen, Niels Jacob, Lars Vabbersgaard Andersen, Erik Damgaard Christensen, Christian Mørch, Sten Frandsen, and Bjarne Kallesøe, 2009, “Comparing Sources of Damping of Cross-Wind Motion”. In: *European Offshore Wind 2009 Conference & Exhibition*.
- Wolf, Torben K., Kristian L. Rasmussen, Mette Hansen, Hanne Ravn Roesen, and Lars Bo Ibsen, 2013, “Assessment of p-y Curves from Numerical Methods for a non-Slender Monopile in Cohesionless Soil”. In: *DCE Technical Memorandum No. 024*.
- Zachert, Hauke, Torsten Wichtmann, and Theodoros Triantafyllidis, 2016, “Soil Structure Interaction of Foundations for Offshore Wind Turbines”. In: *2016 International Ocean and Polar Engineering Conference*.
-



Appendix

A	EOM SDOF OWT Model	173
B	FEM - Stage 2	175
C	Elasticity	179
D	SDOF Cantilever Beam	181
E	Soil Reaction Curves	187
F	FEM - Stage 3	189
G	Convergence of Extended Model ...	195
H	Modal Decoupling	201
I	<i>p</i>-<i>y</i> Curve Distribution	203
J	Plaxis 3D Theory	211
K	Convergence Analysis	219
L	Free Vibration Analysis Results	221
M	Extraction of <i>p</i>-<i>y</i> Curves	231

A. EOM SDOF OWT MODEL

The governing dynamic equation of motion (EOM) of a SDOF system is given by equation (A.1).

$$m\ddot{u} + c\dot{u} + ku = F(t) \quad (\text{A.1})$$

m	Mass
c	Damping
k	Stiffness
$F(t)$	Time dependent load
u	Displacement
\dot{u}	Velocity
\ddot{u}	Acceleration

Considering an OWT represented by a SDOF system with a harmonic varying load, the system can be represented by the mass on a stick seen in Figure A.1. Here m is the mass, u is the degree of freedom for the SDOF system, the stiffness, k , is representing the bending stiffness of the tower/stick itself, and the damping, c , is structural damping from the system. The load, $F(t)$, is defined as a harmonic load $P \cos(\omega_L t)$, where ω_L is the cyclic load frequency and P defines the magnitude of the harmonic load.

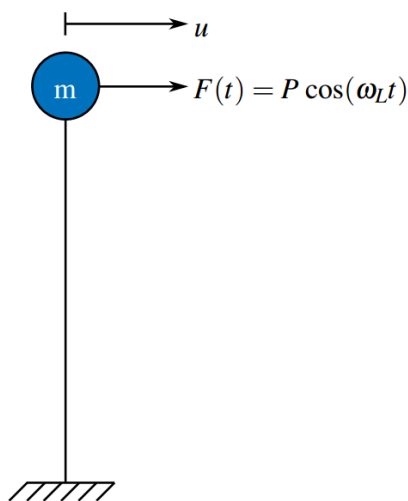


Figure A.1: SDOF system for an OWT with a harmonic varying load.

The EOM for the system shown in Figure A.1 is given in equation (A.2).

$$m\ddot{u} + c\dot{u} + ku = P \cos(\omega_L t) \quad (\text{A.2})$$

Solving the EOM defined in equation (A.2) leads to the solution of the system provided in equation (A.3). For further elaboration on the solution and the rest of the appendix, see Damkilde, 2017.

$$u(t) = \frac{P}{k} f_{amp} \cos(\omega_L t - \varphi) \quad (\text{A.3})$$

φ		Phase shift i.e. the delay between the loading and the displacement response
f_{amp}		Dynamic amplification factor

The phase shift is given by equation (A.4).

$$\varphi = \tan^{-1} \left(\frac{2\zeta \frac{\omega_L}{\omega_1}}{1 - \left(\frac{\omega_L}{\omega_1}\right)^2} \right) \quad (\text{A.4})$$

The dynamic amplification factor is given by equation (A.5).

$$f_{amp} = \sqrt{\frac{1}{\left(1 - \left(\frac{\omega_L}{\omega_1}\right)^2\right)^2 + \left(2\zeta \frac{\omega_L}{\omega_1}\right)^2}} \quad (\text{A.5})$$

ζ		The damping ratio
ω_1		The first cyclic eigenfrequency of the system (only one for SDOF systems)

The first cyclic eigenfrequency is given by equation (A.6).

$$\omega_1 = \sqrt{\frac{k}{m}} \quad (\text{A.6})$$

The damping ratio is given by equation (A.7).

$$\zeta = \frac{c}{2\sqrt{km}} \quad (\text{A.7})$$

It is seen from equation (A.3) and (A.5) that if the damping is neglected i.e. $\zeta = 0$, and if the cyclic load frequency and the cyclic eigenfrequency of the system are the same, then a singularity will appear and the response will in theory go to infinity.

B. FEM - STAGE 2

This appendix is not a cook book explaining how to program models exactly equal to the ones used in this thesis. Instead, it is highlighting some of the theory that is not covered in the main report. The appendix is based on R. D. Cook et al., 2002. In Stage 2, two different models are used, the models are illustrated in Figure B.1. The blue ball on top of the beam is illustrating a lumped mass that covers the weight of the nacelle, blades and rotor for the OWT.

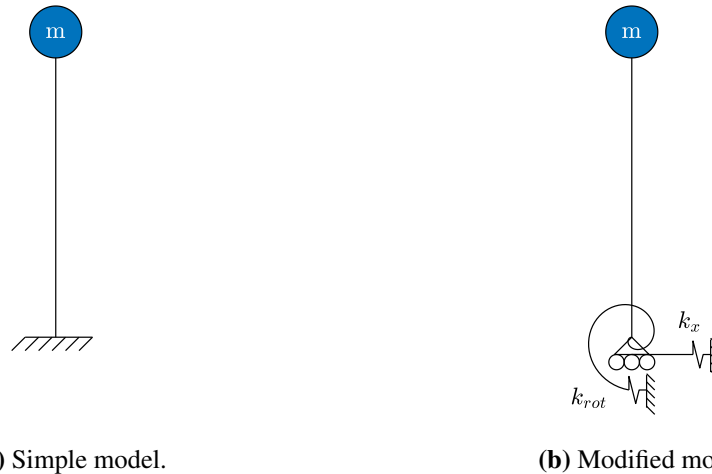


Figure B.1: Illustration of the two models of a stick with a mass at the top.

The difference between the simple and the modified model is explained in the main report.

B.1 Model Description

The model is a simple 1D FE model that is modelled with Bernoulli-Euler beam elements as seen in Figure B.2.

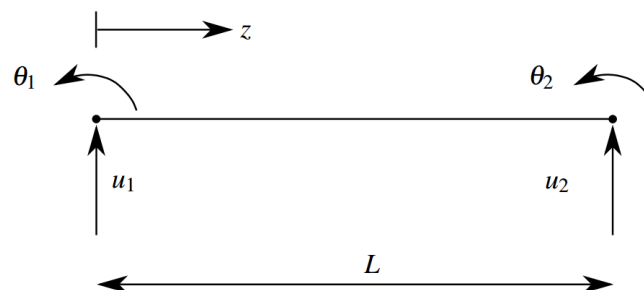


Figure B.2: Illustration of beam element with two degrees of freedom per node.

The Bernoulli-Euler beam element has the shape functions illustrated in Figure B.3.

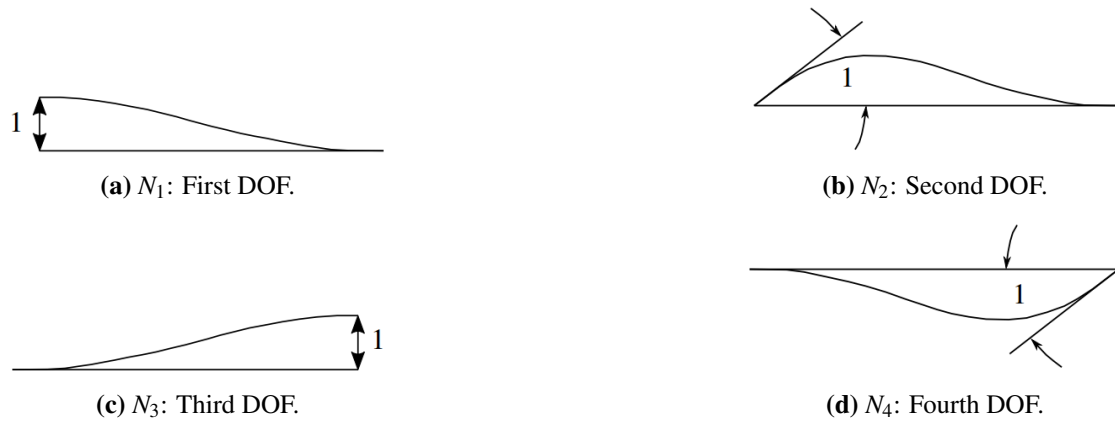


Figure B.3: The different shape functions for the DOFs.

The shape functions are third order polynomials given in Table B.1, together with the boundary conditions for each shape function.

Table B.1: Shape functions and boundary conditions.

Shape function	At $x = 0$		At $x = L$	
	N_i	$N_{i,x}$	N_i	$N_{i,x}$
$N_1(x) = 1 - \frac{3x^2}{L^2} + \frac{2x^3}{L^3}$	1	0	0	0
$N_2(x) = x - \frac{2x^2}{L} + \frac{x^3}{L^2}$	0	1	0	0
$N_3(x) = \frac{3x^2}{L^2} - \frac{2x^3}{L^3}$	0	0	1	0
$N_4(x) = -\frac{x^2}{L} + \frac{x^3}{L^2}$	0	0	0	1

The shape functions are combined into the displacement interpolation matrix given by equation (B.1).

$$[\mathbf{N}] = \begin{bmatrix} N_1 & N_2 & N_3 & N_4 \end{bmatrix} \quad (\text{B.1})$$

B.2 Model Purpose

The purpose of the simple 1D FE model is to determine the eigenfrequencies of the system. To determine the eigenfrequencies an eigenvalue problem has to be solved. The eigenvalue problem can be seen in equations (B.2).

$$\det([\mathbf{K}] - \omega^2[\mathbf{M}]) = 0 \quad (\text{B.2})$$

$[\mathbf{K}]$	Global stiffness matrix
$[\mathbf{M}]$	Global mass matrix
ω	Cyclic eigenfrequencies

B.3 Setting up Stiffness Matrix

The global stiffness matrix, $[\mathbf{K}]$, is a matrix combining the stiffness matrices from all beam elements into one full stiffness matrix. The local stiffness matrices for beam elements are calculated by equation (B.3).

$$[\mathbf{k}] = \int_V [\mathbf{B}]^T [\mathbf{D}] [\mathbf{B}] dV \quad (\text{B.3})$$

$[\mathbf{B}]$		Strain interpolation matrix
$[\mathbf{D}]$		Constitutive matrix
V		Volume

The constitutive matrix in this case is the bending stiffness given by equation (B.4).

$$[\mathbf{D}] = EI \quad (\text{B.4})$$

E		Young's modulus
I		Area moment of inertia

The strain interpolation matrix is found by differentiating the displacement interpolation matrix. A displacement interpolation matrix related to bending needs to be differentiated twice, which gives the strain interpolation matrix given in equation (B.5).

$$[\mathbf{B}] = \frac{d^2}{dx^2} [\mathbf{N}] = \left[\frac{d^2}{dx^2} N_1 \quad \frac{d^2}{dx^2} N_2 \quad \frac{d^2}{dx^2} N_3 \quad \frac{d^2}{dx^2} N_4 \right] \quad (\text{B.5})$$

B.4 Setting up Mass Matrix

The global mass matrix, $[\mathbf{M}]$, is like the global stiffness matrix a combination of local matrices. The local mass matrix used is the continuous mass matrix given by equation (B.6).

$$[\mathbf{m}] = \int_V \rho [\mathbf{N}]^T [\mathbf{N}] dV \quad (\text{B.6})$$

$[\mathbf{N}]$		Displacement interpolation matrix
ρ		Density

C. ELASTICITY

To be able to watch the influence of different input parameters, the elasticity between the input and output is calculated. The elasticity is defined as the ratio between the percentage change in the input and output, see equation (C.1).

$$E_{A-B} = \frac{\text{Relative change in output}}{\text{Relative change in input}} \quad (\text{C.1})$$

Here E_{A-B} defines the elasticity in the range from A to B, which is illustrated in Figure C.1.

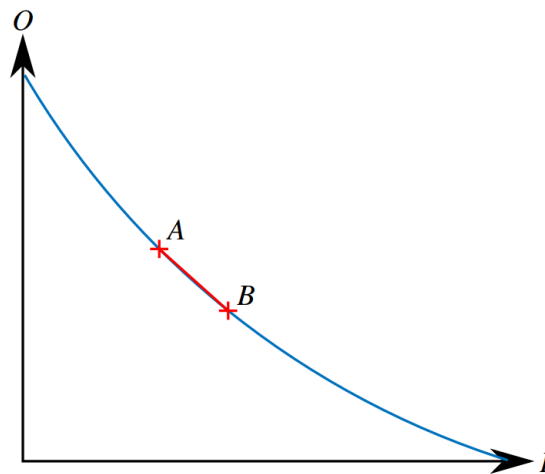


Figure C.1: Principle graph to illustrate the elasticity between input and output.

I is the input parameter and O is the output parameter. In this report the first eigenfrequency could be the output and the input could be the height of the turbine tower. The elasticity from $A - B$ is then calculated as:

$$E_{A-B} = \frac{\left(\frac{\Delta O_{A-B}}{O_{AVG_{A-B}}} \cdot 100 \right)}{\left(\frac{\Delta I_{A-B}}{I_{AVG_{A-B}}} \cdot 100 \right)} \quad (\text{C.2})$$

ΔO_{A-B}	The change in the output parameter in the range A-B
$O_{AVG_{A-B}}$	Mean value of the output parameter in the range A-B
ΔI_{A-B}	The change in the input parameter in the range A-B
$I_{AVG_{A-B}}$	Mean value of the input parameter in the range A-B

D. SDOF CANTILEVER BEAM

D.1 Eigenfrequency of Cantilever Beam

In this section an approximation for the first eigenfrequency of a cantilever beam is derived. The cantilever beam has a distributed load from the self weight of the beam, ρ , and a mass, m , at the end. The cantilever beam is illustrated in Figure D.1.

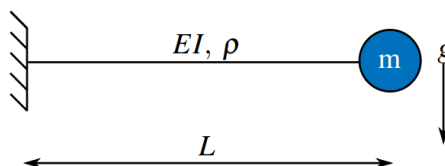


Figure D.1: Cantilever beam with a point mass at the end.

E	Young's modulus
I	Area moment of inertia
m	Point mass
g	Gravity
L	Length of the cantilever beam

In order to obtain a solution for the cantilever beam where both the mass of the beam and the point mass are considered, each case is considered separately and superposition is then used to obtain the solution for the full system.

D.1.1 Weightless Cantilever Beam with End Mass

The solution for a cantilever beam with end mass is based in Irvine, 2010. Figure D.2 illustrates a free body diagram of the cantilever beam presented in Figure D.1.

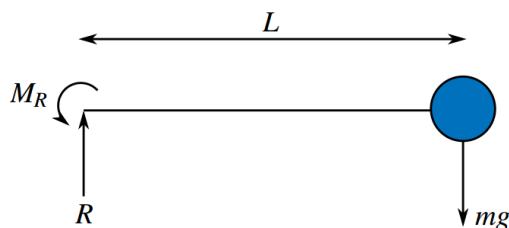


Figure D.2: Free body diagram of cantilever beam.

M_R	Moment reaction from the support
R	Vertical reaction from the support

Newton's second law for static equilibrium is applied.

$$\sum F_y \uparrow^+ = 0 = R - mg \quad \Rightarrow \quad R = mg \quad (\text{D.1})$$

$$\sum \hat{M}_{left}^+ = 0 = M_R - mgL \quad \Rightarrow \quad M_R = mgL \quad (\text{D.2})$$

A beam segment as illustrated in Figure D.3 is considered.

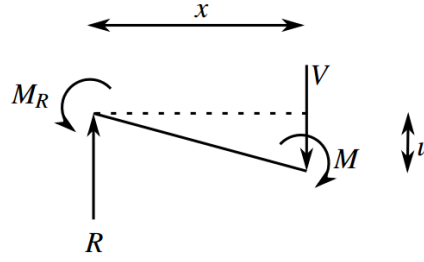


Figure D.3: Cut at coordinate x .

u	Displacement at coordinate x
M	Bending moment
V	Shear force

Moment equilibrium around the right end of the beam segment.

$$\sum \overset{\curvearrowright}{M}_{right} = 0 = M_R - Rx - M \quad \Rightarrow \quad M = M_R - Rx \quad (\text{D.3})$$

Bernoulli-Euler's beam theory yields a relation between the bending moment, M , and the displacement, u .

$$M = EI \frac{d^2 u}{dx^2} \quad \Rightarrow \quad M_R - Rx = EI \frac{d^2 u}{dx^2} \quad (\text{D.4})$$

↓

$$EI \frac{d^2 u}{dx^2} = mgL - mgx = mg(L - x) \quad \Rightarrow \quad \frac{d^2 u}{dx^2} = \left(\frac{mg}{EI} \right) (L - x) \quad (\text{D.5})$$

This is integrated twice to obtain an expression for the displacement $u(x)$.

$$\frac{du}{dx} = \frac{mg}{EI} \left(Lx - \left(\frac{x^2}{2} \right) \right) + a \quad (\text{D.6})$$

$$u(x) = \frac{mg}{EI} \left(L \left(\frac{x^2}{2} \right) - \left(\frac{x^3}{6} \right) \right) + ax + b \quad (\text{D.7})$$

The integration constants a and b are solved from the boundary conditions of the cantilever beam, where it is known that at $x = 0$ there is no rotation or displacement i.e.:

$$u(0) = 0 \quad \Rightarrow \quad b = 0 \quad (\text{D.8})$$

$$u'(0) = 0 \quad \Rightarrow \quad a = 0 \quad (\text{D.9})$$

This leads to the following expression for the displacement at x , and as the displacement only is desired at the full length, L , the expression becomes:

$$u(x) = \frac{mg}{EI} \left(L \left(\frac{x^2}{2} \right) - \left(\frac{x^3}{6} \right) \right) \quad (\text{D.10})$$

↓

$$u(L) = \frac{mg}{EI} \left(L \left(\frac{L^2}{2} \right) - \left(\frac{L^3}{6} \right) \right) = \frac{mgL^3}{3EI} \quad (\text{D.11})$$

Hooke's law is used to relate force, stiffness and displacement of the SDOF cantilever system. It is also known the force, F , is equal to the mass, m , times gravity, g .

$$F = ku \quad \Rightarrow \quad k = \frac{F}{u} \quad (\text{D.12})$$

$$\Downarrow$$

$$k = \frac{mg}{\left(\frac{mgL^3}{3EI}\right)} = \frac{3EI}{L^3} \quad (\text{D.13})$$

The eigenfrequency of a SDOF system with a weightless cantilever beam and a point mass is thereby given by:

$$f_1 = \frac{1}{2\pi} \sqrt{\frac{k}{m}} = \frac{1}{2\pi} \sqrt{\frac{3EI}{mL^3}} \quad (\text{D.14})$$

D.1.2 Cantilever Beam with Beam Mass

A cantilever beam with a mass per length, μ , is considered, where the cross section is uniform. In order to use the principle of superposition of the two systems, the distributed mass per length has to be related to a point mass at the end of the beam. This point mass is called the effective mass, and is a percentage of the total distributed mass along the beam. The effective mass is calculated such that the response of a cantilever beam with distributed mass is identical to the response of a cantilever beam without distributed mass but with the effective mass applied as a point mass at the end of the beam. The solution for this case is based on Irvine, 2010.

In general the approach for determining the effective mass is to set up an expression for the total potential energy and the total kinetic energy in the beam. These expressions for the different energies are set equal to each other and the cyclic eigenfrequency, ω , is isolated. The expression for ω is then transformed to the eigenfrequency, f_1 , and reduced. The expression for the eigenfrequency can be seen in equation (D.15). For further derivation of this expression, see Irvine, 2010.

$$f_1 \approx \left(\frac{1}{2\pi}\right) \left(\frac{3.664}{L^2}\right) \sqrt{\frac{EI}{\mu}} \quad (\text{D.15})$$

The terms in equation (D.16), (D.17) and (D.18) is known, and from these, equation (D.19) can be set up for the effective mass.

$$f_1 = \frac{\omega}{2\pi} \quad (\text{D.16})$$

$$\omega = \sqrt{\frac{k}{m}} \quad (\text{D.17})$$

$$k = \frac{3EI}{L^3} \quad (\text{D.18})$$

$$m_{eff} = \frac{k}{(2\pi f_1)^2} = \frac{3EI}{L^3(2\pi f_1)^2} \quad (\text{D.19})$$

Equation (D.15) is substituted into equation (D.19) and reduced, which results in equation (D.20) for the effective mass.

$$m_{eff} = 0.2235\mu L \quad (D.20)$$

D.1.3 Cantilever Beam with Beam- and Point Mass

The total mass at the end of the beam is obtained from the sum of the point load and the effective mass obtained from Appendix D.1.2. [Irvine, 2010]

$$m_t = 0.2235\mu L + m \quad (D.21)$$

The total mass is substituted into the solution for the cantilever beam with an end mass, which was obtained from equation (D.14) in Appendix D.1.1, where the mass used was the effective mass. This gives equation (D.22) for the first eigenfrequency of the SDOF system. [Irvine, 2010]

$$f_1 \approx \frac{1}{2\pi} \sqrt{\frac{3EI}{(0.2235\mu L + m)L^3}} \quad (D.22)$$

The parameter for the mass per unit length of the tower, μ , can be determined from the density, ρ , and the cross-section area for the tower, A , see equation (D.23).

$$\mu = A\rho \quad (D.23)$$

The cross-section area can be determined from the area of a circle with the inner diameter subtracted from the area determined from the outer diameter. This can be seen from the following derivation, where the expression is reduced.

$$A = \left(\frac{d}{2}\right)^2 \pi - \left(\frac{d}{2} - t\right)^2 \pi = \left(\left(\frac{d}{2}\right)^2 - \left(\frac{d}{2} - t\right)^2\right) \pi \quad (D.24)$$

$$\Downarrow$$

$$= \left(\frac{d^2}{4} - \left(\frac{d^2}{4} + t^2 - 2\frac{dt}{2}\right)\right) \pi = (-t^2 + dt) \pi \quad (D.25)$$

This results in the mass per unit length, μ , is given as.

$$\mu = \rho \pi (dt - t^2) \quad (D.26)$$

The final equation for the first eigenfrequency can then be derived as seen in equation (D.27).

$$f_1 \approx \frac{1}{2\pi} \sqrt{\frac{3EI}{(0.2235L\rho \pi (dt - t^2) + m)L^3}} \quad (D.27)$$

D.2 Area Moment of Inertia

The derivation of the expression for the area moment of inertia, I , used in the report can be seen below.

The first expression can be seen in equation (D.28), where the different radii used can be seen in Figure D.4.

$$I = \frac{\pi}{4} (r_2^4 - r_1^4) \quad (\text{D.28})$$

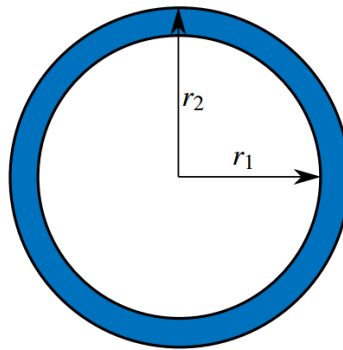


Figure D.4: Cross section of a tube, with inner and outer radius respectively r_1 and r_2 .

The equation is rewritten for only depending on the parameters used in the report.

$$I = \frac{\pi}{4} (r_2^4 - r_1^4) = \frac{\pi}{4} \left(\left(\frac{d}{2} \right)^4 - \left(\frac{d}{2} - t \right)^4 \right) \quad (\text{D.29})$$

↓

$$I = \frac{\pi}{4} \left(\frac{d^4}{16} - \frac{(d-2t)^4}{16} \right) = \frac{\pi}{64} (d^4 - (d-2t)^4) \quad (\text{D.30})$$

E. SOIL REACTION CURVES

E.1 Lateral Resistance - Stiff Clay

The determination of the A -factor can be made from Figure E.1.

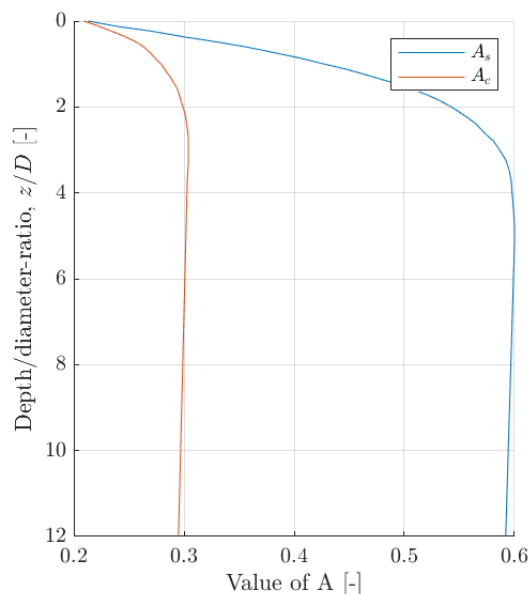


Figure E.1: Variation of the constants A_s and A_c in regards to the depth-diameter-ratio, z/D [Reese, Cox, and Koop, 1975].

E.2 Lateral Resistance - Sand

The C -constants used in the estimation of the ultimate lateral soil resistance for sand can be determined by the following equations:

$$C_1 = \frac{(\tan \beta)^2 \tan \alpha}{\tan(\beta - \phi')} + K_0 \left(\frac{\tan \phi' \sin \beta}{\cos \alpha \tan(\beta - \phi')} + \tan \beta (\tan \phi' \sin \beta - \tan \alpha) \right) \quad (\text{E.1})$$

$$C_2 = \frac{\tan \beta}{\tan(\beta - \phi')} - K_a \quad (\text{E.2})$$

$$C_3 = K_a \left((\tan \beta)^8 - 1 \right) + K_0 \tan \phi' (\tan \beta)^4 \quad (\text{E.3})$$

Here ϕ' is the effective angle of internal friction, and the rest of the parameters are determined below.

$$\alpha = \frac{\phi'}{2} \quad (\text{E.4})$$

$$\beta = 45 + \frac{\phi'}{2} \quad (\text{E.5})$$

$$K_0 = 0.4 \quad (\text{E.6})$$

$$K_a = \frac{1 - \sin \phi'}{1 + \sin \phi'} \quad (\text{E.7})$$

The variation of the different C -constants, when changing the effective angle of internal friction can be seen in Figure E.2.

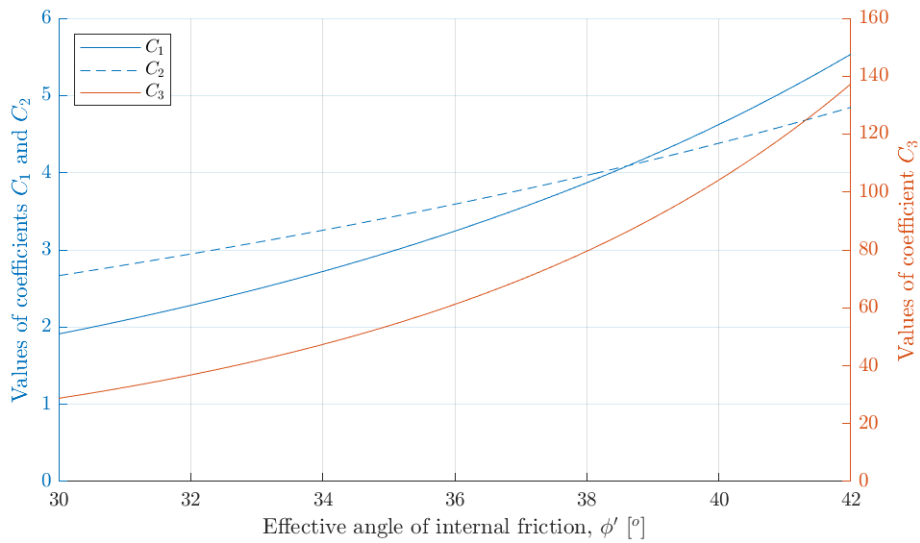


Figure E.2: Variation of the C -coefficients as a function of the effective angle of internal friction, ϕ' .

The initial modulus of subgrade reaction can be determined from Figure E.3.

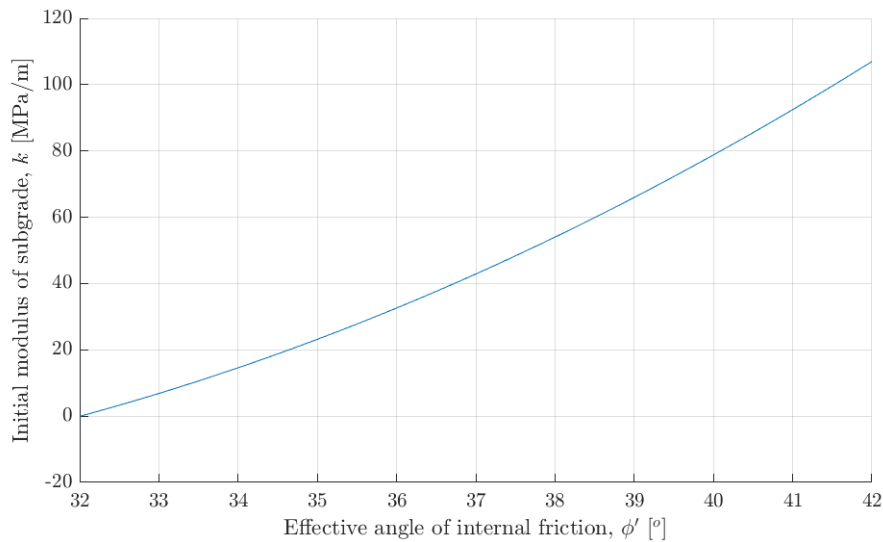


Figure E.3: Variation of the initial modulus of subgrade, k , as a function of the effective angle of internal friction, ϕ' .

F. FEM - STAGE 3

This appendix is not a cook book explaining how to program models exactly equal to the ones used in this thesis. It is instead highlighting some of the theory that is not covered in the main report. The appendix is based on R. D. Cook et al., 2002. In Stage 3 the model is different from the one used in Stage 2, as the pile is now submerged into the soil, and the stiffness of the soil is represented by springs. The model is illustrated in Figure F.1.

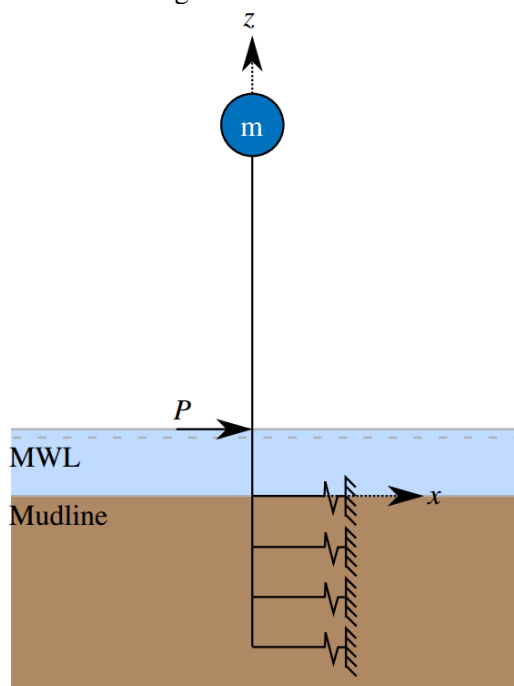


Figure F.1: Illustration of the Extended Model.

F.1 Model Description

The model illustrated in Figure F.1 is modelled with the same beam elements as used in Stage 2, see Appendix B. Besides the beam elements, the Stage 3 model is modelled with distributed springs below mudline, to represent the stiffness from the soil. This is done using the Winkler approach, which is described in the following section, and the stiffness from each spring comes from the API p - y curves presented in Chapter 5.

F.1.1 Winkler Beam

A Winkler beam is a beam resting on a infinite number of springs, that only acts in the direction normal to the beam element. An illustration of a beam element with the length L , resting on springs normal to the longitudinal direction of the beam, is illustrated in Figure F.2.

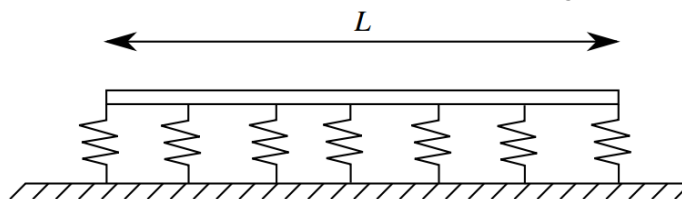


Figure F.2: Illustration of a Winkler beam element.

As an infinite number of springs is not possible for FE models, a finite number is chosen, i.e. a spring is attached at every node of a beam element. To calculate the stiffness of each spring the integral in equation (F.1) is used, to calculate the addition of stiffness to each beam element.

$$[\mathbf{k}_{py}] = \int_L \{\mathbf{N}\}^T \beta \{\mathbf{N}\} dL \quad (\text{F.1})$$

$\{\mathbf{N}\}$	Displacement interpolation matrix
β	Soil-structure stiffness
L	Beam element length

The soil-structure stiffness is the slope of the p - y curve, which can either be the tangential- or the secant slope of the curve according to a given displacement.

F.1.1.1 Numerical use of Winkler

A numerical integration will be performed based on equation (F.1), resulting in equation (F.2).

$$[\mathbf{k}_{py}] = \sum_{i=1}^{n_{int}} \{\mathbf{N}\}^T \beta \{\mathbf{N}\} dL \quad (\text{F.2})$$

Figure F.3 illustrates a single beam element, divided into 4 sub elements. Each subelement has the length dL . Dividing a single beam element into 4 subelements results in 4 integration points, illustrated in Figure F.3, i.e. $n_{int} = 4$.

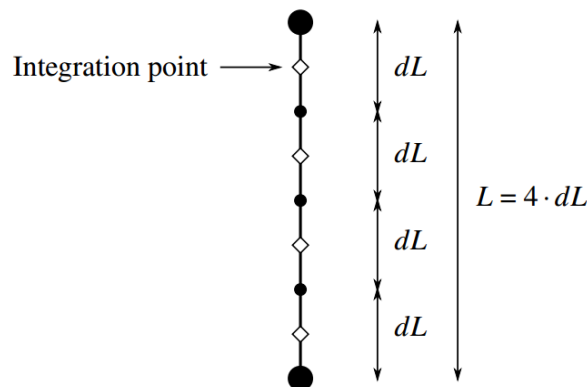


Figure F.3: Illustration of a single beam element. The white rhombi with the black outline shows the integration points used for the numerical integration.

F.2 Model Purpose

The purpose of the 1D FE model in Stage 3 is to integrate the soil into the model and analyse how this affects the eigenfrequencies of the system. The eigenvalue is solved exactly as in Stage 2, just with a different stiffness- and mass matrix.

F.3 Stiffness Matrix

The global stiffness matrix in Stage 3 is a combination of the Bernoulli-Euler beam stiffness and the soil stiffness from the p - y curves as stated in equation (F.3).

$$[\mathbf{K}] = [\mathbf{K}_B] + [\mathbf{K}_{py}] \quad (\text{F.3})$$

$[\mathbf{K}_B]$ | Bernoulli-Euler stiffness matrix, given in equation (B.3) page 177
 $[\mathbf{K}_{py}]$ | p - y stiffness matrix, given in equation (F.1)

F.4 Mass Matrix

The Stage 3 model differs from the Stage 2 model by taking water and soil into consideration. This results in the influence from these have to be added to the global mass matrix. In Stage 2 the mass matrix was a combination of the lumped mass, representing nacelle, hub and blades and the mass from the beam elements themselves, where in Stage 3, the soil and water inside the pile has to be added together with the added mass for the part of the pile that is moving in the water. An illustration of the added masses can be seen in Figure F.4.

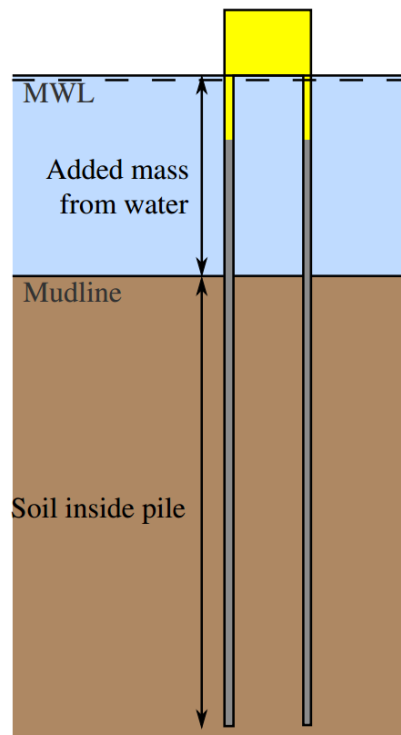


Figure F.4: Illustration of the positions for the different masses that are added to the global mass matrix.

F.4.1 Added Mass from Water

The added mass from the water around the pile is corresponding to the inertia added to the system as a result of an accelerating body is moving the surrounding fluid as it moves through it. The

movement is a result of the body and the fluid can not be at the same physical space simultaneously. The added mass per unit length for a cylinder can be calculated from equation (F.4) [Dansk Standard, 1983].

$$m_{add} = \rho(1 + C_a)A \quad (\text{F.4})$$

Here the added mass coefficient, C_a , can be found from standard tables to the value 1.0 and the area of the cross section, A , is found to be $\pi(d/2)^2$. The division of the mass into the nodes is then done with the use of integration.

F.4.2 Extra Mass from Water and Soil Inside Pile

The extra masses that has to be substituted into the global mass matrix are calculated as the continuous mass matrix used for the beam elements as explained in Appendix B.4. The soil levels inside the pile are assumed the same as the layers outside the pile.

F.5 Soil-Structure Stiffness

As the p - y curves used for determining the soil-structure stiffness are non-linear, the p - y stiffness matrix has to be obtained by a residual calculation. In this case the residual is an expression for the imbalance between the external and internal loads in the FE calculation. The internal loads are given by equation (F.5).

$$\{\mathbf{F}_I\} = [\mathbf{K}]\{\mathbf{u}\} \quad (\text{F.5})$$

The residual then becomes as stated in equation (F.6).

$$\{\mathbf{r}\} = \{\mathbf{F}_E\} - \{\mathbf{F}_I\} \quad (\text{F.6})$$

$[\mathbf{K}]$		Global stiffness matrix
$\{\mathbf{u}\}$		Global displacement vector
$\{\mathbf{F}_E\}$		Global external load vector

F.5.1 Residual Algorithm

In this thesis a load P is attached to the node in the height of the mean water level. This load is used for determining the tolerance for the residual. The tolerance is set to:

$$tolerance = \max \begin{cases} 1 \text{ N} \\ P \cdot 10^{-6} \end{cases} \quad (\text{F.7})$$

The residual is calculated using the Newton-Raphson method. The goal is to obtain the correct deformation vector, according to the external load P . To solve this residual algorithm some input has to be predefined. The predefined input and the algorithm itself can be seen in Algorithm 1.

Algorithm 1: Solving the residual using Newton-Raphson iteration.

Predefined input

$\{\mathbf{F}_E\}$	External load P at mean water level
$\{\mathbf{u}\} = \{\mathbf{0}\}$	Initial displacement to start the algorithm
$[\mathbf{K}_B]$	Bernoulli-Euler stiffness of the pile
$\{\mathbf{F}_I\} = \{\mathbf{0}\}$	Initial internal load vector
$\{\mathbf{r}\} = \{\mathbf{F}_E\} - \{\mathbf{F}_I\}$	Initial residual according to external and internal loads
$[\mathbf{K}_{py}]$	Initial soil-structure stiffness at $\{\mathbf{u}\} = \{\mathbf{0}\}$
$[\mathbf{K}] = [\mathbf{K}_B] + [\mathbf{K}_{py}]$	Initial system stiffness matrix

Solving the residual using Newton-Raphson

while $\{\mathbf{r}\} > \textit{tolerance}$

Calculation of $\{\Delta\mathbf{u}\}$ according to current stiffness and imbalance in internal and external forces

$$\{\Delta\mathbf{u}\} = [\mathbf{K}]^{-1} \{\mathbf{r}\}$$

Updating the displacement vector $\{\mathbf{u}\}$

$$\{\mathbf{u}\} = \{\mathbf{u}\} + \{\Delta\mathbf{u}\}$$

Updating the soil structure stiffness $[\mathbf{K}_{py}]$ according to current displacement $\{\mathbf{u}\}$ using the tangential stiffness from the p - y curves

$$[\mathbf{K}_{py}] = [\mathbf{K}_{py}] (\{\mathbf{u}\})$$

Update the system stiffness $[\mathbf{K}]$

$$[\mathbf{K}] = [\mathbf{K}_B] + [\mathbf{K}_{py}]$$

Update the internal loads $\{\mathbf{F}_I\}$

$$\{\mathbf{F}_I\} = [\mathbf{K}] \{\mathbf{u}\}$$

Update the residual $\{\mathbf{r}\}$

$$\{\mathbf{r}\} = \{\mathbf{F}_E\} - \{\mathbf{F}_I\}$$

end

G. CONVERGENCE OF EXTENDED MODEL

In this chapter, all of the convergence analyses are presented. Only the most relevant ones are presented in the main rapport.

G.1 Sand

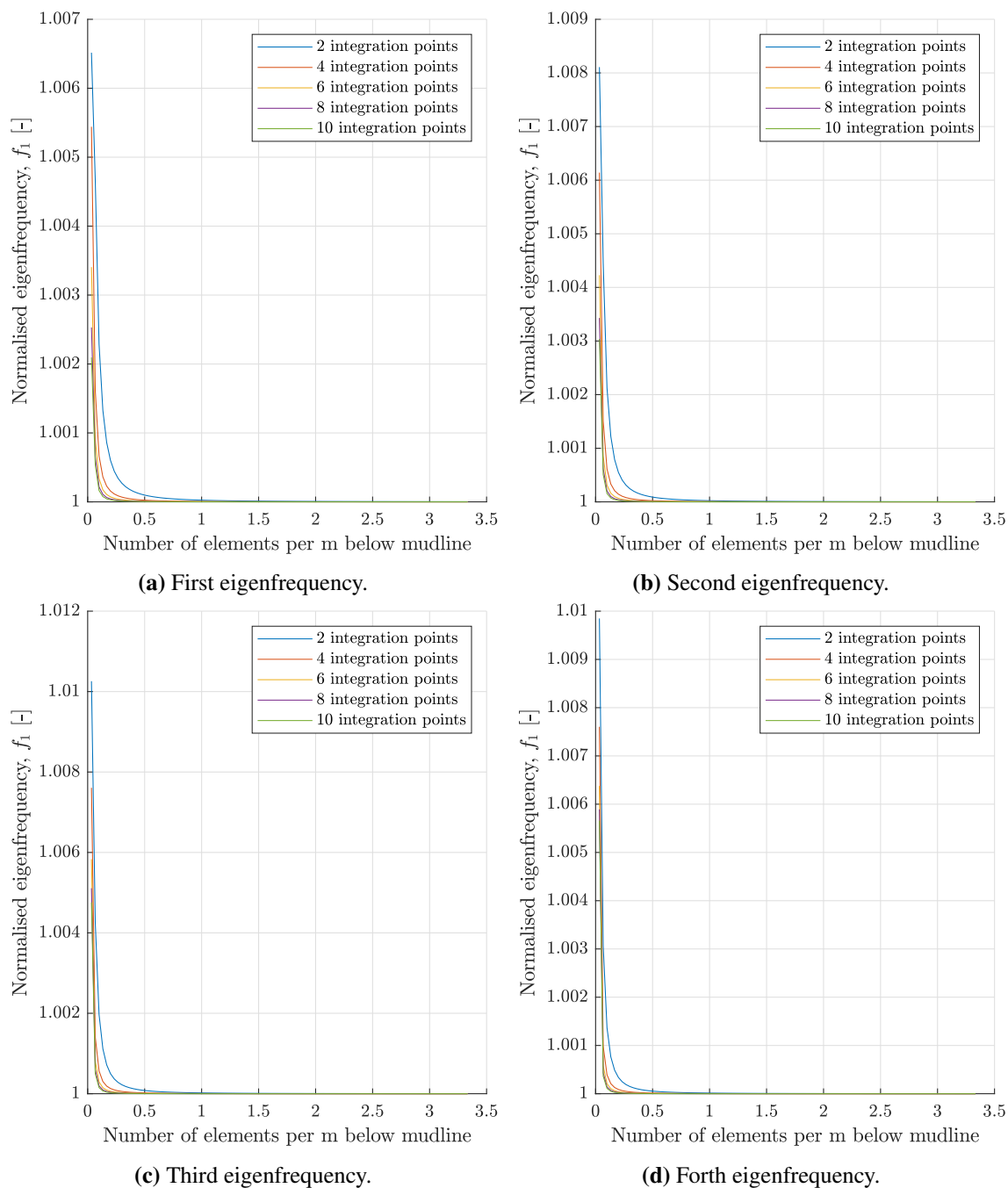


Figure G.1: Convergence analysis of the number of elements and integration points below the mudline in regards to the first four eigenfrequencies.

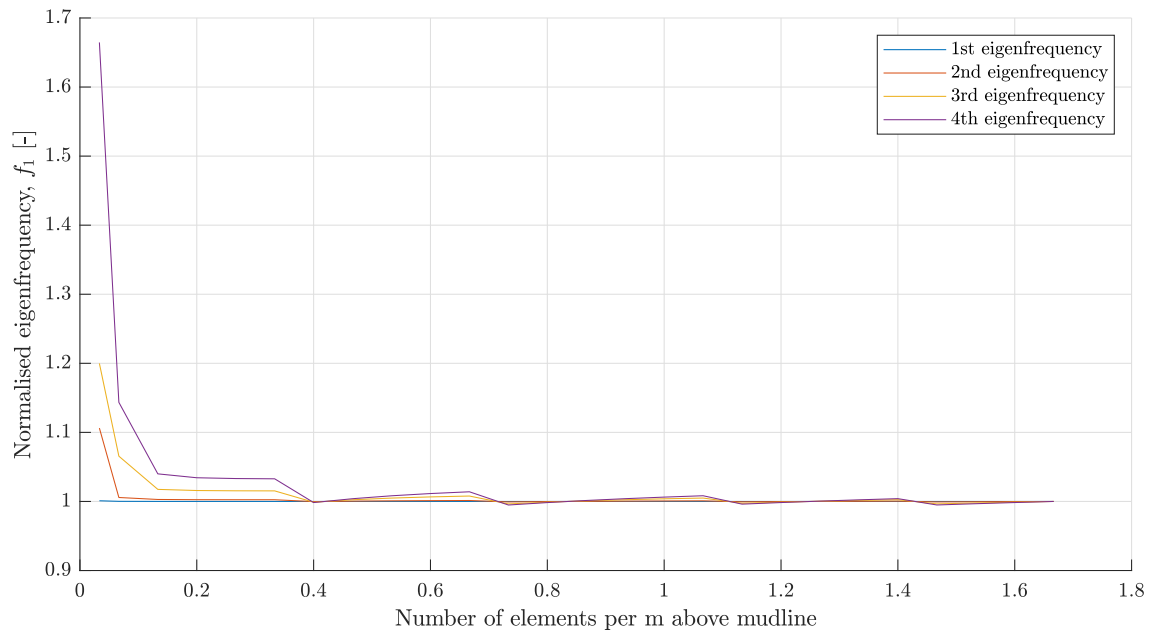


Figure G.2: Convergence analysis above the mudline in sand performed by the Extended Model.

G.2 Soft Clay

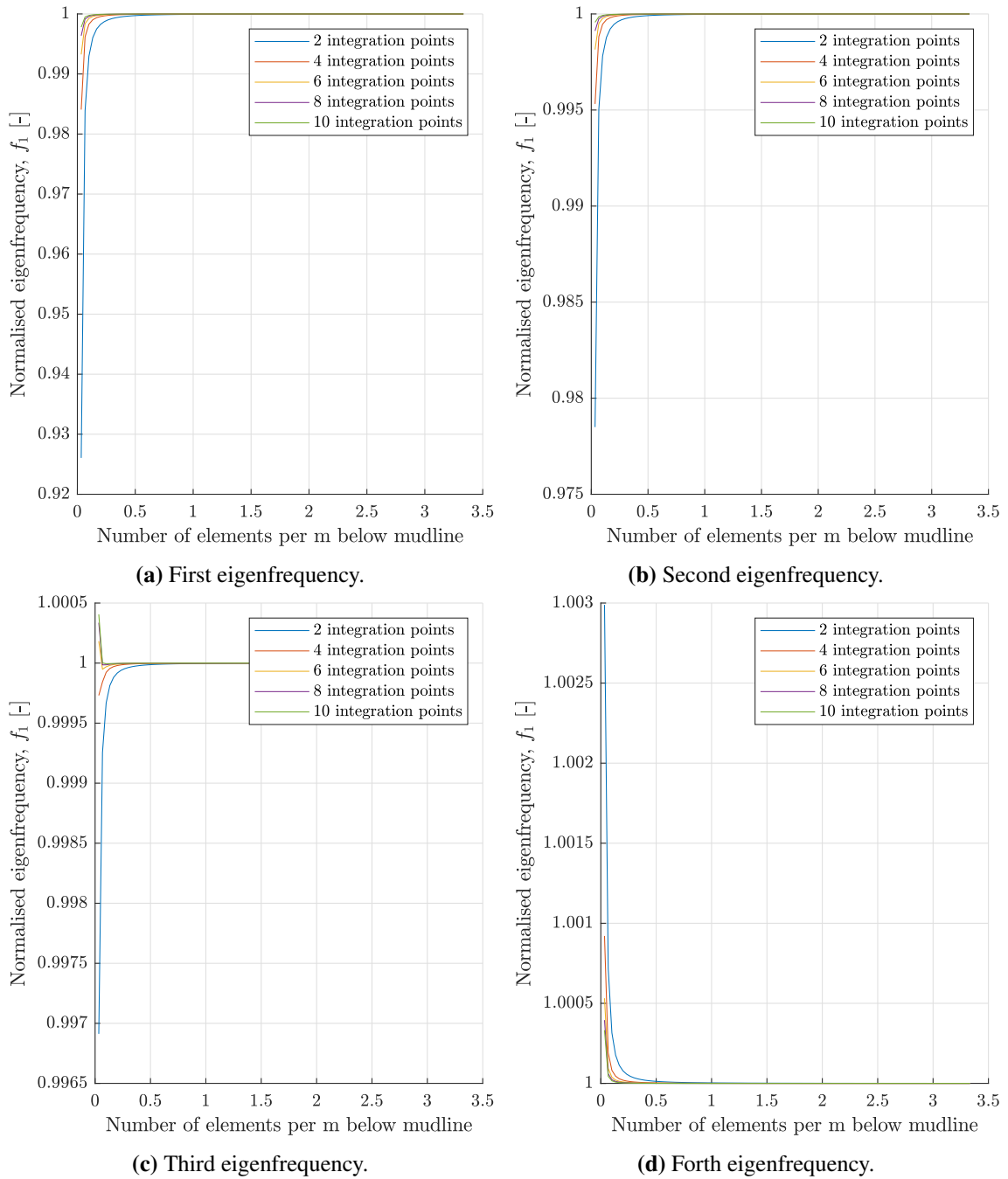


Figure G.3: Convergence analysis of the number of elements and integration points below the mudline in regards to the first four eigenfrequencies.

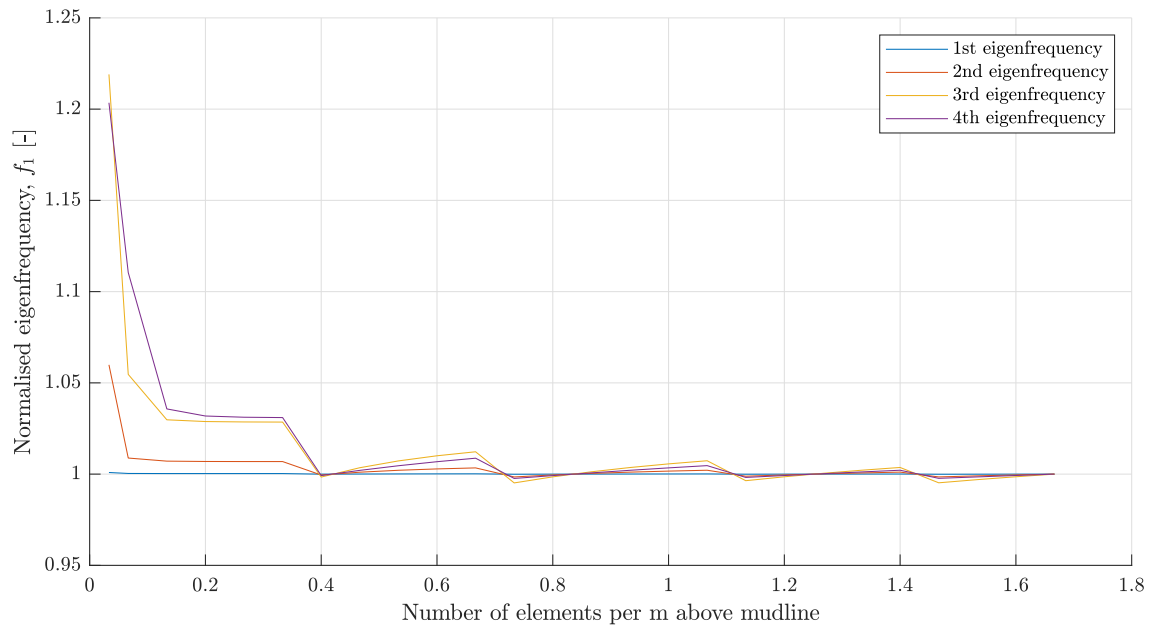


Figure G.4: Convergence analysis above the mudline in soft clay performed by the Extended Model.

G.3 Stiff Clay

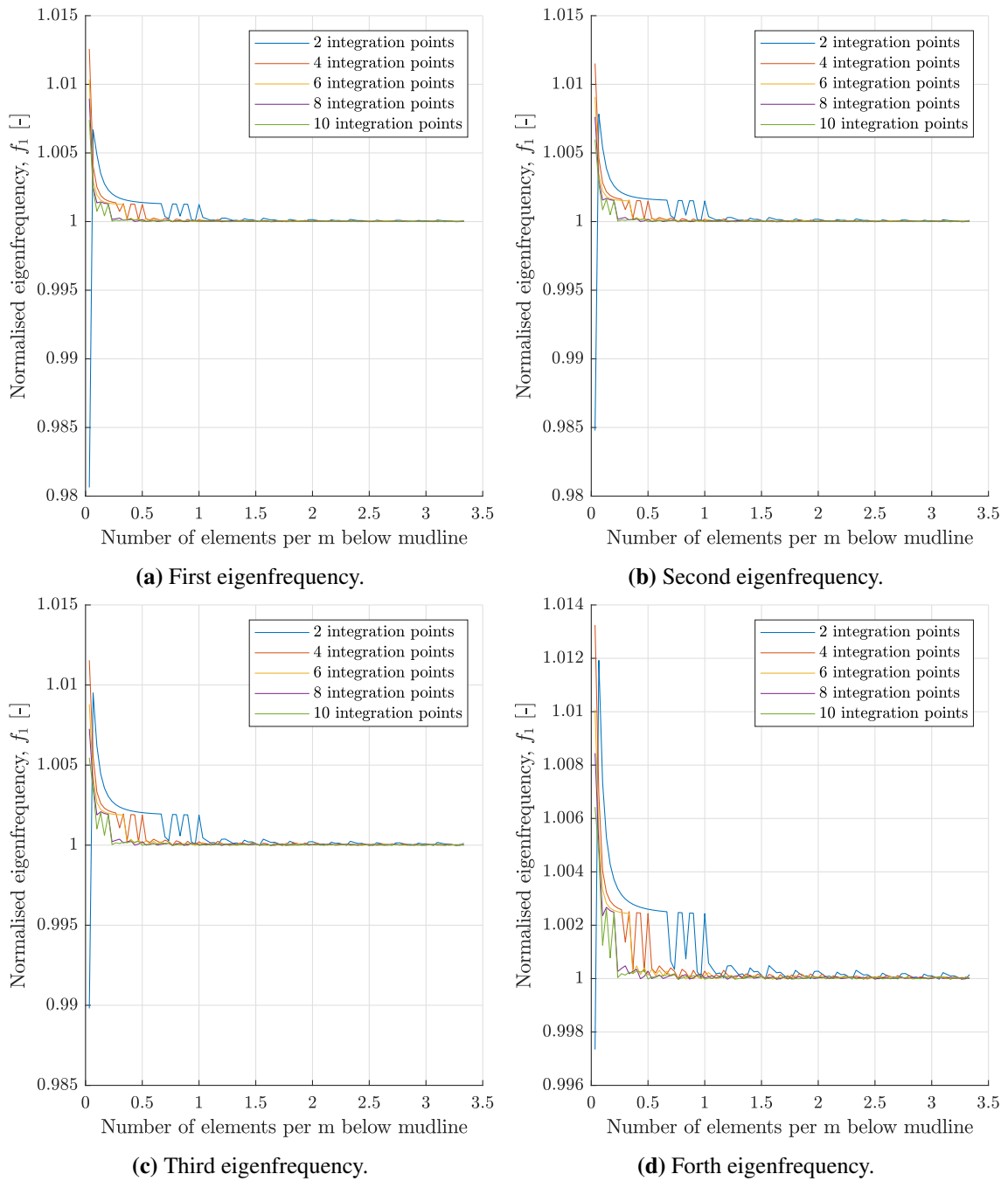


Figure G.5: Convergence analysis of the number of elements and integration points below the mudline in regards to the first four eigenfrequencies.

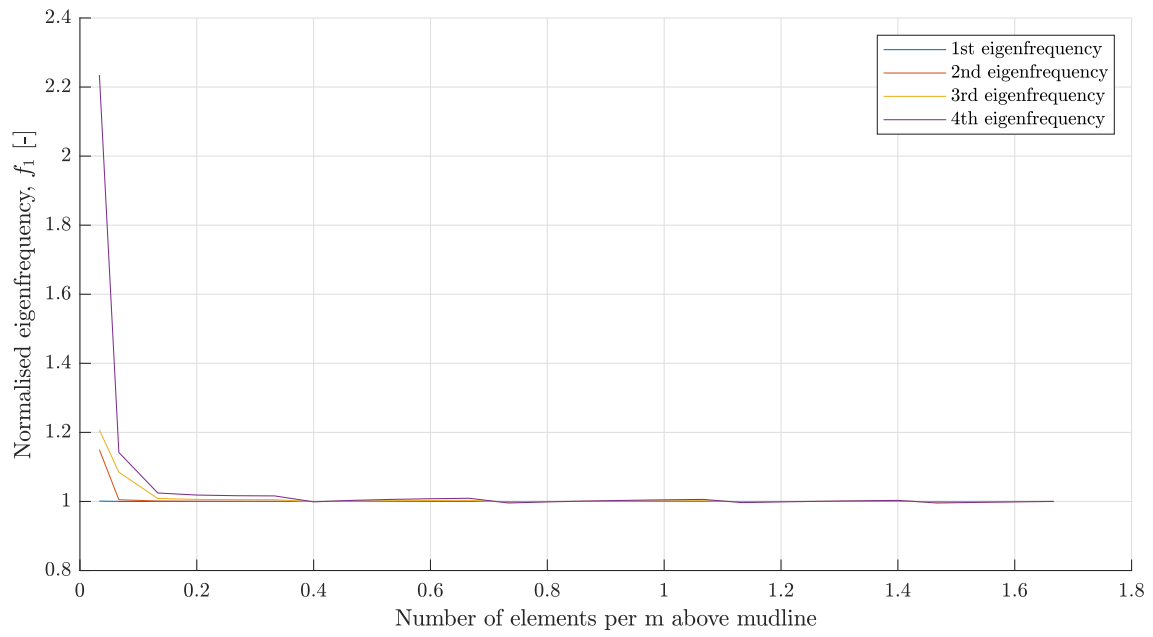


Figure G.6: Convergence analysis above the mudline in stiff clay performed by the Extended Model.

H. MODAL DECOUPLING

The equation of motion for a damped system is given in equation (H.1).

$$[\mathbf{M}]\{\ddot{\mathbf{u}}(t)\} + [\mathbf{C}]\{\dot{\mathbf{u}}(t)\} + [\mathbf{K}]\{\mathbf{u}(t)\} = \{\mathbf{F}(t)\} \quad (\text{H.1})$$

$[\mathbf{M}]$	Global mass matrix
$[\mathbf{C}]$	Global damping matrix
$[\mathbf{K}]$	Global stiffness matrix
$\{\mathbf{F}(t)\}$	Load vector
$\{\mathbf{u}\}$	Displacement vector
$\{\dot{\mathbf{u}}\}$	Velocity vector
$\{\ddot{\mathbf{u}}\}$	Acceleration vector

To do a modal decoupling of such a system, the global stiffness-, mass- and damping matrix have to be known. The global stiffness- and mass matrix are used to determine the eigenfrequencies and the mode shapes of the system. This is done by solving equation (H.2), which is introduced in Stage 2 on page 30. The cyclic eigenfrequencies and mode shapes are determined using the command *eigs* in MATLAB, which return a vector containing all cyclic eigenfrequencies $\{\omega\}$ and a matrix containing all mode shapes $[\phi]$.

$$([\mathbf{K}] - \omega^2[\mathbf{M}])\{\bar{\mathbf{D}}\} = \{\mathbf{0}\} \quad (\text{H.2})$$

ω	Cyclic eigenfrequency
$\{\bar{\mathbf{D}}\}$	Nodal amplitude vector i.e. mode shape vector

Based on the modal expansion theorem, the global system can be decoupled into multiple single degree of freedom systems [R. D. Cook et al., 2002].

The stiffness, mass and damping for each individual system are calculated as stated in equation (H.3), (H.4) and (H.5), where the individual values for each eigenfrequency are located in the diagonal of the matrices.

$$\{\phi\}^T [\mathbf{M}] \{\phi\} = \begin{bmatrix} m_1 & & \\ & \ddots & \\ & & m_n \end{bmatrix} \quad (\text{H.3})$$

$$\{\phi\}^T [\mathbf{K}] \{\phi\} = \begin{bmatrix} k_1 & & \\ & \ddots & \\ & & k_n \end{bmatrix} \quad (\text{H.4})$$

$$\{\phi\}^T [\mathbf{C}] \{\phi\} = \begin{bmatrix} c_1 & & \\ & \ddots & \\ & & c_n \end{bmatrix} \quad (\text{H.5})$$

I. p - y CURVE DISTRIBUTION

I.1 API Examples

Table I.1: Input parameters used to illustrate the application of p - y curves. *Reference strain level is the strain occurring at 50 % of the maximum principal stress in an undrained compression laboratory test.

Parameter	Symbol	Unit	Sand	Soft clay	Stiff clay
Effective angle of internal friction	ϕ'	°	37.5	-	-
Undrained shear strength	s_u	kPa	-	125	350
Effective unit weight of soil	γ'	kN/m ³	19.5	19	20
Reference strain level*	ϵ_{50}	-	-	0.015	0.008
Empirical constant	J	-	-	0.5	0.25
Diameter of the monopile	d	m	8	8	8
Length of the monopile below mudline	h_{pile}	m	30	30	30
External load applied at MWL	P	MN	27	5	10

I.1.1 Sand

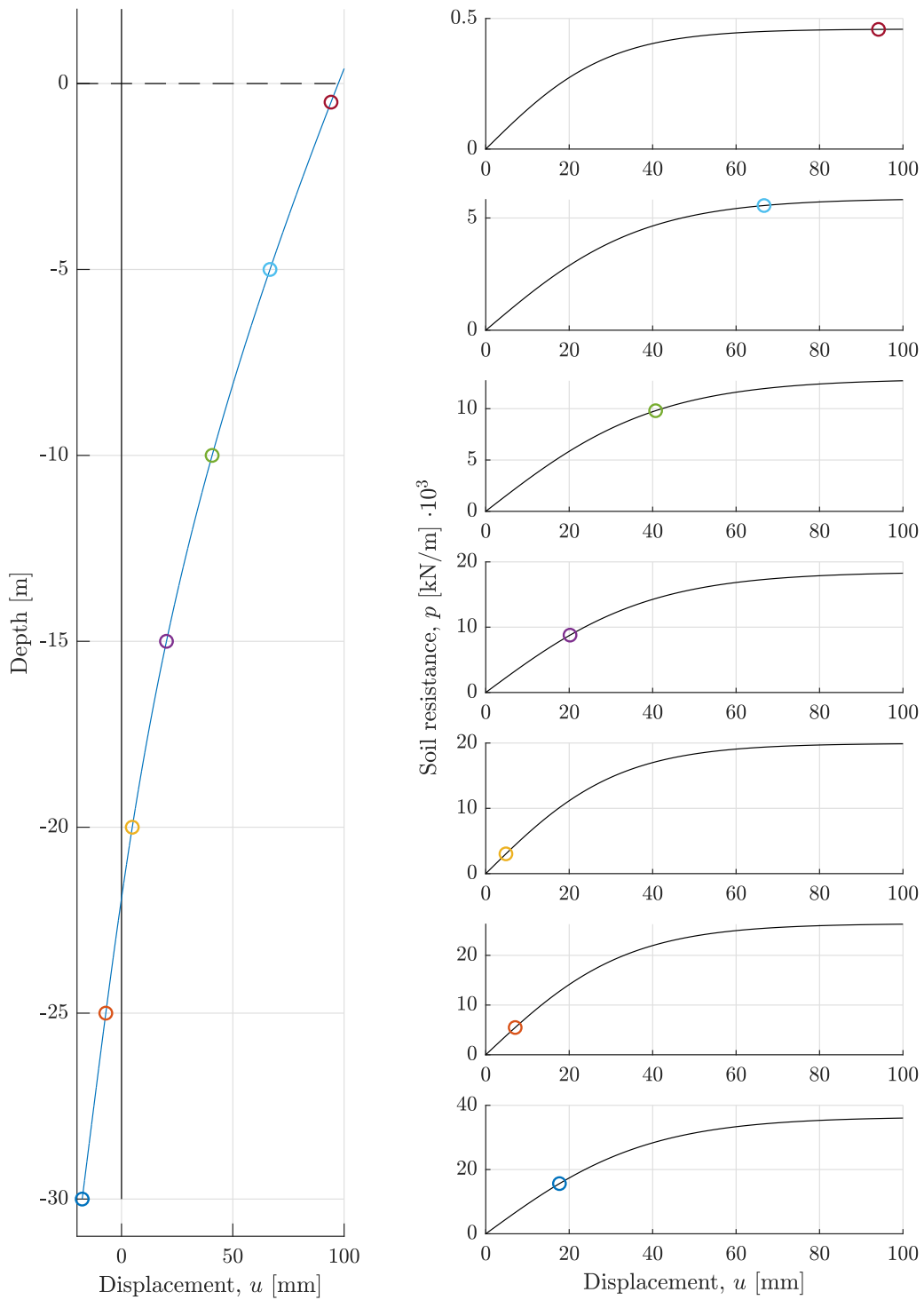


Figure I.1: Illustration of an example of the application of p - y curves for sand. The left hand side figure illustrates the mudline (dashed black line), the undeformed structure (solid black line) and the deformed structure (solid blue line).

I.1.2 Soft Clay

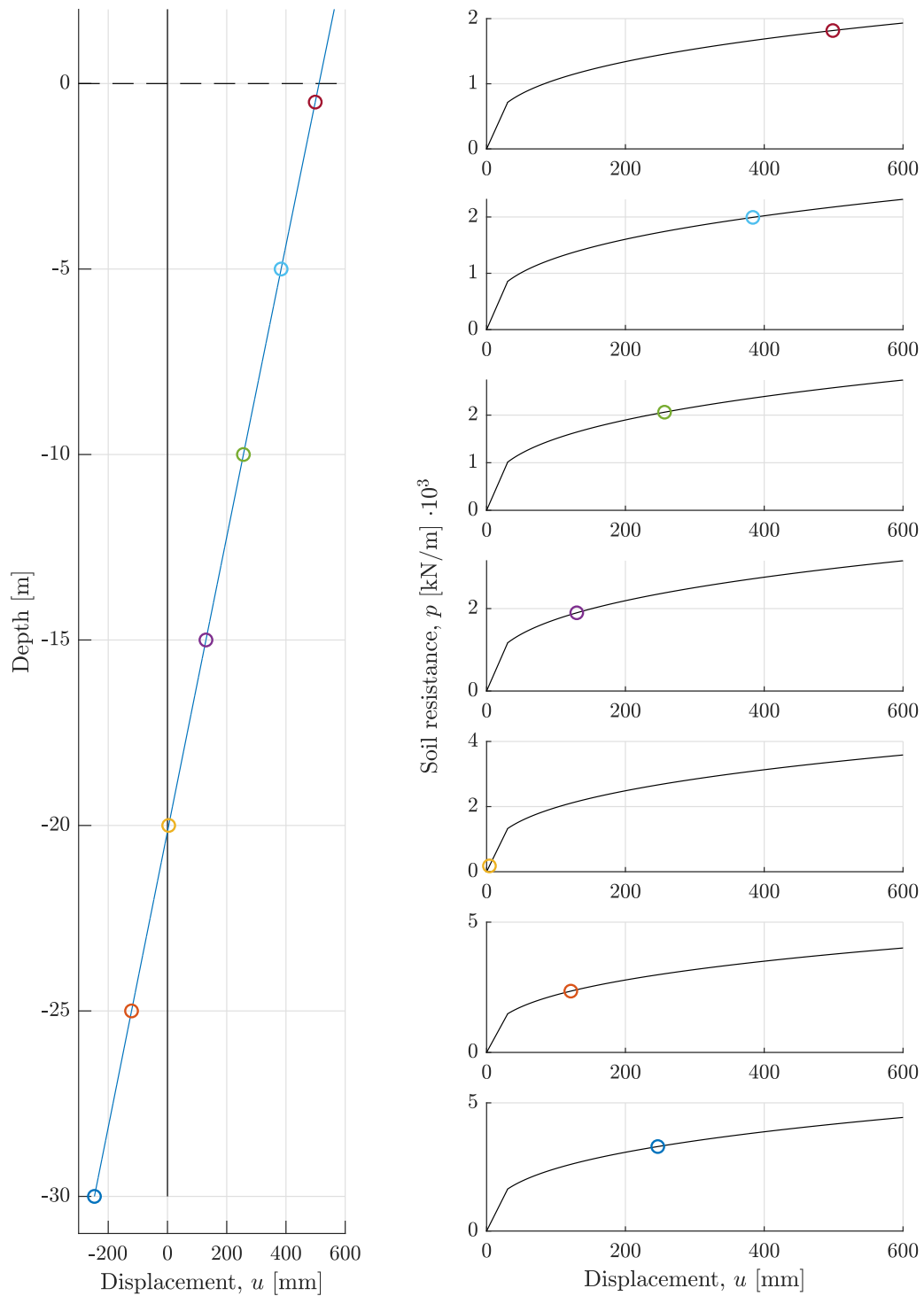


Figure I.2: Illustration of an example of the application of p - y curves for soft clay. The left hand side figure illustrates the mudline (dashed black line), the undeformed structure (solid black line) and the deformed structure (solid blue line).

I.1.3 Stiff Clay

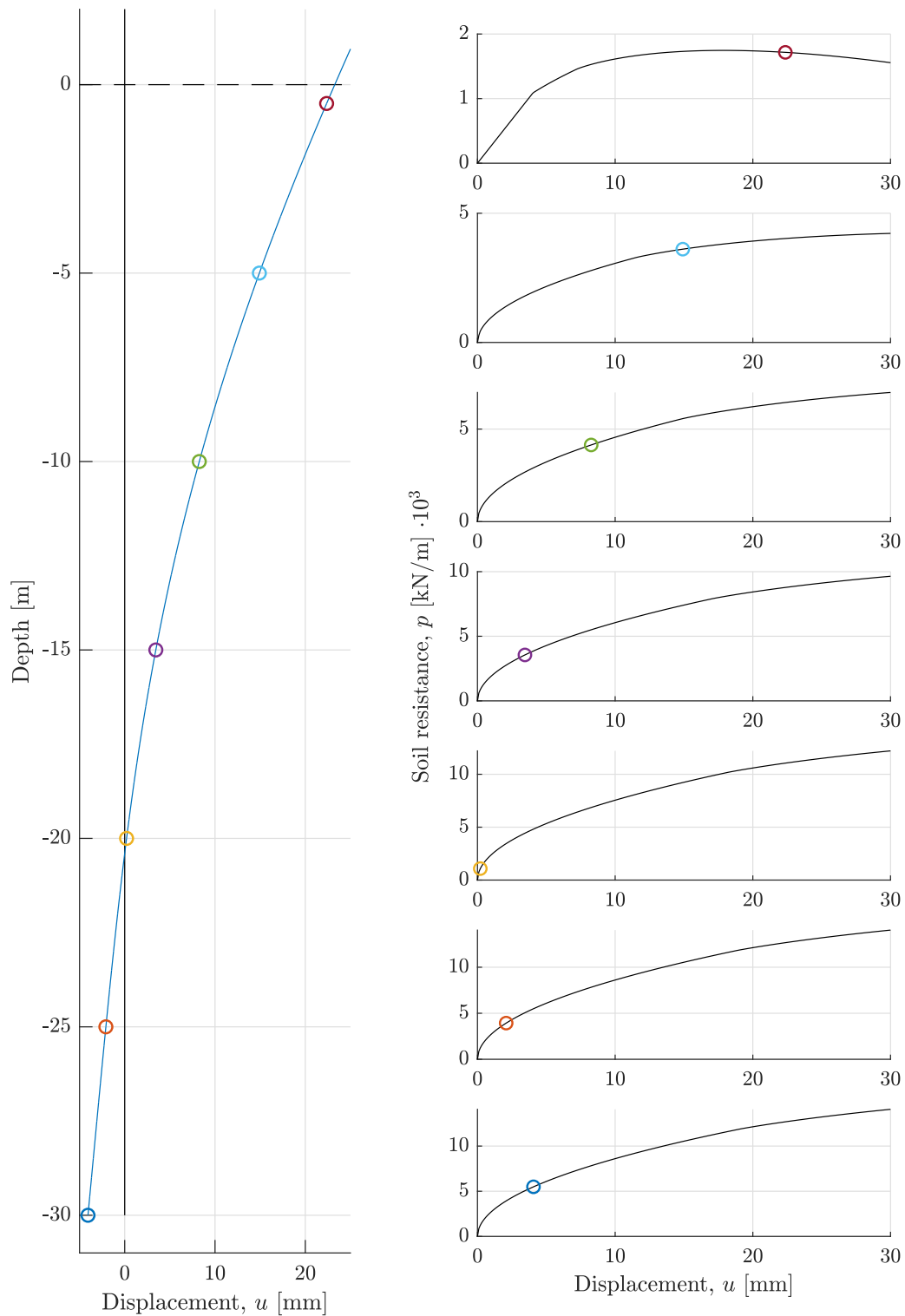


Figure I.3: Illustration of an example of the application of p - y curves for stiff clay. The left hand side figure illustrates the mudline (dashed black line), the undeformed structure (solid black line) and the deformed structure (solid blue line).

I.2 Numerical Error - Soft Clay

Figure I.4 and I.5 illustrates the numerical error that happens due to the definition of the API p - y curves for soft clay. This error results in a jump in the eigenfrequency by increasing the load by a small load step. The error happens due to the linear initial stiffness of the p - y curves for soft clay. As seen on the figures, the linear part is much steeper than the rest of the curve. This means that when a single point of the structure goes from being located on the linear initial part to the curved part of the API p - y curve for soft clay, then the soil-structure stiffness is drastically decreased. As the stiffness is decreased this much, it will cause almost all points of the structure to move from the initial part to the curved part with less stiffness, which causes the massive drop in eigenfrequency.

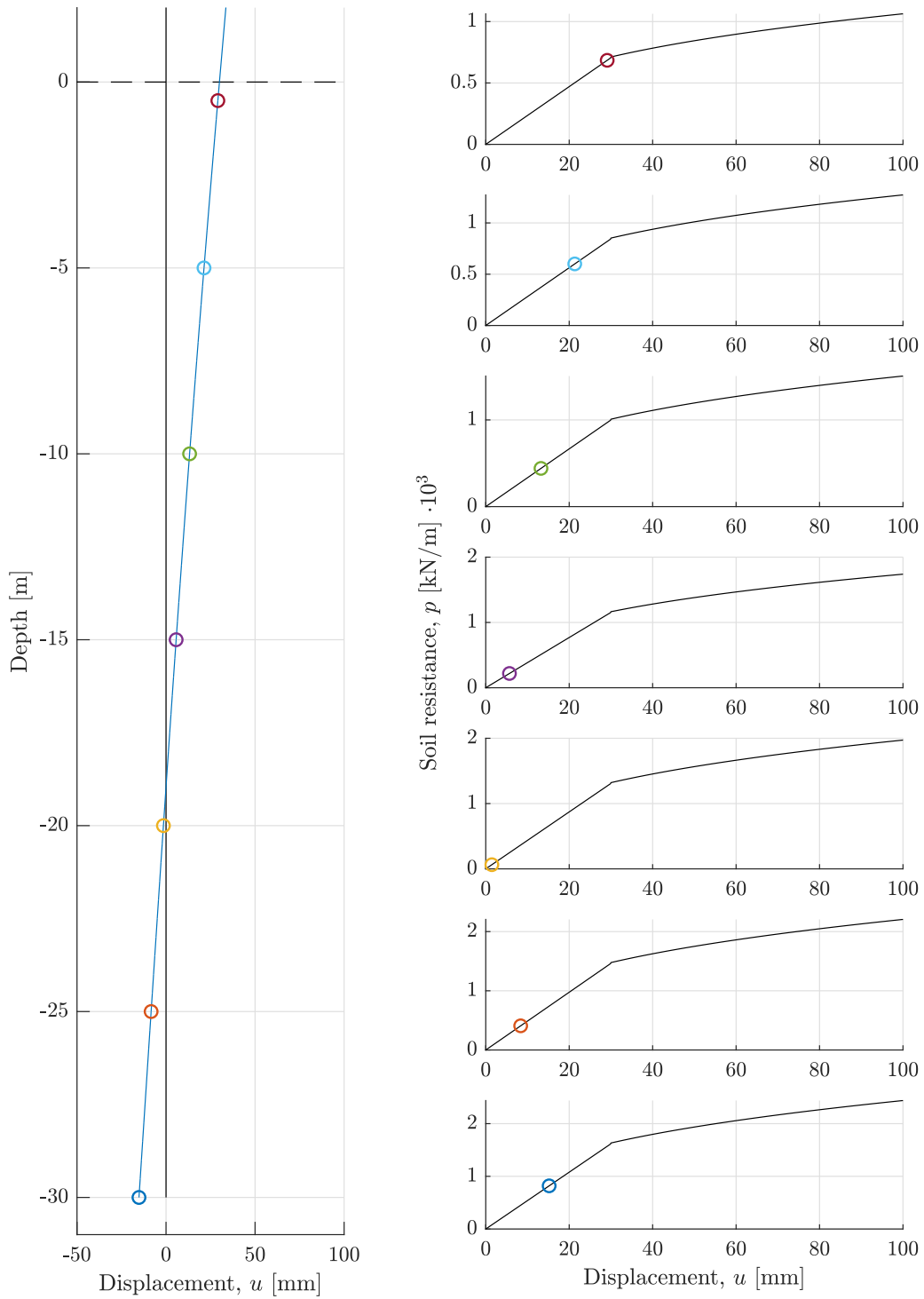


Figure I.4: p - y curves for soft clay. Loaded in such a manner that all displacements are in the range of the initial linear part of the p - y curve.

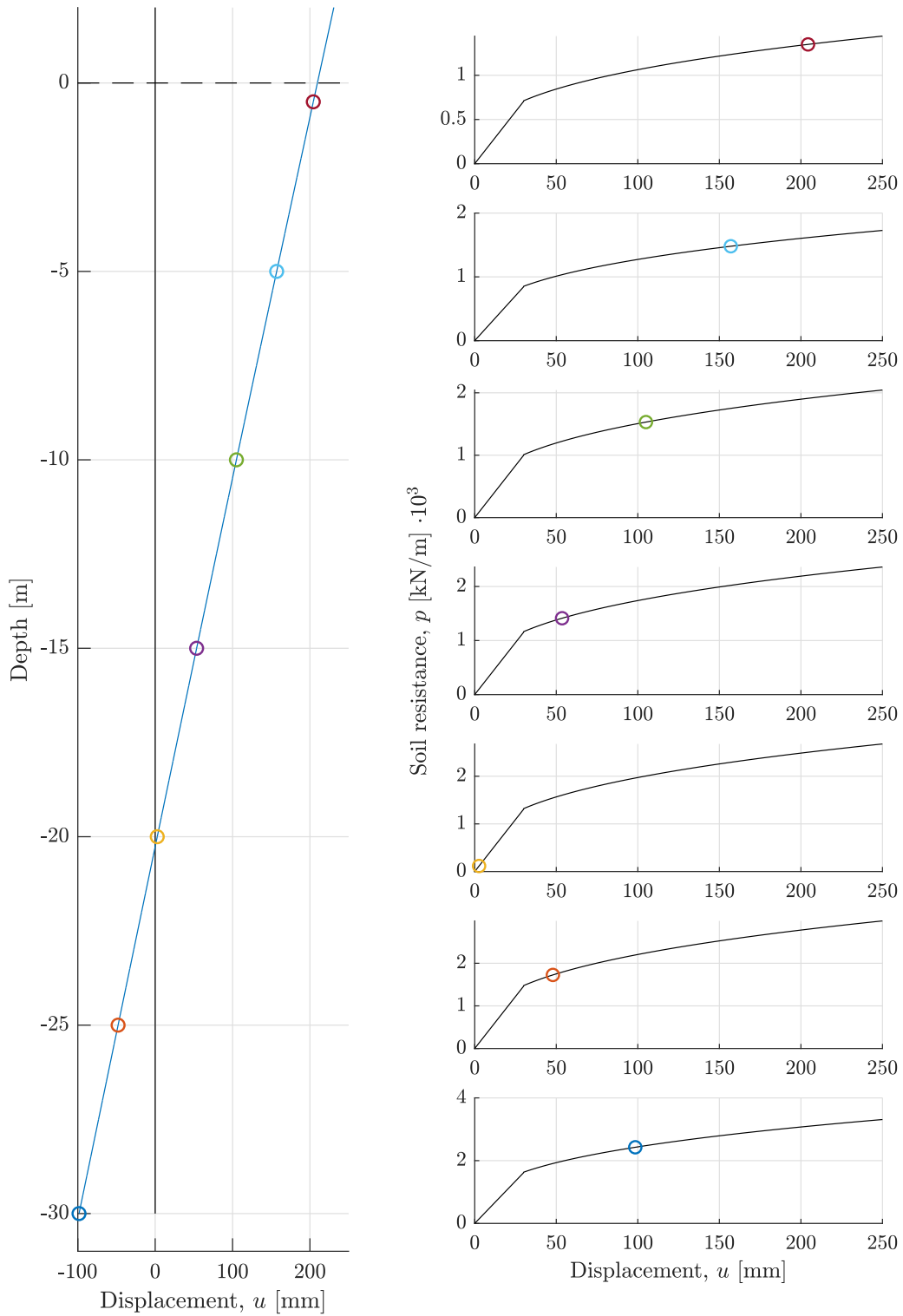


Figure I.5: p - y curves for soft clay. Loaded just above the load, that causes the displacement illustrated in Figure I.4

J. PLAXIS 3D THEORY

In this appendix, some of the relevant Plaxis 3D theory for the project is covered. This is not a general Plaxis 3D theory appendix, but the sections are created to supply subjects in the main report of this thesis.

J.1 Parameters for Material Models

J.1.1 Stiffness Parameters

Three different elasticity moduli are used in the Hardening Soil material model and the Hardening Soil Small-strain material model.

The stiffness modulus E_{50}^{ref} and E_{ur}^{ref} can be determined from a drained triaxial test. E_{50}^{ref} represents the secant stiffness at 50 % of the maximum deviatoric stress when using a cell pressure represented by a reference stress p^{ref} . E_{ur}^{ref} represents the unloading/reloading stiffness for the triaxial test. Figure J.1 shows the definitions of the two mentioned stiffness parameters from a drained triaxial test.

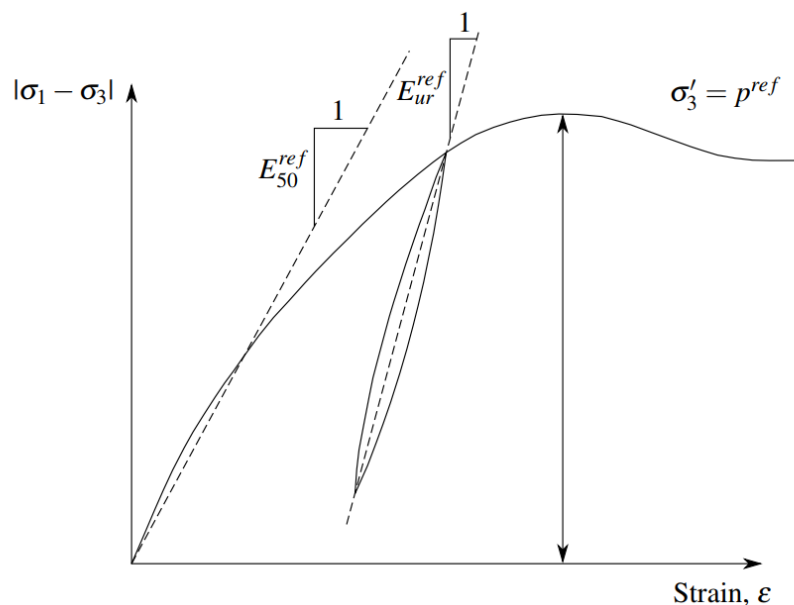


Figure J.1: Definition of E_{50}^{ref} and E_{ur}^{ref} for a drained triaxial test.

A third stiffness parameter is the oedometer stiffness, E_{oed}^{ref} , which is obtained from an oedometer test. E_{oed}^{ref} is a tangent stiffness modulus, which is obtained from the oedometer test at a reference stress, p^{ref} . Figure J.2 shows the definition of the oedometer stiffness from an oedometer test.

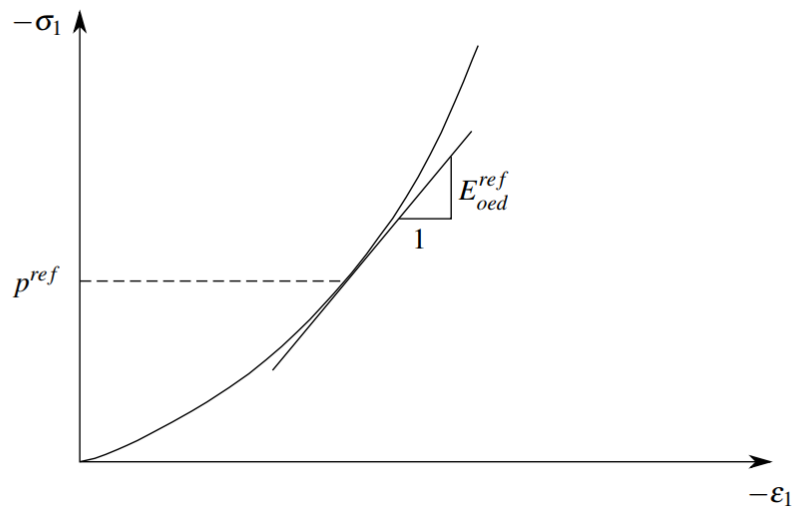


Figure J.2: Definition of E_{oed}^{ref} for an oedometer test.

The parameter m is defining the power for stress level dependency of stiffness. This parameter is automatically set to 1 in Plaxis as standard.

The Hardening Soil material model and the Hardening Soil Small-strain material model use two Poisson's ratios, a ratio for the primary loading and a ratio for the unloading/reloading. Most commonly, the Poisson's ratio for primary loading are in the range of 0.3 to 0.4, where the Poisson's ratio for unloading/reloading is in the range of 0.15 to 0.25.

J.1.2 Angle of Dilatancy, ψ

Normally, the angle of dilatancy is much smaller than the friction angle. For sand the dilatancy angle depends on the density and the friction angle. For clay, this parameter is often set to zero, except when considering heavily over-consolidated clay layers. When considering a positive dilatancy angle in drained conditions, the soil will continue to dilate as long shear deformations occur. This is not realistic because the soil should reach a critical state, where further shear will occur without volume changes. For soil modelled as clay, the friction angle is equal to zero and the dilatancy angle is thereby zero as well.

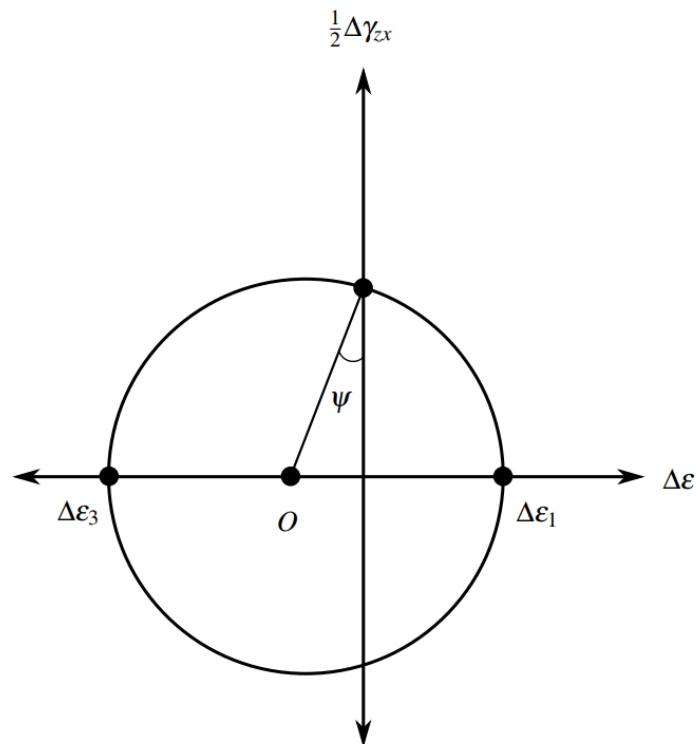


Figure J.3: Determination of the dilatancy angle by Coulomb's failure theory [Budhu, 2010].

Figure J.3 illustrates how the dilatancy angle is found, according to the Mohr-Coulomb theory. In general, the dilatation angle indicates how the change in volumetric strains behave with respect to the change in the shear strain. If the value is positive, the soil expands during shearing. If the dilatancy angle is negative, the soil contracts as it is sheared. [Budhu, 2010]

J.2 Soil Parameters Excluded in the Reference Soil Profile

This section covers the derivation of the necessary soil parameters, which are not listed in the reference soil profile in Table 9.1 page 113.

J.2.1 Young's Modulus

As Young's modulus is not given in the provided soil data, it can be calculated using Hooke's law as expressed in equation (J.1).

$$E = \frac{E_{oed}(1-2\nu)(1+\nu)}{(1-\nu)} \quad (\text{J.1})$$

J.2.2 Small-Strain Stiffness

The small-strain shear modulus G_0^{ref} is calculated with equation (J.2), where it is assumed that the sand has a void ratio of 0.5.

$$G_0^{ref} = 33 \cdot \frac{(2.97 - e)^2}{1 + e} [\text{MPa}] \quad \text{for} \quad p^{ref} = 100 \text{ kPa} \quad (\text{J.2})$$

$$G_0^{ref} = 33 \cdot \frac{(2.97 - 0.5)^2}{1 + 0.5} = 134,22 \text{ MPa} \quad (\text{J.3})$$

The reference strain level is determined according to a graph provided in the Plaxis manual, see Figure J.4. As Stage 4 in this thesis is based on sand, the plasticity index, PI , is equal to 0 and thereby the shear strain amplitude at 70 % of G_0 can be determined to approximately to $\gamma_s \approx 10^{-4}$.

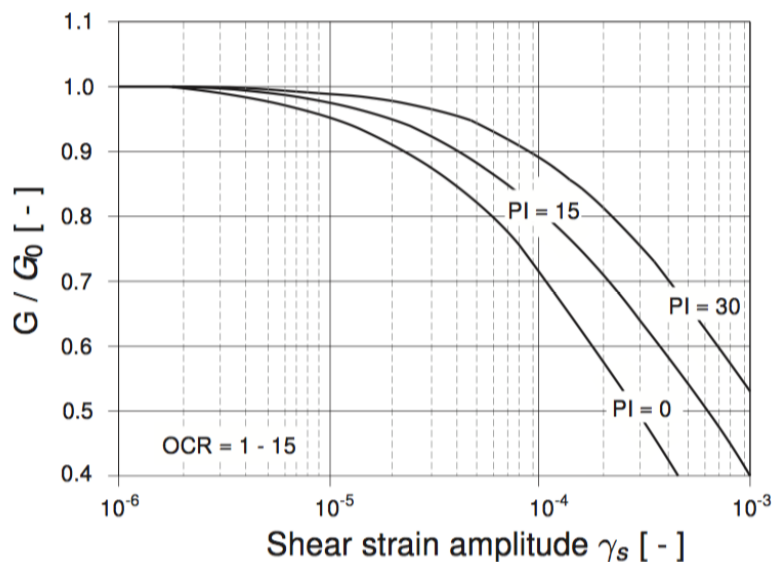


Figure J.4: Determination of stiffness reduction [Plaxis, 2017a].

J.3 Time Integration

For the dynamic calculation type in Plaxis 3D, a Newmark time integration scheme is used. The theory for the time integration is based on Plaxis, 2017c. The time step in this integration is constant and equal to the critical time step during the full analysis. The method can predict the displacement and velocity at a point in time $t + \Delta t$ where the previous known point is t and Δt is the time step. The equations for predicting the displacement, u , and velocity, \dot{u} , can be seen in equation (J.4) and (J.5) respectively.

$$\dot{u}^{t+\Delta t} = \dot{u}^t + \ddot{u}^t \Delta t + \left(\left(\frac{1}{2} - \alpha \right) \ddot{u}^t + \alpha \ddot{u}^{t+\Delta t} \right) \Delta t^2 \quad (\text{J.4})$$

$$u^{t+\Delta t} = u^t + \dot{u}^t \Delta t + \left((1 - \beta) \ddot{u}^t + \beta \ddot{u}^{t+\Delta t} \right) \Delta t^2 \quad (\text{J.5})$$

The coefficients α and β are used for the time integration and they determine the accuracy of the numerical time integration. For being able to obtain a stable solution from the time integration, the conditions in equation (J.6) and (J.7) must be fulfilled.

$$\beta \geq 0.5 \quad (\text{J.6})$$

$$\alpha \geq \frac{1}{4} \left(\frac{1}{2} + \beta \right)^2 \quad (\text{J.7})$$

The Plaxis 3D manual recommend to use the default settings for these constants, which are $\alpha = 0.25$ and $\beta = 0.50$.

As the critical time step is used for the calculation in order to obtain a stable solution, this must be determined. The critical time step is used, as a too large time step will give a solution with substantial deviations and the calculated response will not be reliable. The critical time step can be calculated using equation (J.8) for all elements in the model and using the minimum critical time step obtained. This time step ensures that a wave during a single step does not travel a distance which is larger than the minimum dimension of an element and thereby accurate model wave propagation.

$$\Delta t_{\text{critical}} = \frac{l_e}{\alpha \sqrt{\frac{E(1-\nu)}{\rho(1+\nu)(1-2\nu)}} \sqrt{1 + \frac{B^4}{4S^2} - \frac{B^2}{2S} \left(1 + \frac{1-2\nu}{4} \frac{2S}{B^2} \right)}} \quad (\text{J.8})$$

B	Largest dimension of the finite element
S	Surface area of the finite element
α	Factor dependent of element type
ν	Poisson's ratio
l_e	Average length of an element

Plaxis 3D uses the theory by rewriting equation (J.4) and (J.5) which gives equation (J.9), (J.10) and (J.11).

$$\ddot{u}^{t+\Delta t} = c_0 \delta u - c_2 \dot{u}^t - c_3 \ddot{u}^t \quad (\text{J.9})$$

$$\dot{u}^{t+\Delta t} = \dot{u}^t + c_6 \ddot{u}^t + c_7 \ddot{u}^{t+\Delta t} \quad (\text{J.10})$$

$$u^{t+\Delta t} = u^t + \Delta u \quad (\text{J.11})$$

Here equation (J.10) can also be written as equation (J.12).

$$\dot{u}^{t+\Delta t} = c_1 \Delta u - c_4 \dot{u}^t - c_5 \ddot{u}^t \quad (\text{J.12})$$

The dynamic integration coefficients used by Plaxis 3D can be determined from equation (J.13) to (J.20) when the time step is determined.

$$ca0 = \frac{1}{\alpha \Delta t^2} \quad (\text{J.13})$$

$$ca1 = \frac{\delta}{\alpha \Delta t} \quad (\text{J.14})$$

$$ca2 = \frac{1}{\alpha \Delta t} \quad (\text{J.15})$$

$$ca3 = \frac{1}{2\alpha} - 1 \quad (\text{J.16})$$

$$ca4 = \frac{\delta}{\alpha} - 1 \quad (\text{J.17})$$

$$ca5 = \frac{\Delta t}{2} \left(\frac{\delta}{\alpha - 2} \right) \quad (\text{J.18})$$

$$ca6 = \Delta t (1 - \delta) \quad (\text{J.19})$$

$$ca7 = \delta \Delta t \quad (\text{J.20})$$

In these constants, α and δ are Newmark parameters which can be determined so the integration is accurate and stable.

For an implicit time integration the equation of motion still has to be fulfilled, which is why equation (J.21) for the system can be set up.

$$M \ddot{u}^{t+\Delta t} + C \dot{u}^{t+\Delta t} + K u^{t+\Delta t} = F^{t+\Delta t} \quad (\text{J.21})$$

By using this equation together with equation (J.9), (J.11) and (J.12), equation (J.22) can be set up.

$$(c_0 M + c_1 C + K) \Delta u = F_{ext}^{t+\Delta t} + M (c_2 \dot{u}^t + c_3 \ddot{u}^t) + C (c_4 \dot{u}^t + c_5 \ddot{u}^t) - F_{int}^t \quad (\text{J.22})$$

This equation matches the equation for a static analysis ($Ku = F$), where the stiffness at the left side of the equal sign has contributions from the mass and damping, and the force at the right side has contributions in the form of extra terms which specifies velocity and acceleration at the start of the time step.

J.4 Rayleigh Damping

The material damping in dynamic calculations are caused by the viscous soil properties, friction and the development of irreversible strains. None of the material models in Plaxis 3D has the capability to capture all these effects at the same time for all scenarios, and additional damping is needed for modelling realistic damping characteristics of the soil in dynamic calculations. Plaxis uses Rayleigh damping in order to model this realistic damping characteristics of the soil in the dynamic calculations.

Rayleigh damping a numerical feature where the damping matrix is estimated by contributions from the mass- and stiffness matrix. The damping matrix when using Rayleigh damping is estimated using equation (J.23).

$$C = \alpha M + \beta K \quad (J.23)$$

The input in Plaxis 3D is the Rayleigh coefficients α , which determines the influence of the mass in the damping matrix, and β , which determines the influence of the stiffness in the damping matrix. High α values are damping the lower frequencies while higher β values are damping the higher frequencies more. The coefficients can be defined for each material data set for soil, interfaces and plates which gives the ability to define viscous damping characteristics for each individual material.

The Rayleigh coefficients can be estimated by a relationship between these and the damping ratio. This relation can be seen from equation (J.24).

$$\alpha + \beta \omega^2 = 2\omega\xi \quad \text{and} \quad \omega = 2\pi f \quad (J.24)$$

ω	Angular frequency
f	Frequency
ξ	Damping ratio

The two Rayleigh coefficients can be solved when two target frequencies with corresponding damping ratios are known. The isolation of the coefficients can be seen in equation (J.25).

$$\alpha = 2\omega_1\omega_2 \frac{\omega_1\xi_2 - \omega_2\xi_1}{\omega_1^2 - \omega_2^2} \quad \text{and} \quad \beta = 2 \frac{\omega_1\xi_1 - \omega_2\xi_2}{\omega_1^2 - \omega_2^2} \quad (J.25)$$

Plaxis 3D will automatically calculate the Rayleigh coefficients if the target damping ratios and the target frequencies are specified in the input of the material.

K. CONVERGENCE ANALYSIS

In this appendix, additional analyses performed regarding the convergence analysis of the size of the soil domain and the mesh size are presented.

K.1 Convergence Analysis for the Dynamic Models

During the convergence analysis performed with a load-level corresponding to failure in the soil, the extensive computational time of a dynamic model was discovered. An additional convergence analysis of the domain size is therefore performed, where the applied load correspond to the smaller load, which is applied in the dynamic models. This convergence analysis is presented in the following sections.

K.1.1 Convergence Analysis of Length and Width of the Soil Domain

The convergence analysis of length and width of the soil domain is performed similarly to the identical convergence analysis performed in Chapter 10, and the procedure will therefore not be repeated here. The results from the convergence analysis of the length and width of the soil domain are presented in Figure K.1.

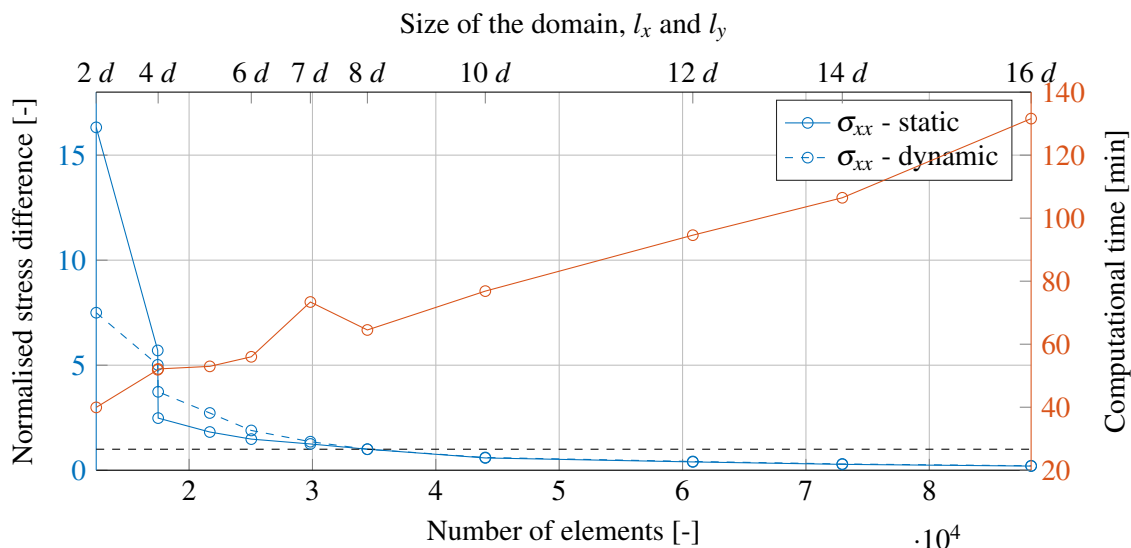


Figure K.1: Convergence analysis of the length and width of the soil domain. The length, l_x , and the width l_y , are varied equally i.e. $l_x = l_y$. The stress difference is normalised against the maximum stress difference in the selected soil domain size.

From Figure K.1 it is observed that the convergence analysis for the length and width of the soil domain is similar to the one performed for the static analyses with the Mohr-Coulomb material model. However, the stress difference is not as significant in the dynamic convergence analysis, because the applied load is much smaller. A length and width of the soil domain is therefore

selected to $8d$, because this value provides a good compromise between the level of convergence and the number of elements involved in the model.

K.1.2 Convergence Analysis of Height of the Soil Domain

The convergence analysis of height of the soil domain is performed similarly to the identical convergence analysis performed in Chapter 10, and the procedure will therefore not be repeated here. The results from the convergence analysis of the height of the soil domain are presented in Figure K.2.

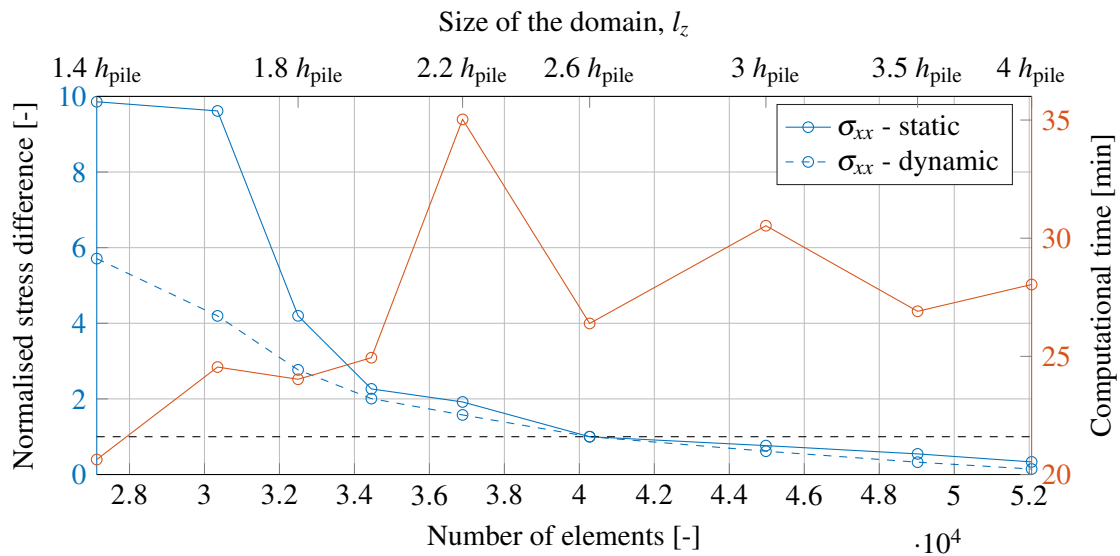


Figure K.2: Convergence analysis of the height of the soil domain. The stress difference is normalised against the maximum stress difference in the selected soil domain size.

From Figure K.2 it is observed that the convergence analysis for the length and width of the soil domain is similar to the one performed for the static analyses with the Mohr-Coulomb material model. However, according to this convergence analysis, the height of the soil domain can not be reduced, because this would yield a too big stress difference. The height of the soil domain is therefore selected to $2.6 h_{pile}$.

L. FREE VIBRATION ANALYSIS RESULTS

L.1 Fast Fourier Transformation

For being able to convert the results from the time domain to the frequency domain, a fast Fourier transformation, FFT, is used. The FFT is an algorithm which is used to make a Fourier transformation. The reason for converting the response from the time domain to the frequency domain is for being able to see the frequencies containing most energy and thereby represents the eigenfrequencies of the structure.

A Fourier transformation can be performed for a continuous function, where the transformation is given by the integral in equation (L.1). This transformation type is a Discrete Fourier Transformation.

$$X(F) = \int_{-\infty}^{\infty} x(t) e^{-j2\pi Ft} dt \quad (\text{L.1})$$

However, as a result of the measurements can be sampled continuously, the results are a set of discrete points and a discrete Fourier transformation is used. The formula for a discrete Fourier transformation can be seen in equation (L.2).

$$X_k = \sum_{n=0}^{N-1} x_n e^{-\frac{j2\pi kn}{N}} \quad (\text{L.2})$$

The FFT can be used for reducing the calculation time for a DFT, as this algorithm takes advantage of the symmetry of a signal.

L.2 Displacement Signals

The results for the displacement signals for the different models using different material models are shown in this section.

L.2.1 Linear-Elastic

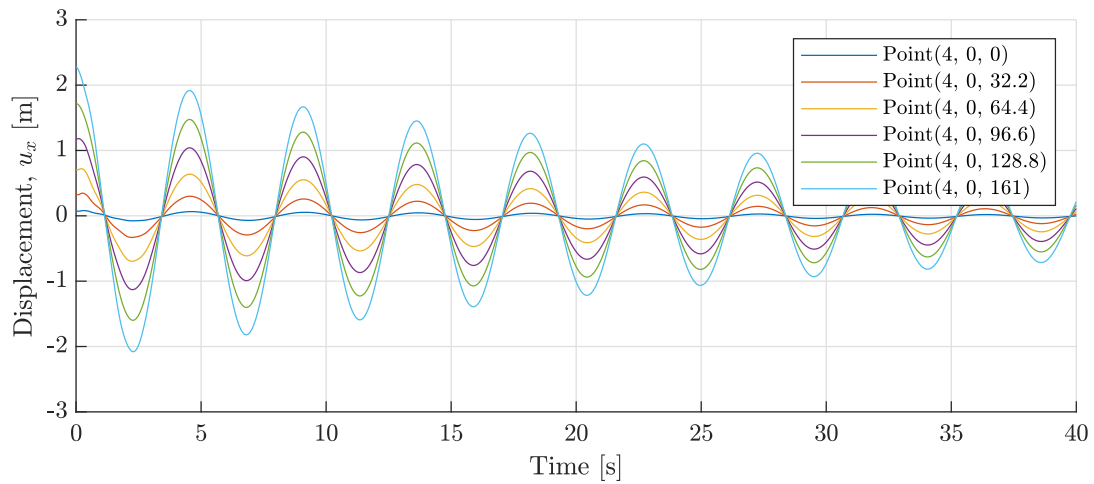


Figure L.1: Displacement over time signal obtained using the Linear-Elastic material model and a horizontal point load, $P_x = 2$ MN.

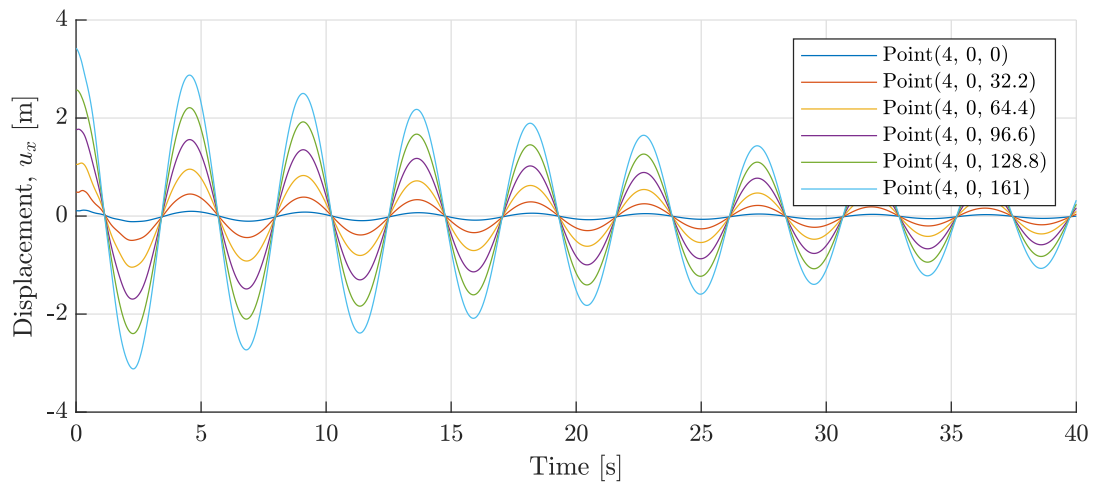


Figure L.2: Displacement over time signal obtained using the Linear-Elastic material model and a horizontal point load, $P_x = 3$ MN.

L.2.2 Mohr-Coulomb

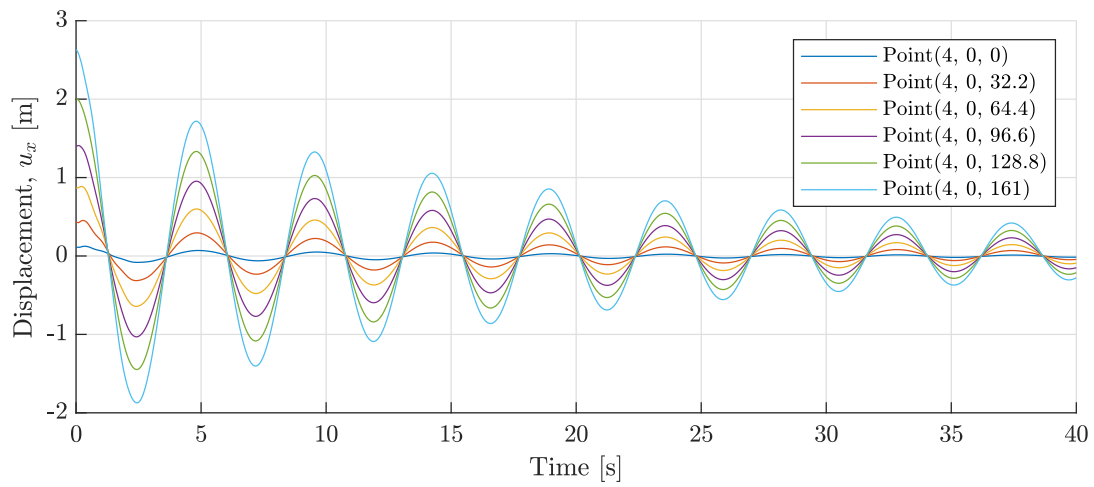


Figure L.3: Displacement over time signal obtained using the Mohr-Coulomb material model and a horizontal point load, $P_x = 2$ MN.

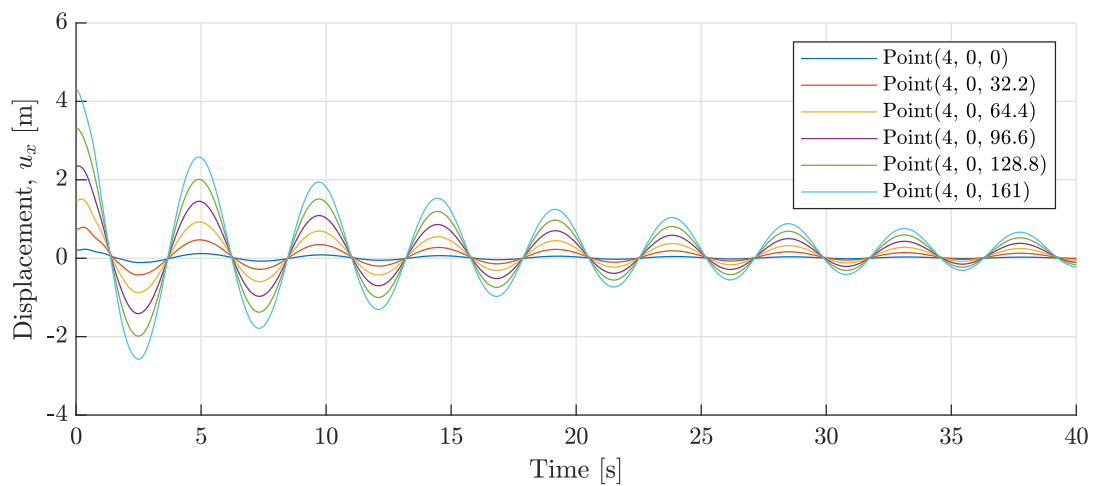


Figure L.4: Displacement over time signal obtained using the Mohr-Coulomb material model and a horizontal point load, $P_x = 3$ MN.

L.2.3 Hardening Soil

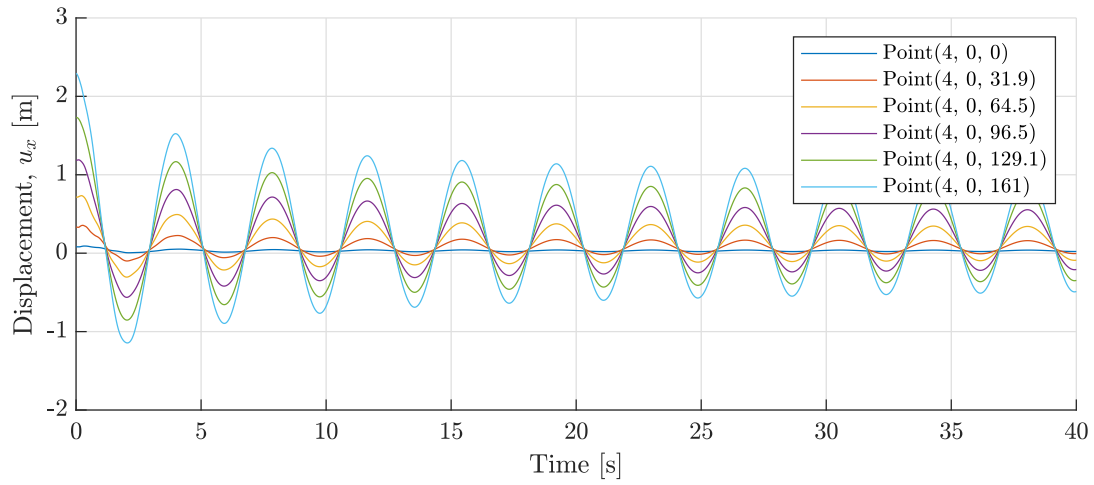


Figure L.5: Displacement over time signal obtained using the Hardening Soil material model and a horizontal point load, $P_x = 2$ MN.

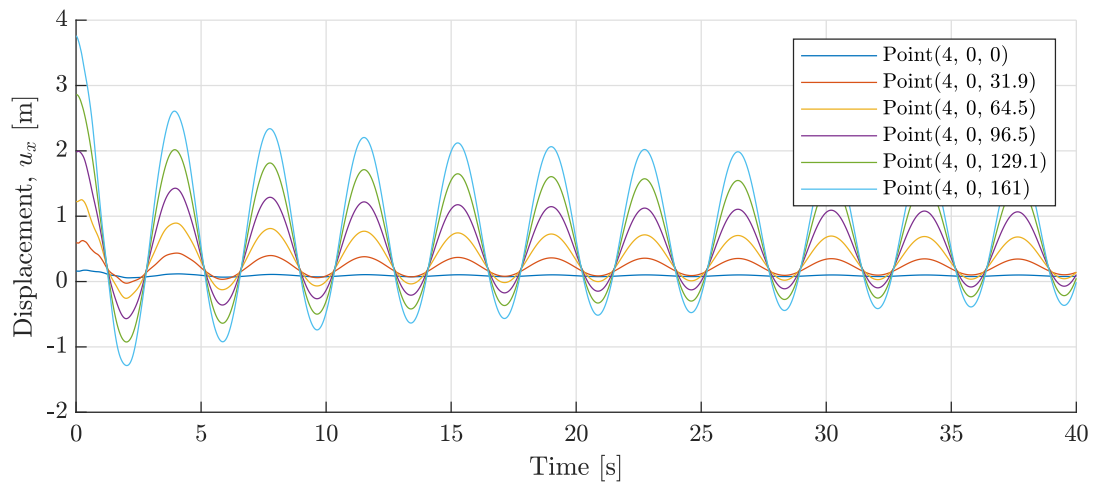


Figure L.6: Displacement over time signal obtained using the Hardening Soil material model and a horizontal point load, $P_x = 3$ MN.

L.2.4 Hardening Soil Small-Strain

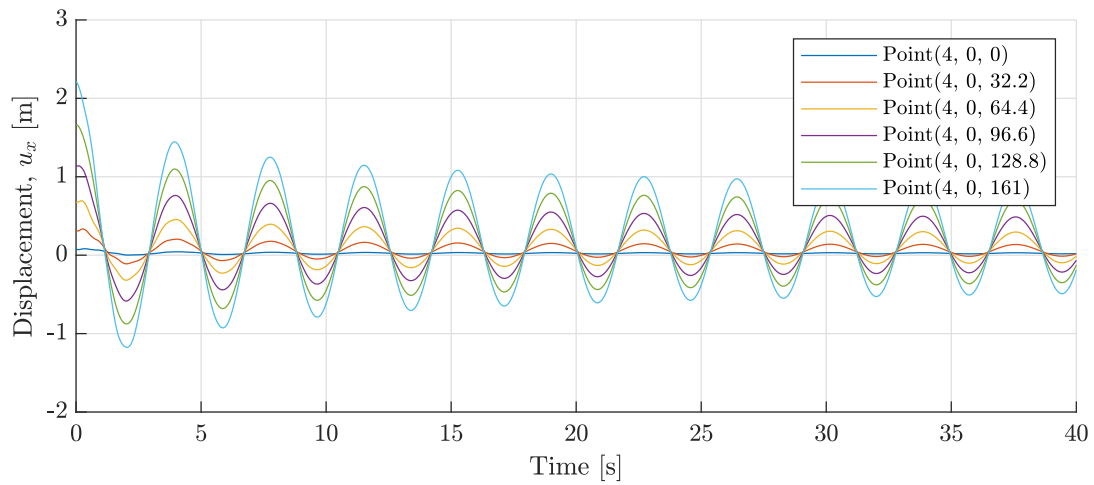


Figure L.7: Displacement over time signal obtained using the Hardening Soil Small-strain material model and a horizontal point load, $P_x = 2$ MN.

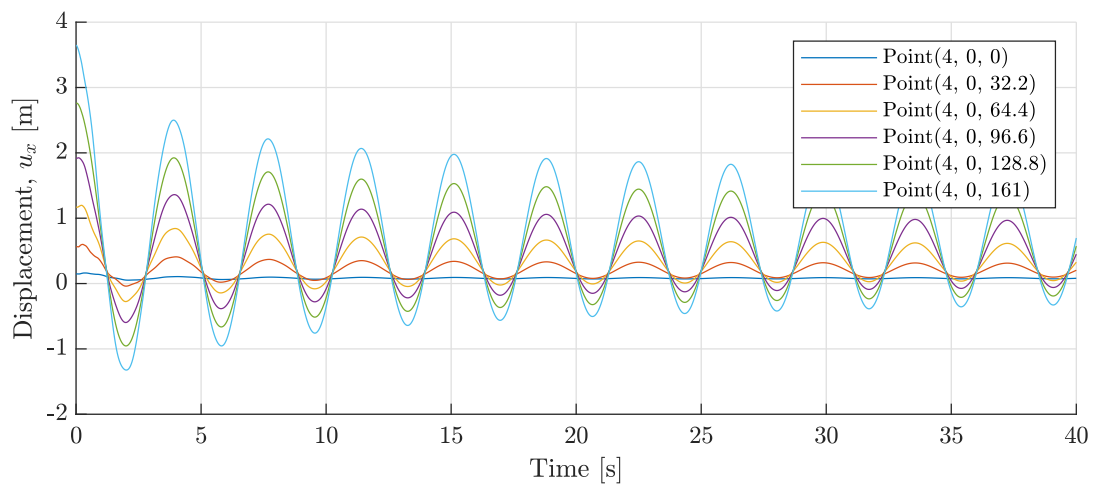


Figure L.8: Displacement over time signal obtained using the Hardening Soil Small-strain material model and a horizontal point load, $P_x = 3$ MN.

L.3 Frequency Domain

The results for the frequency domain for the different models using different material models are shown in this section.

L.3.1 Linear-Elastic

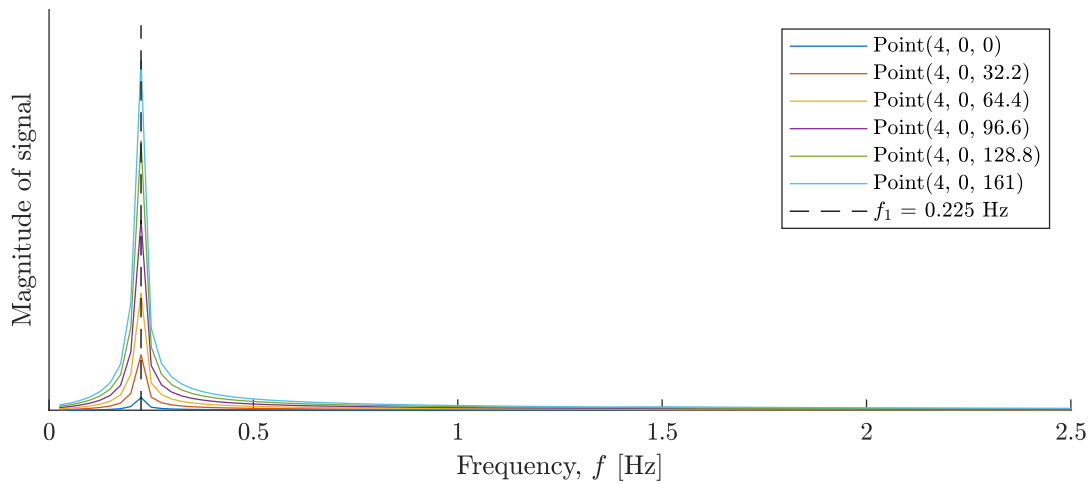


Figure L.9: Results of the FFT performed on the displacement signal obtained using the Linear-Elastic material model and a horizontal point load, $P_x = 2$ MN.

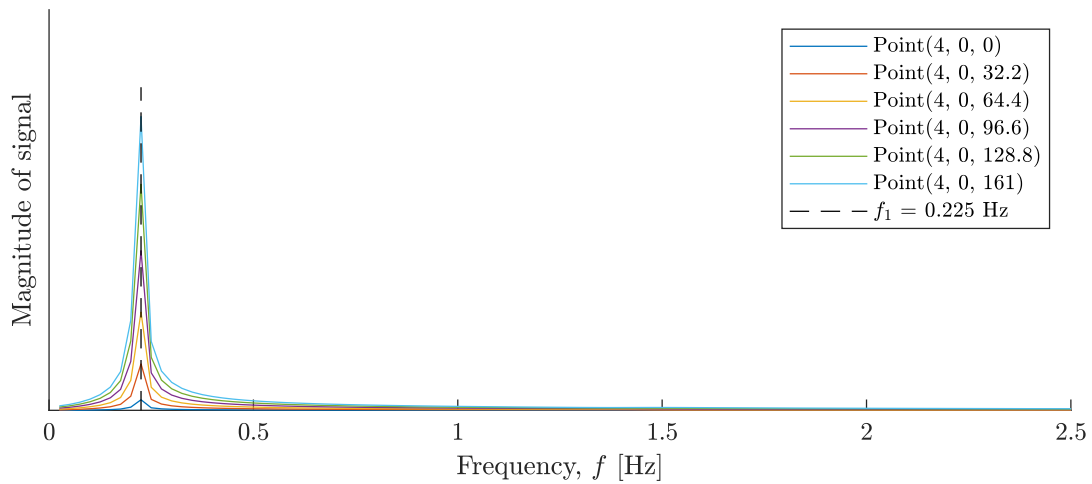


Figure L.10: Results of the FFT performed on the displacement signal obtained using the Linear-Elastic material model and a horizontal point load, $P_x = 3$ MN.

L.3.2 Mohr-Coulomb

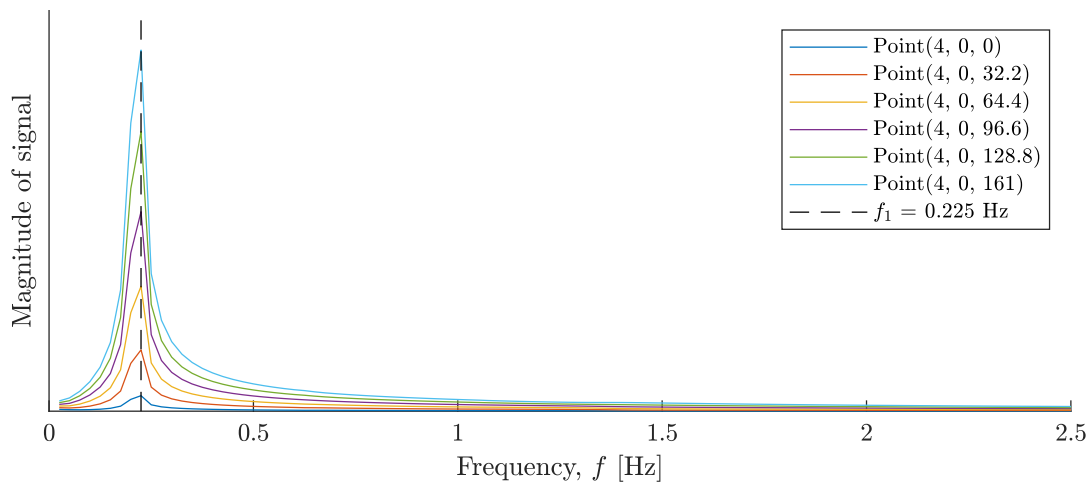


Figure L.11: Results of the FFT performed on the displacement signal obtained using the Mohr-Coulomb material model and a horizontal point load, $P_x = 2$ MN.

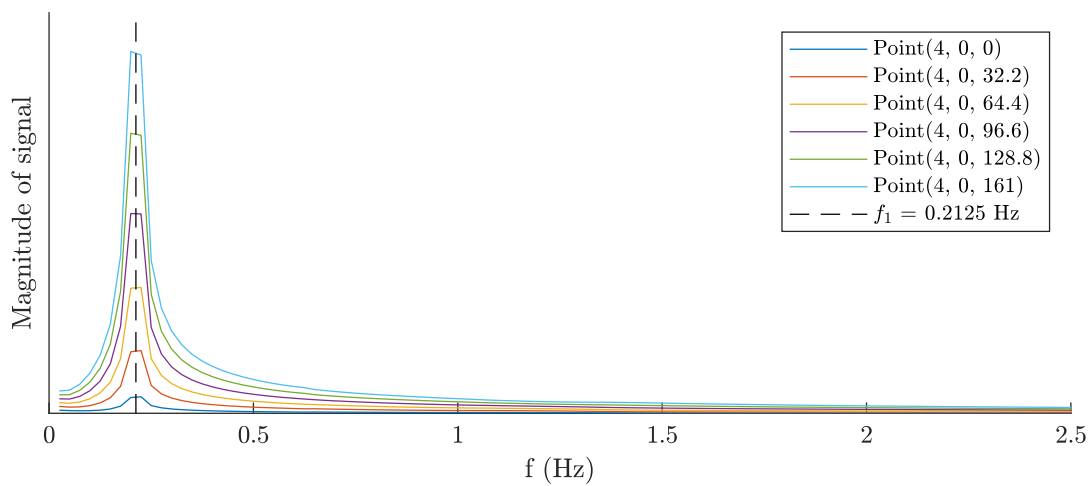


Figure L.12: Results of the FFT performed on the displacement signal obtained using the Mohr-Coulomb material model and a horizontal point load, $P_x = 3$ MN.

L.3.3 Hardening Soil

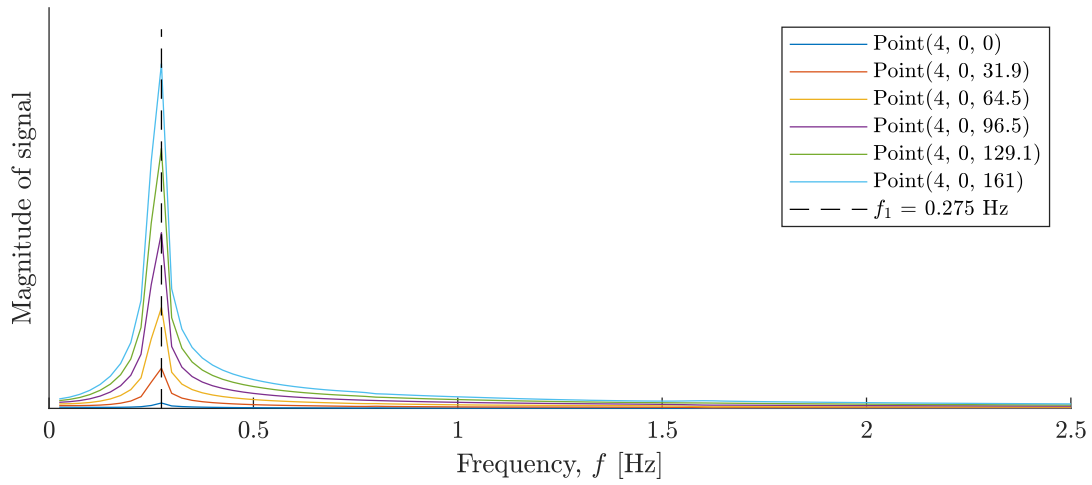


Figure L.13: Results of the FFT performed on the displacement signal obtained using the Hardening Soil material model and a horizontal point load, $P_x = 2$ MN.

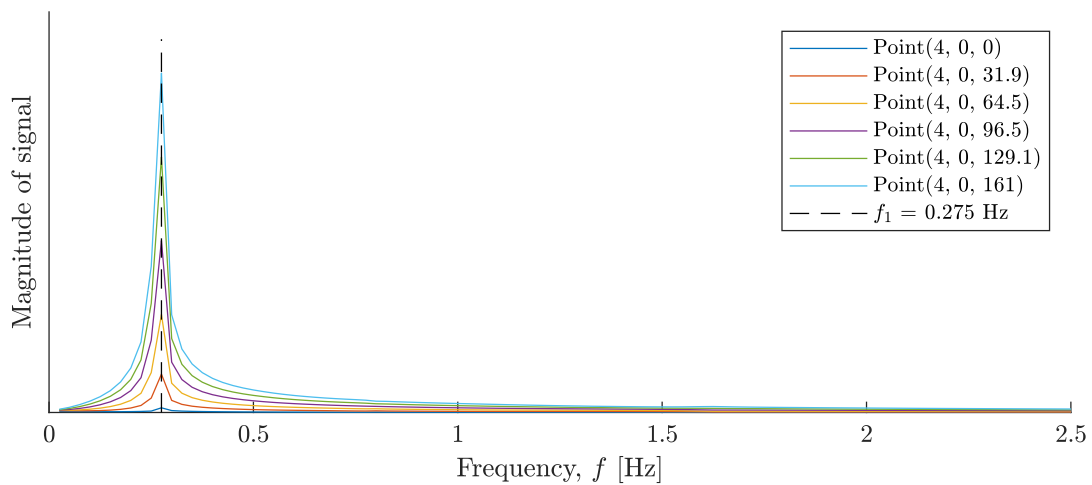


Figure L.14: Results of the FFT performed on the displacement signal obtained using the Hardening Soil material model and a horizontal point load, $P_x = 3$ MN.

L.3.4 Hardening Soil Small-Strain

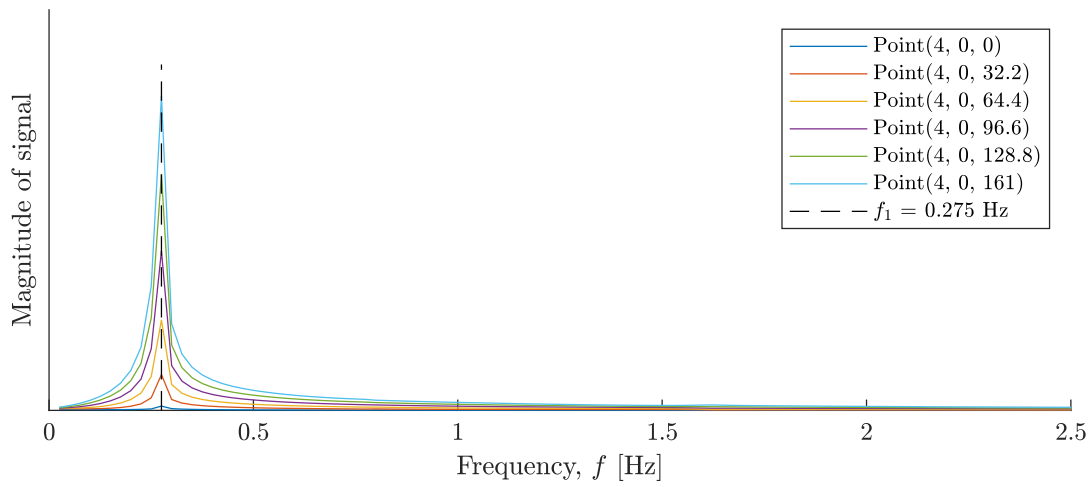


Figure L.15: Results of the FFT performed on the displacement signal obtained using the Hardening Soil Small-strain material model and a horizontal point load, $P_x = 2$ MN.

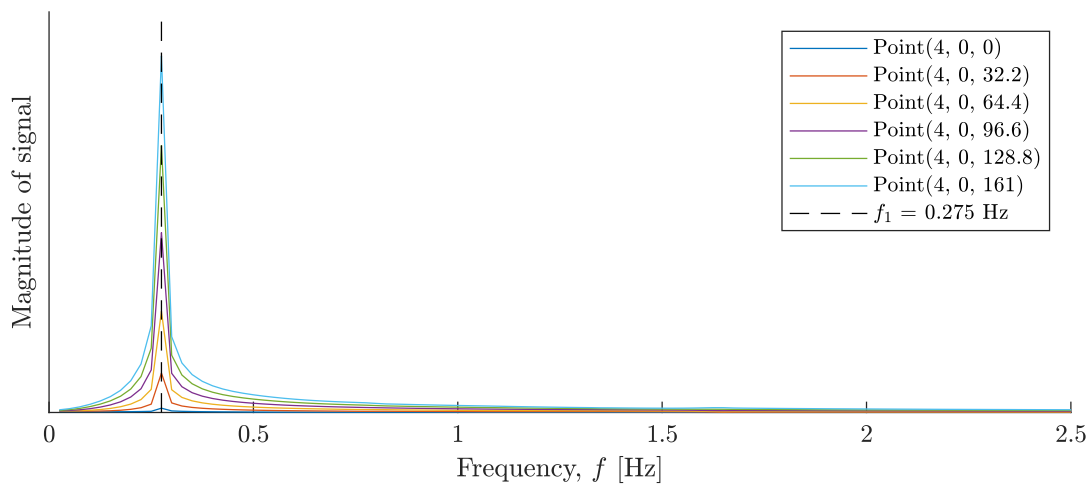


Figure L.16: Results of the FFT performed on the displacement signal obtained using the Hardening Soil Small-strain material model and a horizontal point load, $P_x = 3$ MN.

L.4 *p*-*y* Curve Distribution

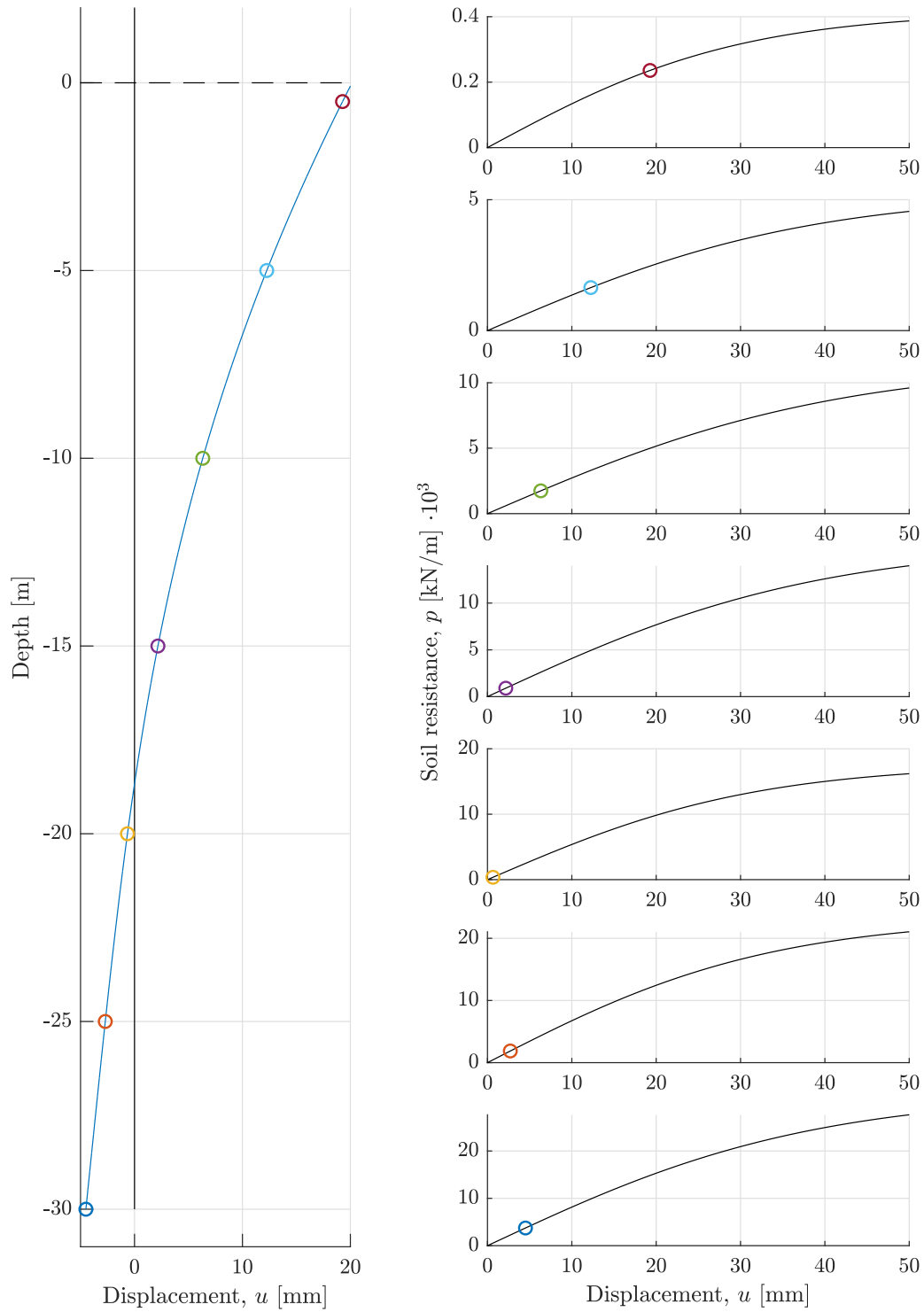


Figure L.17: The *p*-*y* curves used for comparing the Plaxis 3D calculated eigenfrequency to the 1D FE model from Stage 3. The first eigenfrequency is 0.189 Hz.

M. EXTRACTION OF p - y CURVES

M.1 Verification of the Principle of Division

In this section the principle of dividing the monopile into several sections is verified. This verification is performed by comparing the displacements along a monopile consisting of one section to the displacements along a monopile consisting of 30 sections. This comparison is shown in Figure M.1.

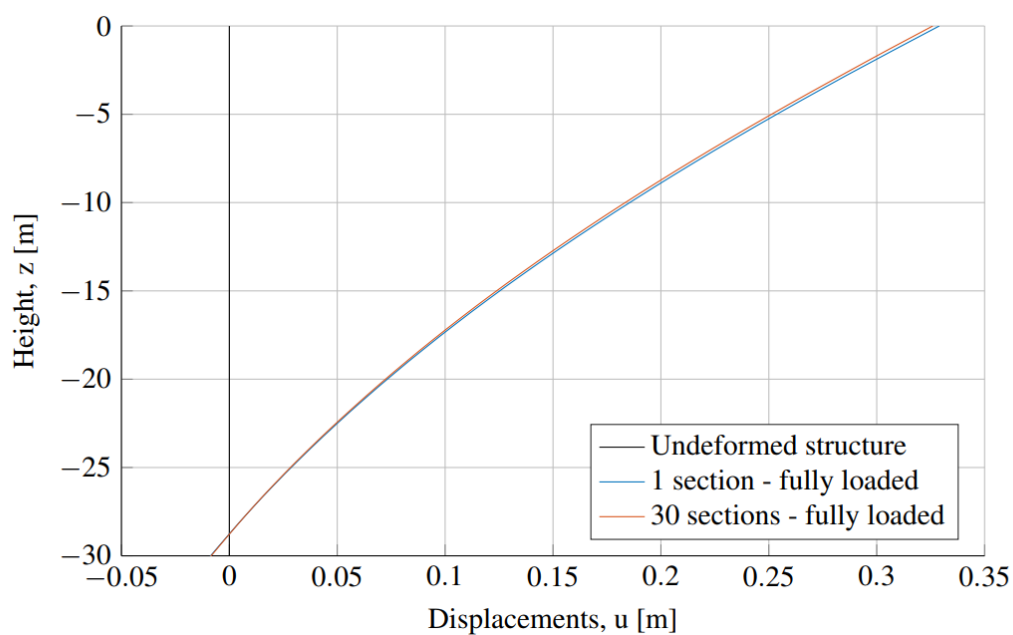


Figure M.1: Verification of the principle of dividing the monopile into several sections.

From the comparison in Figure M.1 almost no difference in the displacement can be observed, and the principle of dividing the monopile into several sections is therefor verified.

M.2 Traction Vector

In this section, the determination of the traction vector is elaborated. The traction vector is illustrated in Figure M.2.

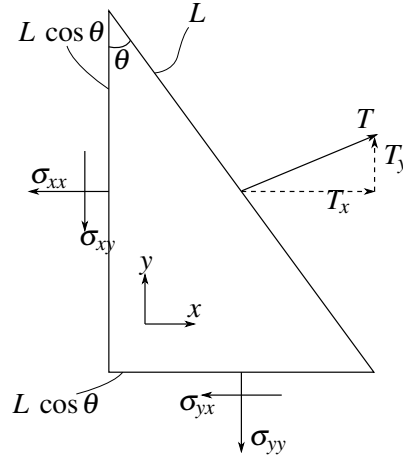


Figure M.2: Illustration of the traction vector [McGinty, 2016, Modified].

The traction vector can be derived from a consideration of horizontal equilibrium, see Figure M.2.

$$T_x L = \sigma_{xx} L \cos \theta + \sigma_{xy} L \cos \theta \quad (\text{M.1})$$

The length, L , cancels out:

$$T_x = \sigma_{xx} \cos \theta + \sigma_{xy} \cos \theta \quad (\text{M.2})$$

By considering the components of unit normal to the surface considered, the equation above can be expressed in terms of:

$$\begin{aligned} T_x &= \sigma_{xx} n_x + \sigma_{xy} n_y \\ n_x &= \cos \theta \\ n_y &= \sin \theta \end{aligned} \quad (\text{M.3})$$

M.3 Load Displacement Curves

M.3.1 Mohr-Coulomb Material Model

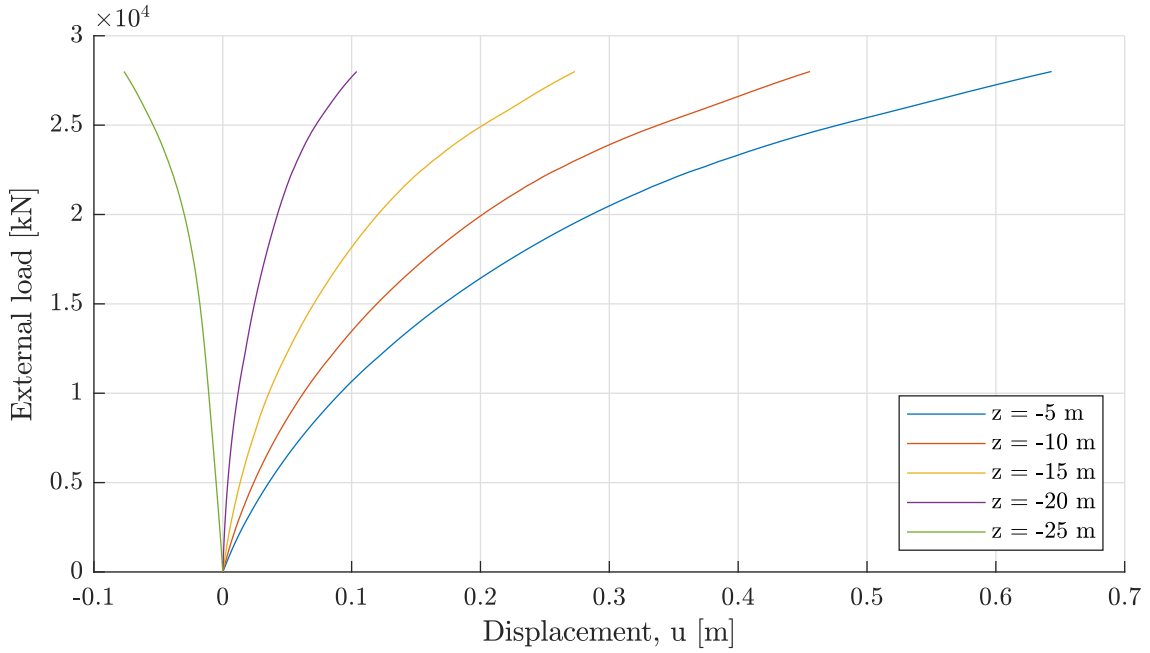


Figure M.3: Load displacement curve extracted from the Mohr-Coulomb material model.

M.3.2 Mohr-Coulomb Material Model

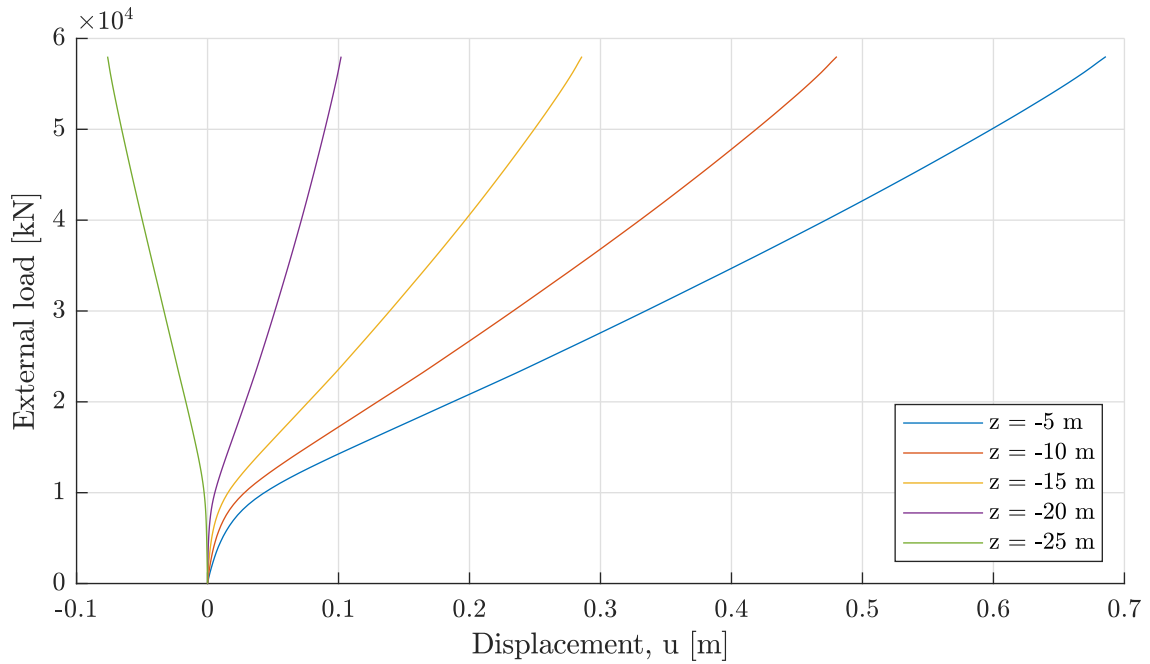


Figure M.4: Load displacement curve extracted from the Hardening Soil Small-strain material model.